Graphene in Strong Light Fields: Floquet Bands and Their Topology

Dissertation
zur Erlangung des Doktorgrades
an der Fakultät für Mathematik, Informatik und
Naturwissenschaften
Fachbereich Physik der Universität Hamburg

vorgelegt von

Frederik Bartelmann

Hamburg

2023

Gutachter/innen der Dissertation:	Prof. Dr. Daniela Pfannkuche Prof. Dr. Tim Wehling
Zusammensetzung der Prüfungskommission:	Prof. Dr. Daniela Pfannkuche Prof. Dr. Tim Wehling Dr. Marta Prada Prof. Dr. Michael Potthoff Prof. Dr. Michael A. Rübhausen
Vorsitzende/r der Prüfungskommission:	Prof. Dr. Michael Potthoff
Datum der Disputation:	21. Juni 2023
Vorsitzender Fach-Promotionsausschuss PHYSIK:	Prof. Dr. Günter H. W. Sigl
Leiter des Fachbereichs PHYSIK:	Prof. Dr. Wolfgang J. Parak
Dekan der Fakultät MIN:	Prof. Dr.-Ing. Norbert Ritter

Zusammenfassung

Die Auswirkungen von starken Lichtfeldern auf die Floquet-Bandstruktur von Graphen werden in einem Multi-Orbital-Tight-Binding-Modell untersucht. Dabei liegt ein besonderer Fokus auf der Spin-Orbit-Wechselwirkung. Bei linearer und zirkularer Polarisation des Lichts wird beobachtet, dass Graphen entsprechend ein $\mathbb{Z}_2$-topologischer Isolator oder ein Chern-Isolator ist. Für Frequenzen im PHz-Bereich wird das frequenzabhängige Verhalten der Bulk-Floquet-Bandstruktur an und um die Dirac-Punkte herum numerisch berechnet und auf topologische Eigenschaften gemäß des „Tenfold Way“ zurückgeführt. Für THz-Frequenzen wird eine Oszillation von Valenz- und Leitungsband als eine Funktion der eingestrahlten Frequenz beobachtet. In Graphen-Streifen mit endlicher Breite führen die Änderungen in der Topologie zu entsprechenden Änderungen in den Randzuständen. Unter Einstrahlung mit zirkular polarisiertem Licht wird die Spin-Entartung der topologisch geschützten Randzustände aufgrund eines photovoltaischen Hall-Effekts, der mit dem intrinsischen Spin-Hall-Effekt konkurriert, aufgehoben. Die Beobachtungen zur Topologie werden für leichte Ablenkungen der Lichtquelle geprüft, und es wird bestätigt, dass die Ergebnisse sich dadurch nicht ändern.

Abstract

The effects of intense light fields on the Floquet band structure of graphene are studied in a multi-orbital tight-binding model, paying special attention to spin-orbit interaction. Under linear and circular polarisation, graphene is observed to be a $\mathbb{Z}_2$- or Chern-topological insulator, respectively. For frequencies in the PHz regime, the frequency-dependent behaviour of the bulk Floquet band structure at and around the Dirac points is computed numerically and attributed to topological properties according to the tenfold way. For THz frequencies, an oscillating behaviour of valence and conduction band as a function of the irradiated frequency is observed. In graphene ribbons of finite width, the changes in topology result in respective changes to the topological edge states. Under irradiation with circularly polarised light, the spin degeneracy of the topologically protected edge states is lifted as a consequence of the competing intrinsic spin-Hall effect of graphene and a light-induced photovoltaic Hall effect. The observations on the topology are further confirmed to hold up under small deflections of the light source.

Contents

Chapter 1

Introduction

In physics, it is often the simplest systems that shape our understanding the most. While for atomic physics this system is, without a doubt, the hydrogen atom, it is less obvious for condensed matter physics. After all, condensed matter involves countless atoms, often of many different kinds. Nonetheless, concepts like Bragg's law [1] and the Bloch theorem [2] have allowed researchers to reduce these complex systems to simpler, periodic models (cf. [3–5]). Still, even in this simpler picture, there are materials that stand out with their simplicity. One such material is graphene. Even though this two-dimensional allotrope of carbon was theorised to exist in 1962 already [6], it was not before 1990 that researchers confirmed its existence [7]. Originally only discovered out of the motivation to "make films of graphite as thin as possible" [7], graphene has since then led to many unique discoveries like Dirac cones [8, 9] and the Klein paradox [10]. Moreover, it was graphene that sparked the research field of topological insulators [11].

The latter has become a major part of condensed matter theory in general, as several properties of materials can be attributed to the topology of their band structures [12]. Most prominently, the quantum Hall effect, as discovered by Berry, [13] is an entirely topological phenomenon (cf. [14] for integer and fractional quantum Hall effect). The results of Berry have been applied to graphene as well, first with the Haldane model that describes a Chern insulator [15, 16], and later with the Kane-Mele model that describes a $\mathbb{Z}_2$-insulator [17, 18]. As a $\mathbb{Z}_2$-insulator, graphene exhibits a spin-Hall effect, a phenomenon that was predicted by Dyakonov and Perel [19, 20].

Based on random matrix theory, Altland and Zirnbauer have fully categorised the multitude of different topological and non-topological insulators into four types of $\mathbb{Z}$, $\mathbb{Z}_2$, $2\mathbb{Z}$ and trivial [21]. Depending on its spatial dimensions and its behaviour under a set of three symmetry operations, every time-independent insulator can be classified as one of these four types [22–24]. For time-dependent systems, insulators are categorised into four analogous types of topological and non-topological insulators [25].

Topological insulators are band insulators whose valence and conduction band have non-trivial so-called topological quantum numbers, quantum numbers that cannot change unless valence and conduction band touch. As formulated in the bulk-boundary correspondence, bulk insulators in which valence and conduction band have different topological quantum numbers exhibit edge states which cross the band gap (cf. [26]). These edge states are topologically protected, i.e. as long as there is a band gap between valence and conduction band, and as long as this gap prevents the topological quantum numbers from becoming trivial, the edge states will always cross the gap.

Since in graphene the band gap between valence and conduction band is small, it took a great effort to show its existence [27–29]. Its magnitude is of 42 µeV [30, 31], and it is generated by spin-orbit interaction between the atomic d-orbitals of the carbon atoms [29, 32].

In this thesis, a tight-binding model with atomic $\mathrm{p_z}$-, $\mathrm{d_{xz}}$- and $\mathrm{d_{yz}}$-orbitals is employed, using the Slater-Koster method [33]. Whenever necessary, additional orbitals are considered. The focus of this thesis lies on the general band structure of graphene and its topological properties in intense light fields. The latter are described via time-dependent electric fields within a dipole approximation. In chapter 3, the effects of these fields are studied analytically at the K-point, a point of high symmetry in the first Brillouin zone of graphene. These results are then used to explain the phenomena of the subsequent chapters.

Chapter 4 considers fully periodic graphene, whereas chapter 5 studies graphene ribbons of finite width, with focus on the edge states. In both chapters, a main focus lies on the effects of different frequencies and polarisations of the light field the graphene sample is irradiated with. In particular the polarisation has been shown to have a significant impact on the edge states of graphene (cf. [34–36]). In this thesis, the time-dependence is handled via Floquet formalism [37–39], a formalism that allows to reduce a linear differential equation that has a periodic dependence on its parameters, to a purely algebraic problem.

In the process of the Floquet formalism, the original band structure of graphene is split into multiple copies that, in this work, are identified with photonic absorptions and emissions. The formalism gives rise to the field of Floquet engineering (cf. [40]) that, in turn, allows to heavily modify the band structures of existing systems via a periodic drive. This has been done in graphene as well, with a plethora of interesting results (e.g. [41–46]).

Floquet engineering with a circularly polarised light field gives rise to the so-called photovoltaic Hall effect, an anomalous Hall effect that is induced by the electric field of the light. This effect in graphene was predicted by Oka at al. [47] and later confirmed experimentally by McIver at al. [48]. Their results are reproduced in chapter 5, but in a system that satisfies different symmetries than [47]. As a result, a competition between the intrinsic spin-Hall effect in graphene and the induced photovoltaic Hall effect is observed to lift the original spin degeneracy of the graphene edge states.

The lift of spin degeneracy can also be noted in the bulk states, i.e. the states of fully periodic graphene. Analytical results of section 3.3 are used to determine the correlation between the spin splitting of bulk states and the polarisation of the light in section 4.2. In addition to this, light of a range of frequencies in the PHz regime is studied, to determine its effect on the band structure of the dressed states. As one consequence, the originally 42 µeV wide band gap increases to the size of several meV.

Due to the originally small width of the band gap, thermal excitations can transfer electrons from valence to conduction band, turning graphene into a metal. Hence, to ensure the insulating properties of graphene, there have been many attempts to increase the band gap [49], be it e.g. via doping [50–53], strain [54, 55] or substrates [56, 57].

Many of these methods bear the risk of breaking symmetries of the graphene sample and, as a result, inducing unwanted effects. In particular the Rashba effect [58, 59] bears the potential of rendering graphene topologically trivial. While this is very well possible for the irradiation with light as well, no Rashba effects are found in this thesis, as is shown in sections 4.2.3 and 5.2.2.

While the rest of this thesis focusses on frequencies in the PHz regime, sections 4.3 and 5.3 discuss the effects of frequencies in the regime of only a few THz up to the ultraviolet spectrum. In section 4.3.2, an oscillation of the band gap in periodic graphene is observed as a function of the frequency of the irradiated light. This oscillation is explained with analytical results from section 3.3. In section 4.3.3, the surrounding band structure is studied, using the results of a bachelor thesis [60] that was supervised by the author.

For graphene ribbons of finite width, THz frequencies are used in section 5.3, to study a finite-size effect. The latter is found to lift the topological protection of the crossing edge states that, in turn, split apart.

The chapters of this thesis are structured as follows:

Chapter 2 introduces the basic concepts, beginning with the graphene lattice, the Bloch theorem, linear combinations of atomic orbitals and spin-orbit interaction. These concepts are then used to explain topology, edge states and Floquet formalism.

Afterwards, the effects of time-dependent electric fields at the K-point are studied in chapter 3. These results serve as a basis for explaining the phenomena of the subsequent chapters.

Chapter 4 is the first of two chapters that contain the physical results of this thesis. It focusses on the effects of different frequencies at the K-point. After some general observations in 4.1, section 4.2 studies how linearly and circularly polarised light affects the band structure at the K-point. These results are verified for angular deflections of the laser setup in section 4.2.3. Section 4.3 then studies the effects of lower frequencies, with a focus on the low THz regime in 4.3.2 and 4.3.3.

The second results chapter, chapter 5, studies the edge states of the graphene band structure. The two main parts of the chapter are the sections 5.2 and 5.3. Section 5.2 focusses again on PHz frequencies, whereas section 5.3 studies finite-size effects and their consequences for the topological protection of the edge states.

The results of this thesis are summarised and evaluated in chapter 6, together with a discussion on possible next steps.

Chapter 2

Basics

2.1 Graphene

Graphene is an allotrope of carbon, the sixth element of the periodic table. Via sp^2 hybridisation, every bulk atom is connected to three respective neighbours, giving rise to a honeycomb lattice structure as depicted in Figure 2.1. The lattice itself is not a Bravais lattice, but can be constructed by overlaying two hexagonal Bravais lattices. This is realised by taking a unit cell with two basis atoms A and B separated by a displacement vector

$$\vec{\delta} = \frac{a}{\sqrt{3}} \begin{pmatrix} 0 \\ 1 \end{pmatrix} \tag{2.1}$$

with the lattice constant a, the value of which is given in appendix A together with all other numerical parameters of this thesis. As depicted in the left-

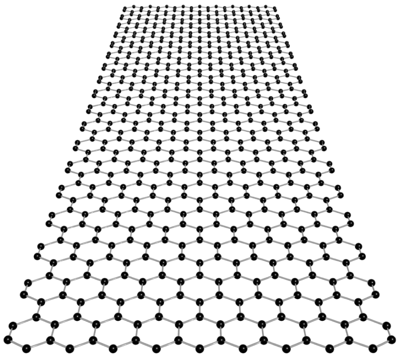

Figure 2.1: Graphene; Carbon atoms (black) form a honeycomb lattice. A rectangular sheet has two types of edges, zigzag and armchair. Here, the horizontal edges are zigzag ones while the vertical ones are of the armchair type.

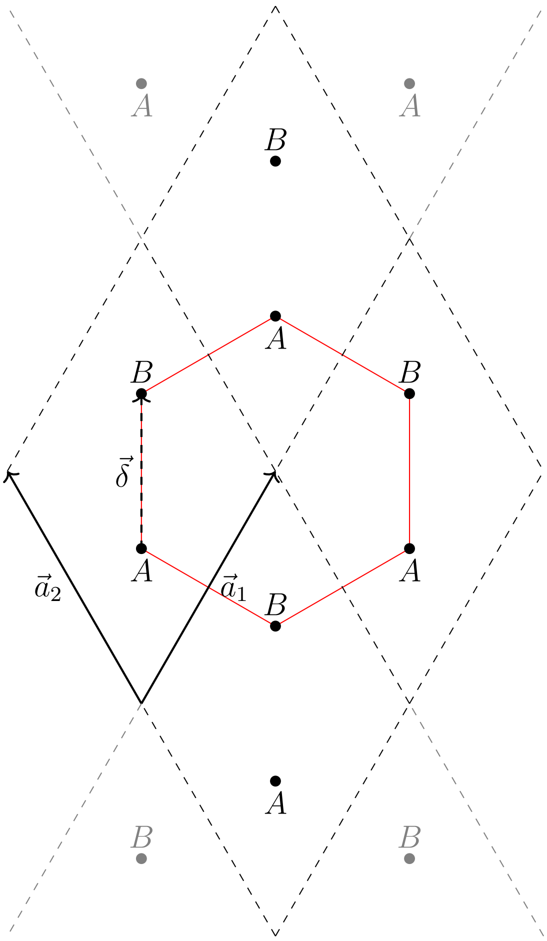

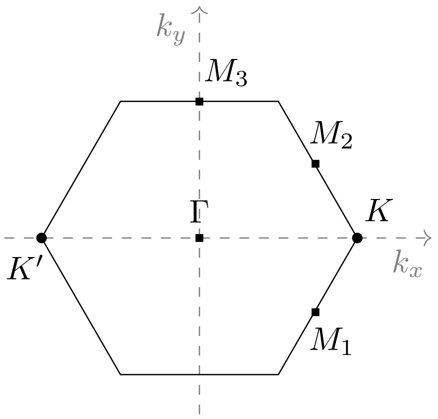

Figure 2.2:
Left: Honeycomb lattice - two identical atoms A and B per unit cell form a hexagon (red) after translation to other cells via the lattice vectors $\vec{a}_{1/2}$. The atoms are separated by a displacement vector $\vec{\delta}$, and both give rise to a respective hexagonal sublattice.
Above: First Brillouin zone - the first Brillouin zone is hexagonal as well. Points of high symmetry have been equipped with their respective labels.

hand side of Fig. 2.2, the translation vectors

$$\vec{a}_1 = \frac{a}{2}\begin{pmatrix} 1 \\ \sqrt{3} \end{pmatrix} \qquad \text{and} \qquad \vec{a}_2 = \frac{a}{2}\begin{pmatrix} -1 \\ \sqrt{3} \end{pmatrix} \tag{2.2}$$

then give rise to the hexagonal lattice structure of the honeycomb lattice via translational symmetry. The first Brillouin zone is hexagonal as well, as depicted in the upper right part of Fig. 2.2. Points of high symmetry are the Γ-point, the K- and K'point and the M_i-points with $i \in \{1, 2, 3\}$. They have been labelled accordingly in the figure. The notion of "K-points" or "M-points" in this thesis will always refer to all points of the respective type. The K-points are located at

$$\vec{K} = \frac{1}{a}\begin{pmatrix} \frac{4\pi}{3} \\ 0 \end{pmatrix} \qquad \text{and} \qquad \vec{K}' = \frac{1}{a}\begin{pmatrix} -\frac{4\pi}{3} \\ 0 \end{pmatrix}. \tag{2.3}$$

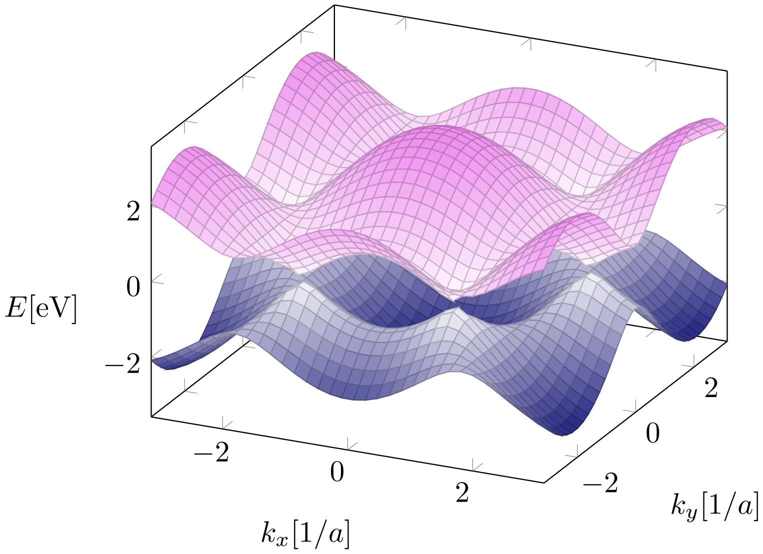

Figure 2.3: Graphene band structure; Valence (blue) and conduction band (purple) would touch at the K-points within the first Brillouin zone if it were not for Spin-orbit interaction opening a band gap between them.

Neither point can be transformed into the respective other by translation with a reciprocal translation vector. However, translation does relate their positions to two other corners of the Brillouin. Hence, each K-point is equivalent to the points obtained via rotations by $2\pi/3$ and $4\pi/3$, respectively.

Every carbon atom in graphene has three respective neighbours. However, carbon has four electrons in its outer shell, one more than possible partners to bond to. The fourth electron resides in a $2\mathrm{p_z}$-orbital that hybridises with the $\mathrm{p_z}$-orbitals of other carbon atoms to form π-bonds responsible for most of the electronic properties of graphene. Most importantly, these electrons and therefore the $2\mathrm{p_z}$-orbitals are the main contributors to valence and conduction band. If it were not for an additional, small contribution from d-orbitals and a spin-orbit interaction between the latter, valence and conduction band would touch at the K-points. This is depicted in Fig. 2.3. The following section will cover the tight-binding model used to describe graphene in this thesis. Concepts like spin and topology will follow in the subsequent sections.

2.2 Periodic Wave Functions

Parts of this section, in particular its subsections 2.2.1 and 2.2.2, are largely based on the book of Czycholl [3]. The corresponding proofs and derivations can be read in greater detail there.

2.2.1 Bloch Theorem

As depicted in Fig. 2.2, the honeycomb lattice can be constructed from the repeated alignment of a two-atomic unit cell. From this, it becomes apparent that graphene satisfies a translational symmetry. More precisely, consider an operation $T_{\vec{R}}$ that translates a function $f(\vec{r})$ such that

$$T_{\vec{R}} f(\vec{r}) = f(\vec{r} + \vec{R}) \tag{2.4}$$

with a translation vector $\vec{R}$.
The lattice being symmetric under translation means that the Hamiltonian H commutes with $T_{\vec{R}}$, i.e.

$$[H, T_{\vec{R}}] = H T_{\vec{R}} - T_{\vec{R}} H = 0. \tag{2.5}$$

The combination of two translational operations is once again a translation,

$$T_{\vec{R}'} T_{\vec{R}} = T_{\vec{R}'+\vec{R}} \qquad \text{and} \qquad T_{-\vec{R}} T_{\vec{R}} = T_0 = \mathbb{1}. \tag{2.6}$$

Thus, the order of application does not matter, resulting in

$$[T_{\vec{R}'}, T_{\vec{R}}] = 0 \tag{2.7}$$

for any translational vectors $\vec{R}$ and $\vec{R}'$.
Eq. (2.5) allows for a choice of simultaneous eigenvectors $\psi(\vec{r})$ for both H and $T_{\vec{R}}$, such that

$$H\psi(\vec{r}) = E\psi(\vec{r}) \qquad \text{and} \qquad T_{\vec{R}}\psi(\vec{r}) = c(\vec{R})\psi(\vec{r}). \tag{2.8}$$

Because of eq. (2.6), the eigenvalue function c must satisfy

$$c(\vec{R}' + \vec{R}) = c(\vec{R}') \cdot c(\vec{R}) \quad \text{and} \quad c(\vec{R}) \cdot c(-\vec{R}) = 1. \tag{2.9}$$

Furthermore, because of the normalisation of the wave function, $c(\vec{R})$ must be normalised as well, since

$$|c(\vec{R})|^2 = \int d^3\vec{r} |c(\vec{R})|^2 \, |\psi(\vec{r})|^2 = \int d^3\vec{r} |\psi(\vec{r} + \vec{R})|^2 = \int d^3\vec{r} |\psi(\vec{r})|^2 = 1. \tag{2.10}$$

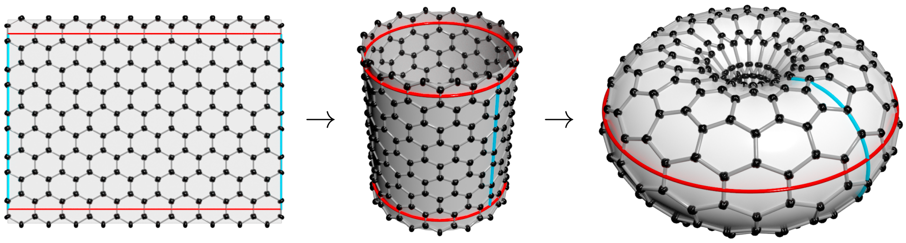

Figure 2.4: Periodic boundary conditions; Electrons that pass one red or cyan line re-emerge from the other line of the same respective colour. By identification of first the cyan and then the red lines, the originally rectangular sheet can first be interpreted mathematically as a cylinder and then as a torus, but without the depicted curvatures. For illustrative purposes, a larger number of atoms than in Fig. 2.2 is depicted within one cell.

Eq. (2.9) and (2.10) lead to the conclusion that $c(\vec{R})$ can be written as

$$c(\vec{R}) = e^{\mathrm{i}\vec{k}\vec{R}} \tag{2.11}$$

with some *reciprocal vector* $\vec{k}$.
Thus, the eigenfunctions to the Hamiltonian need to be of the form

$$\psi_{\vec{k}}(\vec{r}) = \frac{1}{\sqrt{N}} e^{\mathrm{i}\vec{k}\vec{r}} \cdot u_{\vec{k}}(\vec{r}) \tag{2.12}$$

with normalising prefactor $1/\sqrt{N}$ and the lattice-periodic *Bloch factor*

$$u_{\vec{k}}(\vec{r}) = u_{\vec{k}}(\vec{r} + \vec{R}), \tag{2.13}$$

where $\vec{R}$ is an arbitrary translation vector $\vec{R}$ that leaves the overall system invariant. Eq. (2.12) is known as the *Bloch theorem* [2]. It allows to restrict the overall system to only a single unit cell and treat every electron moving to a neighbouring cell as if it would re-enter the original cell from the other side. This allows to consider the unit cell mathematically like a torus as conceptually illustrated in Fig. 2.4.

Any translation vector $\vec{R}$ that describes a symmetry operation on the lattice like above, can be written as a sum of integer multiples n_i of the lattice vectors $\vec{a}_i$,

$$\vec{R} = \sum_i n_i \cdot \vec{a}_i. \tag{2.14}$$

Eq. (2.9) can thus be written as

$$c(\vec{R}) = \prod_i c(\vec{a}_i)^{n_i}. \tag{2.15}$$

It is therefore convenient to write $\vec{k}$ in terms of *reciprocal lattice vectors* $\vec{b}_i$ defined by the relations

$$\vec{a}_i\vec{b}_j = 2\pi\delta_{ij} \qquad \text{and} \qquad \vec{k} = \sum_i k_i\vec{b}_i \tag{2.16}$$

with coordinates k_i in the *reciprocal space*.

To discuss the consequences of the Bloch theorem for the Schrödinger equation, assume a general time-independent Hamiltonian

$$H(\vec{r}) = -\frac{\hbar^2\nabla^2}{2m} + V(\vec{r}). \tag{2.17}$$

Application to the wave function (2.12) leads to

$$\begin{aligned} H(\vec{r})\psi_{\vec{k}}(\vec{r}) &= \left(-\frac{\hbar^2\nabla^2}{2m} + V(\vec{r})\right)\frac{1}{\sqrt{N}}e^{\mathrm{i}\vec{k}\vec{r}}u_{\vec{k}}(\vec{r}) && (2.18)\\ &= \epsilon(\vec{k})\frac{1}{\sqrt{N}}e^{\mathrm{i}\vec{k}\vec{r}}u_{\vec{k}}(\vec{r}) && (2.19)\\ &= \frac{1}{\sqrt{N}}e^{\mathrm{i}\vec{k}\vec{r}}\underbrace{\left(\frac{\hbar^2}{2m}\left(-\mathrm{i}\nabla + \vec{k}\right)^2 + V(\vec{r})\right)}_{=:h(\vec{k})}u_{\vec{k}}(\vec{r}). && (2.20)\end{aligned}$$

where the last two lines form a new differential equation

$$h(\vec{k})u_{\vec{k}}(\vec{r}) = \epsilon(\vec{k})u_{\vec{k}}(\vec{r}) \tag{2.21}$$

for only $u_{\vec{k}}(\vec{r})$ and for a fixed $\vec{k}$. The solutions $u_{n,\vec{k}}(\vec{r})$ to this differential equation and their eigenvalues $\epsilon_n(\vec{k})$ are both lattice-periodic, making eq. (2.21) a boundary value problem within a single unit cell. The $u_{n,\vec{k}}(\vec{r})$ can thus be orthonormalised within one unit cell, such that for identical $\vec{k}$ they satisfy

$$\frac{1}{V_{\mathrm{UC}}}\int_{V_{\mathrm{UC}}} d\vec{r}\; u^*_{n,\vec{k}}(\vec{r})u_{n',\vec{k}}(\vec{r}) = \delta_{nn'} \tag{2.22}$$

with the volume V_{UC} of the unit cell. The same orthonormality is passed on to the wave functions $\psi_{n,\vec{k}}(\vec{r})$ that then satisfy

$$\int_V \psi^*_{n,\vec{k}}(\vec{r})\psi^*_{n',\vec{k}'}(\vec{r})d\vec{r} = \delta_{nn'}\delta_{\vec{k}\vec{k}'}. \tag{2.23}$$

Note that here the integral is over the entire volume of the lattice, V.

The overall wave function $\psi_{n,\vec{k}}(\vec{r})$ and its energy eigenvalues $\epsilon_n(\vec{k})$ are thus classified by n, which will be labelled the *band index*, and a reciprocal vector $\vec{k}$. The latter only takes discrete values. However, since these values are dense in reciprocal space, they will often be treated as if they were continuous. Furthermore, due to the periodicity of the wave functions and the eigenvalues, the vectors $\vec{k}$ can, due to their periodicity, be restricted to the first *Brillouin zone* in reciprocal space. This thesis will use the names Brillouin zone and first Brillouin zone interchangeably, as only the first will be considered. The first Brillouin zone for graphene is depicted in the top-right part of Fig. 2.2.
The eigenvalues $\epsilon_n(\vec{k})$ are therefore continuous functions of $\vec{k}$ and form *energy bands* throughout the first Brillouin zone. The set of these bands labelled by n is called the *band structure*. The *valence* and *conduction band* of graphene, i.e. the energetically highest band that is occupied by electrons and the lowest that is unoccupied, are depicted in Fig. 2.3. Between them lies the *Fermi energy*, the highest energy of the unperturbed occupied band structure.
The following subsections will introduce the tight-binding model as a means to compute the band structure.

2.2.2 Tight-binding Model

The tight-binding model is a means to simplify lattice-periodic systems and to therefore ease the computation of the band structure while also improving the intuitive understanding of the system. It is based on the assumption that the electrons are localised close to the atoms inside the lattice. The overall system will therefore be treated as a combination of single-atomic systems.
Let ϕ_n be the eigenfunction to a Hamiltonian of such an isolated atom at position $\vec{R}$, i.e.

$$H_{\vec{R}}(\vec{r})\phi_n(\vec{r}-\vec{R}) = E_n\phi_n(\vec{r}-\vec{R}) \tag{2.24}$$

with n here labelling the different quantum numbers. Here, it has been assumed that the system only consists of identical atoms and that E_n is therefore independent of $\vec{R}$. The Hamiltonian

$$H_{\vec{R}}(\vec{r}) = \frac{\vec{p}^2}{2m} + v(\vec{r}-\vec{R}) \tag{2.25}$$

includes the atomic potential $v(\vec{r}-\vec{R})$ generated from the core charge. A Hamiltonian describing a lattice system can then be written as a sum of such atomic Hamiltonians, i.e.

$$H(\vec{r}) = \frac{\vec{p}^2}{2m} + \sum_{\vec{R}} v(\vec{r} - \vec{R}) \tag{2.26}$$

$$= H_{\vec{R}}(\vec{r}) + \Delta V_{\vec{R}}(\vec{r}) \tag{2.27}$$

$$\text{with } \Delta V_{\vec{R}}(\vec{r}) = \sum_{\vec{R}' \neq \vec{R}} v(\vec{r} - \vec{R}'). \tag{2.28}$$

The term $\Delta V_{\vec{R}}(\vec{r})$ is the potential of all atoms *not* at position $\vec{R}$, evaluated at position $\vec{r}$, and will be considered as a small perturbation.
Assuming $\Delta V_{\vec{R}}(\vec{r})$ is approximately zero[1] in the close vicinity of $\vec{R}$, the solutions $\phi_n(\vec{r} - \vec{R})$ to $H_{\vec{R}}$ in eq. (2.24) are a good approximation for solutions to $H(\vec{r})$ in eq. (2.26) as well, i.e.

$$H\phi_n(\vec{r} - \vec{R}) \;=\; (H_{\vec{R}}(\vec{r}) + \underbrace{\Delta V_{\vec{R}}(\vec{r})}_{\approx 0})\phi_n(\vec{r} - \vec{R}) \;\approx\; E_n\phi_n(\vec{r} - \vec{R}). \tag{2.29}$$

While these solutions are not yet Bloch states, they can be constructed to be, via

$$\psi_{n\vec{k}}(\vec{r}) = \frac{1}{\sqrt{N}} \sum_{\vec{R}} e^{\mathrm{i}\vec{k}\vec{R}} \phi_n(\vec{r} - \vec{R}). \tag{2.30}$$

These new wave functions $\psi_{n,\vec{k}}(\vec{r})$ are both periodic in $\vec{R}$ and satisfy

$$H(\vec{r})\psi_{n,\vec{k}}(\vec{r}) \approx E_{n,\vec{k}}\psi_{n,\vec{k}}(\vec{r}). \tag{2.31}$$

They are, however, not orthonormal as

$$\begin{aligned} \langle \psi_{n,\vec{k}} | \psi_{n',\vec{k}} \rangle &= \frac{1}{N} \sum_{\vec{R}_1, \vec{R}_2} e^{i\vec{k}(\vec{R}_1 - \vec{R}_2)} \int d\vec{r}\; \phi_n^*(\vec{r} - \vec{R}_2)\phi_{n'}(\vec{r} - \vec{R}_1) \\ &= \sum_{\vec{R}} e^{i\vec{k}\vec{R}} \int d\vec{r}\; \phi_n^*(\vec{r} - \vec{R})\phi_{n'}(\vec{r}) \\ &=: \delta_{nn'} + \sum_{\vec{R} \neq 0} e^{i\vec{k}\vec{R}} \alpha_{nn'}(\vec{R}) \end{aligned} \tag{2.32}$$

with

$$\alpha_{nn'}(\vec{R}) = \int d\vec{r}\; \phi_n^*(\vec{r} - \vec{R})\phi_{n'}(\vec{r}). \tag{2.33}$$

---

[1] Near the position $\vec{R}$ of an atom, the distribution of the other atoms is nearly isotropic. Thus, their contribution is suppressed by screening effects.

Due to the strong localisation of the atomic wave functions $\phi_n(\vec{r})$, the term $\alpha_{nn'}(\vec{R})$ can be assumed to be small. However, it is typically non-zero, meaning that the scalar product (2.32) does not vanish for $n \neq n'$. Hence, the Bloch states (2.30) are not perfectly orthogonal.
Nonetheless, the term $\alpha_{nn'}(\vec{R})$ is typically small. Hence, albeit not being exact, the expression

$$\epsilon_n(\vec{k}) = \frac{\langle \psi_{n\vec{k}} | H(\vec{r}) | \psi_{n\vec{k}} \rangle}{\langle \psi_{n,\vec{k}} | \psi_{n,\vec{k}} \rangle} \tag{2.34}$$

is a good approximation to the energy values of the system. While its denominator has been computed in Eq. (2.32), its numerator is

$$\begin{aligned} \langle \psi_{n\vec{k}} | H(\vec{r}) | \psi_{n\vec{k}} \rangle &= E_n \langle \psi_{n\vec{k}} | \psi_{n\vec{k}} \rangle \\ &\quad + \frac{1}{N} \sum_{\vec{R}_1, \vec{R}_2} e^{i\vec{k}(\vec{R}_1 - \vec{R}_2)} \int d\vec{r}\; \phi_n^*(\vec{r} - \vec{R}_2) \sum_{\vec{R}_3 \neq \vec{R}_1} v(\vec{r} - \vec{R}) \phi_{n'}(\vec{r} - \vec{R}_1). \end{aligned} \tag{2.35}$$

The product over the three functions $\phi_n^*(\vec{r} - \vec{R}_2)$, $v(\vec{r} - \vec{R})$ and $\phi_n(\vec{r} - \vec{R}_1)$ will not be discussed here. A full discussion can instead be found in [3, pg. 121-122] where they show that the energy $\epsilon_n(\vec{k})$ can, in good approximation, be assumed to only involve terms coupling nearest and possibly next-nearest neighbouring atoms.

To solve the issue of the non-orthogonal states that was shown in equation (2.32), the basis will be modified in the following. The resulting basis functions consists of the so-called *Wannier functions*, also called *Wannier states*.

Wannier Functions

The problem with the tight-binding approach as introduced in the parent subsection is that the atomic wave functions $\phi_n(\vec{r} - \vec{R})$ in Eq. (2.30) do not lead to an orthogonal basis of Bloch states $\psi_{n\vec{k}}(\vec{r})$. To solve this issue, instead assume that the $\psi_{n\vec{k}}(\vec{r})$ are orthogonal to begin with, and therefore replace the atomic wave functions with Wannier functions defined as

$$w_n(\vec{r} - \vec{R}) := \frac{1}{\sqrt{N}} \sum_{\vec{k}} e^{-\mathrm{i}\vec{k}\vec{R}} \psi_{n\vec{k}}(\vec{r}) \tag{2.36}$$

with discrete reciprocal lattice points $\vec{k}$. For an infinite lattice, the sum is replaced with an integral. The Wannier functions are orthonormal to one another with respect to their index n. The Bloch states, in turn, are re-obtained via

$$\psi_{n\vec{k}}(\vec{r}) = \frac{1}{\sqrt{N}} \sum_{\vec{R}} e^{\mathrm{i}\vec{k}\vec{R}} w_n(\vec{r} - \vec{R}). \tag{2.37}$$

With the use of Wannier functions, Eq. (2.35) simplifies to

$$\epsilon_n(\vec{k}) := \langle \psi_{n\vec{k}} | H(\vec{r}) | \psi_{n\vec{k}} \rangle = \tilde{E}_n(\vec{k}) + \sum_{\vec{R} \neq 0} e^{-\mathrm{i}\vec{k}\vec{R}} \tilde{\lambda}(\vec{R}) \tag{2.38}$$

$$\text{with } \tilde{E}_n(\vec{k}) = \int d\vec{r}\; w_n^*(\vec{r}) \left(\frac{\vec{p}^2}{2m} + \sum_{\vec{R}} v(\vec{r} - \vec{R}) \right) w_n(\vec{r}) \tag{2.39}$$

$$\text{and } \tilde{\lambda}_{\vec{R}}(\vec{k}) = \int d\vec{r}\; w_n^*(\vec{r} - \vec{R}) v(\vec{r} - \vec{R}) w_n(\vec{r}), \tag{2.40}$$

where three-centre integrals have been neglected. The argument for why those can be neglected, is given in [3, pg. 121-122], but will not be discussed further, here.

The same reasoning also states that $\tilde{\lambda}(\vec{R})$ is non-vanishing only if $\vec{R}$ connects two nearest neighbours or possibly second-nearest neighbours. Equation (2.38) therefore allows to intuitively write the tight-binding Hamiltonian in matrix form as

$$H(\vec{k}) = \sum_{n,\vec{R}} \tilde{E}(\vec{k}) |n, \vec{R}\rangle\langle n, \vec{R}| + \sum_{n,\vec{R},\vec{R}'} t_{\vec{R}\vec{R}'}(\vec{k}) |n, \vec{R}\rangle\langle n, \vec{R}'| \tag{2.41}$$

with the *hopping matrix elements*

$$t_{\vec{R}\vec{R}'}(\vec{k}) = \begin{cases} t := \tilde{\lambda}_{\vec{R}}(\vec{k}) & \text{for } \vec{R} \text{ connecting nearest neighbours} \\ 0 & \text{else} \end{cases}. \tag{2.42}$$

The Wannier states are related to Eq. (2.41) via

$$w_n(\vec{r} - \vec{R}) = \langle \vec{r} | n, \vec{R} \rangle. \tag{2.43}$$

The hopping matrix elements describe the tunnelling of an electron between two lattice sites which can be imagined as an electron "hopping" from one lattice site to another. Computations throughout this thesis will only assume hopping between nearest neighbours like in Eq. (2.42), unless stated otherwise.

2.2.3 LCAO Method

The Wannier states (2.36) of a system can be difficult to obtain. A common approach is to instead use a *linear combination of atomic orbitals* or short the *LCAO* method. This method uses the same point of departure as the previous section, but the Wannier states are replaced with sums of atomic orbital wave functions

$$w(\vec{r}-\vec{R}) = \sum_n a_n \phi_n(\vec{r}-\vec{R}). \tag{2.44}$$

with coefficients a_n denoting the contribution of the respective orbital. The label n here denotes all the quantum numbers corresponding to it.

While a single atomic orbital typically does not suffice to properly describe the physical properties of a tight-binding system, an increasing number of orbitals gradually improves this situation and makes for a better approximation. The computation of the resulting matrix elements of the Hamiltonian matrix (2.41) is then simplified by the incorporation of the symmetries of the atomic orbitals.

Slater and Koster [33][2] have computed which terms contribute the most to the tight-binding Hamiltonian based on angle, orbitals involved and two-centre integrals between the respective nearest-neighbour orbitals up to atomic d-orbitals. The numerical values of these two-centre integrals are given in appendix A. The Slater-Koster terms allow to easily construct a lattice Hamiltonian where every atomic orbital for every lattice site is represented by one respective basis vector. For graphene, a frequent choice throughout this thesis will be the basis of $2\mathrm{p_z}$-, $3\mathrm{d_{xz}}$- and $3\mathrm{d_{yz}}$-orbitals.[3] The resulting vector representation for this configuration is then

$$\left(|A,\mathrm{p_z}\rangle,\ |A,\mathrm{d_{xz}}\rangle,\ |A,\mathrm{d_{yz}}\rangle,\ |B,\mathrm{p_z}\rangle,\ |B,\mathrm{d_{xz}}\rangle,,\ |B,\mathrm{d_{yz}}\rangle\right), \tag{2.45}$$

where the first entry A/B denotes the sublattice and the second the atomic orbital. In the choice of basis (2.45), e.g. a vector

$$v = \frac{1}{\sqrt{3}}(1,0,0,0,1,1)^t \tag{2.46}$$

would consist of equal portions of an electron in the $\mathrm{p_z}$-orbital on sublattice A and in the $\mathrm{d_{xz}}$- and $\mathrm{d_{yz}}$-orbital on sublattice B.

---

[2] See [32, pg. 14] for a notation that is more in agreement with the notation used here.

[3] As mentioned in section 2.1, the $\mathrm{p_z}$-orbitals are most relevant for the graphene band structure. The energetically closest orbitals that have non-vanishing matrix elements with $\mathrm{p_z}$, are the $\mathrm{d_{xz}}$- and $\mathrm{d_{yz}}$-orbitals. Some of their effects will be discussed in section 2.3.

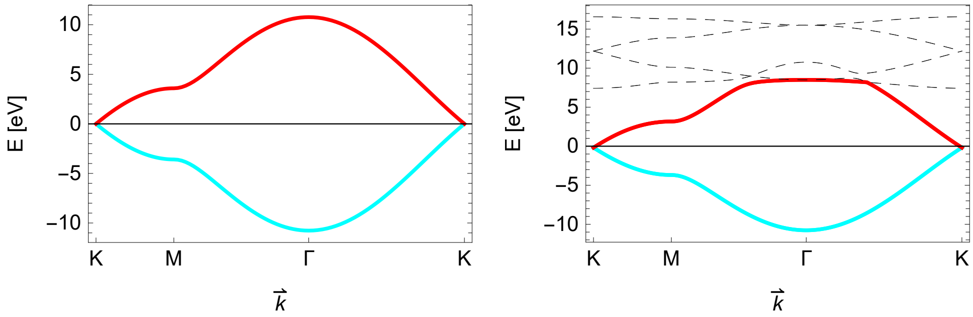

(a) without d-orbitals (b) with d-orbitals

Figure 2.5: Graphene band structure plotted along points of high symmetry; With the introduction of d-bands (dashed, black), valence (cyan) and conduction band (red) change in shape. Furthermore, the Fermi energy gets shifted slightly towards negative values. Since the band structure is symmetric in the reciprocal space, it has not been specified which K- or M-points are depicted.

Note that the addition of d-orbitals has a notable effect to valence and conduction band as depicted in Fig. 2.5. As a consequence, particle-hole symmetry, a symmetry that relates every state of energy $E(\vec{k})$ to a a state with energy $-E(\vec{k})$, is broken. The resulting discrepancy between valence and conduction band is illustrated in Fig. 2.6. This will be of particular importance in section 2.5.2.

The system will be expanded further via the inclusion of spin. The latter doubles the dimension of the vector space by assigning every orbital to either the configuration spin-up or spin-down, with z as the spin quantisation axis. Spin-orbit interaction between the d-orbitals then opens a band gap between valence and conduction band at the K-points. Before the corresponding discussion in section 2.3, however, the completeness and compatibility of the system under inclusion of an external electric field will be discussed in the remainder of section 2.2.

Completeness of the Orbital Basis

The orbital basis (2.45) consists of $2\mathrm{p_z}$- and $3\mathrm{d_{xz/yz}}$-orbitals. As will be shown in section 2.3, this basis suffices to describe unperturbed graphene with spin-orbit interaction. However, it is insufficient for the description of general electric perturbations acting on a single atom (cf. [61–65]).

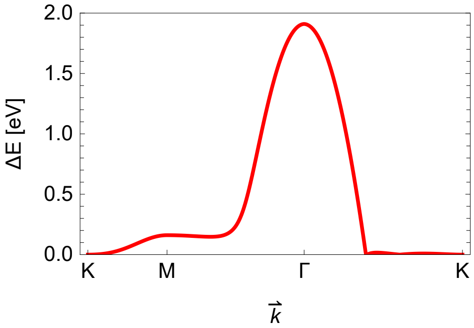

Figure 2.6: Asymmetry between valence and conduction band; With the introduction of d-orbitals, valence and conduction band are no longer energetically symmetric around the Fermi energy. The deviation from the symmetry, $\Delta E = ||E_{\mathrm{CB}} - E_{\mathrm{F}}| - |E_{\mathrm{VB}} - E_{\mathrm{F}}||$, gives a measure for the asymmetry. Here, CB and VB denote conduction and valence band, and F denotes the Fermi energy.

To understand this, consider a spatially constant electric field in x-direction with a field strength E_0. It corresponds (possibly after a gauge transformation) to a scalar potential $\Phi(x) = E_0 \cdot x$. Similarly, fields in y- and z directions correspond to potentials proportional to y and z. The problem with the orbital basis then becomes aware by considering the following diagram:

$$\begin{tikzcd}
\mathrm{d_{yz}} \arrow[r, leftrightarrow, "x"] \arrow[d, leftrightarrow, "y"] & ? \arrow[d, leftrightarrow, "y"] \\
\mathrm{p_z} \arrow[r, leftrightarrow, "x"] & \mathrm{d_{xz}}
\end{tikzcd} \tag{2.47}$$

Since the n-quantum number is always $n = 2$ for $\mathrm{p_z}$ and $n = 3$ for $\mathrm{d_{xz/yz}}$ in this chapter, it has no longer been written explicitly.

A spatially constant electric field in x-direction couples the $\mathrm{p_z}$- and the $\mathrm{d_{xz}}$-orbital, whereas a field in y-direction analogously couples the $\mathrm{p_z}$- and the $\mathrm{d_{yz}}$-orbital. However, a field in y-direction does not couple the $\mathrm{d_{xz}}$-orbital to anything. Similarly, the $\mathrm{d_{yz}}$-orbital has no coupling partner for a field in x-direction. Hence, the diagram (2.47) does not commute, and neither do the scalar potentials, i.e.

$$[E_0 \cdot x, E_0 \cdot y] = E_0^2 \cdot [x, y] \neq 0 \tag{2.48}$$

in the restricted orbital space. Thus, the system depends on the order of application of electric fields in x- and y- direction. This is particularly problematic for circularly polarised light that oscillates between both.

To solve this issue, it is necessary to include an additional, artificial 4$\mathrm{f_{xyz}}$-orbital. With it, the diagram does commute:

$$\begin{tikzcd}
\mathrm{d_{yz}} \arrow[r, leftrightarrow, "x"] \arrow[d, leftrightarrow, "y"] & \mathrm{f_{xyz}} \arrow[d, leftrightarrow, "y"] \\
\mathrm{p_z} \arrow[r, leftrightarrow, "x"] & \mathrm{d_{xz}}
\end{tikzcd} \tag{2.49}$$

This $\mathrm{f_{xyz}}$-orbital is not a natural one, as will be derived below. The following steps are based on similar computations by Foreman [61].

Consider a basis of orbitals centred at only one single atom. For the basis

$$(|\mathrm{p_z}\rangle,\ |\mathrm{d_{xz}},\rangle,\ |\mathrm{d_{yz}}\rangle)\,, \tag{2.50}$$

compute the matrix elements

$$\langle l_1|\hat{o}|l_2\rangle \tag{2.51}$$

with $l_{1/2} \in \{\mathrm{p_z}, \mathrm{d_{xz}}, \mathrm{d_{yz}}\}$ and $\hat{o} \in \{x, y\}$. The only non-zero elements are

$$\langle \mathrm{p_z}|x|\mathrm{d_{xz}}\rangle = \langle \mathrm{p_z}|y|\mathrm{d_{yz}}\rangle =: c \in \mathbb{R} \tag{2.52}$$

and their identical conjugates, with some real value c. Thus, when written as a matrix in the basis (2.50), the operators corresponding to x and y become

$$x = \begin{pmatrix} 0 & c & 0 \\ c & 0 & 0 \\ 0 & 0 & 0 \end{pmatrix} \qquad \text{and} \qquad y = \begin{pmatrix} 0 & 0 & c \\ 0 & 0 & 0 \\ c & 0 & 0 \end{pmatrix} \tag{2.53}$$

whose commutator is

$$[x, y] = \begin{pmatrix} 0 & 0 & 0 \\ 0 & 0 & c^2 \\ 0 & -c^2 & 0 \end{pmatrix} \neq 0. \tag{2.54}$$

However, via the inclusion of the 4$\mathrm{f_{xyz}}$-orbital, one obtains additional non-zero matrix elements

$$\langle \mathrm{f_{xyz}}|y|\mathrm{d_{xz}}\rangle = \langle \mathrm{f_{xyz}}|x|\mathrm{d_{yz}}\rangle =: b \in \mathbb{R} \tag{2.55}$$

which in the basis

$$(|\mathrm{p_z}\rangle,\ |\mathrm{d_{xz}},\rangle,\ |\mathrm{d_{yz}}\rangle,\ |\mathrm{f_{xyz}}\rangle) \tag{2.56}$$

lead to a change in the matrices (2.53) and thus to the new commutator

$$[x, y] = \begin{pmatrix} 0 & 0 & 0 & 0 \\ 0 & 0 & c^2 - b^2 & 0 \\ 0 & b^2 - c^2 & 0 & 0 \\ 0 & 0 & 0 & 0 \end{pmatrix}. \tag{2.57}$$

This commutator does indeed vanish for $b = \pm c$. For that reason, assume

$$b \equiv c. \tag{2.58}$$

This condition is *not* satisfied by natural $4\mathrm{f}_{\mathrm{xyz}}$-orbitals as they appear in graphene. Hence is why the notion of *artificial* orbitals is emphasised here. This may seem unintuitive, since for real graphene the coordinates x and y do commute. However, to exactly describe real graphene, one would need to include *all* orbitals. Since this cannot be done in this thesis, one singular artificial $\mathrm{f}_{\mathrm{xyz}}$-orbital will serve in their stead.

The new effective $4\mathrm{f}_{\mathrm{xyz}}$-orbital has been found to restore the commutativity if its effective Bohr radius is approximately 5/3 times that of the other orbitals in graphene. Similarly to the Slater-Koster approach, the leading terms connecting the $\mathrm{f}_{\mathrm{xyz}}$-orbitals with orbitals of neighbouring atoms are provided by Lendi [66]. Since no reference for the corresponding two-centre integrals has been found in the literature, they have been estimated based on a comparison with the other orbitals, under consideration of the modified effective Bohr radius. However, there has neither been a notable change to valence- and conduction band nor to the d-bands based on the choice of these parameters at all. This is due to the significant energetic difference of the $\mathrm{f}_{\mathrm{xyz}}$-orbital. Its onsite energy has been set to $\epsilon_{\mathrm{f}_{\mathrm{xyz}}} = 26\,\mathrm{eV}$. This is an estimate based on the comparison of the energy levels of graphene to those of fullerenes for which the f-orbital energies have been computed by multiple groups [67–69].

2.2.4 Envelope Functions

Since the external fields affecting graphene in this thesis typically do not satisfy the symmetries of the lattice, it is necessary to introduce the notion of *envelope functions*. The latter will be used to further isolate the part of the wave function that resides within a unit cell, and to then apply the non-periodic part of the perturbation only to these external envelope functions. The following derivation will be based on and largely copied from the lecture notes of Schmalian [70].

Assume a spatially non-periodic perturbation $V_{\mathrm{ext}}(\vec{r},t)$ to the Schrödinger equation, i.e.

$$H(\vec{r},t) = \frac{(-\mathrm{i}\hbar\nabla)^2}{2m} + U(\vec{r}) + V_{\mathrm{ext}}(\vec{r},r) \; = \; H_0(\vec{r}) + V_{\mathrm{ext}}(\vec{r},t). \tag{2.59}$$

The typical perturbation in this thesis will be of the form $V_{\mathrm{ext}}(\vec{r},t) = -e\Phi(\vec{r},t)$. Assume the resulting electric force $e\vec{E}(\vec{r},t) = -\nabla V_{\mathrm{ext}}(\vec{r},t)$ to be small in comparison to the energy scales of the unperturbed Hamiltonian. Further assume wave functions like in Eqs. (2.36) and (2.37), i.e.

$$\psi_{n\vec{k}}(\vec{r}) = \frac{1}{\sqrt{N}} \sum_{\vec{R}} e^{\mathrm{i}\vec{k}\vec{R}} w_n(\vec{r}-\vec{R}) \tag{2.60}$$

with lattice vectors $\vec{R}$ and Wannier functions

$$w_n(\vec{r}-\vec{R}) = \frac{1}{\sqrt{N}} \sum_{\vec{k}} e^{-\mathrm{i}\vec{k}\vec{R}} \psi_{n\vec{k}}(\vec{r}). \tag{2.61}$$

Application of H_0 to Eq. (2.61) yields

$$H_0 w_n(\vec{r}-\vec{R}) = \frac{1}{\sqrt{N}} \sum_{\vec{k}} e^{-\mathrm{i}\vec{k}\vec{R}} \epsilon_{n,\vec{k}} \psi_{n\vec{k}}(\vec{r}), \tag{2.62}$$

where the $\epsilon_{n,\vec{k}}$ are the respective eigenvalues $\epsilon_n(\vec{k})$ of the $\psi_{n,\vec{k}}$ under application of H_0, as defined in Eq. (2.38). The functional dependency on $\vec{k}$ has been demoted to an index, since all computations in this subsection are performed in real space.

Expanding Eq. (2.62) according to (2.61) then leads to

$$\begin{aligned} H_0 w_n(\vec{r}-\vec{R}) &= \sum_{\vec{R}'} \frac{1}{N} \sum_{\vec{k}} e^{\mathrm{i}\vec{k}(\vec{R}'-\vec{R})} \epsilon_{n,\vec{k}} w_n(\vec{r}-\vec{R}) \\ &= \sum_{\vec{R}'} \epsilon_n(\vec{R}'-\vec{R}) w_n(\vec{r}-\vec{R}) \end{aligned} \tag{2.63}$$

with

$$\epsilon_n(\vec{R}) := \frac{1}{N} \sum_{\vec{k}} \epsilon_{n,\vec{k}} e^{\mathrm{i}\vec{k}\vec{R}}. \tag{2.64}$$

Now define envelope functions $f_{n,\vec{R}}(t)$ as a part of a general wave function

$$\psi(\vec{r},t) = \sum_{n,\vec{R}} f_{n,\vec{R}}(t) e^{\mathrm{i}\vec{k}\vec{R}} w_n(\vec{r}-\vec{R}) \tag{2.65}$$

in such a way that they satisfy normalisation conditions. Their physical interpretation will follow at the end of this subsection, when their connection to the Schrödinger equation has been established. The latter reshapes to

$$\begin{aligned}
\mathrm{i}\hbar\frac{\partial\psi(\vec{r},t)}{\partial t} &= (H_0(\vec{r}) + V_{\text{ext}}(\vec{r},t))\psi(\vec{r},t) \\
&= \sum_{n,\vec{R}} f_{n,\vec{R}}(t)(H_0(\vec{r}) + V_{\text{ext}}(\vec{r},t))w_n(\vec{r}-\vec{R}) \\
&= \sum_{n,\vec{R}} f_{n,\vec{R}}(t)\sum_{\vec{R}'}\epsilon_n(\vec{R}'-\vec{R})w_n(\vec{r}-\vec{R}) \\
&\quad + \sum_{n,\vec{R}} f_{n,\vec{R}}(t)V_{\text{ext}}(\vec{r},t)w_n(\vec{r}-\vec{R}).
\end{aligned} \tag{2.66}$$

The completeness of the Wannier basis allows for a comparison of coefficients. By taking the scalar product with $w_m(\vec{r}-\vec{R}')$ from the left, Eq. (2.66) can thus be reduced to

$$\begin{aligned}
\mathrm{i}\hbar\frac{\partial f_{m,\vec{R}'}(t)}{\partial t} &= \sum_{\vec{R}} f_{m,\vec{R}}(t)\epsilon_m(\vec{R}'-\vec{R}) \\
&\quad + \sum_{n,\vec{R}} f_{n,\vec{R}}(t)\int w_m^*(\vec{r}-\vec{R}')V_{\text{ext}}(\vec{r},t)w_n(\vec{r}-\vec{R})\ d^3r.
\end{aligned} \tag{2.67}$$

The first resulting term is then rewritten as

$$\begin{aligned}
\sum_{\vec{R}} f_{m,\vec{R}}(t)\epsilon_m(\vec{R}'-\vec{R}) \ &= \ \sum_{\vec{R}''}\epsilon_m(\vec{R}'')f_{m,\vec{R}'-\vec{R}''}(t) \\
=\sum_{\vec{R}''}\epsilon_m(\vec{R}'')e^{-\mathrm{i}\vec{R}''(-\mathrm{i}\nabla_{\vec{R}'})}f_{m,\vec{R}'}(t) \ &= \ \epsilon_m(\vec{k}\to -\mathrm{i}\nabla_{\vec{R}'})f_{m,\vec{R}'}(t),
\end{aligned} \tag{2.68}$$

where in the second step it was assumed that $f_{m,\vec{R}'}(t)$ is a smooth function of a spatial coordinate $\vec{R}'$.

The second term on the right-hand side of Eq. (2.67) is approximated as

$$\begin{aligned}
&\sum_{n,\vec{R}} f_{n,\vec{R}}(t)\int w_m^*(\vec{r}-\vec{R}')V_{\text{ext}}(\vec{r},t)w_n(\vec{r}-\vec{R})\ d^3r \\
\approx\, &V_{\text{ext}}(\vec{R},t)f_{m,\vec{R}'}(t),
\end{aligned} \tag{2.69}$$

making Eq. (2.67) diagonal in $f_{m,\vec{R}'}(t)$. For this approximation to hold, $V_{\text{ext}}(\vec{r},t)$ must vary slowly on the scale of a unit cell while the Wannier functions are localised to one cell (cf. Eq. (2.44)). For this reason, the assumption

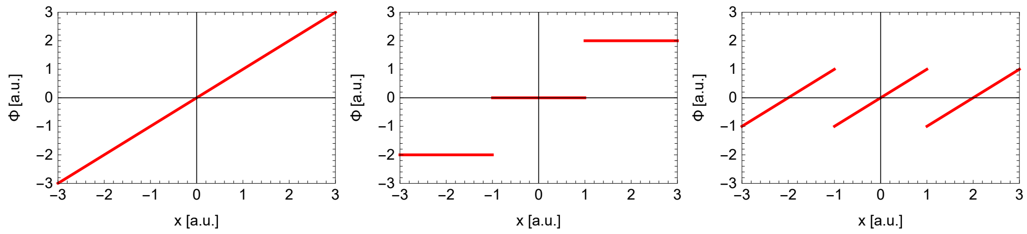

(a) (b) (c)

Figure 2.7: Separation of a linear potential; The overall potential (a) can be separated into a sum of a staggered (b) and a sawtooth potential (c). The latter is periodic in the spatial parameter x.

of the electric force $e\vec{E}(\vec{r},t) = -\nabla V_{\text{ext}}(\vec{r},t)$ being weak was made at the beginning of this subsection.
As a result of Eq. (2.69), Eq. (2.67) becomes a Schrödinger equation for the envelope functions $f_{n,\vec{R}}$ as

$$\mathrm{i}\hbar\frac{\partial f_{n,\vec{R}}(t)}{\partial t} = (\epsilon_m(\vec{k} \to -\mathrm{i}\nabla_{\vec{R}}) + V_{\text{ext}}(\vec{R},t))f_{n,\vec{R}}(t). \tag{2.70}$$

For an electromagnetic perturbation as considered at the beginning of the subsection, this equation further reshapes to

$$\mathrm{i}\hbar\frac{\partial f_{n,\vec{R}}(t)}{\partial t} = \left(\epsilon_m\left(\vec{k} \to \left(-\mathrm{i}\nabla_{\vec{R}} + \frac{e}{\hbar c}\vec{A}\right)\right) + \Phi(\vec{R},t)\right) f_{n,\vec{R}}(t), \tag{2.71}$$

i.e. the envelope functions $f_{n,\vec{R}}$ perceive the electromagnetic potentials similarly to how it would naïvely be expected.
It is now intriguing to separate the perturbation into one part that acts on the envelope functions and one that acts on the Wannier functions. Under this premise, Emin and Hart have separated a linear potential into a staggered and a sawtooth one [71, 72]. This is illustrated in Fig. 2.7 where only the sawtooth potential in part (c) is assumed to act on the unit cell while the full potential (a) is only to be considered on the envelope function.

However, as was shown by Kleinman [73], this separation is an approximation that is not universally applicable, as there arise terms not diagonal in the reciprocal vector $\vec{k}$. These $\vec{k}$-non-diagonal terms will be computed in section 3.1.1 of this thesis. This allows to estimate their effect while restricting the scalar potential $\Phi(\vec{r},t)$ to a sawtooth-like potential that is defined only within one unit cell.

2.3 Spin-orbit Interaction (SOI)

So far, the tight-binding model has been introduced with the LCAO method to include multiple atomic orbitals. The remaining degree of freedom for electrons to be included into the model is spin. While spin itself can be introduced by merely doubling the dimension of the Hilbert space and assigning spin-up and spin-down to the respective halves of the new Hilbert space, the existence of an atomic orbital basis requires the consideration of spin-orbit interaction (SOI) between those orbitals and their respective spins. This thesis will differentiate between *intrinsic* SOI that originates from the electromagnetic potential of the nuclei, and *Rashba* SOI that arises from a broken out-of-plane symmetry.

Intrinsic SOI is obtained as a correction term for the Schrödinger equation after deriving the latter as a classical limit from the Dirac equation as performed by Foldy and Wouthuysen [74]. The schematic derivation and discussion in the following is based on the notes of Murayama [75].
For the electric field originating from the charge of the nucleus, assume a time-independent electric four-potential $A = (\phi, \vec{A})$ consisting of a scalar potential ϕ and a vector potential $\vec{A}$. Both are constant in time, but have a spatial dependence that, for the sake of readability, will not be written explicitly. The momentum then is replaced by $\vec{p} \to \vec{p} - \frac{e}{c}\vec{A}$, and the time-independent Dirac equation for an electron can be written

$$\begin{pmatrix} (e\phi + mc^2)\mathbb{1}_{2\times2} & c\vec{\sigma}\cdot\left(-\mathrm{i}\hbar\nabla - \frac{e}{c}\vec{A}\right) \\ c\vec{\sigma}\cdot\left(-\mathrm{i}\hbar\nabla - \frac{e}{c}\vec{A}\right) & (e\phi - mc^2)\mathbb{1}_{2\times2} \end{pmatrix} \psi(\vec{r}) = E\psi(\vec{r}) \tag{2.72}$$

with the speed of light c, the particle mass m, the momentum operator $\vec{p} = -\mathrm{i}\hbar\nabla$ and the Pauli vector $\vec{\sigma} = (\sigma_x, \sigma_y, \sigma_z)$ consisting of the 2×2 Pauli matrices σ_i acting on the spin. Eq. (2.72) describes a four-component spinor ψ depending on position $\vec{r}$ and time t.

The solutions to the Dirac equation can then be found perturbatively as an expansion in orders of $\vec{\sigma}\cdot\left(-\mathrm{i}\hbar\nabla - \frac{e}{c}\vec{A}\right)$ which is analogue to an expansion in orders of the momentum. During this procedure, Eq. (2.72) gives rise to the Hamiltonian

$$\begin{aligned}H =&\beta\left(mc^2+\frac{\left(\vec{p}-\frac{e}{c}\vec{A}\right)^2}{2m}-\frac{\vec{p}^4}{8m^3c^2}\right)+e\phi-\frac{e\hbar}{2mc}\beta\sigma\cdot\vec{B}\\&-\frac{\mathrm{i}e\hbar^2}{8m^2c^2}\vec{\sigma}\cdot\left(\nabla\times\vec{E}\right)-\underbrace{\frac{e\hbar}{4m^2c^2}\vec{\sigma}\cdot\left(\vec{E}\times\vec{p}\right)}_{=:H_{\mathrm{SOI}}}-\frac{e\hbar^2}{8m^2c^2}\nabla\cdot\vec{E}.\end{aligned} \tag{2.73}$$

The focus of this section lies on the SOI term H_{SOI}. Before going into further detail on it, the other terms will be discussed briefly, to allow for an isolated discussion of the SOI term.

β is a diagonal 4×4-matrix acting on the components of $\psi(\vec{r},t)$. $\vec{B}$ is a possible external magnetic field. The terms in the first line are, in order, the rest energy, the relativistic kinetic energy, a relativistic correction to it, the Coulomb potential, and the coupling to the external magnetic field. The first term in the second line vanishes for a gradient field like that from the nucleus potential. The last term is the so-called Darwin- or *Zitterbewegung*-term.[4]

The SOI term can be reshaped to

$$H_{\mathrm{SOI}}=\frac{e\hbar}{4m^2c^2}\vec{\sigma}\cdot\left(\vec{E}\times\vec{p}\right)=\frac{e\hbar}{4m^2c^2}\vec{\sigma}\cdot|\vec{E}|\left(\frac{\vec{r}}{|\vec{r}|}\times\vec{p}\right)=\frac{e\hbar}{4m^2c^2}\frac{dV}{dr}\frac{1}{|\vec{r}|}\vec{\sigma}\cdot\vec{L}. \tag{2.74}$$

It describes the intrinsic SOI with angular momentum operator $\vec{L}$ and the electric core potential $V(\vec{r})$. Via ladder operators $L_\pm = 1/2\cdot(L_x \pm \mathrm{i}L_y)$ and $\sigma_\pm = 1/2\cdot(\sigma_x \pm \mathrm{i}\sigma_y)$, the scalar product in the last term in Eq. (2.74) reshapes to

$$\vec{\sigma}\vec{L}=\frac{1}{2}\left(\sigma_-L_+ + \sigma_+L_- + 2\sigma_zL_z\right). \tag{2.75}$$

This expression can be evaluated in matrix form on the basis atomic orbitals with spin. For the basis[5]

$$\{\mathrm{s}^{\uparrow/\downarrow},\mathrm{p}_{\mathrm{x}}^{\uparrow/\downarrow},\mathrm{p}_{\mathrm{y}}^{\uparrow/\downarrow},\mathrm{p}_{\mathrm{z}}^{\uparrow/\downarrow},\mathrm{d}_{\mathrm{xy}}^{\uparrow/\downarrow},\mathrm{d}_{x^2-y^2}^{\uparrow/\downarrow},\mathrm{d}_{\mathrm{xz}}^{\uparrow/\downarrow},\mathrm{d}_{\mathrm{yz}}^{\uparrow/\downarrow},\mathrm{d}_{z^2}^{\uparrow/\downarrow}\}, \tag{2.76}$$

---

[4] The Zitterbewegung as well as other relativistic corrections except for SOI will not be taken into account in this thesis, since their effects are negligibly small.

[5] The electron shell quantum number n is not displayed here, since the SOI operator does not affect it. The matrix (2.77) looks identical for any two orbitals that share the same n.

Eq. (2.75) can be expressed as a matrix

$$\vec{\sigma}\vec{L} = \frac{\hbar}{2} \begin{pmatrix} 0 & & & & & & & & \\ & 0 & -\mathrm{i}\sigma_z & \mathrm{i}\sigma_y & & & & & \\ & \mathrm{i}\sigma_z & 0 & -\mathrm{i}\sigma_x & & & & & \\ & -\mathrm{i}\sigma_y & \mathrm{i}\sigma_x & 0 & & & & & \\ & & & & 0 & \mathrm{i}2\sigma_z & -\mathrm{i}\sigma_x & \mathrm{i}\sigma_y & 0 \\ & & & & -\mathrm{i}2\sigma_z & 0 & \mathrm{i}\sigma_y & \mathrm{i}\sigma_x & 0 \\ & & & & \mathrm{i}\sigma_x & -\mathrm{i}\sigma_y & 0 & -\mathrm{i}\sigma_z & \mathrm{i}\sqrt{3}\sigma_y \\ & & & & -\mathrm{i}\sigma_y & -\mathrm{i}\sigma_x & \mathrm{i}\sigma_z & 0 & -\mathrm{i}\sqrt{3}\sigma_x \\ & & & & 0 & 0 & -\mathrm{i}\sqrt{3}\sigma_y & \mathrm{i}\sqrt{3}\sigma_x & 0 \end{pmatrix} \tag{2.77}$$

with the Pauli matrices acting on the spin. The matrix is block diagonal, since SOI only couples orbitals with identical n-quantum number. All entries that are not written explicitly in Eq. (2.77) are zero. Since the effect of SOI is small compared to the hopping parameters, intrinsic SOI will only be taken into account on-site and otherwise be assumed to be zero.

In the graphene tight-binding model, SOI couples the $\mathrm{d_{xz}}$- and $\mathrm{d_{yz}}$-orbitals which, in third order perturbation theory (cf. [76]) leads to a band gap between valence and conduction band as illustrated in Fig. 2.8. The gap has a width of

$$\Delta_{\mathrm{SOI}} \propto \frac{V_{\mathrm{pd}\pi}}{(\epsilon_p - \epsilon_d)^2}\lambda_{\mathrm{I}}, \tag{2.78}$$

where $V_{\mathrm{pd}\pi}$ is the hopping strength between a p- and a d-orbital that are coupled via a π-bond. The terms $\epsilon_{\mathrm{p/d}}$ are the onsite energies of the respective orbitals. λ_{I} is the combined prefactor of the SOI term in Eq. (2.74) and determines the strength of the intrinsic SOI via[6]

$$H_{\mathrm{SOI}} = \lambda_{\mathrm{I}} \cdot \frac{2}{\hbar}\vec{\sigma}\vec{L}. \tag{2.79}$$

Note that while the matrix (2.77) is independent of the electron shell quantum number n, the overall SOI term H_{SOI} is not, as the SOI strength varies for different l quantum numbers. Since the graphene band gap is known to be of $\Delta_{\mathrm{SOI}} = 42\,\mu\mathrm{eV}$, the value of λ_{I} in this thesis will be adapted to reproduce this value measured by Sichau at al. [30, 77]. The numerical values of the parameters mentioned in this section are listed in appendix A.

---

[6] The prefactor $2/\hbar$ is the inverse to the prefactor of the matrix (2.77) and therefore allows to compute H_{SOI} as the product of only λ_{I} and the entries *inside* the matrix.

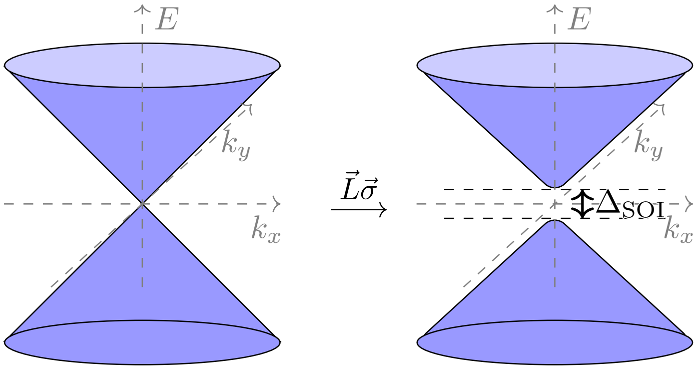

Figure 2.8: Gap opening; Intrinsic spin-orbit interaction lifts the degeneracy at the Dirac points and thus leads to a band gap between the Dirac cones of graphene.

2.3.1 Rashba SOI

An external field parallel to the z-axis breaks mirror symmetry through the xy-plane. Since this symmetry relates an arrow that points out of the graphene plane to its counterpart mirrored through the graphene sheet, it will be called *out-of-plane* symmetry.

As a result of this broken symmetry, the substitution to $\vec{L}$ as performed in Eq. (2.74) is impossible. Instead, the *Rashba SOI* [58] arises. The following computation will use H_{SOI} from Eq. (2.73) as a starting point as well, but will then derive matrix elements connecting nearest neighbours based on the computations of [78].

Via permutation of the triple product and insertion of an external electric field $\vec{E}_{\mathrm{ext}} = E_0 \cdot \vec{e}_z$, the term H_{SOI} in Eq. (2.73) reshapes to

$$H_{\mathrm{SOI}} = \frac{e\hbar}{4m^2c^2}\vec{\sigma} \cdot \left(\vec{E}_{\mathrm{ext}} \times \vec{p}\right) = \frac{e\hbar}{4m^2c^2} \cdot E_0\vec{e}_z\,(\vec{p} \times \vec{\sigma}) = \frac{E_0 e\hbar}{4m^2c^2}(p_x\sigma_y - p_y\sigma_x), \tag{2.80}$$

where again the σ matrices act on the spin. To translate the term $(p_x\sigma_y - p_y\sigma_x)$ to the tight-binding formalism, consider a Wannier function $w(\vec{r} - \vec{R}_i)$. A derivation by $\vec{r}$ can then be written as

$$\nabla w(\vec{r} - \vec{R}_i) = \lim_{\vec{d}\to 0} \frac{\vec{d}}{|\vec{d}|} \frac{\left(w(\vec{r} - \vec{R}_i + \vec{d}) - w(\vec{r} - \vec{R}_i)\right)}{|\vec{d}|}. \tag{2.81}$$

For small $|\vec{d}|$, it is a good approximation to drop the limit and instead say

$$\nabla w(\vec{r}-\vec{R}_i) \approx \frac{\vec{d}}{d}\frac{\Big(w(\vec{r}-\vec{R}_i+\vec{d})-w(\vec{r}-\vec{R}_i)\Big)}{d} \tag{2.82}$$

with $\vec{d} =: d_x\vec{e}_x + d_y\vec{e}_y + d_z\vec{e}_z$ and $d := |\vec{d}|$. This $\vec{d}$ will later be the vector connecting two nearest neighbours in the lattice.

This approximation of the derivative together with definition (2.37) allows to evaluate the action of the momentum operator $\vec{p}$ on a general wave function $\Psi(\vec{r})$ in a piecewise manner via

$$\begin{aligned} p_x\Psi(\vec{r}) &= -\mathrm{i}\hbar\frac{\partial}{\partial_x}\sum_i c_i e^{\mathrm{i}\vec{k}\vec{R}_i} w_n(\vec{r}-\vec{R}_i) = -\mathrm{i}\hbar\sum_i c_i e^{\mathrm{i}\vec{k}\vec{R}_i}\frac{\partial}{\partial_x} w_n(\vec{r}-\vec{R}_i) \\ &= -\mathrm{i}\hbar\sum_i c_i e^{\mathrm{i}\vec{k}\vec{R}_i}\frac{d_x}{d^2}\Big(w(\vec{r}-\vec{R}_i+\vec{d})-w(\vec{r}-\vec{R}_i)\Big) \end{aligned} \tag{2.83}$$

with coefficients c_i that satisfy the overall normalisation condition of the wave function. Eq. (2.83) leads to

$$\begin{aligned} &\int_{\mathbb{R}^3} \Psi^\dagger(\vec{r}) p_x \Psi(\vec{r})\; d\vec{r} \\ &= -\mathrm{i}\hbar\sum_{i,j} c_i^\dagger c_j e^{\mathrm{i}\vec{k}(\vec{R}_j-\vec{R}_i)}\frac{d_x}{d^2}\int_{\mathbb{R}^3} w^\dagger(\vec{r}-\vec{R}_i)\Big(w(\vec{r}-\vec{R}_j+\vec{d})-w(\vec{r}-\vec{R}_j)\Big)\, d\vec{r} \\ &= -\mathrm{i}\hbar\sum_{\langle i,j\rangle} c_i^\dagger c_j \frac{d_x}{d^2}, \end{aligned} \tag{2.84}$$

where the orthogonality of the Wannier functions has been used to reduce the sum over all i and j to a sum over nearest neighbours $\langle i,j\rangle$, as the integral $\int_{\mathbb{R}^3} w^\dagger(\vec{r}-\vec{R}_i)w(\vec{r}-\vec{R}_j+\vec{d})\; d\vec{r}$ vanishes unless[7] $\vec{R}_j = \vec{R}_i + \vec{d}$. Similarly, p_y yields

$$\int_{\mathbb{R}^3} \Psi^\dagger(\vec{r}) p_y \Psi(\vec{r})\; d\vec{r} = -\mathrm{i}\hbar\sum_{\langle i,j\rangle} c_i^\dagger c_j \frac{d_y}{d^2}. \tag{2.85}$$

Under the assumption that the vectors $\vec{d}$ connecting two neighbouring sites are small enough to allow for the approximation (2.82), it is therefore possible to translate Eq. (2.80) into the tight-binding formalism as

$$(H_{\mathrm{SOI}})_{i,j} = -\mathrm{i}\frac{E_0 e\hbar^2}{4m^2c^2d^2}((\vec{R}_i-\vec{R}_j)_x\sigma_y - (\vec{R}_i-\vec{R}_j)_y\sigma_x), \tag{2.86}$$

---

[7] Since the honeycomb lattice contains two atoms per unit cell, $\vec{R}_i - \vec{d}$ is no lattice vector. The sublattices instead need to be incorporated into the index n in the definition (2.36) of the Wannier functions $w_n(\vec{r}-\vec{R})$. One then has orthogonal $w_n(\vec{r}-\vec{R})$ and $w_{n'}(\vec{r}-\vec{R})$ centred at $\vec{R}$ for n and at $\vec{R}+\vec{\delta}$ for n', with the displacement vector $\vec{\delta}$ from Eq. (2.1).

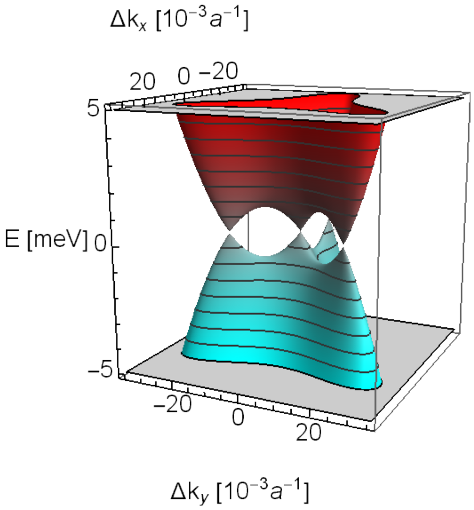

Figure 2.9: Trigonal warping at the K-point; As a consequence of the Rashba effect, the Dirac cones of graphene split into four, respectively. Of these four cones, one lies in the centre and is surrounded by the other three in a triangular formation.

where the indices x and y refer to the components of the vector $(\vec{R}_i - \vec{R}_j)$. The Pauli matrices σ_x and σ_y act on the spin.

Eq. (2.86) relates the sublattices and spins. Its effects are most notable at the K-points. However, since some of these effects need the definition of topology to be discussed in appropriate detail, this section will only focus on a select few effects. A further discussion will follow in section 2.4.3.

The Rashba effect leads to a coupling of one K-point to the other. As a result, the symmetries of both respective pairs of cones interfere. Consequently, the cones reshape as depicted in Fig. 2.9. This effect is known as *triangular warping*. Furthermore, the Rashba effect lifts spin degeneracy. As a result, valence and conduction band are split into two energetically non-degenerate pairs. They will be referred to as *inner* and *outer* valence band, based on their proximity to the Fermi energy. This is illustrated via the dashed red cones in Fig. 2.10.

A similar Rashba effect can also be caused by the combined effects of intrinsic SOI, nearest-neighbour hopping, sp^2 hybridisation and broken out-of-plane symmetry. When the latter is broken, the matrix elements between the p$_\mathrm{z}$-orbitals and the s-orbitals are no longer zero. The s-orbitals, in turn, are coupled to the p$_\mathrm{x}$- and p$_\mathrm{y}$-orbitals via sp^2 hybridisation. This hybridisation together with the intrinsic SOI between the p$_\mathrm{x}$- and p$_\mathrm{y}$-orbitals then causes an effect similar to expression (2.86). In this thesis, both effects will be considered, and systems with possibly broken out-of-plane symmetry will therefore always involve s- and p$_{\mathrm{x/y}}$-orbitals.

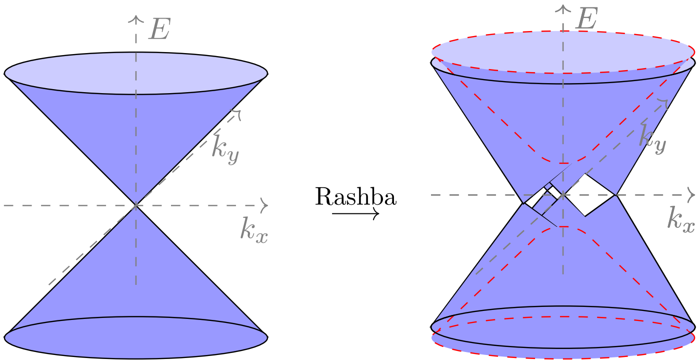

Figure 2.10: Separation of cones; A broken out-of-plane symmetry induces Rashba SOI which makes one Dirac cone split into four, with the three outer cones aligned like in Fig. 2.9. The formerly spin-degenerate valence and conduction band split, forming a second pair (red) with a gap in between. The trigonally warped cones do not exhibit a gap except for a possible intrinsic one.

2.4 Topological Insulators: Haldane Model

Graphene with intrinsic SOI between the d-orbitals exhibits a band gap between valence and conduction band. Therefore, it is a band insulator. However, valence and conduction band both have a non-trivial *topological quantum number*, i.e. a quantum number that only changes when a band gap closes or a new one opens. This quantum number, as will be explained in this section, leads to gap-crossing edge states that make graphene a *topological insulator*.

The classification of materials and band structures based on topology was pioneered by Thouless et al. [79] and has since become a major field of research. In the following, a modified version of the Haldane model [15] will be defined, to study the topological properties of spinless graphene. Via the inclusion of spin, the Haldane model will then be extended to the Kane-Mele model [17]. The models will be used to derive the first Chern number and the so-called Z_2-topological invariant. Since this section will only cover the details that are important for graphene, the course by Asbóth, Oroszlány and Pályi [12] is recommended for a broader understanding of topological insulators.

2.4.1 Haldane Model and Symmetry

In the following, a model analogous to the Haldane model [15] will be derived. The original Haldane model can be obtained from the model used in this section via a basis transformation. This section will use the same basis as the overall thesis, to ensure coherence of the interpretations and results.

To concentrate the focus on only the valence and conduction band of graphene, assume a model without spin and with only $\mathrm{p_z}$-orbitals, where only nearest neighbour hopping is considered. The graphene tight-binding Hamiltonian (in reciprocal space) then becomes a 2×2-matrix

$$H_0(\vec{k}) = \begin{pmatrix} 0 & h(\vec{k}) \\ h^\dagger(\vec{k}) & 0 \end{pmatrix} \tag{2.87}$$

with

$$h(\vec{k}) = t_1 \sum_i \exp(\mathrm{i}\vec{k}\vec{a}_i) = t_1 \left(1 + 2e^{-\mathrm{i}\frac{\sqrt{3}}{2}k_y} \cos\left(\frac{k_x}{2}\right)\right), \tag{2.88}$$

where the lattice vectors $(0,0)^t$, $\vec{a}_1$ and $\vec{a}_2$ from section 2.1 have been inserted. The lattice constant a has been set to 1. k_x and k_y therefore assume real values without a unit. The parameter t_1 denotes the hopping strength between two p-orbitals. Eq. (2.87) gives rise to the band structure of Fig. 2.3 (pg. 7) without a band gap. $H_0(\vec{k})$ can be written in terms of Pauli matrices acting on the sublattice:

$$H_0(\vec{k}) = \vec{\sigma}\vec{d}(\vec{k}) \tag{2.89}$$

with

$$\vec{d}(\vec{k}) = \begin{pmatrix} \Re(h(\vec{k})) \\ -\Im(h(\vec{k})) \\ 0 \end{pmatrix} = t_1 \cdot \begin{pmatrix} 1 + 2\cos\left(\frac{k_x}{2}\right)\cos\left(\frac{\sqrt{3}k_y}{2}\right) \\ -2\cos\left(\frac{k_x}{2}\right)\sin\left(\frac{\sqrt{3}k_y}{2}\right) \\ 0 \end{pmatrix} \tag{2.90}$$

and the vector of Pauli matrices $\vec{\sigma} = (\sigma_x, \sigma_y, \sigma_z)^t$. This definition will become advantageous for solving the eigenvalue problem, especially when additional terms proportional to σ_z will be added, later.
Furthermore, the notation introduces the effective sublattice spin analogous to the real spin, but with the Pauli matrices acting on the sublattices instead. The components of $\vec{d}$ are therefore directly related to the components of the sublattice spin. Note that, since Eq. (2.90) contains no term proportional to σ_z, the bands can and do touch at the K-points.

Two fundamental symmetries of graphene[8] can be concluded from the model, namely

- **sublattice** or **chiral symmetry** $\sigma_z H_0(\vec{k})\sigma_z = -H_0(\vec{k})$ and
- **time-reversal symmetry** $H_0(\vec{k}) = H_0^*(-\vec{k})$.

One important effect of the time-reversal symmetry is that it exchanges the K- and the K'-point in the Brillouin zone (cf. Fig. 1.2 on page 6).
When combined, these two symmetries give rise to **particle-hole symmetry** $\sigma_z H_0^*(-\vec{k})\sigma_z = -H_0(\vec{k})$ that, in turn, relates every energy $E_+(\vec{k})$ to an opposite energy $E_-(-\vec{k}) = -E_+(\vec{k})$.
Since $(H_0(\vec{k}))^2 = \vec{d}^2\mathbb{1}_2$, the absolute value of its eigenvalues is $|\vec{d}|$. Thus, they are $E_\pm(\vec{k}) = \pm|\vec{d}(\vec{k})| = \pm|h(\vec{k})|$.

The model (2.89) does not yet give rise to any topological quantum numbers. Hence, it defines merely a conventional semi-metal. This is because, for non-trivial topological quantum numbers to arise, a system must have a specific behaviour under symmetry transformations, depending on the dimension of the system. The exact dependencies for general systems will be discussed later in section 2.5.2, but the consequence for the model (2.89) is that, for it to be topologically non-trivial, time-reversal symmetry needs to be broken.

Symmetry Breaking

Before breaking time-reversal symmetry, it is instructive to first break sublattice symmetry. Not only is this achieved by simpler means, but also will knowledge about it be of great advantage in later discussions. Sublattice symmetry can be broken by adding a σ_z matrix to the system, i.e.

$$H_0(\vec{k}) \to H_0(\vec{k}) + M\sigma_z \tag{2.91}$$

with a real-valued parameter M. This new term leads to a potential $+M$ on site A and $-M$ on site B. As a result, the new eigenvalues of H_0 become $E_\pm(\vec{k}) = \pm\sqrt{|h(\vec{k})|^2 + M^2}$, i.e. a band gap opens, depending on the absolute value $|M|$. With increasing $|M|$, the eigenstates become localised on the respective sublattices.

---

[8] As will be shown in section 2.4.2, the definitions for these symmetries differ for bosons and fermions.

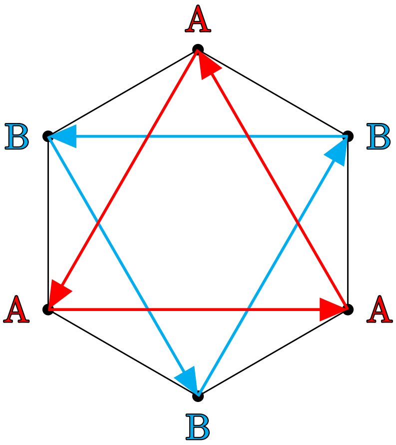

Figure 2.11: Next-nearest neighbour hopping; The red and blue arrows indicate how tunnelling across two edges leads back to the same sublattice. The picture is based on a similar illustration in [80].

Time-reversal symmetry will be broken via a term proportional to σ_z as well. However, the new term will not define an onsite potential like the previous one proportional to M. Instead, it will describe an effective next-nearest-neighbour hopping. Fig. 2.11 illustrates how next-nearest-neighbour hopping translates a particle from one sublattice to the same sublattice.

For the next-nearest-neighbour hopping, define an amplitude[9] $+\mathrm{i}t_2$ if the hopping direction is the same as that of the arrows in Fig. 2.11 and $-\mathrm{i}t_2$ for the opposite direction. The model (2.89) then reshapes to

$$H(\vec{k}) = H_0(\vec{k}) + M\sigma_z + \underbrace{2t_2 \sum_{\vec{b}_i} \sin(\vec{k}\vec{b}_i)\sigma_z}_{\text{time-reversal symmetry breaking}} \tag{2.92}$$

with vectors $\vec{b}_i \in \{\vec{a}_1, (\vec{a}_1 - \vec{a}_2), -\vec{a}_2\}$ translating between the unit cells of next-nearest neighbours.[10] Again, a is set to 1. The new term breaks time-reversal symmetry, since it assumes opposite values, depending on whether the hopping depicted in Fig. 2.11 is performed in the direction of the arrows or oppositely to them. The new symmetry-breaking term will be labelled $g(\vec{k})$.

---

[9] The complex prefactor i before t_2 is necessary, since the direction-dependent hopping would otherwise be non-Hermitian.

[10] The sum would originally run over six vectors $\vec{b}_i$. However, since for every vector $\vec{b}_i$ there is a partner vector $\vec{b}_j = -\vec{b}_i$, and since these pairs have respective hopping amplitudes $+\mathrm{i}t_2$ and $-\mathrm{i}t_2$, the sum over six Bloch phases $\exp(\mathrm{i}\vec{k}\vec{b}_i)$ becomes a sum over three sines.

With the definitions for $\vec{a}_{1/2}$ from section 2.1, Eq. (2.92) further reshapes to

$$g(\vec{k}) =: 2t_2 \sum_{\vec{b}_i} \sin(\vec{k}\vec{b}_i) = 2t_2 \left(2\cos\left(\frac{\sqrt{3}k_y}{2}\right) \sin\left(\frac{k_x}{2}\right) - \sin(k_x) \right). \tag{2.93}$$

Since model (2.92) is identical to the Haldane model, except for its different rotational symmetry, it will be called the *modified* Haldane model.[11] Analogously to the notation of Eqs. (2.89) and (2.90), the modified Haldane model can again be expressed as a sum of sigma matrices

$$H(\vec{k}) = \vec{\sigma}\vec{d}(\vec{k}) \tag{2.94}$$

with the vectors

$$\vec{d}(\vec{k}) = \begin{pmatrix} \Re(h(\vec{k})) \\ -\Im(h(\vec{k})) \\ M + g(\vec{k}) \end{pmatrix} \qquad \text{and} \qquad \vec{\sigma} = \begin{pmatrix} \sigma_x \\ \sigma_y \\ \sigma_z \end{pmatrix}. \tag{2.95}$$

The Hamiltonian matrix then satisfies $(H(\vec{k}))^2 = \vec{d}^2 \mathbb{1}_2$. Hence, the eigenvalues of $H(\vec{k})$ are

$$E_\pm(\vec{k}) = \pm|\vec{d}(\vec{k})| = \pm\sqrt{|h(\vec{k})|^2 + (M + g(\vec{k}))^2} \tag{2.96}$$

with the index "−" for valence and "+" for conduction band. The corresponding eigenstates are

$$|\vec{k}_\pm\rangle = \frac{1}{N_\pm(\vec{k})} \begin{pmatrix} h^*(\vec{k}) \\ E_\pm(\vec{k}) + (M + g(\vec{k})) \end{pmatrix} \tag{2.97}$$

with a normalising term

$$N_\pm(\vec{k}) = \sqrt{2E_\pm(\vec{k})\left(E_\pm(\vec{k}) + M + g(\vec{k})\right)}. \tag{2.98}$$

As a result of the broken time-reversal symmetry, the relation $E_-(-\vec{k}) = -E_+(\vec{k})$ no longer holds. This is particularly notable, at the K-points, i.e. $\vec{k} \in \{\vec{K}, \vec{K}'\}$. There,

$$E_\pm(\vec{k} = \vec{K}) = \pm|M + 3\sqrt{3}t_2| \qquad \text{and} \qquad E_\pm(\vec{k} = \vec{K}') = \pm|M - 3\sqrt{3}t_2|. \tag{2.99}$$

---

[11] The unmodified Haldane model can be obtained via a basis transformation $H_{\text{unmod.}}(\vec{k}) = B^\dagger H(\vec{k}) B$ with the basis matrix $B = \text{diag}(e^{-\frac{i}{2}\vec{k}\vec{\delta}}, e^{+\frac{i}{2}\vec{k}\vec{\delta}})$ and the displacement vector $\vec{\delta}$ from equation (2.1).

There is a different sign between M and $3\sqrt{3}t_2$ in the energy solutions at the K-points. As a result, the band gaps $\Delta(\vec{K}^{(\prime)})$ at the K-points are

$$\Delta(\vec{K}) = 2|M + 3\sqrt{3}t_2| \quad \neq \quad 2|M - 3\sqrt{3}t_2| = \Delta(\vec{K}'), \tag{2.100}$$

i.e. they are of different magnitude if both M and t_2 are non-zero and satisfy $3\sqrt{3}M \neq t_2$.

In the following, it will be shown how the modified Haldane model makes graphene a so-called *Chern insulator*.

2.4.2 Berry Phase and Chern Number

Graphene as described by model (2.92) is a Chern insulator, i.e. a band insulator whose valence and conduction band exhibit non-trivial, topologically protected first Chern numbers. The latter and the meaning of its topological protection will be derived in the following, beginning with the definition of the Berry phase.

Berry Phase

The Berry phase, in condensed matter physics, is a geometrical property, associated with the change a state perceives upon transport through the Brillouin zone. To quantify it, imagine an adiabatic time-evolution of a non-degenerate[12] state $\Psi(\vec{k}(t))$ with energy $E(\vec{k}(t))$ moving along the path C as depicted in Fig. 2.12. After a time T, the state $\Psi(\vec{k}(t))$ will again be at its initial position in reciprocal space, i.e.

$$\vec{k}(t=T) \ = \ \vec{k}(t=0) \quad \Rightarrow \quad \Psi(\vec{k}(T)) \ = \ c \cdot \Psi(\vec{k}(0)), \tag{2.101}$$

The prefactor $c = e^{\tau} \cdot e^{\gamma}$ that the wave function picks up along the path C is composed of two phases. One is the so-called *dynamical phase*

$$\tau := -\mathrm{i} \int_0^T E(\vec{k}(t))dt \tag{2.102}$$

as a result of the time evolution. The other is the *Berry phase*[13]

$$\gamma := \oint_C \vec{A}(\vec{k})d\vec{k} \tag{2.103}$$

---

[12] The state needs to be non-degenerate for a path C to be unambiguous. Otherwise, a transition between bands would be possible.

[13] For a derivation of the Berry phase, the Berry connection and any related quantities, see e.g. [14] or [81].

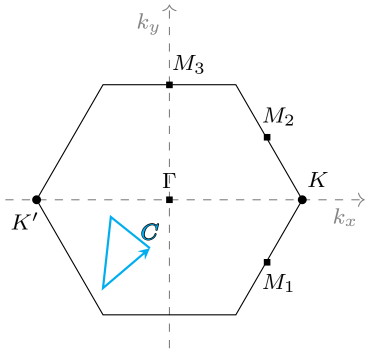

Figure 2.12: Closed path in reciprocal space; The path C begins and ends at the same point.

with the *Berry connection*

$$\vec{A}(\vec{k}) = \mathrm{i}\langle\psi(\vec{k})|\nabla_{\vec{k}}\psi(\vec{k})\rangle. \tag{2.104}$$

With these definitions, it is possible to define the first Chern number.

First Chern Number

The Berry phase bears notable similarity to the Peierls phase, a phase systems obtain from electromagnetic vector potentials [82, 83]. Indeed, via the Berry connection (2.104), the Berry phase can be related to a vector potential as well. The latter also gives rise to an analogue quantity to a magnetic field, in momentum space. This field is called the *Berry curvature*

$$\vec{\Omega}(\vec{k}) = \nabla_{\vec{k}} \times \vec{A}(\vec{k}) = \mathrm{i}\left(\left\langle\frac{\partial\psi(\vec{k})}{\partial k_x}\middle|\frac{\partial\psi(\vec{k})}{\partial k_y}\right\rangle - \left\langle\frac{\partial\psi(\vec{k})}{\partial k_y}\middle|\frac{\partial\psi(\vec{k})}{\partial k_x}\right\rangle\right)\vec{e}_z. \tag{2.105}$$

Through Stokes' theorem, the Berry curvature can be used to compute the Berry phase around the entire Brillouin zone. The result is

$$\oint_{\partial\mathrm{BZ}} \vec{A}(\vec{k})d\vec{k} = \iint_{\mathrm{BZ}} \vec{\Omega}(\vec{k})d\vec{S} = 2\pi W \tag{2.106}$$

with the *first Chern number* $W \in \mathbb{Z}$. It is zero if and only if $\vec{A}(\vec{k})d\vec{k}$ is an exact differential form on the entire (periodic) Brillouin zone. If it is not, then the Berry phase (2.103) is bound to be a multiple of 2π, since the wave function (2.101) does not depend on the path that lead to it. Thus, the first Chern number must be integer-valued.

There are higher Chern numbers as well. Since those, however, will not be discussed in this thesis, the notion *first* will be omitted in the following, and it will instead be called *the Chern number*.
The Chern number is a topological invariant of the system. This means that it does not change under continuous transformations of the system it belongs to. This system, in this case, is the band structure of graphene. Thus, the Chern number remains unchanged upon any deformations of the band structure as long as no band gaps close or new ones open.

A non-zero Chern number can be understood similarly to the existence of a magnetic monopole, but in momentum space. To understand this, note that the Berry curvature has been defined as the $\vec{k}$-curl of a vector potential in Eq. (2.105), similar to a magnetic field in real space. The integral over the Berry curvature can thus be identified with an effective magnetic flux.
For graphene, there are two such monopoles, namely at the K- and the K'-point. Under time-reversal symmetry, they together add up to a net-zero flux. This will be discussed in more detail in section 2.4.3.

Before that, however, an alternative formula for the computation of the Berry curvature will be presented. This formula will be better suited for numerical computations. First, consider two eigenstates $|\phi\rangle \neq |\psi\rangle$ to a Hamiltonian H, with eigenvalue E_ψ. The following steps are copied and adapted from [12]:

$$\begin{aligned} H|\psi\rangle &= E_\psi|\psi\rangle \\ \Rightarrow (\nabla_{\vec{k}}H)|\psi\rangle + H|\nabla_{\vec{k}}\psi\rangle &= (\nabla_{\vec{k}}E_\psi)|\psi\rangle + E_\psi|\nabla_{\vec{k}}\psi\rangle \\ \Rightarrow \langle\phi|(\nabla_{\vec{k}}H)|\psi\rangle + \langle\phi|H|\nabla_{\vec{k}}\psi\rangle &= E_\psi\,\langle\phi|\nabla_{\vec{k}}\psi\rangle \\ \Rightarrow \langle\phi|\nabla_{\vec{k}}\psi\rangle &= \frac{\langle\phi|(\nabla_{\vec{k}}H)|\psi\rangle}{E_\psi - E_\phi}. \end{aligned} \tag{2.107}$$

From the first line to the second, a gradient in $\vec{k}$ has been applied. From the second to the third line, $\langle\phi|$ has been multiplied from the left, and the scalar product has been performed. Rearrangement of the terms then leads to the fourth line.
Eq. (2.107) can be substituted into Eq. (2.105), as first mentioned by Berry [13]. The resulting term

$$\vec{\Omega}_\psi(\vec{k}) = \Im \sum_{\phi\neq\psi} \frac{\langle\psi(\vec{k})|\left(\nabla_{\vec{k}}H(\vec{k})\right)|\phi(\vec{k})\rangle \times \langle\phi(\vec{k})|\left(\nabla_{\vec{k}}H(\vec{k})\right)|\psi(\vec{k})\rangle}{(E_\phi(\vec{k}) - E_\psi(\vec{k}))^2} \tag{2.108}$$

no longer depends on the derivatives of the states, but instead only involves the derivative of the Hamiltonian. Since it is typically significantly easier to obtain an analytical Hamiltonian than it is to obtain analytical eigenstates to it, this formula is often better suited for the computation of the Berry curvature than Eq. (2.105).

2.4.3 Chern Number and Berry Curvature

The Chern number (2.106) equals an integral of the Berry curvature (2.108) over the entire Brillouin zone. For that reason, it is instructive to further study the Berry curvature.

In the modified Haldane model (2.92), the parameter t_1 describes the amplitude of conventional nearest-neighbour hopping, t_2 the amplitude of time-reversal breaking next-nearest-neighbour hopping, and M is the sublattice potential that opens a band gap and breaks sublattice symmetry.

For the time-reversal symmetric system, i.e. for $t_2 = 0$, the Berry curvature takes opposite values for opposite lattice momenta $\vec{k}$,

$$\vec{\Omega}_\psi(\vec{k}) \;=\; -\vec{\Omega}_\psi(-\vec{k}). \tag{2.109}$$

Thus, the integral of the Berry curvature over the whole Brillouin zone is bound to be zero. The relation (2.109) can be seen for the valence band in Fig. 2.13 where the sublattice potential has been set to $M = 0.1$ to open a band gap everywhere.[14]

For the Chern numbers not to be trivial, time-reversal symmetry must therefore be broken. This is achieved by setting $t_2 \neq 0$. The resulting Berry curvatures for the valence band with $t_2 = \pm 0.1$ are depicted in Fig. 2.14. Relation (2.109) no longer holds, and instead the Berry curvature throughout the entire Brillouin zone is positive or negative semi-definite, respectively. The Chern number can therefore no longer possibly be zero. Instead, it is $W = +1$ for $t_2 > M/(3\sqrt{3})$, and it is $W = -1$ for $t_2 < -M/(3\sqrt{3})$. The Chern number for the conduction band satisfies $W_{\mathrm{CB}} = -W_{\mathrm{VB}}$, i.e. it always has the opposite sign compared to the valence band.[15]

As a consequence of the non-trivial Chern numbers, graphene exhibits topologically protected conducting edge states. This concept will be introduced and discussed in the following subsection.

---

[14] A similar figure, but for the unmodified Haldane model, can be found in [80]. Notably, that figure does not exhibit the same vertical white lines as Fig. 2.13 This is a result of the different choice of periodic boundary conditions.

[15] Since the energy eigenvalues of the modified Haldane model have been computed in Eq. (2.108), one can insert the diagonalised Hamiltonian into Eq. (2.96) to easily verify all results for Berry curvature and Chern number.

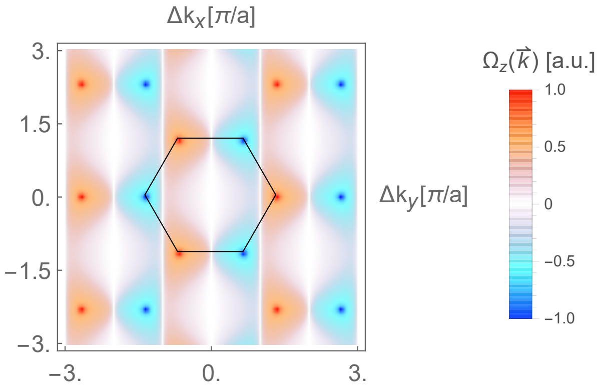

$t_1 = 1,\ t_2 = 0,\ M = 0.2$

Figure 2.13: Berry curvature of the graphene valence band in the modified Haldane model (2.92); The curvature assumes its maxima (red) and minima (blue) at the vertices of the Brillouin zone. The total curvature inside the Brillouin zone adds up to zero.

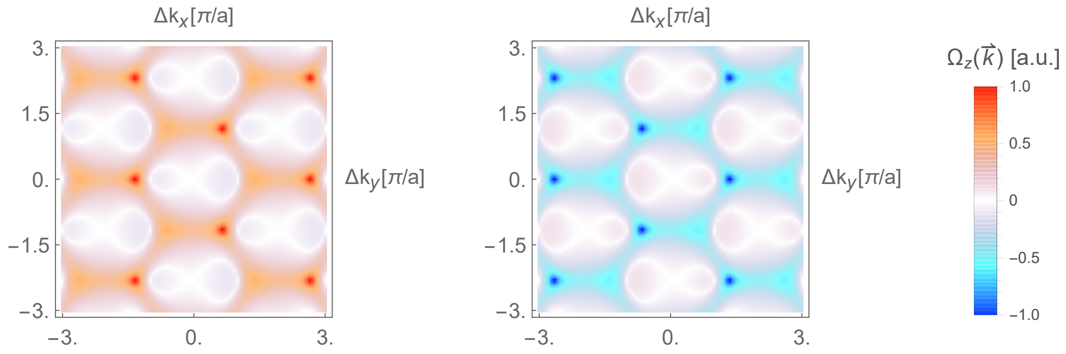

$t_2 = +0.1$ $t_2 = -0.1$

$t_1 = 1,\ M = 0.2$

Figure 2.14: Berry curvature of the valence band of the Haldane model; Upon a change of the sign of the next-nearest-neighbour hopping term t_2, the curvature vanishes at one set of Dirac points and emerges with opposite sign at the other set.

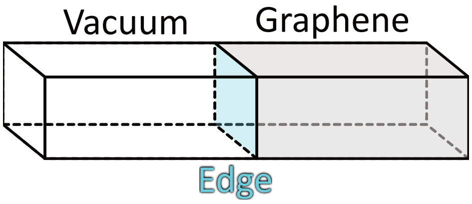

Figure 2.15: Interface between two topologies; At the edge of the material, there must be a transition between the non-trivial topology of graphene and the trivial one of the vacuum. As a result, the bands with non-trivial topological quantum numbers are bound to cross at the edges.

2.4.4 Edge States

The Chern numbers of the modified Haldane model cannot change unless valence and conduction band touch. However, the Chern numbers do disappear upon transition from a topologically non-trivial material to a trivial one, e.g. at the interface between graphene and the vacuum as depicted in Fig. 2.15. As a consequence, valence and conduction band are bound to touch at the edges of the material.

States that reside at the edges of a material are called *edge states*. Edge states can be obtained by considering a graphene unit cell that is periodic in only one direction, but not in the other. Such a unit cell is depicted in Fig. 4.16.[16] These new periodic boundary conditions are also illustrated in the second part of Fig. 2.4 (pg. 9) where the unit cell forms a cylinder instead of a torus like in the fully periodic case.

Since a semi-finite lattice like that in Fig. 4.16 is periodic in only one direction, its reciprocal space is one-dimensional. The resulting band structure can be related to bulk and edge. The bulk part, i.e. the part that is localised within the lattice, is a projection of band structure in two reciprocal dimensions onto one dimension. This projection is depicted in Fig. 2.17.

The actual band structure of graphene with a unit cell like in Fig. 4.16, however, also has edge states. For topologically non-trivial graphene, these edge states cross at $k = \pi/a$ as depicted in Fig. 2.18. In the figure, the hopping parameter has been set to $t_1 = 3.59\,\mathrm{eV}$, in accordance to the parameters given in appendix A. This has been done in order to be able to relate the

---

[16] The unit cell has zigzag edges at its upper and lower end. It is also possible to consider armchair edges that, however, do not lead to edge states (cf. Castro Neto at al. [84]). For this reason, this thesis only considers unit cells like that depicted in Fig. 4.16.

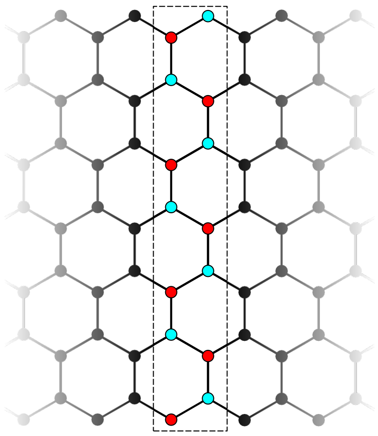

Figure 4.16: Graphene ribbon; By applying periodic boundary conditions in only one direction, the reciprocal space becomes one-dimensional. This unit cell (grey, dashed) contains 14 carbon atoms (red and cyan). Wider graphene sheets can be constructed by including more atoms in the y-direction. The atoms on the outer parts of the edges belong to sublattice A (red) and sublattice B (cyan), respectively.

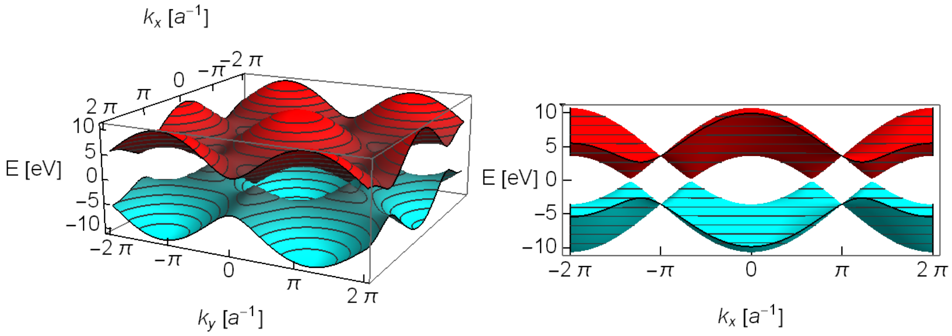

Figure 2.17: Valence and conduction band of p-band graphene; Without d-orbitals, valence and conduction band are energetically symmetric around the Fermi energy of $E = 0\,\mathrm{eV}$. The left picture shows the bands in a vanishing-point perspective, whereas the right shows an orthographic projection onto the k_x-E-axis. The band gap assumes its local maxima at $k_x = 0$ and at $k_x = \pm\pi a^{-1}$. It closes at $k_x = \pm\frac{2\pi}{3}a^{-1}$ and $k_x = \pm\frac{4\pi}{3}a^{-1}$.

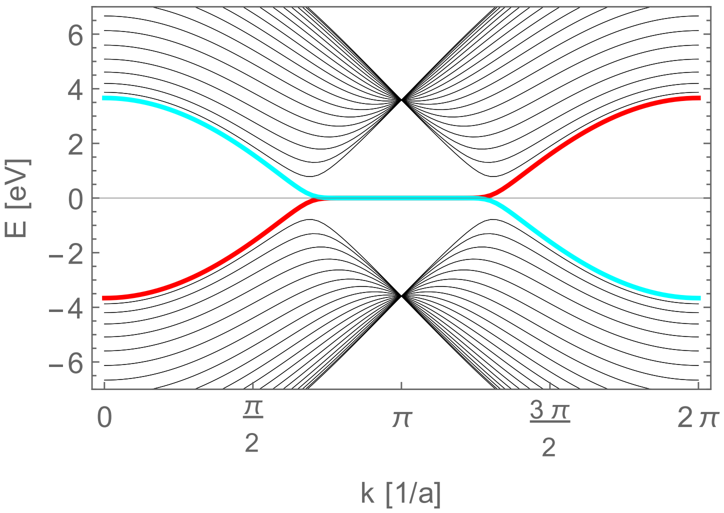

Figure 2.18: Band structure of a graphene ribbon with only p_z-orbitals; The bands are one-dimensional due to the lattice only being periodic in one direction. All bands lie either above or below the Fermi energy at $E = 0\,\mathrm{eV}$, except for the two edge states depicted in red/cyan. The unit cell used for the computation consists of 40 carbon atoms that are aligned like the 14 illustrated in Fig. 4.16.

figure to the results of chapter 5.

The bands in figure 2.18 that are depicted in black correspond to bulk states like exemplified in Fig. 2.17. The other bands, depicted in red and cyan, belong to states that only lie within the bulk for $k < 4\pi/(3a)$ and $k > 4\pi/(3a)$. Within the interval $k \in [-4\pi/(3a), 4\pi/(3a)]$, they are localised on the edges.[17]

Furthermore, both states are localised on opposite edges, respectively. The colours red and cyan in Fig. 2.18 correspond to the same colours in Fig. 4.16, i.e. one edge state is localised entirely at the top edge (cyan atoms) while the other is localised at the lower edge (red atoms) of the graphene ribbon. Since the slope of the lines is positive (red) or negative definite (cyan), this has an effect on the conductance of graphene. The group velocity of electrons in a material (cf. [85, 86]),

$$\vec{v}(\vec{k}) = \frac{1}{\hbar}\nabla_{\vec{k}}E(\vec{k}) \tag{2.110}$$

is proportional to the dispersion relation. Hence, currents can flow only in one direction at one edge and the opposite direction at the other. Thus,

---

[17] This relation repeats with the 2π-periodicity of the band structure.

graphene is a *quantum Hall insulator*. It is also possible to compute a quantised Hall conductivity[18] of $\sigma_{xy} = W \cdot e^2/h$ for the (modified) Haldane model (cf. [87]), with the Chern number W as defined in Eq. (2.106).

Since this Hall effect together with the crossing of the edge states is a consequence of the Chern numbers, both are topologically protected as well. As long as the band gap in the bulk, i.e. for the band structure of fully periodic graphene, does not close, the crossing of the edge states and therefore the quantised Hall effect prevail. This is true under any perturbation to the system that does not change the topology. The relation between the topology of the bulk and the existence (and number) of crossing edge states is called *bulk-boundary correspondence*.

In the following subsection, the concept of sublattice spin will be elaborated on, and it will be motivated via its relation to the Chern number.

2.4.5 Sublattice Spin Winding Number

As shown by de Lisle et al. [88] and elaborated on by Alba, Pachos and García-Ripoll [89], the Chern number of the Haldane model is related to winding numbers of the sublattice spin.

Since graphene has two sublattices and therefore an even-dimensional Hilbert space, the vector components that correspond to the respective sublattices can be treated similar to spinor components. For the sublattice spin, the first component of the spinor, i.e. the component of sublattice A, then corresponds to spin-up and the second component relates sublattice B to spin-down.
Similarly to the real spin, the expectation value for this sublattice spin can be defined via Pauli matrices. For a state $(1, 0)^t$ that is fully localised on sublattice A, one then obtains

$$\langle \sigma_z \rangle = (1, 0)\sigma_z \begin{pmatrix} 1 \\ 0 \end{pmatrix} = 1. \tag{2.111}$$

Similarly, a state $(0, 1)^t$ has a sublattice spin $\langle \sigma_z \rangle = -1$. At the K-points, the sublattice spin of unperturbed graphene is $\langle \sigma_z \rangle = \pm 1$. Away from them, however, the absolute value $|\langle \sigma_z \rangle|$ is no longer 1. Instead, the states gain

---

[18] The relation between the quantised Hall conductivity and the Chern number is a direct consequence of the Kubo formula. For a definition and proof of the latter, see e.g. the Lecture notes of Tong [14].

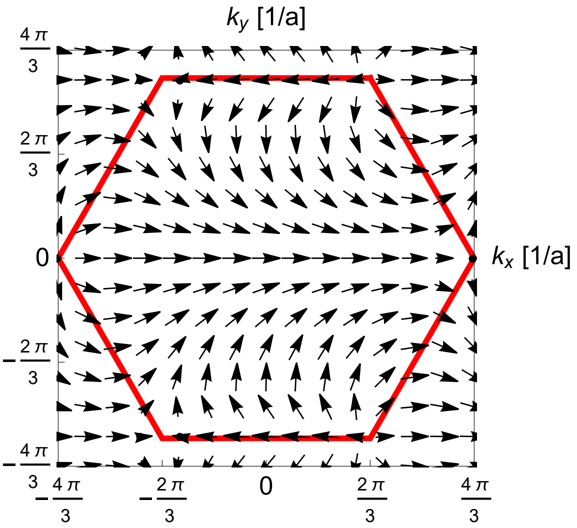

Figure 2.19: In-plane components of the sublattice spin; The two sublattices can be treated as the two components of a spin. It is therefore possible to assign a direction to them. The sublattice spin directions of the valence band of the modified Haldane model with $t_1 = 1$, $t_2 = 0.1$ and $M = 0.2$ are depicted as arrows throughout the Brillouin zone (red). The length of the arrows depends linearly on the length of the projection of the vector $\langle \vec{\sigma}(\vec{k}) \rangle$ onto the xy-plane.

sublattice spins parallel to the graphene plane. These are given by the components of the Pauli matrix vector $\vec{\sigma} = (\sigma_x, \sigma_y, \sigma_z)^t$ whose $\vec{k}$-dependent expectation values are defined as

$$\langle \sigma_i(\vec{k}) \rangle = \langle \psi(\vec{k}) | \sigma_i \psi(\vec{k}) \rangle \qquad \text{with } i \in \{x, y, z\}. \tag{2.112}$$

The in-plane sublattice spins of the valence band of the model (2.126) are depicted in Fig. 2.19. They mostly follow closed paths, except at the K-points.

The expectation value of the sublattice spin vector (2.112) is almost parallel to the xy-plane everywhere except in the vicinity of the K-points where it obtains a z-component that becomes ± 1 exactly at the K-points. On circular paths around the K-points, the sublattice spin rotates, either with or against the rotation direction of the path. This rotation is illustrated in Figs. 2.20 for valence and conduction band at both the K- and the K'-point, and in Fig. 2.21 for only the valence band at the K-point.

This phenomenon allows for the computation of individual winding numbers

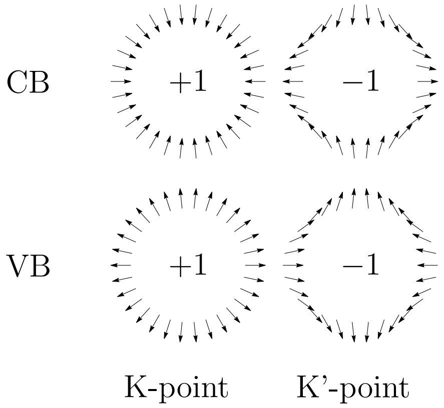

Figure 2.20: Sublattice spin winding numbers; the expectation values of the sublattice spin components (2.112) in a vicinity around the K- and K'-point are projected onto the xy-plane, allowing for an illustration as arrows. The number of rotations the sublattice spin performs around itself during a full rotation around the respective Dirac point results in the depicted winding numbers for valence and conduction band (VB and CB).

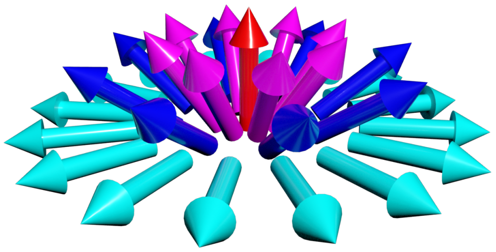

Figure 2.21: Sublattice spin structure; Around the K-point, the sublattice spin of the valence band aligns in the xy-plane (cyan), whereas in the centre it is perpendicular to the plane (red). Conduction band and K'-point are analogous, in correspondence to Fig. 2.20. The structure resembles a Skyrmion, with the difference that the spins on the outside are not fully inverted.

of the sublattice spin around the Dirac points via (cf. [12, 90])

$$n = \frac{1}{2\pi}\int_0^{2\pi} \vec{e}_z \cdot \left(\frac{1}{4}\langle\vec{\sigma}(\phi)\rangle \times \left(\frac{d}{d\phi}\langle\vec{\sigma}(\phi)\rangle\right)\right) d\phi, \tag{2.113}$$

where ϕ is the rotational angle of the path around the respective Dirac point. The overall winding numbers are additive (cf. [91]), i.e. the sum of the winding numbers of two paths equals that of the combined path. Thus, the winding numbers around the Dirac points can be used to construct the winding number for a more general path through the Brillouin zone. For that reason, take the modified Haldane model of Eq. (2.92) evaluated in the vicinity of the K-points, i.e.

$$H'_\kappa(\Delta k_x, \Delta k_y) := H\left(\vec{\kappa} + \begin{pmatrix}\Delta k_x \\ \Delta k_y\end{pmatrix}\right) \qquad \text{with } \vec{\kappa} \in \{\vec{K}, \vec{K}'\}. \tag{2.114}$$

Expanding this expression in first orders of Δk_x and Δk_y then yields

$$\begin{align} & H'_{K/K'}(\Delta k_x, \Delta k_y) \tag{2.115}\\ =& \frac{\sqrt{3}}{2} t_1(\mp\sigma_x \Delta k_x + \sigma_y \Delta k_y) + (M \pm 3\sqrt{3}t_2)\sigma_z \tag{2.116}\\ =& \begin{pmatrix} M \pm 3\sqrt{3}t_2 & \frac{\sqrt{3}}{2}t_1(\mp\Delta k_x + \mathrm{i}\Delta k_y) \\ \frac{\sqrt{3}}{2}t_1(\mp\Delta k_x - \mathrm{i}\Delta k_y) & -(M \pm 3\sqrt{3}t_2) \end{pmatrix} \tag{2.117}\\ =:& \begin{pmatrix} \pm 3\sqrt{3}t_2 & \mp\frac{\sqrt{3}}{2}t_1 e^{\mp\mathrm{i}\phi} r \\ \mp\frac{\sqrt{3}}{2}t_1 e^{\pm\mathrm{i}\phi} r & -(M \pm 3\sqrt{3}t_2) \end{pmatrix} \tag{2.118} \end{align}$$

with

$$r := \sqrt{\Delta k_x^2 + \Delta k_y^2} \qquad \text{and} \qquad \phi := \arctan\left(\frac{\Delta k_x}{\Delta k_y}\right). \tag{2.119}$$

The eigenvectors to the matrix (2.118) are at the K-point

$$|\Psi_{K,\pm}(r,\phi)\rangle = \frac{1}{\sqrt{1 + (c_K^{\pm})^2}} \begin{pmatrix} c_K^{\pm} \cdot e^{-\mathrm{i}\phi/2} \\ e^{+\mathrm{i}\phi/2} \end{pmatrix} \tag{2.120}$$

and at the K'-point

$$|\Psi_{K',\pm}(r,\phi)\rangle = \frac{1}{\sqrt{1 + (c_{K'}^{\mp})^2}} \begin{pmatrix} c_{K'}^{\mp} \cdot e^{+\mathrm{i}\phi/2} \\ e^{-\mathrm{i}\phi/2} \end{pmatrix} \tag{2.121}$$

with

$$c_K^{\pm} := \frac{-2M - 6\sqrt{3}t_2 \mp \sqrt{4M^2 + 3r^2t_1^2 + 24\sqrt{3}Mt_2 + 108t_2^2}}{\sqrt{3}rt_1} \tag{2.122}$$

and

$$c_{K'}^{\pm} := \frac{+2M - 6\sqrt{3}t_2 \mp \sqrt{4M^2 + 3r^2t_1^2 - 24\sqrt{3}Mt_2 + 108t_2^2}}{\sqrt{3}rt_1}. \tag{2.123}$$

Close to the K-points, i.e. in the limit $r \to 0$, and for $t_1 > 0$ and $M > 0$, the terms $c_\kappa^{\pm}$ behave as

$$\lim_{r\to 0} c_\kappa^{+} = 0 \qquad \text{and} \qquad \lim_{r\to 0} c_\kappa^{-} = \infty \tag{2.124}$$

for $\kappa \in \{K, K'\}$.
Thus, either the first or the second component of the solutions (2.120) and (2.121) vanishes. Hence, for $r = 0$, they are perfectly localised at one sublattice and have $\langle\sigma_z\rangle = \pm 1$.
For $r > 0$, however, the other respective component increases. Furthermore, there is a phase $e^{\pm i\phi}$ between the two components. Because of this phase, the sublattice spin alignment rotates across a path around the K- or K'-point as is depicted in Fig. 2.20.

It is also possible to compute the Chern number from the sublattice spin via (cf. [88, 89])

$$W = \frac{1}{4\pi} \iint_{\mathrm{BZ}} \langle\vec{\sigma}(\vec{k})\rangle \cdot \left(\left(\frac{\partial}{\partial k_x} \langle\vec{\sigma}(\vec{k})\rangle \right) \times \left(\frac{\partial}{\partial k_y} \langle\vec{\sigma}(\vec{k})\rangle \right) \right) d\vec{k}. \tag{2.125}$$

There are two major differences between Eqs. (2.113) and (2.125). The triple product in the latter equation contains a third term $\langle\vec{\sigma}(\vec{k})\rangle$ that is multiplied with the cross product instead of a vector $\vec{e_z}$. Also, the integration domain is no longer only an interval from $\phi = 0$ to 2π around one Dirac cone. Instead, Eq. (2.125) includes an integration over the entire Brillouin zone. Still, the main contribution to the integral comes from the Dirac points, since they are where the derivatives in Eq. (2.125) become the largest.

This discussion on the significance of the sublattice spin concludes the study of spinless graphene. As will be demonstrated in the next section, the existence of spin leads to a different topological quantum number with another type of Hall effect related to it.

2.5 Topological Insulators: Spinful Models

Without external perturbations, graphene satisfies time-reversal symmetry and can therefore neither be a Chern insulator nor can it exhibit a quantum Hall effect.[19] However, as opposed to the electrons of the (modified) Haldane model of the previous section, real electrons actually have spin. Furthermore, there is SOI coupling opposing spins. It was first noted in [11] and later discussed in [17] how, due to SOI, a new topological invariant, the $\mathbb{Z}_2$ invariant, characterises a new type of topological insulators. This subsection is based on a course on topological insulators by Kane [92].

2.5.1 $\mathbb{Z}_2$-topological Insulators

As discussed in section 2.3, SOI in graphene opens a band gap between the Dirac cones. In the (modified) Haldane model (2.89), such a band gap is generated by a sublattice potential (2.91) or a time-reversal breaking term (2.93) which are both proportional to σ_z. For a spinful model, these terms no longer act only on the sublattices, but also on the spins. Hence, the new model is of the form

$$H_{\mathrm{KM}}(\vec{k}) = \mathbb{1}_2 \otimes H_0(\vec{k}) + s_z \otimes \sigma_z \cdot (M + t_2 \cdot g(\vec{k})), \tag{2.126}$$

where the new matrix $s_z = \sigma_z$ acts as a third Pauli matrix, but on real spin instead of sublattice spin. The sublattice potential M and the time-reversal breaking term $g(\vec{k})$ thus obtain opposite signs for the respective spins. The matrix $\mathbb{1}_2$ in front of the Haldane Hamiltonian $H_0(\vec{k})$ creates two identical copies of the time-reversal symmetric modified Haldane model (2.87), one for each real spin component. While time-reversal symmetry is broken for both individual spins in model (2.126), the overall model is again symmetric. It is equivalent to the Kane-Mele model [11], except for the periodic boundary conditions. This spin-dependent setup leads to *spin-polarised edge states.*

Spin-polarised Edge States

The model (2.126) gives rise to a band structure that is mostly identical to that of the modified Haldane model, except for one major difference. Every band in Fig. 2.18 now has a spin-degenerate counterpart. Recall that the colours in the figure denote the edges the corresponding states are localised at. Cyan denotes the upper edge whereas red denotes the lower.

---

[19] The classical and the quantum Hall effect themselves are odd under time-reversal symmetry, i.e. they pick up a minus sign when reversed.

While in the original figure there is only a cyan line with negative slope and a red line with positive slope the spinful system has two more lines. These are a red line with negative slope and a cyan line with positive slope, i.e. the same lines as before, but with inverted colours.
Thus, there indeed is no typical quantum Hall effect. However, a *spin-Hall effect* is present. This effect was first predicted by Dyakonov and Perel [19, 20] and leads to two quantum Hall currents in opposite directions for opposite spins. Hence, while they individually break time-reversal symmetry, together the spin currents do not. The additional currents manifest in Fig. 2.18 in form of the additional two lines mentioned above.

The term $s_z \otimes \sigma_z$ in the model (2.126) leads to a correlation of sublattice and real spin while generating two Chern insulators, one for each respective spin. Since one edge of the graphene lattice always corresponds to one respective sublattice (cf. Fig. 4.16), this correlation separates the spin-dependent edge states by real and sublattice spin.
By the same reasoning as in section 2.4.4, the definite group velocities of the respective bands lead to edge currents that depend on both the spin they have and which edge they are localised at, i.e. graphene exhibits spin-polarised edge states. This phenomenon is illustrated in Fig. 2.22 and defines graphene as a *spin-Hall insulator* (SHI).

One more difference to Fig. 2.18 arises from SOI, but is not captured by the model (2.126). In real graphene, the bands bend in the vicinity around $k = \pi/a$. As discussed in section 2.3, the band gap is caused not directly by a coupling of $\mathrm{p_z}$-orbitals, but rather by SOI between d-orbitals that are coupled to the $\mathrm{p_z}$-orbitals. Since the d-orbitals are energetically significantly higher than the $\mathrm{p_z}$-orbitals, this coupling induces an energetic shift that ultimately leads to bending of the bands near $k = \pi/a$. This phenomenon is depicted in Fig. 2.23. For the model (2.126) without d-orbitals, the edge states assume the form depicted in Fig. 2.23a.

Because of their definite relation between spin and lattice momentum, the edge states are commonly called *helical*, a terminology stemming from high-energy physics where the momentum of a particle is used as the quantisation axis for its spin (cf. [93]). Helicity is defined as the projection of the spin onto the momentum as depicted in Fig. 2.24.

To fully understand what causes the spin-polarised edge states, it is necessary to introduce a more general notion of time-reversal symmetry as well as *Kramers' degeneracy*.

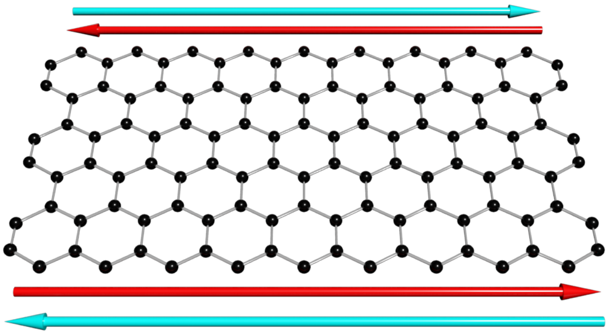

Figure 2.22: Spin-polarised edge states; States with spin up (red) and down (cyan) only move in one direction depending on the edge of the graphene sheet. The illustration is inspired by [31], but adapted to fit the geometry used in this thesis. The colours are correlated to, but not in direct correspondence with those in Figs. 2.18 and 2.23.

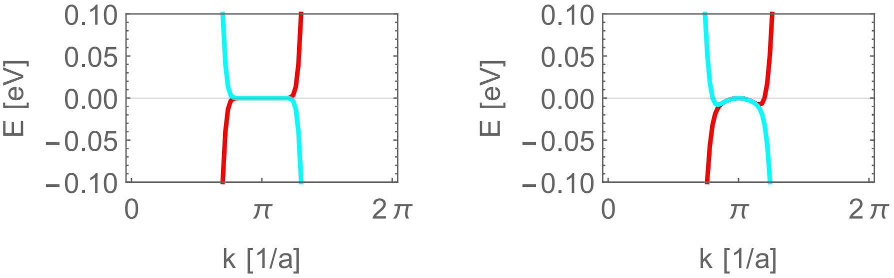

(a) (b)

Figure 2.23: Edge states without (a) and with (b) d-orbitals and SOI; The bands curve due to an effective next-nearest neighbour coupling via the SOI and the d-orbitals. A linear energy offset has been added in (b) such that the band crossing occurs at $E = 0\,\mathrm{eV}$. Each line is doubly spin-degenerate.

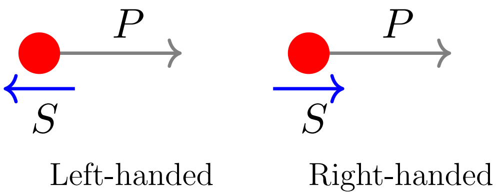

Figure 2.24: Helicity is the projection of the spin onto the momentum of a particle. If both point into the same direction, the particle is called *right-handed*. For opposite directions, it is called *left-handed*. The figure is inspired by a similar one in [94]. In the case of helical edge states in graphene, the momenta are replaced with lattice momenta.

Time-reversal Symmetry and Kramers' Degeneracy

For spinful systems, the time-reversal operation is no longer only the conjugation of the Hamiltonian matrix, but instead the conjugation with the antiunitary operator (cf. Altland and Zirnbauer [21])

$$T = \underbrace{\exp\left(\frac{\mathrm{i}\pi}{\hbar}S_y\right)}_{=:U} K, \tag{2.127}$$

where S_y is the y-component of the total spin operator and K is the complex conjugation operator. For a single free spin-$\frac{1}{2}$ particle, the expression simplifies to

$$T = -\mathrm{i}\sigma_y K = \begin{pmatrix} 0 & -1 \\ 1 & 0 \end{pmatrix} K. \tag{2.128}$$

For fermions in general, operator (2.127) exhibits the property

$$T^2 = -\mathbb{1}. \tag{2.129}$$

For bosons, the sign would be positive. With definition (2.127), time reversal symmetry for the tight-binding model assumes the form

$$TH(\vec{k})T^\dagger = H(-\vec{k}) \quad \Leftrightarrow \quad TH(\vec{k}) = H(-\vec{k})T. \tag{2.130}$$

As performed in [12], one can conclude from Eq. (2.127) that for two wave functions $|\Phi\rangle$ and $|\Psi\rangle$,

$$\langle T\Phi|T\Psi\rangle = (U|\Phi^*\rangle)^\dagger U|\Psi^*\rangle = |\Phi^*\rangle^\dagger U^\dagger U|\Psi^*\rangle = \langle\Phi^*|\Psi^*\rangle = \langle\Phi|\Psi\rangle^* . \tag{2.131}$$

Note that $U^\dagger U = \mathbb{1}$ is not in disagreement with (2.129). The next conclusion is that

$$\langle T\Psi|\Psi\rangle \overset{2.131}{=} \left\langle T^2\Psi\middle|T\Psi\right\rangle^* \overset{2.129}{=} -\langle\Psi|T\Psi\rangle^* = -\langle T\Psi|\Psi\rangle \tag{2.132}$$

and thus that $|\Psi\rangle$ and $T|\Psi\rangle$ are orthogonal to each other. From Eq. (2.130, it follows for these two distinct states that first

$$H(\vec{k})\ |\Psi(\vec{k})\rangle = \tag{2.133}$$

$$UH(-\vec{k})^{*}U^{\dagger}\ |\Psi(\vec{k})\rangle = E(\vec{k})\ |\Psi(\vec{k})\rangle \tag{2.134}$$

and then, by conjugating both sides of line (2.134)and multiplying from the left with $U^{\dagger}$,

$$H(-\vec{k})\ U^{\dagger}|\Psi(\vec{k})\rangle^{*} = E(\vec{k})\ U^{\dagger}|\Psi(\vec{k})\rangle^{*}. \tag{2.135}$$

Thus, when $|\Psi(\vec{k})\rangle$ is an eigenvector to $H(\vec{k})$ with eigenvalue $E(\vec{k})$, then $U^{\dagger}|\Psi(\vec{k})\rangle^{*}$ is an eigenvector to $H(-\vec{k})$ with eigenvalue $E(+\vec{k})$, i.e. every state has a time-reversed partner state with its energy mirrored along the $(\vec{k} = 0)$-axis. Such a pair of partner states is known as a *Kramers pair.*

As will be explained below, the states on the same site depicted in red and cyan in Figs. 2.18 and 2.23 are such Kramers pairs. This is how the full system satisfies time-reversal symmetry while the symmetry breaks down when only considering one of the respective partner states. With this information, it is possible to properly define the $\mathbb{Z}_2$-topological invariant.

The $\mathbb{Z}_2$-topological Invariant

From Kramers' degeneracy, it follows that at points where $\vec{k}$ equals $-\vec{k}$, i.e. at $\vec{k} = 0$ and at some points at the edge of the Brillouin zone, the Kramers pair states must be degenerate. Such a point of high symmetry is often referred to as a *time-reversal invariant momentum* (TRIM) and leads to the crossing of the lines for the spinful system at $k = \pi/a$ in Figs. 2.18 and 2.23. At points other than $k = \pi/a$ and $k = 0$ (which is equivalent to $k = 2\pi/a$), SOI lifts the degeneracy in Fig. 2.18.

As a consequence, both the red and cyan line cross the Fermi energy exactly once (for fixed spin), i.e. an odd number of times. This is a crucial attribute of a $\mathbb{Z}_2$-topological insulator. As illustrated in Fig. 2.25, an odd number of crossings leads to a topologically protected conducting edge states. On the other hand, if the Fermi energy is crossed an even number of times, there exists a continuous transformation that moves all energies either above or below the Fermi energy, opening a gap between the edge states. Thus, the conducting behaviour is not topologically protected.[20]

---

[20] For a mathematical proof of this phenomenon, see e.g. Fu and Kane [18].

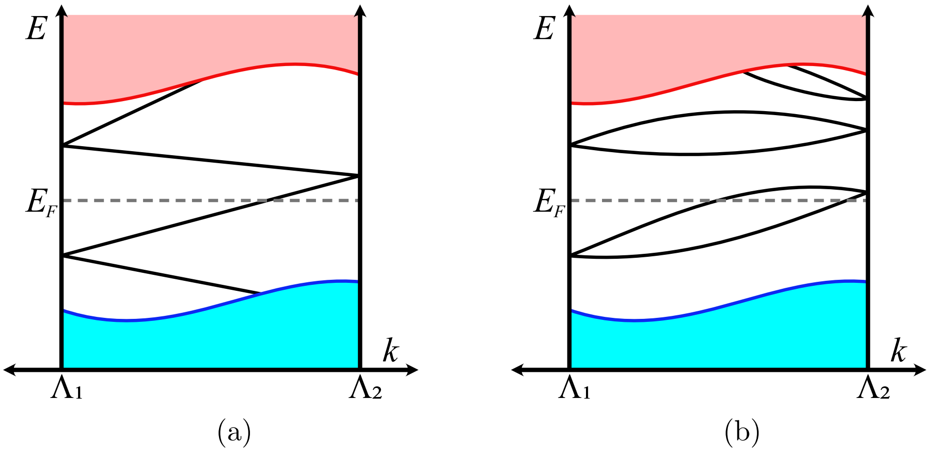

(a) (b)

Figure 2.25: Edge states within the bulk band gap; Red and cyan shaded areas indicate bulk continuum states. There are two ways by which edge states (black) between the bulk states can satisfy Kramers' degeneracy at points of high symmetry $\Lambda_{1/2}$. Either the Fermi energy E_F is crossed an odd (a) or an even number of times (b). In the even case, a continuous transformation can move them above and below the Fermi energy. Only in the odd case, there are topologically protected conducting edge states. The figure is inspired by similar ones created by Fu and Kane [18, 92].

The quantum number associated with this phenomenon is the $\mathbb{Z}_2$-*topological invariant* ν. To define it, choose a set of Bloch functions $u_n(\vec{k})$ continuous throughout the entire Brillouin zone, and define the unitary matrix

$$w_{nm}(\vec{k}) := \langle u_m(\vec{k})|T|u_n(-\vec{k})\rangle. \tag{2.136}$$

One can check that

$$w^t(\vec{k}) = -w(-\vec{k}). \tag{2.137}$$

For a d-dimensional system, there are 2^d points where $\vec{k}$ is equivalent to $-\vec{k}$. In Fig. 2.18, these are $k = 0$ and $k = \pm\pi/a$. In graphene that is periodic in two directions, these points are the Γ-point and the M-points of the Brillouin zone depicted in Fig. 1.2. For such points Λ_i, Eq. (2.137) means that w is skew-symmetric. The Pfaffian $\mathrm{pf}(w(\Lambda_i))$ of a skew-symmetric $2N \times 2N$-matrix w is defined as

$$\mathrm{pf}(w) = \frac{1}{2^N N!} \sum_{\sigma \in S_{2N}} \mathrm{sgn}(\sigma) \prod_{i=1}^{N} w_{\sigma(2i-1)\ \sigma(2i)} \tag{2.138}$$

with the symmetric group S_{2N} of order $(2N)!$ and the signature $\mathrm{sgn}(\sigma)$ of a permutation σ. From this, define

$$\delta_i = \mathrm{sgn}(\mathrm{pf}(w(\Lambda_i))) = \frac{\mathrm{pf}(w(\Lambda_i))}{\sqrt{\det(w(\Lambda_i))}} = \pm 1 \tag{2.139}$$

with the sign $\mathrm{sgn}(x)$ of a complex number x. The second equality in Eq. (2.139) stems from the fact that $\mathrm{pf}(w)^2 = \det(w)$.
The $\mathbb{Z}_2$-topological invariant ν is then defined via

$$(-1)^\nu = \prod_i \delta_i \tag{2.140}$$

with i accounting for all high-symmetry points Λ_i.
For graphene, the computation of the $\mathbb{Z}_2$ invariant can be reduced to the computation of the Chern numbers of the individual spins, as will be explained in the following.

Alternative Methods of Computation

For two-dimensional systems that conserve the spin component s_z, the computation of ν can be simplified considerably by taking the two Chern numbers $W_\uparrow$ and $W_\downarrow$ of the individual spin copies of the Haldane model (cf. [92]). While time-reversal symmetry leads to $W_\uparrow + W_\downarrow = 0$, the quantity

$$W_\sigma = \frac{W_\uparrow - W_\downarrow}{2} \tag{2.141}$$

is typically non-trivial. From it, the $\mathbb{Z}_2$ invariant can be computed as

$$\nu = W_\sigma \mod 2. \tag{2.142}$$

Note that in the presence of s_z-nonconserving terms as they e.g. arise from Rashba SOI (2.150), W_σ is no longer a good quantum number, ν however still is (cf. [18, 92]). To give further interpretation to the $\mathbb{Z}_2$ invariant, one more computation method will be summarised briefly.

It is possible to compute ν from the eigenvalues of the parity operator P as well. The action of P on a spatial wave function $|\psi(\vec{r})\rangle$ is defined as

$$P|\Psi(\vec{r})\rangle = |\Psi(-\vec{r})\rangle. \tag{2.143}$$

At the high-symmetry points in reciprocal space, one obtains the eigenvalues

$$P|\Psi(\Lambda_i)\rangle = \xi_m(\Lambda_i)|\Psi(\Lambda_i)\rangle. \tag{2.144}$$

From this, one obtains (cf. [18, 92])

$$\delta_i = \prod_m \xi_m(\Lambda_i) \tag{2.145}$$

and thus an alternative method to compute ν via Eq. (2.140). The index m in Eq. (2.145) runs over the bands below the gap while only considering one band per (parity-degenerate) Kramers pair.
Even though this procedure will not be used in this thesis, it does help understanding the $\mathbb{Z}_2$ invariant. Parity at the high-symmetry points can be interpreted as either

- a band crossing the gap ($\xi_m(\Lambda_i) = -1$, e.g. at $k = \pi/a$ in the middle of Fig. 2.18) or
- a band avoiding the gap ($\xi_m(\Lambda_i) = +1$, e.g. at $k = 0$ at the left part of Fig. 2.18).

The $\mathbb{Z}_2$ invariant is thus a measure for whether there is an even or odd number of gap crossings, like in Fig. 2.25. ν can therefore be computed via the number $N(E)$ of edge states (cf. [12])

$$\nu = \frac{N(E)}{2} \mod 2 = \frac{N_+(E) + N_-(E)}{2} \mod 2, \tag{2.146}$$

where $N_+(E) + N_-(E) = N(E)$ denote the number of right-moving and left-moving states, respectively. Due to Kramers' theorem, both numbers are identical.

With this additional interpretation at hand, it is possible to discuss the physical meaning of the $\mathbb{Z}_2$ invariant in appropriate detail.

Interpretation

The $\mathbb{Z}_2$-topological invariant $\nu \in \{0, 1\}$ thus defines the parity of the gap crossings and therefore, as argued further above, the existence of conducting edge states in a topological insulator. Unperturbed spinful graphene has $\nu = 1$ and is therefore a $\mathbb{Z}_2$-topological insulator. Both time-reversal asymmetric subsystems, individually, are Chern insulators.
Each of these systems exhibits a Hall conductivity of $\pm e^2/h$, *even without an external magnetic field applied* (cf. Hao at al. [87]). An electric field would thus lead to Hall currents for $s_z = \pm 1$ which cancel each other out, but generate a net spin current as described by Kane [92]

$$\vec{J}_s = \frac{\hbar}{2e}(\vec{J}_\uparrow - \vec{J}_\downarrow) \tag{2.147}$$

with a quantised spin Hall conductivity

$$\sigma^s_{xy} = \frac{e}{2\pi}. \tag{2.148}$$

This quantisation, however, breaks down in the presence of s_z-nonconserving terms, in particular Rashba terms (2.150) that were introduced in section 2.3.1. In the following, it will be briefly discussed how the Rashba effect acts on the topological properties of graphene.

Rashba SOI

Despite being affected by the Rashba effect, the edge states remain robust and retain their spin-polarised properties as long as the Rashba strength is small. For large Rashba strength, the system becomes topologically trivial. This can be demonstrated by adding a term

$$(H_{\mathrm{Rashba}})_{i,j} = -\mathrm{i}\lambda_{\mathrm{R}}((\vec{R}_i - \vec{R}_j)_x s_y - (\vec{R}_i - \vec{R}_j)_y s_x) \tag{2.149}$$

to model (2.126). The matrices $s_i = \sigma_i$ act on the spin. Expression (2.149) depends on the relative positions of neighbouring lattice sites, similar to the equivalent definition in Eq. (2.86).

Near the K-points, the term (2.149) can be approximated to (cf. [11, 29])

$$H_{\mathrm{RSOI},K/K'} = \lambda'_{\mathrm{R}}\left(\pm\sigma_x \mathrm{s}_y - \sigma_y \mathrm{s}_x\right), \tag{2.150}$$

where λ'_{R} is the modified strength λ_{R} after the approximation. σ_i here acts on the sublattice spin and s_i on the real spin. Note that the Rashba effect lifts spin degeneracy. In the following, only the bands closer to the Fermi energy will be considered, i.e. the blue cones of Fig. 2.10 (pg. 29). The approximate combined effect of intrinsic and Rashba SOI on the intrinsic band gap Δ_{SOI} between the blue cones is, according to [11],

$$\Delta_{\mathrm{SOI+R}} = 2(\Delta_{\mathrm{SOI}} - \lambda_{\mathrm{R}}) \tag{2.151}$$

for $0 < \lambda_{\mathrm{R}} < \Delta_{\mathrm{SOI}}$, and it is $\Delta_{\mathrm{SOI+R}} = 0$ for $\lambda_{\mathrm{R}} > \Delta_{\mathrm{SOI}}$.
A strong Rashba effect thus closes the band gap, rendering the Chern numbers trivial. As a consequence, graphene can only be topologically non-trivial when one of the effects is negligibly weak.

This brief discussion on the Rashba effect concludes the discussions that are limited to the topology of graphene. In the following, general topological systems will be discussed under the topic of the so-called *ten-fold way*.

Class	Symmetry			Dimension							
	T^2	P^2	C^2	0	1	2	3	4	5	6	7
A	0	0	0	$\mathbb{Z}$	0	$\mathbb{Z}$	0	$\mathbb{Z}$	0	$\mathbb{Z}$	0
AIII	0	0	1	0	$\mathbb{Z}$	0	$\mathbb{Z}$	0	$\mathbb{Z}$	0	$\mathbb{Z}$
AI	1	0	0	$\mathbb{Z}$	0	0	0	$2\mathbb{Z}$	0	$\mathbb{Z}_2$	$\mathbb{Z}_2$
BDI	1	1	1	$\mathbb{Z}_2$	$\mathbb{Z}$	0	0	0	$2\mathbb{Z}$	0	$\mathbb{Z}_2$
D	0	1	0	$\mathbb{Z}_2$	$\mathbb{Z}_2$	$\mathbb{Z}$	0	0	0	$2\mathbb{Z}$	0
DIII	-1	1	1	0	$\mathbb{Z}_2$	$\mathbb{Z}_2$	$\mathbb{Z}$	0	0	0	$2\mathbb{Z}$
AII	-1	0	0	$2\mathbb{Z}$	0	$\mathbb{Z}_2$	$\mathbb{Z}_2$	$\mathbb{Z}$	0	0	0
CII	-1	-1	1	0	$2\mathbb{Z}$	0	$\mathbb{Z}_2$	$\mathbb{Z}_2$	$\mathbb{Z}$	0	0
C	0	-1	0	0	0	$2\mathbb{Z}$	0	$\mathbb{Z}_2$	$\mathbb{Z}_2$	$\mathbb{Z}$	0
CI	1	-1	1	0	0	0	$2\mathbb{Z}$	0	$\mathbb{Z}_2$	$\mathbb{Z}_2$	$\mathbb{Z}$

Table 2.1: Periodic table of topological invariants; If a system satisfies time-reversal (T), particle-hole (P) or chiral symmetry (C), the squared values of the operators define symmetry classes. If they do not satisfy a symmetry, a 0 is written instead. Depending on the dimension of the system, this results in a topological invariant of either $\mathbb{Z}$, $\mathbb{Z}_2$ or $2\mathbb{Z}$. A 0 denotes the absence of any topological invariant. Graphene with p- and d-orbitals and spin is a two-dimensional system of the class AII and therefore has a $\mathbb{Z}_2$-topological invariant. The table is periodic for dimensions of $d \to d + 8$.

2.5.2 The Tenfold Way

The fact that graphene is a $\mathbb{Z}_2$-topological insulator stems not only from its symmetry, but also from its dimension. In different dimensions, different types of topological and trivial insulators can arise from the same symmetries. Altland and Zirnbauer have detailed this connection[21], which then lead to the creation of the *periodic table of topological invariants* [22–24]. The latter is given in Tab. 2.1. The table is separated into ten classes of random matrices[21] which are characterised by their symmetry based on three operators:

- T is the time-reversal operator as defined in Eq. (2.127).
- P is the particle-hole operator as specified on page 31 and
- C is the chiral operator as also specified on page 31.

---

[21] This thesis will not go into any detail on random matrices. Instead, it will only work with the results of the corresponding computations. For information on random matrices, it is recommended to instead resort to other sources, e.g. [95].

The matrix classes will henceforth be dubbed Altland-Zirnbauer classes.
Graphene satisfies time-reversal symmetry, and the time-reversal operator itself squares to -1. Since the d-orbitals break particle-hole symmetry, the appropriate Altland-Zirnbauer class is AII. In two dimensions, this results in the appropriate $\mathbb{Z}_2$-topological invariant ν.

Graphene in the (modified) Haldane model (2.92) differs from real graphene in two ways. It is particle-hole symmetric, and its particles are spinless. Note that it was the introduction of spin that led to the relation $T^2 = -1$ in section 2.5.1. For the Haldane model, one therefore has $P^2 = 1$ and either $T^2 = 1$ or $T^2 = 0$, depending on whether $t_2 = 0$ or $t_2 \neq 0$. For $t_2 = 0$, the corresponding Altland-Zirnbauer class is therefore BDI which, in two dimensions, has no topological invariant.
For $t_2 \neq 0$, time-reversal symmetry is broken. The corresponding class is D which, in two dimensions, has a topological invariant isomorphic to $\mathbb{Z}$. This invariant is the Chern number computed in section 2.4.3.
The class of the Kane-Mele model with $T^2 = -1$ and $P^2 = 1$ is DIII.

Both the Chern and the Haldane model are models with only one (possibly spin-degenerate) valence and conduction band. In models with more bands, the number of the topologically protected edge states is defined not only by the Chern number of the valence band, but instead by the sum of all Chern numbers of all occupied bands (cf. [96–98]). Accordingly, a Hall conductance is computed as the sum

$$\sigma_{xy} = \sum_{\text{occupied } n} W_n \cdot e^2/h \tag{2.152}$$

with the respective Chern number W_n of the band with index n. This phenomenon is illustrated in Fig. 2.26. In Eq. (2.152), the sum

$$\sum_{\text{occupied } n} W_n =: \mathcal{W} \tag{2.153}$$

equals the number of edge states that cross the Fermi energy in a Chern insulator. For $\mathbb{Z}_2$-topological insulators, the sums over the Chern numbers in Eq. (2.152) and (2.153) only take one spin into account and are taken modulo 2. The Hall conductance then corresponds to only one spin current.

As a final remark to this section on topology, note that the concept of edges of a two-dimensional material can be generalised. As depicted in Fig. 2.27, a three-dimensional object has two-dimensional surfaces. The latter are separated by one-dimensional edges that, again, are separated by zero-dimensional

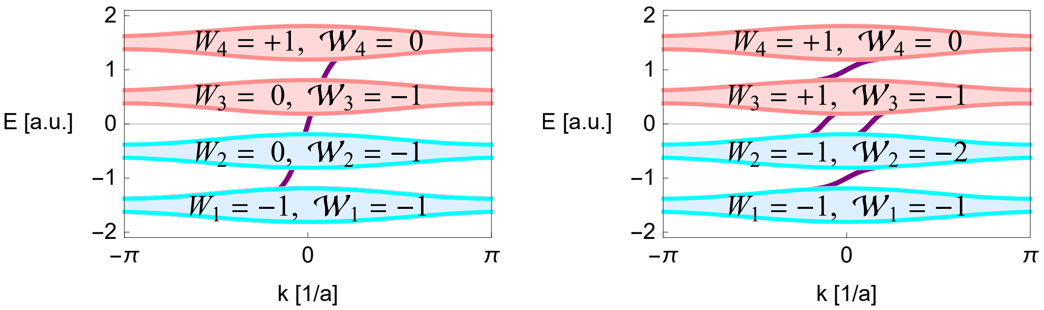

(a) (b)

Figure 2.26: Topological edge states in a multi-band insulator; Bands above the Fermi energy $E_F = 0$ are depicted in red, those below in blue. $\mathcal{W}_n := \sum_{i=1}^{n} W_i$ is the sum over the Chern numbers of the lowest n bands. (a) Even though the Chern numbers of valence and conduction band are both zero, i.e. $W_2 = W_3 = 0$, the sum $\mathcal{W}_2 = -1$ over the Chern numbers of all bands below the Fermi energy is non-zero. Hence, an edge state (purple) between valence and conduction band occurs. The edge states below and above do not contribute directly towards conductivity. (b) The Chern numbers below the Fermi energy add up to $\mathcal{W}_2 = -2$, leading to two currents crossing it. The sum $\mathcal{W}_4$ over all Chern numbers is zero in both (a) and (b).

vertices. Edges and surfaces can both give rise to topologically non-trivial gapped systems that therefore exhibit topologically protected gap-crossing states in the respectively lower dimension. These systems are called *higher-order topological insulators* (HOTI), as defined by Schindler at al. [99]. An n'th-order topological insulator is a d-dimensional system that exhibits topologically protected edge states on its $(d - n)$-dimensional boundary. The topological quantum numbers associated with HOTIs are called *weak topological invariants* and can be obtained from Tab. 2.1 by considering lower dimensions d.

The classes BDI, D and DIII all do have topological invariants for $d = 1$. Thus, both the Haldane and the Kane-Mele model bear the potential of describing HOTIs if their one-dimensional band structures are gapped and have corresponding non-trivial weak topological invariants. In chapters 4 and 5, however, graphene will always be of either the class AII or A. Thus, it will not have a weak topological invariant at $d = 1$, and it will therefore not exhibit any higher-order edge states. Even though one should be aware of the concept of HOTIs, it will thus not affect the results of this thesis.

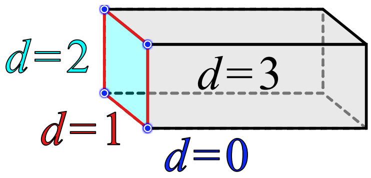

Figure 2.27: Higher-order edges; A three-dimensional object has two-dimensional surfaces (cyan) that, in turn, have one-dimensional edges (red). Those edges have zero-dimensional vertices (blue). These boundaries of boundaries are called higher-order edges. Only a selection of higher-order edges has been highlighted.

On the other hand, time-dependent electric perturbations will affect the topological invariants. The time-dependence will be handled via Floquet formalism which will be discussed in the following, together with its consequences for the topological invariants.

2.6 Time-dependent Systems

All discussions so far have considered systems that have not been explicitly time-dependent. Even time-reversal symmetry has only been applied to the lattice momentum $\vec{k}$. An electromagnetic field generated by continuous irradiation of a sample with laser light, however, is explicitly time-dependent. For such a dependence, the time-reversal symmetry relation (2.130) reshapes to

$$TH(\vec{k},t)T^\dagger = H(-\vec{k},t_0-t) \tag{2.154}$$

with a point in time t_0 about which the system is symmetric (cf. [25]).
While there are typically no static solutions to an explicitly time-dependent system, the periodicity of the light-induced electromagnetic fields gives rise to quasi-static solutions. The latter will be derived in the following as a consequence of *Floquet formalism*.

2.6.1 Floquet Formalism

To derive the Floquet formalism, first assume a Hamiltonian

$$H(t) = H(t+\tau), \tag{2.155}$$

that is periodic by some time τ. This time-dependent Hamiltonian is then Fourier-decomposed to ultimately reduce the corresponding linear first-order differential equations to a purely algebraic problem. The decomposition is performed as

$$H_n = \frac{1}{\tau}\int_0^\tau e^{\mathrm{i}n\omega t} H(t)dt \qquad \text{with } \omega = \frac{2\pi}{\tau}. \tag{2.156}$$

From Floquet's theorem [39] (cf. [37] for a detailed derivation), it follows that a system

$$\mathrm{i}\hbar\frac{\partial}{\partial t}\vec{\Psi}(t) = H(t)\vec{\Psi}(t) \qquad \text{with } H(t) = \sum_{n=-\infty}^{\infty} e^{-\mathrm{i}n\omega t} H_n, \tag{2.157}$$

oscillating in time t with frequency ω is solved by wave functions

$$\vec{\Psi}(t) = \vec{\eta}(t)\exp\left(-\frac{\mathrm{i}}{\hbar}\epsilon t\right) \qquad \text{with } \vec{\eta}(t) = \sum_{n=-\infty}^{\infty} e^{\mathrm{i}n\omega t}\vec{\zeta}_n, \qquad \vec{\zeta}_n \in \mathbb{C}^d \tag{2.158}$$

with respective *Floquet quasi-energies* ϵ. The vectors $\vec{\Psi}(t)$, $\vec{\eta}(t)$ and $\vec{\zeta}_n$ are all d-dimensional, where d is the dimension of the original Hilbert space. The terms ϵ and $\vec{\zeta}_n$ are derived from the recursive formula

$$\epsilon\vec{\zeta}_n = (H_0 + n\hbar\omega\cdot\mathbb{1})\vec{\zeta}_n + \sum_{m\neq n} H_{m-n}\vec{\zeta}_m, \tag{2.159}$$

which can be obtained by inserting Eqs. (2.158) into (2.157). Eq. (2.159) can be written as an eigenvalue problem

$$\epsilon\vec{\zeta} = H_{\mathrm{F}}\vec{\zeta} \tag{2.160}$$

with the infinite-dimensional composite vector

$$\vec{\zeta} := (..,\ \vec{\zeta}_{-2},\ \vec{\zeta}_{-1},\ \vec{\zeta}_0,\ \vec{\zeta}_1,\ \vec{\zeta}_2, ..)^t \tag{2.161}$$

and the *Floquet Hamiltonian matrix*

$$H_{\mathrm{F}} :=$$
$$\begin{pmatrix}
\ddots & \vdots & \vdots & \vdots & & & \\
\cdots & (H_0 - 2\hbar\omega\mathbb{1}) & H_{+1} & H_{+2} & \vdots & & \\
\cdots & H_{-1} & (H_0 - 1\hbar\omega\mathbb{1}) & H_{+1} & H_{+2} & \vdots & \\
\cdots & H_{-2} & H_{-1} & H_0 & H_{+1} & H_{+2} & \cdots \\
 & \vdots & H_{-2} & H_{-1} & (H_0 + 1\hbar\omega\mathbb{1}) & H_{+1} & \cdots \\
 & & \vdots & H_{-2} & H_{-1} & (H_0 + 2\hbar\omega\mathbb{1}) & \cdots \\
 & & & \vdots & \vdots & \vdots & \ddots
\end{pmatrix}. \tag{2.162}$$

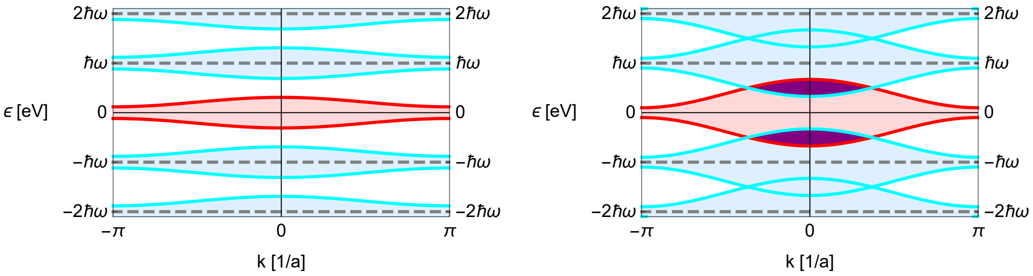

(a) (b)

Figure 2.28: Floquet replica bands; In Floquet formalism, the time-independent part of the band structure (red) is replicated for every integer multiple of $\hbar\omega$. These replica bands (blue) can have gaps between them (a) or intersect one another (b), depending on whether the original spectrum lies within one energy interval of the length $\hbar\omega$. The intersection area between the red and blue bands is highlighted in purple. More intersections can occur, depending on whether the energy interval of the original spectrum surpasses further integer multiples of $\hbar\omega$.

In Eq. (2.162), colours have been used to separate the orders $n = 0$ (black), $n = \pm 1$ (blue) and $n = \pm 2$ (red). Higher order terms $H_{\pm n}$ with $n > 2$ lie on the n'th respective diagonal from the middle, counting upwards or downwards with respect to the sign. The identity matrices $\mathbb{1}$ will be dropped in the following if the expressions are clear without them.

After solving the eigenvalue equation (2.160) for a Floquet energy ϵ and vector $\vec{\zeta}$, the corresponding solution $\vec{\Psi}(t)$ to the original time-dependent system (2.157) is reconstructed via Eqs. (2.158). Since $\vec{\Psi}(t)$ only acquires a phase after a full oscillation period, via

$$\vec{\Psi}(t+\tau) = e^{-\frac{\mathrm{i}}{\hbar}\epsilon\tau}\vec{\Psi}(t), \tag{2.163}$$

it is called *quasi-static* or sometimes *steady*.

The diagonal entries of H_F in Eq. (2.162) are matrices of the form $(H_0 + n\hbar\omega)$ with $n \in \mathbb{Z}$. They are coupled to one another via the matrices $H_{\pm m}$ with $m > 0$. Without the latter, the eigenvalues ϵ of H_F would be copies of the original eigenvalues of H_0 plus integer multiples of $\hbar\omega$. This is illustrated in Fig. 2.28 for a one-dimensional band structure. The copies of the original bands are called *Floquet replica bands*. In the following, these replica bands will be identified with photonic excitations.

2.6.2 Photon Count

The decomposition of electric fields into their Fourier components belonging to specific energies $\hbar\omega$ suggests treating those terms as photon energies as is done in an analysis of Shirley [100]. The term H_{+1} then belongs to the excitation by the absorption of one photon whereas H_{-1} corresponds to the emission. This interpretation can be extended to n photons and $H_{\pm n}$. Note, however, that the fields here are treated only classically, i.e. the formalism does not describe spontaneous emissions or absorptions.

According to this interpretation, a *photon count matrix* can be defined as

$$\Gamma := \begin{pmatrix} \ddots & 0 & & & & & \\ 0 & -2\cdot\mathbb{1} & 0 & & & & \\ & 0 & -1\cdot\mathbb{1} & 0 & & & \\ & & 0 & 0\cdot\mathbb{1} & 0 & & \\ & & & 0 & +1\cdot\mathbb{1} & 0 & \\ & & & & 0 & +2\cdot\mathbb{1} & 0 \\ & & & & & 0 & \ddots \end{pmatrix} \tag{2.164}$$

with unit matrices of dimension d, similar to the $\vec{\zeta}_n$ in Eq. (2.158). The expectation value

$$\langle\Gamma\rangle = \vec{\zeta}^t\Gamma\vec{\zeta} \tag{2.165}$$

will therefore be identified with the number of photons a state has absorbed or emitted. Solutions to H_F with $\langle\Gamma\rangle \approx 0$ will be interpreted has having zero mean absorbed or emitted photons. Together with their respective quasi-energies ϵ, these solutions will therefore be dubbed the *electronic band structure*. Oppositely, those solutions that have $\langle\Gamma\rangle \approx \pm n$ with $n > 0$ can be interpreted as having either absorbed or emitted n photons, depending on the sign. Together with their respective quasi-energies, these solutions will be called *photonic band structure*. As noted by Shirley [100], the identification of the Floquet energies with photonic excitations relies on a large number of photons being present. Thus, both the electronic and the photonic band structure need to be considered inside a continuum of photons.

Based on the definitions (2.161) and (2.183) for $\vec{\zeta}$, the condition $\langle\Gamma\rangle \approx 0$ can be met in two ways:

1. All $\vec{\zeta}_n$ inside $\vec{\zeta}$ vanish, except for $n = 0$.
2. A state $\vec{\zeta}$ satisfies $\sum_{n>0} n \cdot \left|\vec{\zeta}_n\right|^2 = -\sum_{n<0} n \cdot \left|\vec{\zeta}_n\right|^2$.

The second condition in particular includes states with $|\vec{\zeta}_n| = |\vec{\zeta}_{-n}|\ \forall n$. States that satisfy condition 2, but not condition 1 are dressed by virtual photons, i.e. a photon is absorbed and emitted in a coherent process. Such dressed states will be said to have *effectively zero photons*, since it is only the $\vec{\zeta}_0$ contribution that directly corresponds to no photonic excitation. Condition 1 can only be satisfied if there is no interaction with the photon field.

The Floquet band structure illustrated in Fig. 2.28a can be separated into replicas that correspond to certain photon numbers. The electronic band structure is depicted in red. The n-photon replicas are are depicted in blue and are centred around the energies $n\hbar\omega$, for $n \in \mathbb{Z}\backslash\{0\}$. In Fig. 2.28b, the electronic bands intersect with some photonic bands. Such an intersection occurs when $f = \omega/(2\pi)$ is a resonance frequency for the two respective bands. In the Floquet Hamiltonian H_{F} (see Eq. (2.162), such a resonant coupling is generated by the terms $H_{\pm 1}$.
Even though the figure only shows an intersection between the 0- and the 1-photon bands, it is also possible for the 0- and the 2-photon bands to cross. Those bands can then be coupled either via terms $H_{\pm 2}$ or via multiple instances of $H_{\pm 1}$. The coupling via $H_{\pm 1}$ is a second-order process associated with the exchange of two photons, whereas the terms $H_{\pm 2}$ are associated with a single photon of twice the frequency.
These concepts can be generalised to any higher resonances. The processes via multiple $H_{\pm 1}$, however, are typically suppressed, similar to higher-order perturbative processes. All these processes can also occur between two sets of photonic bands. However, as will be explained in the following, it suffices to only consider the effects on the electronic bands.

2.6.3 Electronic and Photonic Band Structure

The 0-photon bands and the n-photon bands are entirely identical, except for two aspects:

1. Their Floquet quasi-energies ϵ differ by $n\hbar\omega$.
2. The entries $\vec{\zeta}_i$ of their eigenvectors $\vec{\zeta}$ (see Eq. (2.161)) are shifted by n places relative to one another inside the vectors. Thus, their photonic expectation values differ by n.

To further exemplify this, consider a 0-photon state with Floquet energy ϵ^0 and eigenvector

$$\vec{\zeta}^{\,0} := (.., \vec{\zeta}^{\,0}_{-2}, \vec{\zeta}^{\,0}_{-1}, \vec{\zeta}_0^{\,0}, \vec{\zeta}_1^{\,0}, \vec{\zeta}_2^{\,0}, ..)^t \tag{2.166}$$

as defined in section 2.6.1. If the state $\vec{\zeta}^{\,0}$ exists, then a similar 2-photon state exists with Floquet energy $\epsilon^2 = \epsilon^0 + 2\hbar\omega$ and eigenvector

$$\vec{\zeta}^{\,2} := (.., \vec{\zeta}^{\,0}_{-4}, \vec{\zeta}^{\,0}_{-3}, \vec{\zeta}^{\,0}_{-2}, \vec{\zeta}^{\,0}_{-1}, \vec{\zeta}^{\,0}_{0}, ..)^t. \tag{2.167}$$

When these solutions are recombined into the solution $\vec{\Psi}(t)$ of the original, time-dependent system via Eq. (2.158), then the the 0-photon state yields

$$\vec{\Psi}^0(t) = \exp\left(-\frac{\mathrm{i}}{\hbar}\epsilon^0 t\right) \sum_{n=-\infty}^{\infty} e^{\mathrm{i}n\omega t}\vec{\zeta}^{\,0}_n. \tag{2.168}$$

The 2-photon state, on the other hand, yields

$$\begin{aligned}
\vec{\Psi}^2(t) =& \exp\left(-\frac{\mathrm{i}}{\hbar}(\epsilon^0 + 2\hbar\omega)t\right) \sum_{n=-\infty}^{\infty} e^{\mathrm{i}n\omega t}\vec{\zeta}^{\,0}_{n-2} && (2.169)\\
=& \exp\left(-\frac{\mathrm{i}}{\hbar}\epsilon^0 t\right) e^{-2\mathrm{i}\omega t} \sum_{n=-\infty}^{\infty} e^{\mathrm{i}(n+2)\omega t}\vec{\zeta}^{\,0}_{n} && (2.170)\\
=& \exp\left(-\frac{\mathrm{i}}{\hbar}\epsilon^0 t\right) \sum_{n=-\infty}^{\infty} e^{\mathrm{i}n\omega t}\vec{\zeta}^{\,0}_{n} && (2.171)\\
=& \vec{\Psi}^0(t). && (2.172)
\end{aligned}$$

Thus, both the 2-photon state and the 0-photon state correspond to the same time-dependent solution of the original system. It therefore suffices to only consider the Floquet energies in an interval

$$\epsilon \in \left(-\frac{\hbar\omega}{2}, +\frac{\hbar\omega}{2}\right] \tag{2.173}$$

to fully understand the time-dependent solutions of the original Schrödinger equation (2.157). Alternatively, if the photon expectation values $\langle\Gamma\rangle$ assume approximately integer values, it is also possible to only consider the electronic band structure, since all n-photon bands with $n \neq 0$ are replicas of it. In the latter case, it is possible to use the instantaneous energy expectation values $\langle E(t)\rangle := \langle\Psi^0|H(t)|\Psi^0\rangle$ of a time-dependent solution $|\Psi^0(t)\rangle$ at times t to make assumptions on the filling of the Floquet states. For actual 0-photon states, one can compute

$$\langle E(t)\rangle = \langle\Psi^0|H(t)|\Psi^0\rangle = \langle\Psi^0|\mathrm{i}\hbar\frac{\partial}{\partial t}|\Psi^0\rangle = \mathrm{i}\hbar(\vec{\zeta}^{\,0})^\dagger \left(e^{+\frac{\mathrm{i}}{\hbar}\epsilon^0 t}\frac{\partial}{\partial t}e^{-\frac{\mathrm{i}}{\hbar}\epsilon^0 t}\right)\vec{\zeta}^{\,0} = \epsilon^0, \tag{2.174}$$

i.e. the energy expectation value is identical to the Floquet energy. For mixed photon states, Eq. (2.174), one needs to take the time average over the interval from $t = 0$ to $t = \tau = 2\pi/\omega$ One then obtains

$$\begin{aligned}
\langle E \rangle &= \frac{1}{\tau} \int_0^\tau \Psi^\dagger(t) \left(\mathrm{i}\hbar \frac{\partial}{\partial t} \right) \Psi(t)\ dt \qquad &(2.175)\\
&= \frac{1}{\tau} \int_0^\tau e^{+\frac{\mathrm{i}}{\hbar}\epsilon t} \eta^\dagger(t) \left(\mathrm{i}\hbar \frac{\partial}{\partial t} \right) e^{-\frac{\mathrm{i}}{\hbar}\epsilon t} \eta(t)\ dt &(2.176)\\
&= \frac{1}{\tau} \int_0^\tau e^{+\frac{\mathrm{i}}{\hbar}\epsilon t} e^{-\frac{\mathrm{i}}{\hbar}\epsilon t} \eta^\dagger(t) \left(-\frac{\mathrm{i}}{\hbar}\epsilon + \mathrm{i}\hbar \frac{\partial}{\partial t} \right) \eta(t)\ dt &(2.177)\\
&= \frac{1}{\tau} \int_0^\tau \epsilon + \eta^\dagger(t) \left(\mathrm{i}\hbar \frac{\partial}{\partial t} \right) \eta(t)\ dt &(2.178)\\
&= \epsilon + \frac{1}{\tau} \int_0^\tau \sum_n e^{-\mathrm{i}n\omega t} \vec{\zeta}_n^\dagger \left(\mathrm{i}\hbar \frac{\partial}{\partial t} \right) \sum_m e^{+\mathrm{i}n\omega t} \vec{\zeta}_m\ dt &(2.179)\\
&= \epsilon - \frac{1}{\tau} \int_0^\tau \sum_n e^{-\mathrm{i}n\omega t} \vec{\zeta}_n^\dagger \sum_m m\hbar\omega e^{+\mathrm{i}n\omega t} \vec{\zeta}_m\ dt &(2.180)\\
&= \epsilon - \sum_{n,m} m\hbar\omega \vec{\zeta}_n^\dagger \vec{\zeta}_m \underbrace{\frac{1}{\tau} \int_0^\tau e^{+\mathrm{i}(n-m)\omega t}\ dt}_{\delta_{nm}} &(2.181)\\
&= \epsilon - \sum_n n\hbar\omega |\vec{\zeta}_n|^2. &(2.182)
\end{aligned}$$

From line (2.175) to (2.176), only definitions have been inserted. In the step to (2.177), the product rule was used. (2.178) was achieved by changing the order of terms and solving some of the products. The insertion of the definition of $\eta(t)$ then leads to line (2.179), where the time-derivative is applied to obtain line (2.180). By pulling the integral into the sum in line (2.181), one can see that only the summands with $n = m$ can contribute towards the final energy expectation value given in line (2.182).

If the condition $\sum_{n>0} n \cdot \left| \vec{\zeta}_n \right|^2 = -\sum_{n<0} n \cdot \left| \vec{\zeta}_n \right|^2$ is satisfied, i.e. if the state is an effective 0-photon state, then the final summand in line (2.182) vanishes, and the Floquet quasi-energy ϵ is identical to $\langle E \rangle$. Thus, for band structures with mostly near-integer photon expectation values, the Floquet quasi-energies can be treated as the energy expectation values. The electronic band structure can then be treated like the band structure of a time-independent system, in particular to predict its filling.

As will be explained in the following, it often suffices to only consider a truncated Floquet Hamiltonian matrix H_F to study the electronic band structure.

2.6.4 Truncation

By restricting the n-photon bands that are being considered to $-N \leq n \leq N$ for $N \in \mathbb{N}$, the vectors $\vec{\zeta}_n$ and the Floquet matrix H_F (cf. Eqs. (2.161) and (2.162)) both become finite-dimensional.[22] The vector

$$\vec{\zeta} = (\vec{\zeta}_{-N}, .., \ \vec{\zeta}_{-1}, \ \vec{\zeta}_0, \ \vec{\zeta}_1, .., \ \vec{\zeta}_N)^t \tag{2.183}$$

is then the solution to a Floquet Hamiltonian matrix of $2N + 1$ times the dimension d of the original Hamiltonian matrix $H(t)$, i.e. it has $d \cdot (2N + 1)$ eigenvalues ϵ and eigenvectors ζ. In this thesis, N will be called the *Floquet order*.

Due to the truncation by N, the original time-dependent Schrödinger equation (2.157) becomes a finite-dimensional algebraic problem, only omitting terms corresponding to multiples of ω higher than N-fold. This involves in particular N-photon processes and processes that involve photons that correspond to N-times the driving frequency.[23] This is further motivated for systems with only one driving frequency, as will be explained in the following.

For processes that oscillate periodically with exactly one frequency, such as irradiation with monochromatic light, the Hamiltonian (2.157) only involves up to three summands, H_0 and $H_{\pm 1}$, as these describe constant systems and systems with time dependence of the form $\cos(\omega t)$ and $\sin(\omega t)$. Thus, after truncation by N, the Floquet Hamiltonian (2.162) assumes the form

$$H_\text{F} = \begin{pmatrix} (H_0 - N\hbar\omega) & H_{+1} & 0 & & & & \\ H_{-1} & \ddots & H_{+1} & 0 & & & \\ 0 & H_{-1} & (H_0 - 1\hbar\omega) & H_{+1} & 0 & & \\ & 0 & H_{-1} & H_0 & H_{+1} & 0 & \\ & & 0 & H_{-1} & (H_0 + 1\hbar\omega) & H_{+1} & 0 \\ & & & 0 & H_{-1} & \ddots & H_{+1} \\ & & & & 0 & H_{-1} & (H_0 + N\hbar\omega) \end{pmatrix}. \tag{2.184}$$

Hence, the electronic bands are only coupled directly to the (± 1)-photon states. When considered perturbatively, a coupling to the $(\pm n)$-photon states

---

[22] The truncation does not need to be symmetrical. All results of this section can be derived analogously for independent upper and lower limits N_+ and N_-.

[23] More precisely, any combinations of n_i-photon processes with $|\sum_i n_i| \geq N$ are omitted. Here, n_i can be positive for absorptions and negative for emissions.

only occurs as an $(2n)$'th order correction to the electronic bands.[24] Thus, if the matrix elements of $H_{\pm 1}$ are smaller than the unperturbed eigenenergies of H_0, it is appropriate to truncate the system by some Floquet order N after which further corrections become negligible.

As a conclusion to this chapter, the effect of time-dependence and Floquet formalism on the general topology of a system will be discussed.

2.6.5 Topology

The effects on the topology due to time-dependence can be of great consequence to the topological invariants and the topological edge states, as has been shown by Roy and Harper [25]. In the following, their work will be summarised and adapted to the notation of this thesis. Analogously to Roy and Harper, consider the time evolution operator[25]

$$U(t) := \mathcal{T} \exp\left(-\frac{\mathrm{i}}{\hbar}\int_0^t H(t')dt'\right) \tag{2.185}$$

with the time ordering operator $\mathcal{T}$ and a time t, such that

$$\vec{\Psi}(t) = U(t)\vec{\Psi}(0). \tag{2.186}$$

The eigenvalues of $U(t)$ are complex and have absolute value 1. Thus, they can be written as $e^{-\frac{\mathrm{i}}{\hbar}\epsilon(t)t}$ with a function $\epsilon(t)$ that satisfies

$$\epsilon:\ t \to \epsilon(t) \in \left(-\frac{\pi\hbar}{t}, +\frac{\pi\hbar}{t}\right] \text{ for } t \neq 0 \tag{2.187}$$

and $\epsilon(0) = 0$. It is not by coincidence that the function $\epsilon(t)$ uses the same symbol as the Floquet quasi-energy. In fact, if $H(t)$ is periodic, the following relation holds

$$e^{-\frac{\mathrm{i}}{\hbar}\epsilon(\tau)\tau} = e^{-\frac{\mathrm{i}}{\hbar}\epsilon\tau}, \tag{2.188}$$

i.e. the function $\epsilon(\tau)$ and the quasi-energy ϵ are identical modulo $2\pi\hbar/\tau$. In accordance with Eq. (2.173), the Floquet energy ϵ can thus be limited to the interval

$$\epsilon \in \left(-\frac{\pi\hbar}{\tau}, +\frac{\pi\hbar}{\tau}\right] = \left(-\frac{\hbar\omega}{2}, +\frac{\hbar\omega}{2}\right] \tag{2.189}$$

---

[24] E.g. a (-1)- and a $(+1)$-photon state $|-1\rangle$ and $|+1\rangle$ are coupled via an intermediate 0-photon state $|0\rangle$. The lowest-order correction term that couples $|-1\rangle$ and $|+1\rangle$ perturbatively is of fourth order and involves an expression proportional to $|\langle +1|H_{+1}|0\rangle\langle 0|H_{+1}|-1\rangle|^2$.

[25] As can be seen from the acquired prefactor in Eq. (2.163), the time evolution operator is not necessarily periodic in time, even if the underlying system is. This is similar to how Bloch wave functions obtain a phase upon translation from one unit cell to another.

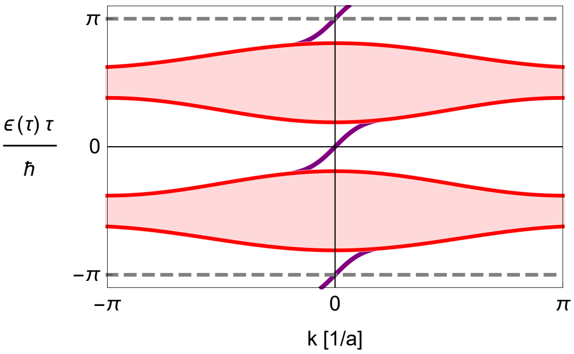

Figure 2.29: Spectrum of a Floquet Hamiltonian H_{F}', defined for a fixed time τ; A time evolution possibly changes the topology of the band structure and can therefore give rise to edge states (purple) between bands (red). In a system that satisfies particle-hole or chiral symmetry, the only topologically non-trivial gaps can occur at $\epsilon(\tau) = 0$ and $\epsilon(\tau) = \pm\frac{\pi\hbar}{\tau}$. If these symmetries are absent from the system, additional non-trivial gaps can occur at arbitrary $\epsilon(\tau)$. Since the eigenvalues $e^{-\frac{\mathrm{i}}{\hbar}\epsilon(\tau)\tau}$ of the time-evolution operator $U(\tau)$ lie on a circle in the complex plane, the values $+\pi$ and $-\pi$ are identified, allowing for edge modes to arise at $\epsilon(\tau) = \pm\frac{\pi\hbar}{\tau}$. The figure is inspired by [25].

with the time τ over which the time-dependent system is periodic. Notably, the interval in Eq. (2.189) has a length equal to the energy $\hbar\omega$ of one photon. It is sometimes referred to as the *first Brillouin zone of the Floquet energy*. An alternative Floquet Hamiltonian can be defined to have its values within the interval (2.189), by

$$H_{\mathrm{F}}' := \mathrm{i}\ln(U(\tau)). \tag{2.190}$$

As opposed to H_{F} from Eq. (2.162), the spectrum of H_{F}' from Eq. (2.190) is bounded from above and below by $\pm\frac{\pi\hbar}{\tau}$. This is because the spectrum identifies a circle. Those values of the Floquet energy ϵ that lie beyond the bounds correspond to values of $\epsilon(\tau)$ that, after a modulo operation, lie again within the bounds.

The identification with a circle allows for topological band gaps that span across the bounds, as the points $\epsilon(\tau) = +\frac{\pi\hbar}{\tau}$ and $\epsilon(\tau) = -\frac{\pi\hbar}{\tau}$ are identified with one another. Since a time-evolution can change the topology of the system, edge modes can arise both within the spectrum and across the bounds as illustrated in Fig. 2.29.

As Roy and Harper have shown, such edge modes, both within the bounds and across them, can arise as a consequence of any time-evolution, not only those that stem from a time-periodic system. Let X be the manifold that describes the periodic Brillouin zone.[26] For a time-periodic system, X is extended by a manifold that describes the periodic time, i.e. the one-dimensional sphere S^1. The new manifold $S^1 \times X$ then gives rise to a new periodic table of Floquet topological invariants that is given at the end of this section in Tab. 2.2.

As proved by Roy and Harper, the topological invariants $\mathcal{G} \in \{\mathbb{Z}, 2\mathbb{Z}, \mathbb{Z}_2\}$ obtain an exponent and are therefore replaced with either $\mathcal{G}^{\times n_p}$ for systems that satisfy particle-hole or chiral symmetry, or $\mathcal{G}^{\times n}$ for systems that do not. The integers $n \in \mathbb{N}\backslash\{0\}$ and $n_p \in \{1, 2\}$ denote the number of *physically relevant* gaps in the spectrum given by $\epsilon(\tau)$. The nomenclature "physically relevant" is based on [25] and denotes d-dimensional bulk bands that still exhibit a band gap after projection onto $d-1$ dimensions. Only if there is a physically relevant gap both at $\epsilon(\tau) = 0$ and $\epsilon(\tau) = \pm\frac{\pi\hbar}{\tau}$, does n_p assume the value 2. n can generally assume any positive integer value.

To elaborate on the meaning of physically relevant band gaps, an example of Rudner at al. [101] will be used.
Consider a two-dimensional particle-hole symmetric two-band insulator with trivial Chern numbers $W = 0$. The latter can be computed for the quasi-bands $\epsilon(\tau)$ as a function of $\vec{k}$ by the same formulae as for a conventional band structure. In the time-independent case, this system would not exhibit any topologically protected conducting edge states. In the time-dependent case, this is not necessarily true. To understand this, consider Fig. 2.30. A topologically trivial system like in Fig. 2.30a can be made non-trivial by closing and reopening the band gap[27] at $\epsilon(\tau)\tau/\hbar = \pm\pi$. In the process, the Chern numbers of valence and conduction band become $W = \pm 1$. As a consequence, chiral edge states (purple) appear in Fig. 2.30b.
By closing and reopening the gap at $\epsilon(\tau)\tau/\hbar = 0$, the Chern numbers can be made trivial again, i.e. $W = 0$. However, the edge states that cross $\epsilon(\tau)\tau/\hbar = \pm\pi$ cannot disappear, since the corresponding band gap remains open. As a consequence, new edge modes arise at $\epsilon(\tau)\tau/\hbar = 0$, as depicted in Fig. 2.30c.

---

[26] Due to its periodicity, the Brillouin zone can be considered mathematically as a torus. This is similar to how it was illustrated for the lattice in Fig. 2.4 (pg. 9).

[27] This closing and reopening of the band gap does not happen on any time scale. In fact, the Chern numbers are time-independent (cf. [102, 103]). Instead, the three systems in Fig. 2.30 should be considered as three topologically different system that therefore have no continuous transformation connecting them. The closing and reopening is an artificial non-continuous transformation to visualise the connection between Chern numbers, topological protection and edge states.

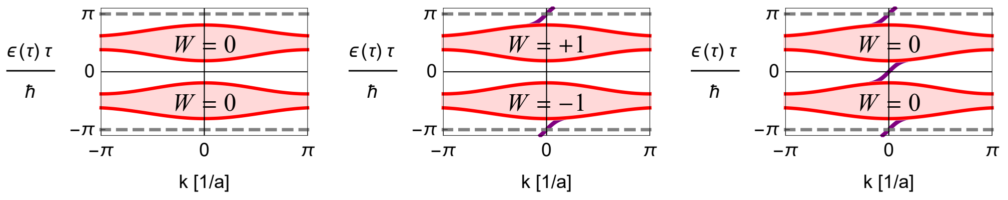

(a) (b) (c)

Figure 2.30: Edge states in a periodic Floquet band structure at time $t = \tau$; A topologically trivial system (a) can become non-trivial (b) by closing and reopening the band gap between bulk bands (red) at the quasi-energy values $\epsilon(\tau)\tau/\hbar = \pm\pi$. As a consequence, topologically protected edge states (purple) arise. By closing and reopening another band gap at $\epsilon(\tau)\tau/\hbar = 0$, the Chern numbers W become trivial again (c). New topologically protected conducting edge states arise to compensate the other ones. The figure is inspired by [25] and [101].

The system described above has $n = 2$ physically relevant band gaps. However, all observations can be generalised to any Floquet topological insulators. The system exhibits two topologically protected edge states despite having trivial Chern numbers $W = 0$. This does not change the fact that non-zero Chern numbers still indicate the existence of topologically protected edge states. However, it is possible that these edge states stretch across the boundary of the Floquet Brillouin zone. In a time-dependent system, the sum of the Chern numbers is therefore no longer equal to the number of edge states that cross $\epsilon(\tau) = 0$ like in Eq. (2.153) and Fig. 2.26.

Rudner at al. [101] instead give an explicit form for the topological invariant of a system as described above in form of what they call the *winding number*[28]

$$W[U] := \frac{1}{8\pi^2} \iiint \mathrm{Tr}\left(U^{-1}\frac{\partial}{\partial t}U \left[U^{-1}\frac{\partial}{\partial k_x}U, U^{-1}\frac{\partial}{\partial k_y}U \right] \right)\, dt\; dk_x\; dk_y, \tag{2.191}$$

where the dependencies of the time-evolution operator U have not been written explicitly. Rudner at al. show that the winding number $W[U]$ is equal to the number of edge states that cross the Floquet Brillouin zone at $\epsilon(\tau)\tau/\hbar = \pm\pi$. Together with the Chern numbers of the n physically relevant

---

[28] This winding number should not be confused with the sublattice spin winding number defined in Eq. (2.113).

band gaps,[29] it is then possible to conclude the number of edge states that cross every respective band, similarly to how it has been done in Eq. (2.153) and Fig. 2.26.

In spinful graphene with d-orbitals, as it is considered in this thesis, a time evolution would replace the $\mathbb{Z}_2$-topological invariant with either a $\mathbb{Z}_2^{\times n}$-topological invariant or a $\mathbb{Z}^n$-topological invariant, depending on the time-reversal symmetry. However, no edge states that cross the boundary of the Floquet Brillouin zone are found in this thesis. Hence, the Chern numbers and the $\mathbb{Z}_2$-topological invariant suffice to describe the topology of the time-dependent system like in the time-independent case.

---

[29] Since the sum over all Chern numbers is zero, it is only necessary to compute $n-1$ of them. Together with the winding number (2.191), this makes a total of n individual $\mathbb{Z}$-topological quantum numbers. Hence, the system is a $\mathbb{Z}^{\times n}$-topological insulator.

Class	Symmetry			Dimension							
	T^2	P^2	C^2	0	1	2	3	4	5	6	7
A	0	0	0	$\mathbb{Z}^{\times n}$	0	$\mathbb{Z}^{\times n}$	0	$\mathbb{Z}^{\times n}$	0	$\mathbb{Z}^{\times n}$	0
AIII	0	0	1	0	$\mathbb{Z}^{\times n_p}$	0	$\mathbb{Z}^{\times n_p}$	0	$\mathbb{Z}^{\times n_p}$	0	$\mathbb{Z}^{\times n_p}$
AI	1	0	0	$\mathbb{Z}^{\times n}$	0	0	0	$(2\mathbb{Z})^{\times n}$	0	$\mathbb{Z}_2^{\times n}$	$\mathbb{Z}_2^{\times n}$
BDI	1	1	1	$\mathbb{Z}_2^{\times n_p}$	$\mathbb{Z}^{\times n_p}$	0	0	0	$(2\mathbb{Z})^{\times n_p}$	0	$\mathbb{Z}_2^{\times n_p}$
D	0	1	0	$\mathbb{Z}_2^{\times n_p}$	$\mathbb{Z}_2^{\times n_p}$	$\mathbb{Z}^{\times n_p}$	0	0	0	$(2\mathbb{Z})^{\times n_p}$	0
DIII	-1	1	1	0	$\mathbb{Z}_2^{\times n_p}$	$\mathbb{Z}_2^{\times n_p}$	$\mathbb{Z}^{\times n_p}$	0	0	0	$(2\mathbb{Z})^{\times n_p}$
AII	-1	0	0	$(2\mathbb{Z})^{\times n}$	0	$\mathbb{Z}_2^{\times n}$	$\mathbb{Z}_2^{\times n}$	$\mathbb{Z}^{\times n}$	0	0	0
CII	-1	-1	1	0	$(2\mathbb{Z})^{\times n_p}$	0	$\mathbb{Z}_2^{\times n_p}$	$\mathbb{Z}_2^{\times n_p}$	$\mathbb{Z}^{\times n_p}$	0	0
C	0	-1	0	0	0	$(2\mathbb{Z})^{\times n_p}$	0	$\mathbb{Z}_2^{\times n_p}$	$\mathbb{Z}_2^{\times n_p}$	$\mathbb{Z}^{\times n_p}$	0
CI	1	-1	1	0	0	0	$(2\mathbb{Z})^{\times n_p}$	0	$\mathbb{Z}_2^{\times n_p}$	$\mathbb{Z}_2^{\times n_p}$	$\mathbb{Z}^{\times n_p}$

Table 2.2: Periodic table of topological invariants for Floquet-topological insulators; Similarly to Tab. 2.1, systems have topological invariants, depending on their time-reversal (T), particle-hole (P) and chiral symmetry (C). The table is periodic for Brillouin zone dimensions of $d \to d + 8$. The integers $n \in \mathbb{Z}^+$ and $n_p\{1, 2\}$ denote the number of physically relevant band gaps of the system. n_p assumes the value 2 only if there is a non-trivial gap both at $\epsilon(\tau) = 0$ and $\epsilon(\tau) = \pm\frac{\pi\hbar}{\tau}$. The exponents $\times n$ and $\times n_p$ denote the respective n- and n_p-fold direct product of a group with itself. The Altland-Zirnbauer class AII in $d = 2$ dimensions has been highlighted with thick borders as it is the class corresponding to graphene.

Chapter 3

Electric Fields in Graphene

This chapter will discuss the effects of a time-dependent electric field on the graphene Floquet band structure analytically. First, section 3.1 will cover the choice of a scalar potential as well as its compatibility with the periodicity of the lattice. Afterwards, section 3.2 will derive analytical solutions for the unperturbed graphene band structure at the K-point. In section 3.3, the discussions of both previous sections will then be combined to predict the behaviour of the Floquet energies of graphene at the K-point under irradiation with circularly polarised light.

3.1 Implementation of the External Electric Field

Since the magnetic component $\vec{B}$ of an electromagnetic field is suppressed by a factor c compared to its electric one $\vec{E}$, i.e.

$$|\vec{B}| = \frac{1}{c}|\vec{E}|, \tag{3.1}$$

this thesis will restrict to only the electric component. In the following, an electric field generated by a laser beam perpendicular to the graphene sample will be considered. It will be assumed perpendicular to ensure that all field components are in-plane. As discussed in section 2.3.1 and at the end of section 2.5.1, an out-of-plane component can lead to a Rashba effect that affects the topology of the band structure. Out-of-plane components and their effect on the topology will be discussed separately in sections 4.2.3 and 5.2.2.

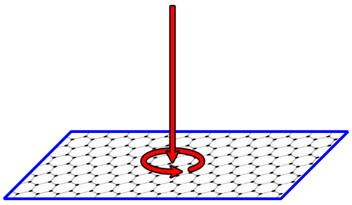

Figure 3.1: The incoming laser beam (straight red arrow), depending on the polarisation (circular red arrow), gives rise to an oscillating electric field in the plane of the graphene sheet (blue).

The polarisation of the laser beam determines the shape of the corresponding electric field. For circular and linear polarisation, the respective in-plane fields are

$$\vec{E}_{\mathrm{circ}}(\vec{r},t) = E_0 \cdot \begin{pmatrix} \cos(\omega t - \vec{\kappa}\vec{r}) \\ \sin(\omega t - \vec{\kappa}\vec{r}) \\ 0 \end{pmatrix} \quad \text{and} \quad \vec{E}_{\mathrm{lin}}(\vec{r},t) = \sqrt{2}E_0 \cdot \begin{pmatrix} 0 \\ \sin(\omega t - \vec{\kappa}\vec{r}) \\ 0 \end{pmatrix} , \tag{3.2}$$

where the indices “circ” and “lin” denote the respective polarisations. The wave vector $\vec{\kappa} = \vec{e}_z \cdot 2\pi/\lambda$ with the wavelength λ points in the z-direction. Linearly polarised light has been equipped with a prefactor $\sqrt{2}$ to ensure that both fields have the same intensity for identical electric field strength E_0. The effects of elliptically polarised light are expected to be a combination of those of circular and linear polarisation. However, the details of elliptical polarisation will be left to future work. The irradiation with circularly polarised light is illustrated in Fig. 3.1.

It is possible to choose a gauge such that the corresponding electromagnetic vector potentials for the electric fields (3.2) are

$$\vec{A}_{\mathrm{circ}}(\vec{r},t) = \frac{E_0}{\omega} \cdot \begin{pmatrix} -\sin(\omega t - \vec{\kappa}\vec{r}) \\ \cos(\omega t - \vec{\kappa}\vec{r}) \\ 0 \end{pmatrix} , \quad \vec{A}_{\mathrm{lin}}(\vec{r},t) = \frac{\sqrt{2}E_0}{\omega} \cdot \begin{pmatrix} 0 \\ \cos(\omega t - \vec{\kappa}\vec{r}) \\ 0 \end{pmatrix} , \tag{3.3}$$

together with trivial scalar potentials

$$\Phi_{\mathrm{circ/lin}}(\vec{r},t) = 0. \tag{3.4}$$

In the following, the indices "circ" and "lin" will only be written explicitly when it is necessary to distinguish between both polarisations. Note that the vector potentials in Eq. (3.3) are not yet rotation-free, i.e. they lead to magnetic fields. The latter, however, disappear under the assumption $\vec{\kappa}\vec{r} \approx 0$. This dipole approximation is justified by the small extent of graphene into the z-direction, as $\lambda \gg a_{\mathrm{Bohr}}$. The approximation takes the spatial dependence from the potential. Via a gauge transformation

$$\begin{aligned} \vec{A}(\vec{r},t) \to \vec{A}'(\vec{r},t) &= \vec{A}(\vec{r},t) + \nabla\chi(\vec{r},t) & (3.5)\\ \Phi(\vec{r},t) \to \Phi'(\vec{r},t) &= \Phi(\vec{r},t) - \frac{\partial\chi(\vec{r},t)}{\partial t}, & (3.6) \end{aligned}$$

it is then possible to change to a gauge where the vector potential is trivial. For circular polarisation, the gauge term

$$\chi_{\mathrm{circ}}(\vec{r},t) = \frac{E_0}{\omega} \cdot \left(x\sin(\omega t) - y\cos(\omega t)\right), \tag{3.7}$$

leads to the new electromagnetic potentials

$$\Phi'_{\mathrm{circ}}(\vec{r},t) = -E_0 \cdot \left(x\cos(\omega t) + y\sin(\omega t)\right) \qquad \text{and} \qquad \vec{A}'_{\mathrm{circ}}(\vec{r},t) = \begin{pmatrix}0\\0\\0\end{pmatrix}. \tag{3.8}$$

An equivalent transformation for linear polarisation leads to

$$\Phi'_{\mathrm{lin}}(\vec{r},t) = -\sqrt{2}E_0 \cdot y\sin(\omega t) \qquad \text{and} \qquad \vec{A}'_{\mathrm{lin}}(\vec{r},t) = \begin{pmatrix}0\\0\\0\end{pmatrix}. \tag{3.9}$$

The Schrödinger equation for a particle of charge q inside a lattice potential $U(\vec{r})$ transforms accordingly from

$$\mathrm{i}\frac{\partial}{\partial t}\psi(\vec{r},t) = \left(\frac{\left(\vec{p} - q\vec{A}(\vec{r},t)\right)^2}{2m} + U(\vec{r})\right)\psi(\vec{r},t). \tag{3.10}$$

to

$$\mathrm{i}\frac{\partial}{\partial t}\psi'(\vec{r},t) = \left(\frac{\vec{p}^2}{2m} - q\Phi'(\vec{r},t) + U(\vec{r})\right)\psi'(\vec{r},t), \tag{3.11}$$

In Eq. (3.11), the wave functions have been transformed as well, according to

$$\psi(\vec{r},t) \to \psi'(\vec{r},t) \;=\; \psi(\vec{r},t) \cdot \exp\left(-\mathrm{i}\frac{q}{\hbar}\chi(\vec{r},t)\right), \tag{3.12}$$

to ensure overall gauge invariance. These two gauges are called *velocity gauge*[1] for $\Phi(\vec{r},t) = 0$ and *length gauge* for $\vec{A}(\vec{r},t) = 0$, respectively (cf. [61]).

Both Schrödinger equations (3.10) and (3.11) are equivalent. However, there is a vast difference in how they are typically handled in a tight-binding model. Eq. (3.10) is commonly treated by means of Peierls substitution [82, 83] where the hopping terms in the Hamiltonian are modified as

$$t_{ij} \to t_{ij} \cdot \exp\left(\mathrm{i}\frac{q}{\hbar}\int_{\vec{r}_i}^{\vec{r}_j} \vec{A}(\vec{r}',t)d\vec{r}'\right) \tag{3.13}$$

with positions $\vec{r}_i$ and $\vec{r}_j$ of the respective atoms i and j.
However, as noted by many of the original authors of this method, it is not suited for a strongly time-dependent LCAO model [105–107]. The reason is that the substitution is the result of a transformation quite similar to the gauge transformation in Eq. (3.12), but performed individually on each lattice site. As a result, one would end up with new, individual effective scalar potentials for every site (cf. [44, 108]).[2]

Instead, this thesis will exclusively work with Eq. (3.11). Nonetheless, this ansatz bears a problem as well. Since the scalar potential of a spatially constant electric field is incompatible with the periodicity condition of the Bloch theorem, the wave functions need to be separated into Wannier and envelope functions (cf. section 2.2.4). As a consequence of this procedure, the Wannier functions are no longer orthogonal for different reciprocal vectors $\vec{k}$. Hence, it is mandatory to discuss the effect of the resulting $\vec{k}$-non-diagonal terms.

3.1.1 Coupling of Different $\vec{k}$

As was shown by Kleinman [73], a separation of a linear potential into a staggered part and a sawtooth part like in Fig. 2.7 (pg. 22) leads to $\vec{k}$-non-diagonal terms between the Wannier functions.

---

[1] The definition of the velocity gauge differs between fields of research as e.g. mentioned in [104] regarding velocity gauge in laser-matter interactions.

[2] These new terms are proportional to the time-derivative of the vector potential and typically only couple different bands. Hence, they can be neglected for slowly varying perturbations or single-band models.

To study the $\vec{k}$-non-diagonal terms that arise from a scalar potential $\Phi(\vec{r}, t)$, the notation of section 2.2 will be modified slightly to write

$$|\psi_{n\vec{k}}, \vec{k}\rangle := e^{\mathrm{i}\vec{k}\vec{r}} \psi_{n\vec{k}}(\vec{r}, t) \tag{3.14}$$

with

$$\psi_{n\vec{k}}(\vec{r}, t) := \frac{1}{\sqrt{N}} \sum_{\vec{R}} \sum_{s=\pm 1} f^{s}_{n,\vec{R}}(t) e^{\mathrm{i}\vec{k}\vec{R}} w_n(\vec{r} - (\vec{R} + s \cdot \vec{\delta}/2)). \tag{3.15}$$

The $\vec{R}$ are lattice vectors and $\vec{\delta}$ the displacement vector according to definitions (2.1) and (2.2). $s \in \{-1, +1\}$ defines whether a wave function is localised on sublattice A (+1) or sublattice B (−1). The $w_n(\vec{r})$ are the Wannier functions composed of atomic orbitals according to Eq. (2.44). The $f^{s}_{n,\vec{R}}(t)$ are envelope functions like in Eq. (2.65), but equipped with a label s for the respective sublattice.[3] n denotes the quantum numbers associated with the atomic orbitals.

The Hamiltonian describing an electron in the graphene lattice together with the scalar potential $\Phi(\vec{r}, t)$ can be expressed as

$$H(\vec{r}, t) = \underbrace{\frac{\vec{p}^{\,2}}{2m} + U(\vec{r})}_{=:H_0} - \underbrace{e^{-} \cdot \Phi(\vec{r}, t)}_{=:H_1}, \tag{3.16}$$

where e^{-} is the electron charge. Note that the minus sign is not included in the definition of H_1. This has no physical relevance and only serves the purpose of easing later computations. The dependencies on $\vec{r}$ and t will not be written explicitly in the following. The matrix elements

$$\langle \psi_{n_1\vec{k}}, \vec{k} | H | \psi_{n_2\vec{k}}, \vec{k}'\rangle \tag{3.17}$$

can be separated into

$$\langle \psi_{n_1\vec{k}}, \vec{k} | H | \psi_{n_2\vec{k}'}, \vec{k}'\rangle = \langle \psi_{n_1\vec{k}}, \vec{k} | H_0 | \psi_{n_2\vec{k}'}, \vec{k}'\rangle - \langle \psi_{n_1\vec{k}}, \vec{k} | H_1 | \psi_{n_2\vec{k}'}, \vec{k}'\rangle, \tag{3.18}$$

where the first summand corresponds to the unperturbed, $\vec{k}$-diagonal Hamiltonian of graphene.

---

[3] Equivalently, one could include the label s into the label $\vec{R}$. This distinction has only been made because of the clear sublattice structure of graphene.

For $H_1 = e^- \cdot \Phi(\vec{r}, t) = (V(t) \cdot x)$, i.e. a spatially homogeneous electric field that varies in time, the second summand becomes

$$
\begin{aligned}
&\langle \psi_{n_1\vec{k}}, \vec{k} | H_1 | \psi_{n_2\vec{k}'}, \vec{k}' \rangle \\
=&\int_{\mathbb{R}^3} e^{\mathrm{i}(\vec{k}-\vec{k}')\vec{r}} \cdot {\psi_{n_1\vec{k}}}^{\dagger}(\vec{r}) \cdot V(t)x \cdot \psi_{n_2\vec{k}'}(\vec{r})\ d\vec{r} \\
=&\sum_{\text{lattice vectors } \vec{R}} \int_{\text{unit cell}} e^{\mathrm{i}(\vec{k}-\vec{k}')(\vec{r}+\vec{R})} \cdot V(t) {\psi_{n_1\vec{k}}}^{\dagger}(\vec{r})(R_x + x)\psi_{n_2\vec{k}'}(\vec{r})\ d\vec{r} \\
=&V(t)\sum_{\vec{R}} e^{\mathrm{i}(\vec{k}-\vec{k}')\vec{R}} \Bigg(R_x \cdot \underbrace{\int_{\text{u.c.}} e^{\mathrm{i}(\vec{k}-\vec{k}')\vec{r}} \cdot {\psi_{n_1\vec{k}}}^{\dagger}(\vec{r})\psi_{n_2\vec{k}'}(\vec{r})\ d\vec{r}}_{=:\eta_{n_1,n_2,k,k'}} \\
&\qquad\qquad + \underbrace{\int_{\text{u.c.}} e^{\mathrm{i}(\vec{k}-\vec{k}')\vec{r}} \cdot {\psi_{n_1\vec{k}}}^{\dagger}(\vec{r})\ x\ \psi_{n_2\vec{k}'}(\vec{r})\ d\vec{r}}_{=:\xi_{n_1,n_2,k,k'}} \Bigg) \\
=&V(t)\sum_{\vec{R}} e^{\mathrm{i}(\vec{k}-\vec{k}')\vec{R}} \cdot R_x \cdot \eta_{n_1,n_2,k,k'} + V(t) \underbrace{\sum_{\vec{R}} e^{\mathrm{i}(\vec{k}-\vec{k}')\vec{R}} \cdot \xi_{n_1,n_2,k,k'}}_{=N\cdot\delta_{kk'}\cdot\xi_{n_1,n_2,k,k'},\ \text{diagonal in } \vec{k}} .
\end{aligned}
\tag{3.19}
$$

Going from the second to the third line, the integral over the $\mathbb{R}^3$ has been separated into a sum of identical integrals over the unit cell.[4] This changes the global x-component into a local one plus the x-component R_x of the respective lattice vector.

Since $\xi_{n_1,n_2,k,k'}$ is independent of $\vec{R}$, the second sum over $\vec{R}$ in Eq. (3.19) obtains a Kronecker delta $\delta_{k,k'}$. For $\vec{k} = \vec{k}'$, the term $\xi_{n_1,n_2,k,k} =: \xi_{n_1,n_2}$ is k-independent and becomes the regular dipole matrix element. The first sum in Eq. (3.19), on the other hand, contains an expression R_x. Because of it, the overall sum is not diagonal with respect to $\vec{k}$. The term $\eta_{n_1,n_2,k,k'}$ corresponds to the integral over the function $e^{\mathrm{i}(\vec{k}-\vec{k}')\vec{r}}$ coupling the two states $\psi_{n_1\vec{k}}$ and $\psi_{n_2\vec{k}'}$. Via Eq. (3.15), the latter states are defined as weighted sums of Wannier functions that, in turn, can be expressed as sums of orbital wave functions (cf. section 2.2.3). In appendix B, the term $\eta_{n_1,n_2,k,k'}$ has been evaluated for wave functions that are localised on the same sublattice. Limiting

---

[4] These integrals still include an integration over the entire z-axis that has not been written explicitly.

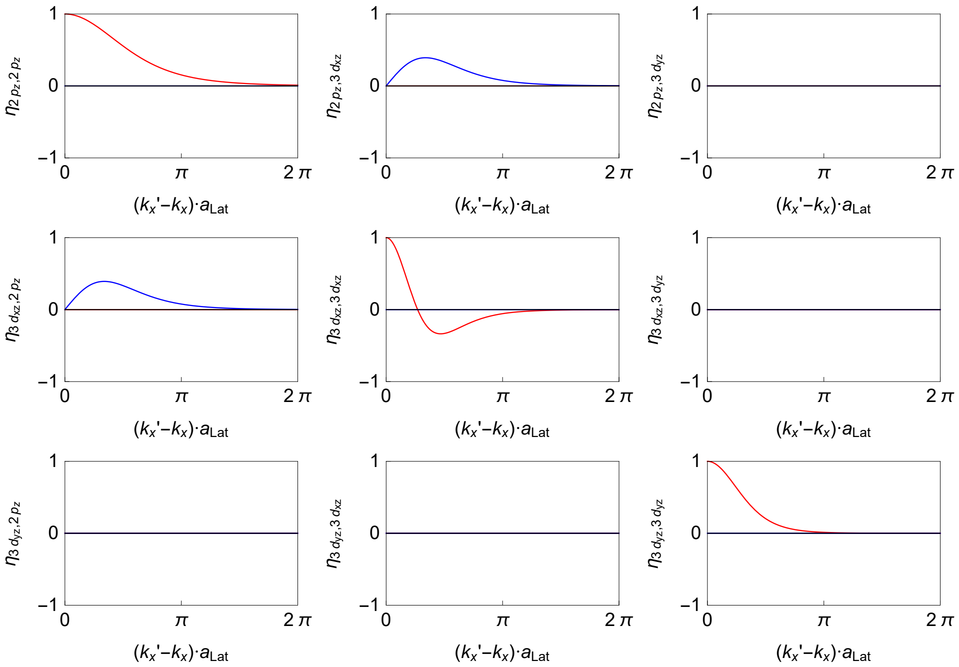

Figure 3.2: Matrix elements of $\eta(k_x' - k_x)$ from eq. (3.20): Rows and columns are ordered $\mathrm{p_z}$, $\mathrm{d_{xz}}$, $\mathrm{d_{yz}}$. Red lines denote real, blue imaginary part. The label "Lat" serves to better distinguish lattice constant and effective Bohr radius.

the wave functions to the orbitals $\mathrm{p_z}$, $\mathrm{d_{xz}}$ and $\mathrm{d_{yz}}$, the term can be expressed as a matrix

$$\begin{aligned} &\left(\eta_{n_1,n_2,k,k'}\right)_{n_1,n_2\in\{2\mathrm{p_z},3\mathrm{d_{xz}},3\mathrm{d_{yz}}\}} \\ &= \begin{pmatrix} \frac{1}{((a_{\mathrm{Lat}}\Delta k_x)^2+1)^3} & \frac{b\cdot \mathrm{i}a_{\mathrm{Lat}}\Delta k_x}{\left(\left(\frac{6}{5}a_{\mathrm{Lat}}\Delta k_x\right)^2+1\right)^4} & 0 \\ \frac{b\cdot \mathrm{i}a_{\mathrm{Lat}}\Delta k_x}{\left(\left(\frac{6}{5}a_{\mathrm{Lat}}\Delta k_x\right)^2+1\right)^4} & \frac{1-7\left(\frac{3}{2}a_{\mathrm{Lat}}\Delta k_x\right)^2}{\left(\left(\frac{3}{2}a_{\mathrm{Lat}}\Delta k_x\right)^2+1\right)^5} & 0 \\ 0 & 0 & \frac{1}{\left(\left(\frac{3}{2}a_{\mathrm{Lat}}\Delta k_x\right)^2+1\right)^4} \end{pmatrix} \end{aligned} \tag{3.20}$$

with[5] $\Delta k_x := (k_x' - k_x)$. The parameter $b = 2^{11}\cdot 3^4/5^7$ has no physical significance and is merely an analytical result. The lattice constant has been equipped with an index "Lat" to avoid confusion with the effective Bohr radius that is used in the computations in appendix B. A field in y-direction

---

[5] In Appendix B, the definition for $\Delta\vec{k}$ differs by a prefactor included there to simplify computations. However, due to the unintuitive nature of that prefactor, the definition here is without it.

would result in a similar expression as Eq. (3.20), but with $\mathrm{d_{xz}}$ and $\mathrm{d_{yz}}$ interchanged. Eq. (3.20) has been plotted in Fig. 3.2. As can be seen from the figure, η, while generally non-zero, does never have entries with absolute values larger than 1. More importantly, η drops off notably after quarter the length of the Brillouin zone. Therefore, since the K-points have a distance of $2\pi/3 \cdot a_{\mathrm{Lat}}^{-1}$ between one another, a coupling between them is suppressed. This motivates the exclusion of the $\vec{k}$-non-diagonal terms in the model in this thesis, in general. Comparison of the results of chapters 4 and 5 will further justify this decision.

Without the $\vec{k}$-non-diagonal terms, the Floquet Hamiltonian matrix (2.184) shapes to

$$H_{\mathrm{F}} = \begin{pmatrix} (H_0 - N\hbar\omega) & -\xi^+ & 0 & & & & \\ -\xi^- & \ddots & -\xi^+ & 0 & & & \\ 0 & -\xi^- & (H_0 - 1\hbar\omega) & -\xi^+ & 0 & & \\ & 0 & -\xi^- & H_0 & -\xi^+ & 0 & \\ & & 0 & -\xi^- & (H_0 + 1\hbar\omega) & -\xi^+ & 0 \\ & & & 0 & -\xi^- & \ddots & -\xi^+ \\ & & & & 0 & -\xi^- & (H_0 + N\hbar\omega) \end{pmatrix} \tag{3.21}$$

with matrix entries

$$\xi^{\pm}_{n_1,n_2,k,k} = \xi_{n_1,n_2,k,k} \cdot \frac{\omega}{2\pi} \cdot \int_0^{\frac{2\pi}{\omega}} V(t) \cdot e^{\pm \mathrm{i}\omega t} \, dt \tag{3.22}$$

in accordance to Eq. (2.156) (pg. 60). The dipole matrix elements $\xi^{\pm}_{n_1,n_2,s_1,s_2}$ couple respective orbitals and sublattices. In Eq. (3.21), the unit matrices $\mathbb{1}$ in front of the multiples of $\hbar\omega$ have been dropped for the sake of readability. The minus signs in front of the matrices $\xi^{\pm}$ correspond to the minus sign in front of H_1 in Eq. (3.16).

3.2 Analytical Solutions at the K-point

A major focus of this thesis lies on the behaviour of valence and conduction band of graphene at the K-points under irradiation with light. To understand the effects that occur, it is crucial to first discuss the properties of unperturbed graphene.

Assume an orbital basis

$$(|A,\mathrm{p_z}\rangle,\ |A,\mathrm{d_{xz}}\rangle,\ |A,\mathrm{d_{yz}}\rangle,\ |B,\mathrm{p_z}\rangle,\ |B,\mathrm{d_{xz}}\rangle,,\ |B,\mathrm{d_{yz}}\rangle)\,, \tag{3.23}$$

similar to that given in Eq. (2.45) on page 15. At the K-point, the spinless multi-orbital tight-binding Hamiltonian for graphene with this basis simplifies to

$$H_{\mathrm{tb}} = \begin{pmatrix} 0 & 0 & 0 & 0 & -\mathrm{i}\frac{3V_{\mathrm{pd}\pi}}{2} & \frac{3V_{\mathrm{pd}\pi}}{2} \\ & \epsilon_d & 0 & \mathrm{i}\frac{3V_{\mathrm{pd}\pi}}{2} & \frac{V_{\mathrm{dd}\delta}-V_{\mathrm{dd}\pi}}{2} & -\mathrm{i}\frac{V_{\mathrm{dd}\delta}-V_{\mathrm{dd}\pi}}{2} \\ 0 & 0 & \epsilon_d & -\frac{3V_{\mathrm{pd}\pi}}{2} & -\mathrm{i}\frac{V_{\mathrm{dd}\delta}-V_{\mathrm{dd}\pi}}{2} & -\frac{V_{\mathrm{dd}\delta}-V_{\mathrm{dd}\pi}}{2} \\ 0 & -\mathrm{i}\frac{3V_{\mathrm{pd}\pi}}{2} & -\frac{3V_{\mathrm{pd}\pi}}{2} & 0 & 0 & 0 \\ \mathrm{i}\frac{3V_{\mathrm{pd}\pi}}{2} & \frac{V_{\mathrm{dd}\delta}-V_{\mathrm{dd}\pi}}{2} & \mathrm{i}\frac{V_{\mathrm{dd}\delta}-V_{\mathrm{dd}\pi}}{2} & & \epsilon_d & 0 \\ \frac{3V_{\mathrm{pd}\pi}}{2} & \mathrm{i}\frac{V_{\mathrm{dd}\delta}-V_{\mathrm{dd}\pi}}{2} & -\frac{V_{\mathrm{dd}\delta}-V_{\mathrm{dd}\pi}}{2} & 0 & 0 & \epsilon_d \end{pmatrix} \tag{3.24}$$

with hopping terms $V_{ij\alpha}$ between two orbitals $i,j \in \{\mathrm{p,d}\}$ on neighbouring atoms. The index $\alpha \in \{\sigma,\pi,\delta\}$ denotes the molecular bond that couples the orbitals. The numerical values of the parameters are given in appendix A.

For the intrinsic SOI matrix, assume the basis

$$(|\mathrm{p_z},\uparrow\rangle,\ |\mathrm{p_z},\downarrow\rangle,\ |\mathrm{d_{xz}},\uparrow\rangle,\ |\mathrm{d_{xz}},\downarrow\rangle,\ |\mathrm{d_{yz}},\uparrow\rangle,\ |\mathrm{d_{yz}},\downarrow\rangle). \tag{3.25}$$

Note that, since SOI is only taken into account within one atom, this basis only considers one lattice site. The SOI matrix is then of the form

$$H_{\mathrm{iSOI}} = \lambda_{\mathrm{I}} \begin{pmatrix} 0 & 0 & 0 \\ 0 & 0 & -\mathrm{i}\sigma_z \\ 0 & \mathrm{i}\sigma_z & 0 \end{pmatrix}, \tag{3.26}$$

where every 0 represents a matrix

$$\begin{pmatrix} 0 & 0 \\ 0 & 0 \end{pmatrix}, \tag{3.27}$$

and the σ_z are Pauli matrices acting on the spins.

It is then possible to combine the matrices (3.24) and (3.26) via

$$H_{\mathrm{graphene}} = H_{\mathrm{tb}} \otimes \mathbb{1}_2 + \mathbb{1}_2 \otimes H_{\mathrm{iSOI}} + \lambda_{\mathrm{SL}} \cdot \sigma_z \otimes \mathbb{1}_6, \tag{3.28}$$

with a basis

$$(|A,\mathrm{p_z},\uparrow\rangle,\ |A,\mathrm{p_z},\downarrow\rangle,\ |A,\mathrm{d_{xz}},\uparrow\rangle,\ |A,\mathrm{d_{xz}},\downarrow\rangle,\ |A,\mathrm{d_{yz}},\uparrow\rangle,\ |A,\mathrm{d_{yz}},\downarrow\rangle,$$
$$|B,\mathrm{p_z},\uparrow\rangle,\ |B,\mathrm{p_z},\downarrow\rangle,\ |B,\mathrm{d_{xz}},\uparrow\rangle,\ |B,\mathrm{d_{xz}},\downarrow\rangle,\ |B,\mathrm{d_{yz}},\uparrow\rangle,\ |B,\mathrm{d_{yz}},\downarrow\rangle).$$

In Eq. (3.28), the Kronecker products with the two-dimensional identity matrices account for the spin in the tight-binding Hamiltonian and the second lattice site in the SOI matrix. λ_I is the strength of the intrinsic SOI in graphene and is also given in appendix A. The final summand is an artificial sublattice potential that elevates one sublattice energetically against the other one. $\lambda_\mathrm{SL} = 0$ throughout this thesis, but the term helps to distinguish the solutions of the eigenproblem and to draw connections to section 2.4.5.

Exact diagonalization of the Hamiltonian (3.28) leads to the the solutions listed in Tab. 3.1. In the table, the notation has been modified to regard for the symmetries of graphene at the K-point and to thus simplify the expressions. The wave functions $\Phi_{3\mathrm{d_{xz}}}$ and $\Phi_{3\mathrm{d_{yz}}}$ that describe $\mathrm{d_{xz}}$- and $\mathrm{d_{yz}}$-orbitals consist of cubic harmonics and therefore have cubic symmetry. Since the honeycomb lattice does not satisfy that symmetry, it is advantageous to switch to spherical harmonics $\boldsymbol{Y}_1^0$, $\boldsymbol{Y}_2^{-1}$ and $\boldsymbol{Y}_2^1$ via

$$\Phi_{2\mathrm{p_z}}(r,\theta,\phi) = \mathbf{R}_{10}(r)\cdot \boldsymbol{Y}_1^0(\theta,\phi) \tag{3.29}$$

$$\Phi_{3\mathrm{d_{xz}}}(r,\theta,\phi) = \mathbf{R}_{32}(r)\cdot \frac{1}{\sqrt{2}}\left(\boldsymbol{Y}_2^1(\theta,\phi) - \boldsymbol{Y}_2^{-1}(\theta,\phi)\right) \tag{3.30}$$

$$\Phi_{3\mathrm{d_{yz}}}(r,\theta,\phi) = \mathbf{R}_{32}(r)\cdot \frac{\mathrm{i}}{\sqrt{2}}\left(\boldsymbol{Y}_2^1(\theta,\phi) + \boldsymbol{Y}_2^{-1}(\theta,\phi)\right), \tag{3.31}$$

where $\mathbf{R}_{nl}$ is the radial part of the wave function and is identical for cubic and spherical symmetry. Since only 2p- and 3d-orbitals are considered, the expressions are abbreviated to what will be called *spherical orbitals*

$$\boldsymbol{Y}_{l,A/B,\updownarrow}^m(\vec{r}) := \mathbf{R}_{(l+1)l}(|\vec{r}-\vec{R}_{A/B}|)\cdot \boldsymbol{Y}_l^m(\vec{r}-\vec{R}_{A/B})\cdot|\updownarrow\rangle, \tag{3.32}$$

where the n-quantum number has been replaced with $l+1$. The angles θ and ϕ in $\boldsymbol{Y}_l^m$ are taken from the argument in spherical coordinates. $\vec{R}_{A/B}$ denotes the position of one of the two basis atoms A and B, and the state $|\updownarrow\rangle$ denotes the spin $\updownarrow\in\{\downarrow,\uparrow\}$. With the expressions (3.29-3.31), every solution in Tab. 3.1 consist of only two spherical orbitals, respectively. Moreover, the table shows a correlation between spin and sublattice as discussed in section 2.4.5. The results at the K'-point can be obtained by interchanging $m=+1$ and $m=-1$ as well as spin-up and spin-down in Tab. 3.1.

#	vector	energy	eV
1	$-\mathrm{i}V_{\mathrm{pd}\pi}\cdot\boxed{\boldsymbol{Y}^0_{1,B\downarrow}}+\left(\epsilon_d-\lambda'_{\mathrm{I}}+2\lambda_{\mathrm{SL}}-\sqrt{V'^2_{\mathrm{pd}\pi}+(\epsilon_d-\lambda'_{\mathrm{I}}+2\lambda_{\mathrm{SL}})^2}\right)\cdot\boldsymbol{Y}^1_{2,A\downarrow}$	$\frac{1}{2}\left(\epsilon_d-\lambda'_{\mathrm{I}}-\sqrt{V'^2_{\mathrm{pd}\pi}+(\epsilon_d-\lambda'_{\mathrm{I}}+2\lambda_{\mathrm{SL}})^2}\right)$	−0.18104
2	$+\mathrm{i}V_{\mathrm{pd}\pi}\cdot\boldsymbol{Y}^{-1}_{2,B\uparrow}+\left(\epsilon_d-\lambda'_{\mathrm{I}}-2\lambda_{\mathrm{SL}}+\sqrt{V'^2_{\mathrm{pd}\pi}+(\epsilon_d-\lambda'_{\mathrm{I}}-2\lambda_{\mathrm{SL}})^2}\right)\cdot\boxed{\boldsymbol{Y}^0_{1,A\uparrow}}$	$\frac{1}{2}\left(\epsilon_d-\lambda'_{\mathrm{I}}-\sqrt{V'^2_{\mathrm{pd}\pi}+(\epsilon_d-\lambda'_{\mathrm{I}}-2\lambda_{\mathrm{SL}})^2}\right)$	−0.18104
3	$-\mathrm{i}V_{\mathrm{pd}\pi}\cdot\boxed{\boldsymbol{Y}^0_{1,B\uparrow}}+\left(\epsilon_d+\lambda'_{\mathrm{I}}+2\lambda_{\mathrm{SL}}-\sqrt{V'^2_{\mathrm{pd}\pi}+(\epsilon_d+\lambda'_{\mathrm{I}}+2\lambda_{\mathrm{SL}})^2}\right)\cdot\boldsymbol{Y}^1_{2,A\uparrow}$	$\frac{1}{2}\left(\epsilon_d+\lambda'_{\mathrm{I}}-\sqrt{V'^2_{\mathrm{pd}\pi}+(\epsilon_d+\lambda'_{\mathrm{I}}+2\lambda_{\mathrm{SL}})^2}\right)$	−0.181
4	$+\mathrm{i}V_{\mathrm{pd}\pi}\cdot\boldsymbol{Y}^{-1}_{2,B\downarrow}+\left(\epsilon_d+\lambda'_{\mathrm{I}}-2\lambda_{\mathrm{SL}}+\sqrt{V'^2_{\mathrm{pd}\pi}+(\epsilon_d+\lambda'_{\mathrm{I}}-2\lambda_{\mathrm{SL}})^2}\right)\cdot\boxed{\boldsymbol{Y}^0_{1,A\downarrow}}$	$\frac{1}{2}\left(\epsilon_d+\lambda'_{\mathrm{I}}-\sqrt{V'^2_{\mathrm{pd}\pi}+(\epsilon_d+\lambda'_{\mathrm{I}}-2\lambda_{\mathrm{SL}})^2}\right)$	−0.181
5	$\left(\lambda'_{\mathrm{I}}+\lambda_{\mathrm{SL}}-\sqrt{\Delta V^2+(\lambda'_{\mathrm{I}}+\lambda_{\mathrm{SL}})^2}\right)\cdot\boldsymbol{Y}^{-1}_{2,A\downarrow}-\Delta V\cdot\boldsymbol{Y}^1_{2,B\downarrow}$	$\epsilon_d-\sqrt{\Delta V^2+(\lambda'_{\mathrm{I}}+\lambda_{\mathrm{SL}})^2}$	7.423
6	$\left(\lambda'_{\mathrm{I}}-\lambda_{\mathrm{SL}}+\sqrt{\Delta V^2+(\lambda'_{\mathrm{I}}-\lambda_{\mathrm{SL}})^2}\right)\cdot\boldsymbol{Y}^{-1}_{2,A\uparrow}+\Delta V\cdot\boldsymbol{Y}^1_{2,B\uparrow}$	$\epsilon_d-\sqrt{\Delta V^2+(\lambda'_{\mathrm{I}}-\lambda_{\mathrm{SL}})^2}$	7.423
7	$+\mathrm{i}V_{\mathrm{pd}\pi}\cdot\boxed{\boldsymbol{Y}^{-1}_{2,B\uparrow}}+\left(\epsilon_d-\lambda'_{\mathrm{I}}-2\lambda_{\mathrm{SL}}-\sqrt{V'^2_{\mathrm{pd}\pi}+(\epsilon_d-\lambda'_{\mathrm{I}}-2\lambda_{\mathrm{SL}})^2}\right)\cdot\boldsymbol{Y}^0_{1,A\uparrow}$	$\frac{1}{2}\left(\epsilon_d-\lambda'_{\mathrm{I}}+\sqrt{V'^2_{\mathrm{pd}\pi}+(\epsilon_d-\lambda'_{\mathrm{I}}-2\lambda_{\mathrm{SL}})^2}\right)$	12.1796
8	$-\mathrm{i}V_{\mathrm{pd}\pi}\cdot\boldsymbol{Y}^0_{1,B\downarrow}+\left(\epsilon_d-\lambda'_{\mathrm{I}}+2\lambda_{\mathrm{SL}}-\sqrt{V'^2_{\mathrm{pd}\pi}+(\epsilon_d-\lambda'_{\mathrm{I}}+2\lambda_{\mathrm{SL}})^2}\right)\cdot\boxed{\boldsymbol{Y}^1_{2,A\downarrow}}$	$\frac{1}{2}\left(\epsilon_d-\lambda'_{\mathrm{I}}+\sqrt{V'^2_{\mathrm{pd}\pi}+(\epsilon_d-\lambda'_{\mathrm{I}}+2\lambda_{\mathrm{SL}})^2}\right)$	12.18
9	$+\mathrm{i}V_{\mathrm{pd}\pi}\cdot\boxed{\boldsymbol{Y}^{-1}_{2,B\downarrow}}+\left(\epsilon_d+\lambda'_{\mathrm{I}}-2\lambda_{\mathrm{SL}}+\sqrt{V'^2_{\mathrm{pd}\pi}+(\epsilon_d+\lambda'_{\mathrm{I}}-2\lambda_{\mathrm{SL}})^2}\right)\cdot\boldsymbol{Y}^0_{1,A\downarrow}$	$\frac{1}{2}\left(\epsilon_d+\lambda'_{\mathrm{I}}+\sqrt{V'^2_{\mathrm{pd}\pi}+(\epsilon_d+\lambda'_{\mathrm{I}}-2\lambda_{\mathrm{SL}})^2}\right)$	12.182
10	$-\mathrm{i}V_{\mathrm{pd}\pi}\cdot\boldsymbol{Y}^0_{1,B\uparrow}+\left(\epsilon_d+\lambda'_{\mathrm{I}}+2\lambda_{\mathrm{SL}}+\sqrt{V'^2_{\mathrm{pd}\pi}+(\epsilon_d+\lambda'_{\mathrm{I}}+2\lambda_{\mathrm{SL}})^2}\right)\cdot\boxed{\boldsymbol{Y}^1_{2,A\uparrow}}$	$\frac{1}{2}\left(\epsilon_d+\lambda'_{\mathrm{I}}+\sqrt{V'^2_{\mathrm{pd}\pi}+(\epsilon_d+\lambda'_{\mathrm{I}}+2\lambda_{\mathrm{SL}})^2}\right)$	12.182
11	$\left(\lambda'_{\mathrm{I}}-\lambda_{\mathrm{SL}}-\sqrt{\Delta V^2+(\lambda'_{\mathrm{I}}-\lambda_{\mathrm{SL}})^2}\right)\cdot\boldsymbol{Y}^{-1}_{2,A\uparrow}+\Delta V\cdot\boldsymbol{Y}^1_{2,B\uparrow}$	$\epsilon_d+\sqrt{\Delta V^2+(\lambda_{\mathrm{I}}-\lambda_{\mathrm{SL}})'^2}$	16.577
12	$\left(\lambda'_{\mathrm{I}}+\lambda_{\mathrm{SL}}+\sqrt{\Delta V^2+(\lambda'_{\mathrm{I}}+\lambda_{\mathrm{SL}})^2}\right)\cdot\boldsymbol{Y}^{-1}_{2,A\downarrow}-\Delta V\cdot\boldsymbol{Y}^1_{2,B\downarrow}$	$\epsilon_d+\sqrt{\Delta V^2+(\lambda'_{\mathrm{I}}+\lambda_{\mathrm{SL}})^2}$	16.577

Table 3.1: Eigenvectors and energies of the tight-binding graphene Hamiltonian at the K-point under consideration of SOI. The numerical values of the parameters can be concluded from appendix A, where $\lambda'_{\mathrm{I}}=\lambda_{\mathrm{I}}/2$, $\Delta V=3/2\ (V_{\mathrm{dd}\delta}-V_{\mathrm{dd}\pi})$ and $V'_{\mathrm{pd}\pi}=3\sqrt{2}\ V_{\mathrm{pd}\pi}$ have been substituted for better readability, and $\lambda_{\mathrm{SL}}=0$, since it does not occur in unperturbed graphene. The functions $\boldsymbol{Y}^m_{l,A/B\updownarrow}$ are defined in Eqs. (3.29-3.31) and denote spherical orbitals with angular quantum numbers l and m on sublattice A/B, equipped with spin $\updownarrow$. The numerical energy values are rounded to four decimal places, unless more are necessary for distinction. The vectors are not normalised. If a function $\boldsymbol{Y}^m_{l,A/B\updownarrow}$ has a frame around it, then the absolute value of its prefactor after normalisation evaluates to more than 0.99, i.e. this function makes up approximately 99 % of the eigenstate. If neither of the functions that constitute an eigenstate is framed, then both prefactors become approximately $1/\sqrt{2}$ after normalisation.

Since each of the twelve states in Tab. 3.1 only consists of only two respective spherical orbitals $\boldsymbol{Y}^0_{1,A/B,\updownarrow}$ and $\boldsymbol{Y}^m_{2,B/A,\updownarrow}$, it is possible to associate every state with a quantum number $m \in \{-1, +1\}$. This m plays a direct role in the coupling to circularly polarised light, as will be shown in the following.

3.3 Electric Fields at the K-point

In the following, the effect of a circularly polarised time-dependent electric field on the basis states in Tab. 3.1 will be studied. The action of the electric field on these is dominated by two contributions: an onsite coupling and an effective sublattice potential. Both will be discussed in the following.

3.3.1 Onsite Coupling

Consider a scalar potential

$$\Phi(\vec{r}, t) = -E_0 \cdot (x \cos(\omega t) + y \sin(\omega t)) \tag{3.33}$$

for a circularly polarised electric field like in Eq. (3.8). Furthermore, consider two spherical orbitals $\boldsymbol{Y}^m_{l,A/B,\updownarrow}(r, \theta, \phi)$ and $\boldsymbol{Y}^{m'}_{l',A/B,\updownarrow}(r, \theta, \phi)$ as defined in Eq. (3.32). Since the electric field does not couple different spins, assume that both spins are identical. Moreover, assume that both orbitals are localised on the same lattice site A/B. As will be seen in chapter 4, the coupling between orbitals on the same site suffices to describe the phenomena at the K-point of graphene. The much smaller matrix elements between different lattice sites will therefore not be discussed in this chapter.
Based on the assumptions above, the matrix element $\langle l, m|\Phi(t)|l', m'\rangle$ is independent of the lattice site and the spin. It is only non-zero if $l' = l \pm 1$ and $m' = m \pm 1$. Hence, assume $l = 1$, $l' = 2$, $m = 0$ and $m' = \pm 1$, to compute

$$\begin{aligned} &\langle l = 1, m = 0|\ \Phi(t)\ |l' = 2, m' = \pm 1\rangle \\ = &\iiint \mathbf{Y}_1^{0*}(\theta, \phi)\mathbf{R}_{10}(r)\ \Phi(r, \theta, \phi, t)\ \mathbf{Y}_2^{\pm 1}(\theta, \phi)\mathbf{R}_{32}(r)\ dr\ d\theta\ d\phi \\ = &\mp E_0 a^*_{\text{Bohr}} \cdot e^{\mp \mathrm{i}\omega t} \cdot c_0 \qquad \text{with } c_0 = \sqrt{2} \cdot \frac{82944}{78125} \approx 1.5. \end{aligned} \tag{3.34}$$

a^*_{Bohr} is the effective Bohr radius. c_0 is derived from the orbital wave functions and, importantly, does not depend on the sign of m'. Under use of Eq. (3.34), it is possible to construct the matrix elements coupling the twelve eigenstates ψ_i of graphene at the K-point that are given in Tab. 3.1. Define the matrix elements as

$$\Xi_{i,j}(t) := \langle \psi_i|\Phi_{\text{onsite}}(t)|\psi_j\rangle \cdot e^{-}. \tag{3.35}$$

$i\downarrow$ $j\rightarrow$	1	2	3	4	5	6	7	8	9	10	11	12
1				$+$	$-$				$+$			$-$
2			$-$			$+$				$-$	$+$	
3		$+$				$-$	$+$				$-$	
4	$-$				$+$			$-$				$+$
5	$+$			$-$				$+$	$-$			
6		$-$	$+$				$-$			$+$		
7			$-$			$+$				$-$	$+$	
8				$+$	$-$				$+$			$-$
9	$-$				$+$			$-$				$+$
10		$+$				$-$	$+$				$-$	
11		$-$	$+$				$-$			$+$		
12	$+$			$-$				$+$	$-$			

Table 3.2: Relative m-quantum numbers $m_{i,j} = \pm 1$ based on the definition in Eq. (3.36); An entry "$-$" denotes $m_{i,j} = -1$, and "$+$" denotes $m_{i,j} = +1$. No entry means that the corresponding matrix element $\xi'_{i,j}$ in Tab. 3.3 is zero. Hence, no $m_{i,j}$ can be defined.

The term e^- denotes the charge of an electron. For the following computations, it will be assumed that the electric field does not couple orbitals on different atoms and that it has the same effect on every respective atom. With the analytical expressions in Tab. 3.1 and Eq. (3.34), one can conclude that there always exists an $m_{i,j} \in \{-1, +1\}$ and some constant $\xi'_{i,j}$ and, such that

$$\Xi_{i,j}(t) = \xi'_{i,j} \cdot e^{\mathrm{i} m_{i,j} \omega t}. \tag{3.36}$$

The $m_{i,j}$ and $\xi'_{i,j}$ are given in Tabs. 3.2 and 3.3. Tab. 3.3 consists of constants c_i that are defined as follows:

$$c_1 = \frac{V'_{\mathrm{pd}\pi}\lambda_{\mathrm{I}}}{V'^2_{\mathrm{pd}\pi} + \epsilon_{\mathrm{d}}^2} \cdot c_0 \cdot E_0 a^*_{\mathrm{Bohr}} \cdot e^- \approx \tilde{E}_0 \cdot 3\,\mathrm{\mu eV} \tag{3.37}$$

$$c_2 = \frac{1}{2}\sqrt{1 + \frac{\epsilon_{\mathrm{d}}}{\sqrt{V'^2_{\mathrm{pd}\pi} + \epsilon_{\mathrm{d}}^2}}} \cdot c_0 \cdot E_0 a^*_{\mathrm{Bohr}} \cdot e^- \approx \tilde{E}_0 \cdot 75\,\mathrm{meV} \tag{3.38}$$

$$c_3 = \frac{1}{2}\sqrt{1 - \frac{\epsilon_{\mathrm{d}}}{\sqrt{V'^2_{\mathrm{pd}\pi} + \epsilon_{\mathrm{d}}^2}}} \cdot c_0 \cdot E_0 a^*_{\mathrm{Bohr}} \cdot e^- \approx \tilde{E}_0 \cdot 9.1\,\mathrm{meV} \tag{3.39}$$

$$c_4 = 1 \cdot c_0 \cdot E_0 a^*_{\mathrm{Bohr}} \cdot e^- \approx \tilde{E}_0 \cdot 107\,\mathrm{meV}, \tag{3.40}$$

$i\downarrow\ \ j\rightarrow$	1	2	3	4	5	6	7	8	9	10	11	12
1				c_1	$\mathrm{i}c_2$				$-c_4$			$-\mathrm{i}c_2$
2			$-c_1$			$-c_2$				$-c_4$	c_2	
3		$-c_1$				$-\mathrm{i}c_2$	$-c_4$				$-\mathrm{i}c_2$	
4	c_1				c_2			$-c_4$				c_2
5	$-\mathrm{i}c_2$			c_2				$-\mathrm{i}c_3$	$-c_3$			
6		$-c_2$	$\mathrm{i}c_2$				c_3			$\mathrm{i}c_3$		
7			$-c_4$			c_3				c_1	$-c_3$	
8				$-c_4$	$\mathrm{i}c_3$				$-c_1$			$-\mathrm{i}c_3$
9	$-c_4$				$-c_3$			$-c_1$				$-c_3$
10		$-c_4$				$-\mathrm{i}c_3$	c_1				$-\mathrm{i}c_3$	
11		c_2	$\mathrm{i}c_2$				$-c_3$			$\mathrm{i}c_3$		
12	$\mathrm{i}c_2$			c_2				$\mathrm{i}c_3$	$-c_3$			

Table 3.3: Matrix elements $\xi'_{i,j}$ based on the definitions in Eqs. (3.35) and (3.36); The onsite component of a circularly polarised field only couples certain states from Tab. 3.1 to one another. The absolute value of this coupling can only assume the values c_i with $i \in \{1,2,3,4\}$. The latter values are defined in Eqs. (3.37-3.40). For the indices $i \in \{2,3,4\}$, $\lambda_\mathrm{I} = 0$ has been assumed. c_1 is the result of a first-order Taylor expansion in λ_I. An empty cell at entry (i,j) indicates $\xi'_{i,j} = 0$.

where $\tilde{E}_0$ is the number value of E_0 in units of V/nm. a^*_{Bohr} is again the effective Bohr radius, and c_0 is defined in Eq. (3.34). The parameters $V'_{\text{pd}\pi} = 3\sqrt{2}\ V_{\text{pd}\pi}$ and $\lambda'_{\text{I}} = \lambda_{\text{I}}/2$ from section 3.2 have been used to simplify the expressions. All numerical values can be concluded from appendix A. For the computation of Eqs. (3.38-3.40), it has been assumed that $\lambda'_{\text{I}} = 0$, since the effect of SOI on them is negligible. This assumption could not be made in Eq. (3.37). Instead, it is the result of a first-order Taylor expansion in λ'_{I}.

Throughout this thesis, the time-dependence of the electric field will be handled via Floquet formalism. The form of the Floquet Hamiltonian H_{F} was given in Eq. (3.21). When only onsite interaction is taken into account, H_{F} can be constructed from the results of Tabs. 3.2 and 3.3 together with Eq. (3.36). In Eq. (3.21), the dipole matrix $\xi^{\pm}$ denotes the coupling between two subsystems of different photon count. Its entries $\xi^{\pm}_{i,j}$ are related to the $\xi'_{i,j}$ of Tab. 3.3 via

$$\xi^{\pm}_{i,j} = -\delta_{m_{i,j},\pm 1} \cdot \xi'_{i,j}. \tag{3.41}$$

The Kronecker deltas are the result of the Fourier decomposition of the Hamiltonian: Depending on whether $m_{i,j} = +1$ or -1, the only non-zero Fourier components of Eq. (3.36) are the components $+1$ and -1. The relative m-quantum number $m_{i,j}$ of Tab. 3.2 therefore relates the polarisation direction of the light to the upper and lower diagonal matrices $\xi^{\pm}$ in Eq. (3.21). The additional minus sign in Eq. (3.41) stems from the definitions in Eqs. (3.16) and (3.21). Since most of the matrix elements $\xi'_{i,j}$ are zero, it is possible to restrict to an isolated selection of the basis vectors of Tab. 3.1. Hence, consider the reduced basis

$$(|\psi_i, -1\rangle,\ |\psi_j, -1\rangle,\ |\psi_i, 0\rangle,\ |\psi_j, 0\rangle) \tag{3.42}$$

composed of the (-1)-photon and 0-photon (replica) states ψ_i and ψ_j. The notion “photon” here refers to the identification of dressed states in Floquet formalism with photonic excitations, as explained in section 2.6.2. With the basis (3.42), it is possible to restrict the overall Floquet Hamiltonian to only the section that couples its elements, to study the matrix

$$\begin{pmatrix} \mathcal{E}_i - \hbar\omega & 0 & 0 & \delta_{m_{i,j},+1}\xi'_{i,j} \\ 0 & \mathcal{E}_j - \hbar\omega & \delta_{m_{j,i},+1}\xi'_{j,i} & 0 \\ 0 & \delta_{m_{i,j},-1}\xi'_{i,j} & \mathcal{E}_i & 0 \\ \delta_{m_{j,i},-1}\xi'_{j,i} & 0 & 0 & \mathcal{E}_j \end{pmatrix}, \tag{3.43}$$

where $\mathcal{E}_{i/j}$ denotes the energy of the unperturbed 0-photon state $\psi_{i/j}$ as given in Tab. 3.1. Based on Eq. (3.43), the onsite component of the electric field couples a (-1)-photon replica of a state ψ_i and a 0-photon state ψ_j if and only if $m_{i,j} = 1$. Since $m_{i,j} = -m_{j,i}$, this directly implies that a (-1)-photon replica of the state ψ_j and the 0-photon state ψ_i are not coupled.

In the following, assume $m_{i,j} = +1$. The eigenvalues that belong to the coupled part of the system are then

$$\epsilon_\pm^{i,j}(\omega) = \frac{1}{2}\left(\mathcal{E}_i + \mathcal{E}_j - \hbar\omega \pm \sqrt{\xi'_{i,j}\xi'_{j,i} + (\mathcal{E}_i - \mathcal{E}_j - \hbar\omega)^2}\right), \tag{3.44}$$

with corresponding eigenstates

$$\begin{aligned}\Psi_\pm^{i,j}(\omega) &= \frac{1}{\sqrt{(\epsilon_\pm^{i,j})^2(\omega) + \xi'_{i,j}\xi'_{j,i}}}\begin{pmatrix}\epsilon_\pm^{i,j}(\omega) - \mathcal{E}_j \\ \xi'_{j,i}\end{pmatrix} \\ &= \frac{1}{\sqrt{(\epsilon_\pm^{i,j})^2(\omega) + \xi'_{i,j}\xi'_{j,i}}}\left((\epsilon_\pm^{i,j}(\omega) - \mathcal{E}_j)|\psi_i, -1\rangle + \xi'_{j,i}|\psi_j, 0\rangle\right). \end{aligned} \tag{3.45}$$

At resonance, the eigenvalues and eigenstates become

$$\lim_{\hbar\omega \to (\mathcal{E}_i - \mathcal{E}_j)} \epsilon_\pm^{i,j}(\omega) = \mathcal{E}_j \pm \sqrt{\xi'_{i,j}\xi'_{j,i}}, \qquad \lim_{\hbar\omega \to (\mathcal{E}_i - \mathcal{E}_j)} \Psi_\pm^{i,j}(\omega) = \frac{1}{\sqrt{2}}\begin{pmatrix}\pm 1 \\ 1\end{pmatrix}. \tag{3.46}$$

At resonance frequencies $f_{i,j} = \omega_{i,j}/(2\pi) := (\mathcal{E}_i - \mathcal{E}_j)/(2\pi\hbar)$, the Floquet energies thus become the energy of the unperturbed state ψ_j plus or minus the absolute value of the matrix element $\xi'_{i,j} = (\xi'_{j,i})^*$, i.e. they exhibit an avoided crossing of width $2|\xi'_{i,j}|$. This is illustrated in Fig. 3.3.

The unperturbed valence and conduction band mostly consist of atomic p-orbitals and will therefore often be referred to as *p-bands*. They correspond to the first four states in Tab. 3.1. According to Tab. 3.3 and Eq. (3.37-3.40), the coupling among those four is negligible compared to the coupling between them and the *d-bands* that correspond to the numbers 5 through 12 in Tab. 3.1. From Tab. 3.2 and the Kronecker deltas in Eq. (3.43), one can see that the only couplings between 0-photon p-bands and (-1)-photon d-bands are the following:

- 1 to 9
- 3 to 7
- 2 to 6 and 11
- 4 to 5 and 12

Their energies satisfy the following relation:

$$\underbrace{\mathcal{E}_1 = \mathcal{E}_2 \lessapprox \mathcal{E}_3 = \mathcal{E}_4}_{\approx -0.18\,\mathrm{eV}} < \underbrace{\mathcal{E}_5 = \mathcal{E}_6}_{\approx 7.42\,\mathrm{eV}} < \underbrace{\mathcal{E}_7 \lessapprox \mathcal{E}_9}_{\approx 12.18\,\mathrm{eV}} < \underbrace{\mathcal{E}_{11} = \mathcal{E}_{12}}_{\approx 16.58\,\mathrm{eV}}, \tag{3.47}$$

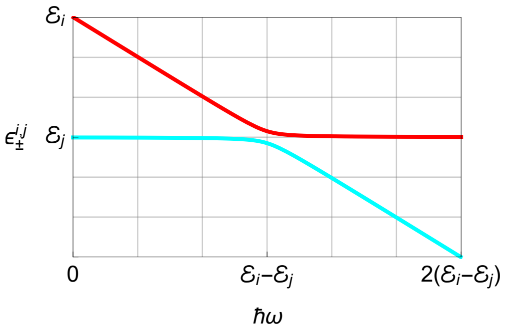

Figure 3.3: Floquet quasi-energies near resonance; The Floquet quasi-energies $\epsilon_-^{i,j}(\omega)$ (cyan) and $\epsilon_+^{i,j}(\omega)$ (red) are defined in Eq. (3.44). Beyond the resonance at $\hbar\omega = \mathcal{E}_i - \mathcal{E}_j$, they behave like the uncoupled photon replica energies $\mathcal{E}_i - \hbar\omega$ and $\mathcal{E}_j$. At resonance, they exhibit an avoided crossing of width $2|\xi'_{i,j}|$. Here, $\xi'_{i,j} = (\mathcal{E}_i - \mathcal{E}_j)/20$ has been assumed.

as can be seen in greater detail in Tab. 3.1. As a consequence of the relation $\mathcal{E}_5 = \mathcal{E}_6 < \mathcal{E}_7 \lessapprox \mathcal{E}_9$, the respective (angular) resonance frequencies $\omega_{i,j}$ also satisfy

$$\underbrace{\omega_{2,6} \lessapprox \omega_{4,5}}_{\approx 2\pi\cdot 1.84\,\mathrm{PHz}} < \underbrace{\omega_{1,9} \lessapprox \omega_{3,7}}_{\approx 2\pi\cdot 2.99\,\mathrm{PHz}}, \tag{3.48}$$

and the couplings 2-6 and 4-5 occur at lower frequencies than the couplings 1-9 and 3-7. This induces an energetic shift, pushing the energies $\epsilon_-^{2,6}(\omega)$ and $\epsilon_-^{4,5}(\omega)$ below the energies $\epsilon_-^{1,9}(\omega)$ and $\epsilon_-^{3,7}(\omega)$.
As a result, the onsite coupling leads to a crossing of the Floquet energies $\epsilon_-^{1,9}(\omega)$ and $\epsilon_-^{4,5}(\omega)$. For frequencies $\omega < \omega_{4,5}$, these Floquet energies correspond to the original spin-down states 1 and 4. The consequence of the relation (3.48) is therefore a band inversion for spin-down states. This will be verified and elaborated on in section 4.2.

Since all states in Tab. 3.1 are eigenstates to the unperturbed Hamiltonian H_{graphene} as defined in Eq. (3.28), they are orthogonal under its induced sesquilinear form, i.e.

$$\langle \psi_i | H_{\mathrm{graphene}} | \psi_j \rangle = \delta_{ij} \mathcal{E}_j. \tag{3.49}$$

Consequently, via the definition (3.45), one obtains for pairwise different $i, j, a, b \in \{1, ..., 12\}$ that

$$\langle \Psi_\pm^{i,j} | H_{\mathrm{graphene}} | \Psi_\pm^{a,b} \rangle = 0. \tag{3.50}$$

Since SOI is part of H_{graphene}, this does in particular mean that SOI does not avoid the crossing of the Floquet energies $\epsilon_-^{1,9}(\omega)$ and $\epsilon_-^{4,5}(\omega)$. However, another component of the electric field does lead to an avoided crossing. So far, only the onsite contribution of $\Phi(\vec{r}, t)$ has been considered. Aside from this contribution, an electric field also induces an effective sublattice potential, as will be discussed in the following.

3.3.2 Sublattice Potential

Because of their relative positions within the unit cell, the two basis atoms on sublattice A and B perceive a different electric potential. This potential oscillates in time, similarly to the original electric field. The result is an effective sublattice potential of $+M\sin(\omega t)$ on sublattice A and $-M\sin(\omega t)$ on sublattice B, with

$$M = \frac{a_{\mathrm{Lat}}}{2\sqrt{3}} E_0 \cdot e^- \approx \tilde{E}_0 \cdot 71\,\mathrm{meV}, \tag{3.51}$$

where $\tilde{E}_0$ is again the number value of the field strength E_0 in V/nm. $a_{\mathrm{Lat}}/(2\sqrt{3})$ is half the distance between two atoms. The lower index "Lat" serves to distinguish the lattice constant from the effective Bohr radius a^*_{Bohr} used in other computations in this chapter. Analogously to Eq. (3.35) and (3.36), the matrix elements of the sublattice potential coupling the basis vectors of Tab. 3.1 can be written as

$$\mathcal{M}_{i,j}(t) := \langle \psi_i | \sigma_{z,\mathrm{sublat.}} M \sin(t) | \psi_j \rangle \cdot e^- = \mu_{i,j} \cdot \sin(t), \tag{3.52}$$

where $\sigma_{z,\mathrm{sublat.}} M \sin(t)$ is the overall sublattice potential with a Pauli matrix σ_z acting on the sublattices. The time-independent matrix elements are given in Tab. 3.4 and depend on functions d_i, $i \in \{1, 2, 3, 4\}$ of the system parameters. They are given in the following:

$$d_1 = \frac{\epsilon_d}{\sqrt{\epsilon_d^2 + V'^2_{\mathrm{pd}\pi}}} \cdot M \approx \tilde{E}_0 \cdot 69\,\mathrm{meV} \tag{3.53}$$

$$d_2 = -\frac{V'_{\mathrm{pd}\pi}}{\sqrt{\epsilon_d^2 + V'^2_{\mathrm{pd}\pi}}} \cdot M \approx -\tilde{E}_0 \cdot 17\,\mathrm{meV} \tag{3.54}$$

$$d_3 = \frac{\lambda'_{\mathrm{I}}}{\Delta V} \cdot M \approx \tilde{E}_0 \cdot 23\,\mu\mathrm{eV} \tag{3.55}$$

$$d_4 = 1 \cdot M \approx \tilde{E}_0 \cdot 71\,\mathrm{meV}. \tag{3.56}$$

The term d_3 is a result of a first-order Taylor expansion in λ'_{I}. For all other terms, the SOI contributions are negligible. Hence, $\lambda_{\mathrm{I}} = 0$ has been assumed. The numerical values of the analytical parameters $V'_{\mathrm{pd}\pi} = 3\sqrt{2}\, V_{\mathrm{pd}\pi}$,

$\Delta V = 3/2(V_{\mathrm{dd}\delta} - V_{\mathrm{dd}\pi})$ and $\lambda'_{\mathrm{I}} = \lambda_{\mathrm{I}}/2$ can be computed from appendix A. Since the sine in Eq. (3.52) consists of two opposing phases $e^{+\mathrm{i}\omega t}$ and $e^{-\mathrm{i}\omega t}$, there is no second table similar to Tab. 3.2 for the effective sublattice potential. Consequently, the polarisation leads to no further limitations as to which basis vectors are coupled to one another. Thus, an expression similar to Eq. (3.43) would not contain any Kronecker deltas.

The most consequential coupling term in Tab. 3.4 is the one between the states ψ_4 and ψ_9. As discussed in the previous subsection, neither the onsite potential nor the graphene Hamiltonian itself would prevent the Floquet quasi-energies $\epsilon_{-}^{1,9}(\omega)$ and $\epsilon_{-}^{4,5}(\omega)$ from crossing. The sublattice potential, however, does couple these states due to their contributions of the states ψ_4 and ψ_9. This will also be verified and elaborated on in section 4.2.

With these analytical results at hand, the next chapter will discuss the quantitative behaviour of the Floquet quasi-energies.

$i\downarrow\ j\rightarrow$	1	2	3	4	5	6	7	8	9	10	11	12
1	$-d_1$							d_2				
2		d_1					d_2					
3			$-d_1$							d_2		
4				d_1					d_2			
5					$-d_3$							d_4
6						d_3					$-d_4$	
7		d_2					$-d_1$					
8	d_2							d_1				
9				d_2					$-d_1$			
10			d_2							d_1		
11						$-d_4$					$-d_3$	
12					d_4							d_3

Table 3.4: Matrix elements $\mu_{i,j}$ based on the definitions in Eqs. (3.35) and (3.36); The spatial dependence of a scalar potential leads to an effective sublattice potential that couples the basis states Tab. 3.1 to one another. The absolute value of this coupling can only assume the values d_i with $i \in \{1,2,3,4\}$. The latter values are computed from the definition (3.53-3.56). For the indices $i \in \{1,2,4\}$, $\lambda_{\mathrm{I}} = 0$ has been assumed. The term d_3 is the result of a first-order Taylor expansion in λ_{I}. An empty cell at entry (i,j) indicates $\mu'_{i,j} = 0$.

Chapter 4

Floquet Band Structure at the K-point

Floquet engineering is a powerful tool for the modification of band structures via time-driven perturbations. In graphene, this has been demonstrated by multiple authors. Among these authors are Mathey and Broers [41, 42] who used the Floquet formalism to open a band gap at the Dirac points as a result of irradiation with light. Oka at al. [47] have derived how circularly polarised light turns topologically trivial graphene into a Chern insulator. This effect has then been verified experimentally by McIver at al. [48].

This chapter and chapter 5 will consider the work of the authors mentioned above and extend it to a spinful model that involves p- and d-orbitals. This extended model will then be studied for circularly and linearly polarised light. The coupling between spin, sublattice and the angular momentum of the d-orbitals will be demonstrated to give rise to several new phenomena. Irradiation with circularly polarised light will lead to a change in topology and to a lift of spin degeneracy. Moreover, a frequency-dependent band gap enhancement will be observed for both linearly and circularly polarised light. Like in section 3.1, the light will be assumed to generate electric fields with corresponding scalar potentials

$$\Phi_{\text{circ}}(\vec{r},t) = -E_0 \cdot (x\cos(\omega t) + y\sin(\omega t)), \qquad \Phi_{\text{lin}}(\vec{r},t) = -\sqrt{2}E_0 \cdot y\sin(\omega t), \tag{4.1}$$

where the indices denote circular and linear polarisation.

This chapter focusses on the behaviour of the Floquet quasi-energies of graphene at the K-point as a result of irradiation with light. It is structured into three parts:

Section 4.1 will discuss the general aspects of the quasi-energy bands, focussing on the band gap at the K-point and the topology of the Floquet band structure. Section 4.2 will then explain the origin of those phenomena and put them into relation with the previous chapter. After the first two parts focus on frequencies in the PHz regime, section 4.3 will focus on lower frequencies.

4.1 General Observations

To gain an intuition for the figures in this chapter, it is instructive to first consider a system where the time-periodic perturbation does not couple to the band structure. This can e.g. be achieved by setting the field strength E_0 of the electric potentials in Eq. (4.1) to zero. For Floquet order $N = 1$, consider the Floquet Hamiltonian

$$H_F = \begin{pmatrix} H_0 - \hbar\omega & 0 & 0 \\ 0 & H_0 & 0 \\ 0 & 0 & H_0 + \hbar\omega \end{pmatrix} \tag{4.2}$$

with the unperturbed graphene LCAO Hamiltonian H_0. For the sake of readability, the dependence of H_F and H_0 has not been written explicitly.
Since $E_0 = 0$, it follows that the only non-zero entries of H_F consist of H_0 and multiples of $\hbar\omega$. The eigenvalues of H_F are $\mathcal{E}_i + n\hbar\omega$ with $n \in \{-1, 0, +1\}$, where the $\mathcal{E}_i$ are the eigenvalues of H_0. The eigenvalues $\mathcal{E}_i(\vec{k} = \vec{K})$ of graphene at the K-point are given in Tab. 3.1 (pg. 83). The Floquet quasi-energies $\mathcal{E}_i(\vec{k} = \vec{K}) + n\hbar\omega$ as functions of the frequency $f = \frac{\omega}{2\pi}$ are depicted in Fig. 4.1.

For the eigenstates of Eq. (4.2), the integer n is identical to the photon expectation value $\langle\Gamma\rangle$ defined in Eq. (2.165) (pg. 62), i.e. $n = \langle\Gamma\rangle$. Accordingly, Floquet states will henceforth be called n-photon states.[1] Since H_F in Eq. (4.2) only consists of uncoupled replicas of the time-independent system, n assumes integer values. If $E_0 \neq 0$, these replicas would be coupled, leading to non-integer values of n. In accordance with the nomenclature of section 2.6.2, the band structure will be labelled electronic or photonic, based on whether n is close to zero or not.

---

[1] As explained in section 2.6.2, the Floquet Hamiltonian H_F does not describe a quantised photon field. The identification of multiples of $\hbar\omega$ with photon energies relies on a large number of photons being present (cf. [100]).

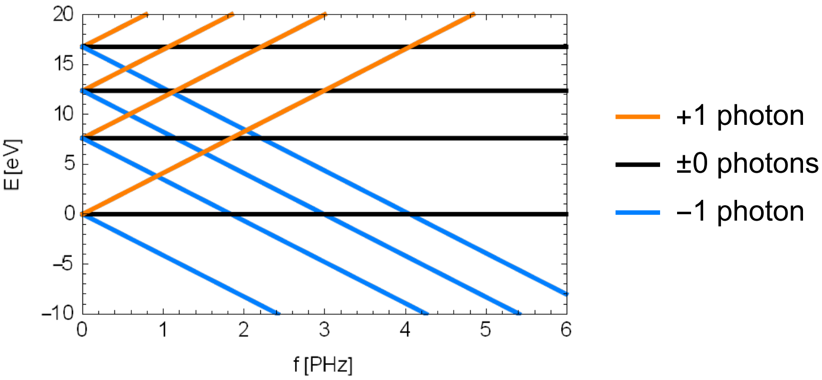

Figure 4.1: Floquet quasi-energies E at the K-point as functions of the frequency f, without an external electric field; Orange, black and azure lines depict energies with $n \in \{-1, 0, +1\}$ photons, respectively. With increasing frequency, they change according to $nhf = n\hbar\omega$. Intersections occur at resonance frequencies.

Fig. 4.1 only shows states that are associated with 0 or ±1 photons. States with $+1$ photon are depicted in orange, those with -1 in azure and those with 0 in black. Their quasi-energies behave linearly with $n\hbar\omega$. The diagonal azure lines and the horizontal black one at 0 eV cross at the resonance frequencies connecting p- and d-bands. The latter can be computed from Tab. 3.1. Since the effect of a light field on the band structure is expected to be strongest close to those resonances, a significant part of this chapter will focus on them.

4.1.1 Frequency-dependent Floquet Energies

When a monochromatic electromagnetic field is assumed to couple to the band structure, i.e. $E_0 \neq 0$ in Eq. (4.1), then the Floquet Hamiltonian assumes the form of Eq. (3.21), i.e.

$$H_{\mathrm{F}} = \begin{pmatrix} (H_0 - N\hbar\omega) & -\xi & 0 & & & & \\ -\xi & \ddots & -\xi & 0 & & & \\ 0 & -\xi & (H_0 - 1\hbar\omega) & -\xi & 0 & & \\ & 0 & -\xi & H_0 & -\xi & 0 & \\ & & 0 & -\xi & (H_0 + 1\hbar\omega) & -\xi & 0 \\ & & & 0 & -\xi & \ddots & -\xi \\ & & & & 0 & -\xi & (H_0 + N\hbar\omega) \end{pmatrix} \tag{4.3}$$

with the unperturbed graphene Hamiltonian H_0, the dipole matrix ξ, the angular frequency $\omega = 2\pi f$ and the Floquet order $N \in \mathbb{N}$. In Eq. (4.2), N was set to 1, for illustrative purposes.

In the following, a constant field strength of $E_0 = 0.8\,\mathrm{V/nm}$ will be assumed for the electromagnetic scalar potentials (4.1). The value has been chosen this way because it is both experimentally achievable (cf. [109]) and large enough to make the qualitative behaviour of the perturbation on the band gap observable. The orbitals to be considered throughout this chapter are, unless stated otherwise, $2\mathrm{p_z}$, $3\mathrm{d_{xz/yz}}$ and, for circular polarisation, the effective $4\mathrm{f_{xyz}}$-orbital. The latter is necessary to ensure that the coordinates x and y commute, as has been discussed in section 2.2.3.

Fig. 4.2 depicts the Floquet quasi-energies of the Floquet Hamiltonian H_F from Eq. (4.3) at the K-point for a circularly polarised electric field. A detailed discussion on the couplings between the individual bands will follow in section 4.2 while this section will focus on the qualitative behaviour instead. There are two major differences between Figs. 4.1 and 4.2a:

1. While the only photonic excitations that are included in Fig. 4.1 are $n \in \{-1, 0, 1\}$, Fig. 4.2a includes excitations up to $n = \pm 4$, as can also be deduced from the greater number of Floquet energies.
2. Since Eq. (4.2) assumes a vanishing field strength of $E_0 = 0$, the lines in Fig. 4.1 cross without interaction. The model with $E_0 \neq 0$, however, leads to avoided crossings. This can be seen in Fig. 4.2b. As will be discussed in section 4.2, these avoided crossings are the same as illustrated in Fig. 3.3 (pg. 89). The crossing at $f = 3\,\mathrm{PHz}$ will also be discussed there.

The dashed black lines in Fig. 4.2b correspond to the unperturbed lines from Fig. 4.1 and have been added as a guide to the eye. From those lines, one can see the exact points of resonance. For the given frequencies, an energetic shift between the horizontal solid and the dashed lines can be observed. This is due to the interaction of p- and d-bands under irradiation:
As discussed in section 2.2.3, the coupling between p- and d-bands in unperturbed graphene lowers the energy eigenvalues of valence and conduction band at the K-point from $0\,\mathrm{eV}$ in graphene without d-orbitals to approximately $E = -181\,\mathrm{meV}$ with d-orbitals (cf. Tab. 3.1). The electric potential of the light field enhances the coupling of the p- and d-bands, further lowering the energy values.

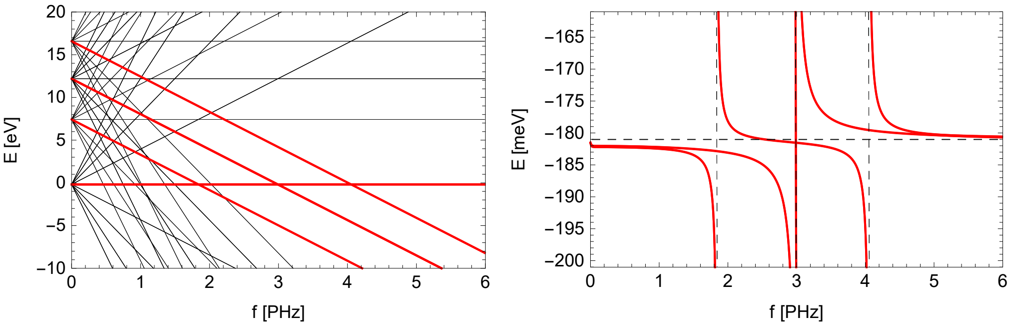

(a) (b)

Figure 4.2: Frequency-dependent Floquet quasi-energies for graphene at the K-point under the effect of a circularly polarised electric field of field strength $E_0 = 0.8\,\mathrm{V/nm}$, with a Floquet order of $N = 4$; (a) With increasing frequency, the energies change depending on the number of photons associated with them. (b) The red lines from (a) have been zoomed in, unveiling avoided crossings. Dashed lines depict the behaviour without interactions, to better pinpoint resonances.

The energetic offset caused by the electric field increases with the field strength. Its magnitude is depicted in Fig. 4.3 where the Floquet quasi-energies associated with valence and conduction band are given as a function of the field strength E_0 of the irradiated light. In the remainder of this chapter, the energies of the graphene band structure will be shifted by 181.02 meV, such that figures like 4.2 are centred around $E = 0\,\mathrm{eV}$.

As the frequency reaches $f = 6\,\mathrm{PHz}$ in Fig. 4.2, the Floquet energies converge towards the field-free limit. Since there are no resonances at frequencies higher than $f = 4.1\,\mathrm{PHz}$ (cf. intersections in Fig. 4.2), the effect of the electric perturbation becomes weaker with increasing frequency. At lower frequencies, higher resonances play an important role, as will be discussed for THz frequencies in section 4.3.2.

Both Figs. 4.2 and 4.3 indicate an increase of the band gap between valence and conduction band. As depicted in Fig. 4.4 for $f = 3.85\,\mathrm{PHz}$,[2] this leads to an increase by two orders of magnitude compared to the natural graphene band gap.

---

[2] The frequency of $f = 3.85\,\mathrm{PHz}$ in Fig. 4.5 has no particular physical significance aside from lying between two resonances. At an early stage of this thesis, before the implementation of the tight-binding model was completed, this frequency denoted a local minimum of the band gap. Since then, it continues to serve as a reference point.

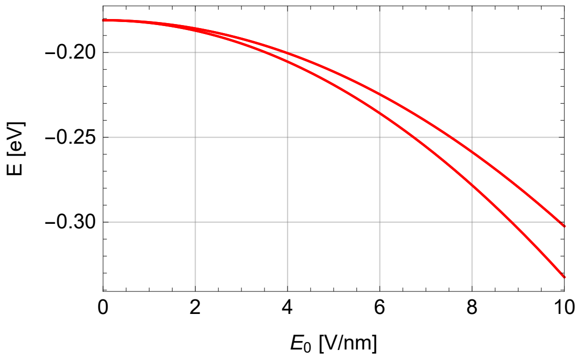

Figure 4.3: Floquet quasi-energies that correspond to the 0-photon valence and conduction band of graphene at the K-point, under irradiation with circularly polarised light of frequency $f = 0.1\,\mathrm{PHz}$; With increasing field strength E_0 of the irradiated light, the quasi-energies of the bands are lowered. At zero field strength, both valence and conduction band lie at approximately $E = -0.181\,\mathrm{eV}$, similar to the unperturbed case given in Tab. 3.1.

Due to the avoided crossings in Fig. 4.2b, the definition of a band gap is not unambiguous. This thesis always refers to the band gap as the gap between those bands that have valence and conduction band character. From Eqs. (3.44,3.45) (pg. 88) and Fig. 3.3, one can conclude that these bands are typically those that are energetically closest to the bands of the unperturbed system. The magnitude of the band gap depends on the field strength E_0 and the frequency f of the electric field, as depicted in Fig. 4.5. It becomes maximal at the resonances. Between the resonances, it increases approximately quadratically, as is implied by Eq. (3.44). This can be seen in Fig. 4.5b. This behaviour is identical for other frequencies away from the resonances and will be discussed in greater detail in section 4.2.

An increase of the band gap can be of great value to experiments that deal with the topological properties of graphene. Since the natural band gap is vanishingly small, thermal excitations can lead to electrons crossing the gap. This in turn makes insufficiently cooled graphene a conductor. Band gaps like those depicted in Fig. 4.5a and 4.4, however, are less prone to such thermal excitations and therefore enable more elaborate experimental setups for the study of quantum Hall effects. In the following, it will be discussed whether graphene is still a topological insulator under irradiation with light, and how the polarisation of the light affects the type of topological insulator.

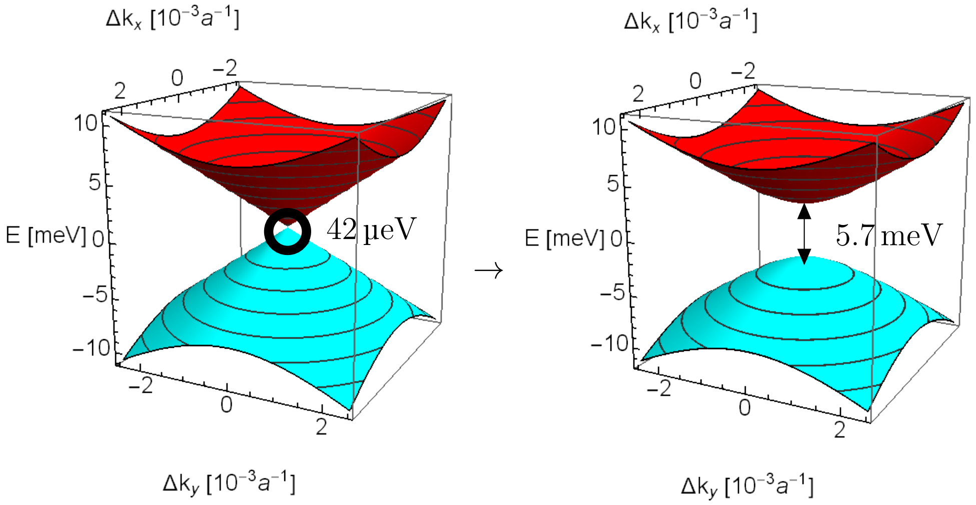

unperturbed enhanced

Figure 4.4: Band gap enhancement under the irradiation of graphene with circularly polarised light of frequency $f = 3.85\,\mathrm{PHz}$ and field strength $E_0 = 0.8\,\mathrm{V/nm}$; The original band gap between valence band (cyan) and conduction band (red) increases by more than a factor of 100. $\Delta k_{x/y}$ denotes the distance from the K-point.

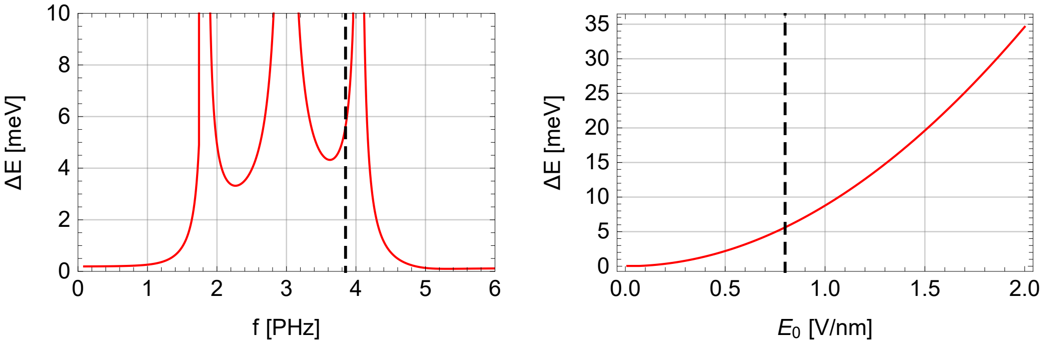

(a) $E_0 = 0.8\,\mathrm{V/nm}$ (b) $f = 3.85\,\mathrm{PHz}$

Figure 4.5: Band gap between valence and conduction band of the graphene Floquet band structure at the K-point; (a) At a field strength of $E_0 = 0.8\,\mathrm{V/nm}$, the band gap is depicted as a function of the frequency f. Close to resonances, the band gap increases quadratically. Hence, its magnitude seems to diverge. (b) The gap is depicted as a function of the field strength for a constant frequency of $f = 3.85\,\mathrm{PHz}$. In both (a) and (b), the frequency and the field strength of the other figure is highlighted via a dashed line.

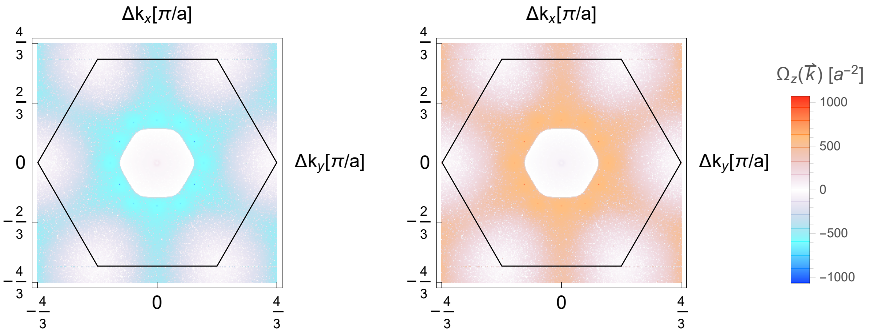

CB, spin: ↓, $W = -1$ CB, spin: ↑, $W = +1$

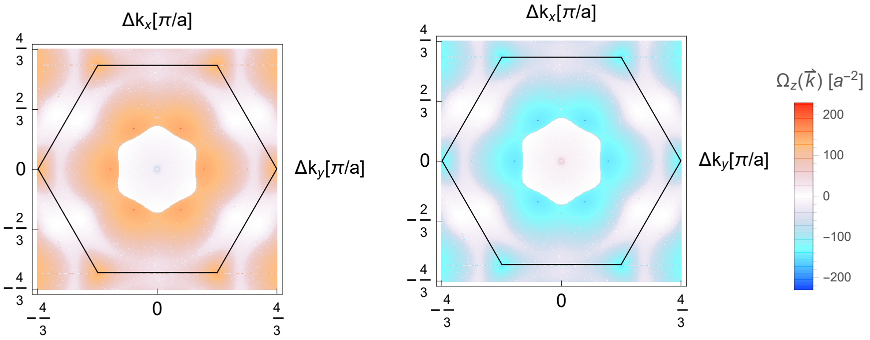

VB, spin: ↓, $W = +1$ VB, spin: ↑, $W = -1$

Figure 4.6: Berry curvature $\Omega_z(\vec{k})$ of the valence (VB) and conduction band (CB) of unperturbed spinful graphene with d-orbitals; The spin-degenerate bands have different Chern numbers W depending on the spin. The first Brillouin zone has been marked.

4.1.2 Topology and Insulating Properties

As discussed in section 2.6.5, a time-dependent perturbation bears the potential of significantly altering the topological properties of a material. One effect is the change from a $\mathbb{Z}$- or $\mathbb{Z}_2$-insulator to a $\mathbb{Z}^{\times n}$- or $\mathbb{Z}_2^{\times n}$-insulator due to the periodicity of the Floquet band structure. The other effect is the breaking of time-reversal that changes the corresponding Altland-Zirnbauer class of a system (cf. Tab. 2.1, pg. 56).

Unperturbed graphene is a spin-Hall insulator whose topological quantum number $\nu \in \mathbb{Z}_2$ can be computed from the difference of the Chern numbers of the spin-degenerate valence and conduction bands via Eqs. (2.141) and (2.142) (pg. 53). As can be concluded from Fig. 4.6, this results in a $\mathbb{Z}_2$-topological quantum number of $\nu = 1$ for unperturbed graphene.

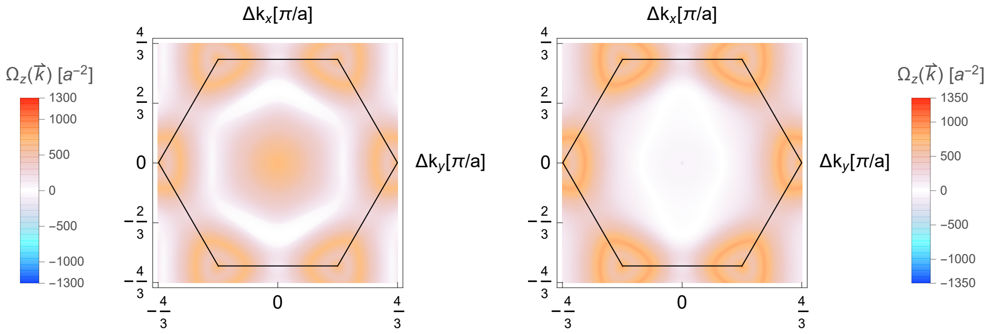

CB, spin: ↓, $W = +1$ CB, spin: ↑, $W = +1$

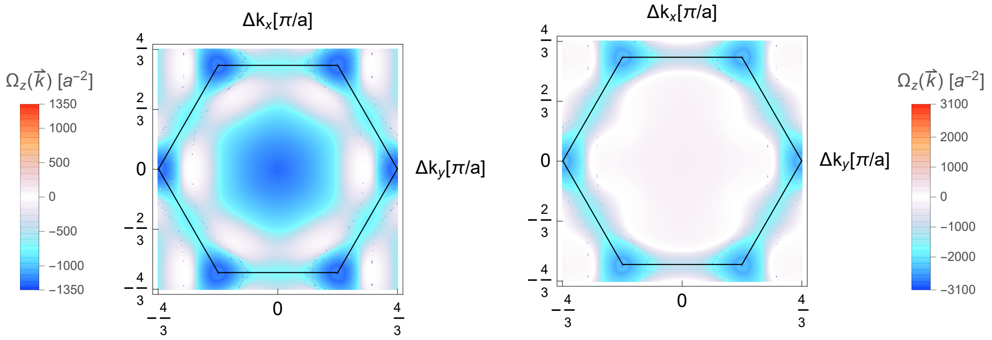

VB, spin: ↓, $W = -1$ VB, spin: ↑, $W = -1$

Figure 4.7: Berry curvature $\Omega_z(\vec{k})$ of the 0-photon bands of graphene irradiated with circularly polarised light of frequency $f = 3.85\,\mathrm{PHz}$ and field strength $E_0 = 0.8\,\mathrm{V/nm}$; As opposed to the unperturbed system in Fig. 4.6, the Chern numbers of both bands above the Fermi energy (CB) are $W = +1$ while those below it are $W = -1$. This implies a spin-independent quantum Hall effect as opposed to a spin-Hall effect. Note the varying scales for the Berry curvature. The first Brillouin zone has been marked.

Fig. 4.6 shows the Berry curvature of unperturbed graphene similarly to the figures in section 2.4.3, but under the inclusion of d-orbitals and spin. Time-reversal symmetry leads to opposite Berry curvature for opposite spins. Irradiation with circularly polarised light breaks this symmetry, as can be seen in Fig. 4.7 for an exemplary frequency of $f = 3.85\,\mathrm{PHz}$.

As discussed by Oka at al. [47] for spinless graphene, circularly polarised light induces a Berry curvature. In Fig. 4.7, for spinful graphene, this curvature is negative for the valence and positive for the conduction band. As a consequence, the valence band has a Chern number of $W = +1$ regardless of spin, while the conduction band has $W = -1$. Graphene is therefore a Chern insulator. A result of this is a *photovoltaic Hall effect*, a quantum Hall effect that is induced by the electric field of the light. It is an anomalous Hall effect, as there is no magnetic field involved. The resulting Hall current in the material aligns with the polarisation direction of the light (cf. [110]). This photovoltaic Hall effect has also been measured by McIver at al. [48].

Linearly polarised light does not break time-reversal symmetry. As a consequence, the Chern numbers do not change, and graphene remains a spin-Hall insulator. The Berry curvatures are not depicted explicitly.

The discussions above only consider the topological quantum numbers of (0-photon) valence and conduction band. As discussed in section 2.6.5, it is possible in Floquet systems that edge states form between all bands, regardless of those quantum numbers. This, however, depends on the existence of edge states that cross the boundary of the first Floquet Brillouin zone. As will be demonstrated in chapter 5, no such states are observed for any polarisation or frequency. Instead, the only edge states between valence and conduction band are those one would naïvely expect based on the discussions above, i.e. those of a quantum (anomalous) Hall or spin-Hall insulator.

Even though only the results for $f = 3.85\,\text{PHz}$ have been depicted explicitly in this section, the results are assumed to be similar for any other frequencies away from resonances. This thesis does not make any assumptions on what happens at resonance.

In the above discussions, it was implicitly assumed that the 0-photon replicas of the original valence and conduction band are also the valence and conduction band of the system irradiated with light. This assumption, however, is not guaranteed and therefore needs to be verified in the following. First, recall the discussion of section 2.6.3: For near-integer photon expectation values $\langle \Gamma \rangle$, the 0-photon band structure can be treated like a regular band structure of a time-independent system. To determine which bands correspond to valence and conduction band, one therefore needs to count the number of 0-photon states. For the system (4.2) with vanishing field strength, these are depicted as black lines in Fig. 4.1. The number of black lines below valence and above conduction band does not change as a function of the frequency. This is also true for the system (4.3), as can be seen in Fig. 4.8.

Fig. 4.8 shows the same energies as Fig. 4.2b, but with the shading of Fig. 4.1. The energies have been shifted by 181.02 meV as discussed in the previous

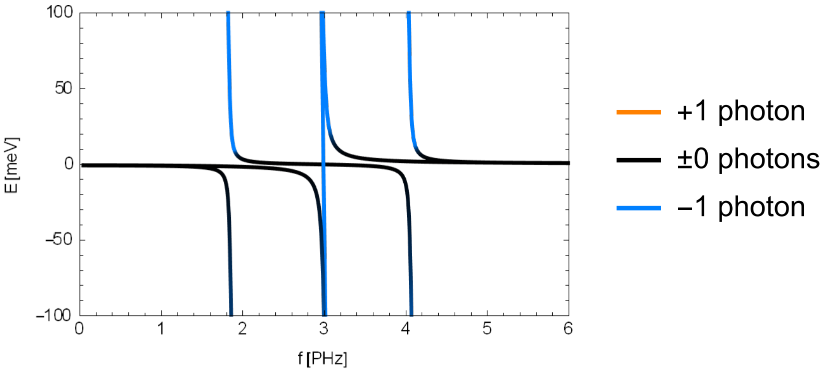

Figure 4.8: Floquet quasi-energies E at the K-point as functions of the frequency f; Orange, black and azure depict quasi-energies that correspond to states with $n \in \{-1, 0, +1\}$ photons, respectively. The lines closest to $E = 0\,\text{meV}$ are all black, except for one azure line crossing at $f = 3\,\text{PHz}$. Hence, they belong to 0-photon states.

subsection. From Fig. 4.8, one can see that the Floquet quasi-energies close to the original valence and conduction band correspond to Floquet bands with a photon expectation value of approximately $n = 0$, i.e. they are part of the electronic band structure.

Alternatively, this can also be concluded from Eqs. (3.44) and (3.45) (pg.88) that, away from resonances, describe one 0- and one (-1)-photon state. Only near the resonance do both states mix. Therefore, this thesis makes again no assumptions on what happens at the resonances. Fig. 4.9 shows the behaviour of the Floquet energies similarly to Fig. 4.8, but at the M- and the Γ-point.

In Fig. 4.9, the 0-photon valence and conduction band lie at $E \approx \pm 3.6\,\text{eV}$ for the M- and $E \approx \pm 10\,\text{eV}$ for the Γ-point. Thus, the gap between them is significantly larger than at the K-point. As a consequence, (-1)- and $(+1)$-photon lines (azure and orange) can cross between them. As mentioned in section 2.6.2, a linear combination of such states could yield an effective 0-photon state, i.e. a new electronic state between valence and conduction band. Consequently, the bulk of graphene could become conducting. Since the Floquet Hamiltonian (3.21) does not allow any direct two-photon processes, a $(+1)$- and a (-1)-photon state can only be coupled via an intermediate (unperturbed) 0-photon state. Let

$$|i, n\rangle \qquad \text{and} \qquad E_{i,n} \qquad \text{with } i \in \{\mathrm{p}, \mathrm{d}\},\ n \in \{-1, 0, +1\} \tag{4.4}$$

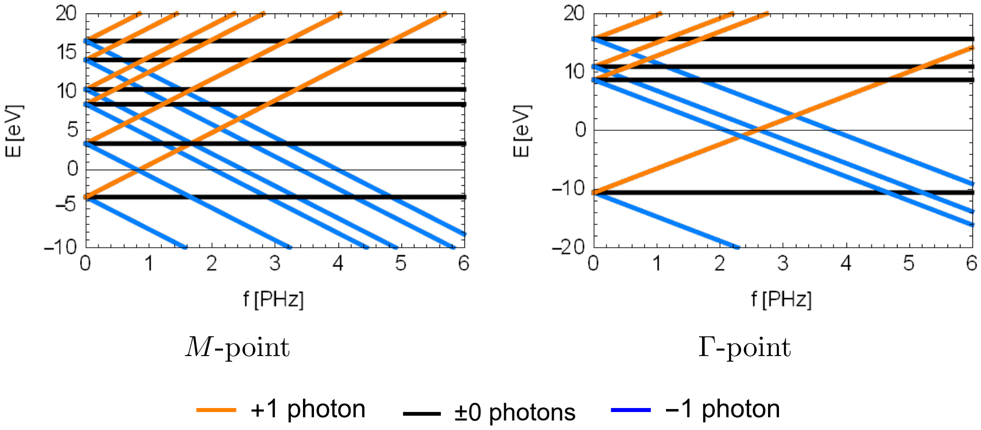

M-point

Γ-point

Figure 4.9: Floquet quasi-energies E at the M- and Γ-point as functions of the frequency f, in the limit of vanishing field strength; At the M-point, valence and conduction band originally reside at $E \approx \pm 3.6\,\mathrm{eV}$. At $f \approx 0.829\,\mathrm{PHz}$, a $(+1)$-photon valence and a (-1)-photon conduction band cross at $E \approx 0\,\mathrm{eV}$. If these bands were to interact, they could form an effective 0-photon band that turns graphene into a conductor. At the Γ-point, the same happens three times between $f = 2.4$ and $3.4\,\mathrm{THz}$. A line at $E = 0\,\mathrm{eV}$ has been added as a guide to the eye.

denote an n-photon i-orbital state with its energy. The first non-zero correction term that couples a $(+1)$-photon p-band and a (-1)-photon d-band arises in fourth order perturbation theory as

$$\frac{\langle \mathrm{p},1|\xi|i,0\rangle\langle i,0|\xi|\mathrm{d},-1\rangle\langle \mathrm{d},-1|\xi|j,0\rangle\langle j,0|\xi|\mathrm{p},1\rangle}{(E_{\mathrm{p},1}-E_{i,0}+\hbar\omega)(E_{\mathrm{p},1}-E_{d,-1}+2\hbar\omega)(E_{\mathrm{p},1}-E_{j,0}+\hbar\omega)} \tag{4.5}$$

with $i, j \in \{\mathrm{p}, \mathrm{d}\}$. The expression ξ denotes the dipole matrix elements from Eq. (4.3) that couple the respective states. A coupling between a $(+1)$-photon state (orange line in Fig. 4.9) and a (-1)-photon state (azure line) is thus suppressed by the product

$$(E_{\mathrm{p},1}-E_{i,0}+\hbar\omega)(E_{\mathrm{p},1}-E_{j,0}+\hbar\omega) \tag{4.6}$$

of the energy differences to the closest 0-photon energies $E_{i,0}$ and $E_{j,0}$ (black lines), possibly with $i = j$. In Fig. 4.9, an azure and an orange line cross at the M-point near $E = 0\,\mathrm{eV}$ at[3] $f \approx 0.829\,\mathrm{PHz}$. At this frequency, the energy differences to the closest 0-photon bands are more than $3\,\mathrm{eV}$. Hence,

---

[3] Without d-orbitals, this frequency would be exactly $f = V_{\mathrm{pp}\pi}/(2\pi\hbar) = 0.87\,\mathrm{PHz}$. However, the energetic shift discussed in the context of Fig. 2.5 (pg. 16) leads to lower resonance frequencies.

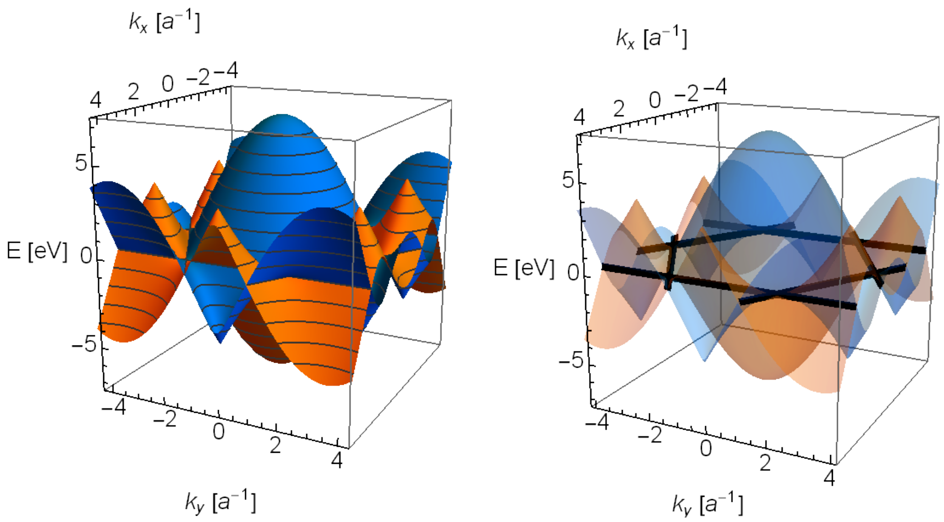

Figure 4.10: Intersection of a (+1)- and a (−1)-photon band; Left: The Floquet replica of the valence band (orange) is shifted by a photon energy of $+\hbar\omega = +3.43\,\text{eV}$ while the replica of the conduction band (blue) is shifted by $-\hbar\omega = -3.43\,\text{eV}$. Consequently, they intersect. Right: Effective 0-photon bands form across the intersection (black) of the replica bands.

Eq. (4.6) assumes large values, and Eq. (4.5) becomes vanishingly small, unless

$$2 \cdot 2\pi f = 2\omega \approx \frac{E_{d,-1} - E_{\mathrm{p},1}}{\hbar}, \tag{4.7}$$

i.e. unless f is a second-order resonance frequency. However, this resonance is also $\vec{k}$-dependent. As can be seen in Fig. 4.10, the values $\vec{k}$ for which the resonance condition (4.7) is satisfied, lie on the intersection lines of the (+1)- and the (−1)-photon band. Thus, the effective 0-photon bands only exist on a quasi-one-dimensional subset of the reciprocal space. Because of this, the bands are expected to be either completely filled or completely empty. Moreover, for frequencies other than $f = 0.829\,\text{PHz}$, the intersection lines form closed paths within the Brillouin zone that are not connected to one another. Hence, the effective 0-photon bands are not expected to contribute towards charge transport. It is, however, expected that these bands can be measured via Shubnikov–de Haas measurements, similarly to impurity bands (cf. [111]).

After the general discussions of this section, the next section will go into more detail on the processes involved in every avoided crossing of Fig. 4.2.

4.2 Orbital Composition (PHz Regime)

Every avoided crossing in Fig. 4.2 of the previous section is of the same type as the one depicted in Fig. 3.3 (pg. 89). As can be seen from Eq. (3.45) (pg. 88), the processes involve two respective basis states from Tab. 3.1 (pg. 83). In this section, all avoided crossings of Fig. 4.2 will be discussed individually, and they will be attributed to two respective states of Tab. 3.1. Due to this analysis, additional spin-dependent features will become apparent. Moreover, it will be demonstrated that the understanding of the processes under circularly polarised light suffices to also explain the processes under linearly polarised light.

Recall that the origin of the band gap is the intrinsic SOI. As discussed in section 2.5.1, SOI couples real spin s_z and sublattice spin σ_z. In unperturbed graphene, both spins are consequently either parallel or antiparallel for valence and conduction band at the K/K'-point, and one obtains[4] $\langle s_z\sigma_z\rangle \approx \pm 1$ for the states 1 through 4 in Tab. 3.1. Due to this spin-spin relation, the selection rules for circularly polarised light from section 3.3 will in the following be observed to lead to a lift of spin degeneracy. Since linearly polarised light has identical contributions from clockwise and anticlockwise polarisation, it does not lift spin degeneracy. Similarly, only circularly polarised light leads to a change of the topological properties of the band structure: As discussed in section 4.1.2, circular polarisation breaks time-reversal symmetry and consequently changes graphene from a $\mathbb{Z}_2$-topological insulator to a Chern insulator that exhibits a quantum anomalous Hall effect. In the following, the orbital and spin composition of valence and conduction band will be studied for both polarisations, with a focus on the quantity $\langle s_z\sigma_z\rangle$.

4.2.1 Circular Polarisation

Fig. 4.11 shows the orbital composition (lower parts of (a-f)) of the states that belong to the respective frequency-dependent Floquet quasi-energies[5] (upper parts of (a-f)) of graphene irradiated with circularly polarised light. The upper parts depict the separate lines of Fig. 4.2, but with shading according to $\langle s_z\sigma_z\rangle$. Only the spin-up states are depicted in the upper parts of Fig. 4.11. As predicted in section 3.3.1, spin degeneracy is lifted, but the lift of degeneracy is not visible on the scale of Fig. 4.11. It will therefore be discussed separately after the discussion of Fig. 4.11.

---

[4] $\langle s_z\sigma_z\rangle$ is not exactly ±1, due to the small d-orbital contributions of the eigenstates.

[5] As explained in the previous section, the quasi-energies in the figures have been shifted by 181.02 meV, to be centred around $E = 0\,\text{eV}$.

#	vector	energy [eV]
2	$0.12\mathrm{i} \cdot \boldsymbol{Y}^{-1}_{2,B\uparrow} + 0.99 \cdot \boldsymbol{Y}^{0}_{1,A\uparrow}$	-0.18104
3	$-0.99\mathrm{i} \cdot \boldsymbol{Y}^{0}_{1,B\uparrow} + 0.12 \cdot \boldsymbol{Y}^{1}_{2,A\uparrow}$	-0.181
6	$0.71 \cdot \boldsymbol{Y}^{1}_{2,B\uparrow} + 0.71 \cdot \boldsymbol{Y}^{-1}_{2,A\uparrow}$	7.423
7	$0.99\mathrm{i} \cdot \boldsymbol{Y}^{-1}_{2,B\uparrow} + 0.12 \cdot \boldsymbol{Y}^{0}_{1,A\uparrow}$	12.1796
10	$-0.12\mathrm{i} \cdot \boldsymbol{Y}^{0}_{1,B\uparrow} + 0.99 \cdot \boldsymbol{Y}^{1}_{2,A\uparrow}$	12.182
11	$0.71 \cdot \boldsymbol{Y}^{1}_{2,B\uparrow} + 0.71 \cdot \boldsymbol{Y}^{-1}_{2,A\uparrow}$	16.577

Table 4.1: Normalised spin-up states of Tab. 3.1 with corresponding eigenenergies in eV; The numbers correspond to the original table. The basis functions $\boldsymbol{Y}^{m}_{l,A/B,\updownarrow}$ are defined in Eq. (3.32). Functions with $l = 1$ and $m = 0$, i.e. $\boldsymbol{Y}^{0}_{1,A/B,\updownarrow}$, correspond to $\mathrm{p_z}$-orbitals. Others belong to $\mathrm{d_{xz}}$- and $\mathrm{d_{yz}}$-orbitals.

Since only spin-up states are depicted in Fig. 4.11, the correlation between real and sublattice spin reduces to $\langle s_z \sigma_z \rangle = \langle \sigma_z \rangle$, i.e. it directly corresponds to the localisation on the sublattices A (red) and B (cyan). The lower parts of the subfigures in Fig. 4.11 depict the orbital compositions of both the spin-up and spin-down states, as they are easily distinguishable via solid and dashed lines.

In the following, the Floquet quasi-energies of Fig. 4.11 will be discussed successively from (a) to (f). (g) is a composite figure providing an overview of the relative energy landscape. The corresponding Floquet states will be related to the numbers 1 to 12 of the unperturbed basis that is given in Tab. 3.1. The relevant entries of Tab. 3.1 are summarised again in Tab. 4.1. First, only the spin-up states will be discussed. The discussion of the spin-down states and their relation to the spin-up states will follow afterwards.

Recall from section 3.3.1 that the onsite component of the electric field only couples certain states to one another. Circularly polarised light has clear selection rules on which 0- and (-1)-photon states are coupled to one another. Precicely, a (-1)-photon state ψ_i and a 0-photon state ψ_j are coupled to one another via onsite terms of the electric field if and only if their respective entry in Tab. 3.2 (pg. 85) is "+". The strongest couplings involving the valence and conduction band states 1 through 4 are the following:

- 1 to 9
- 3 to 7
- 2 to 6 and 11
- 4 to 5 and 12

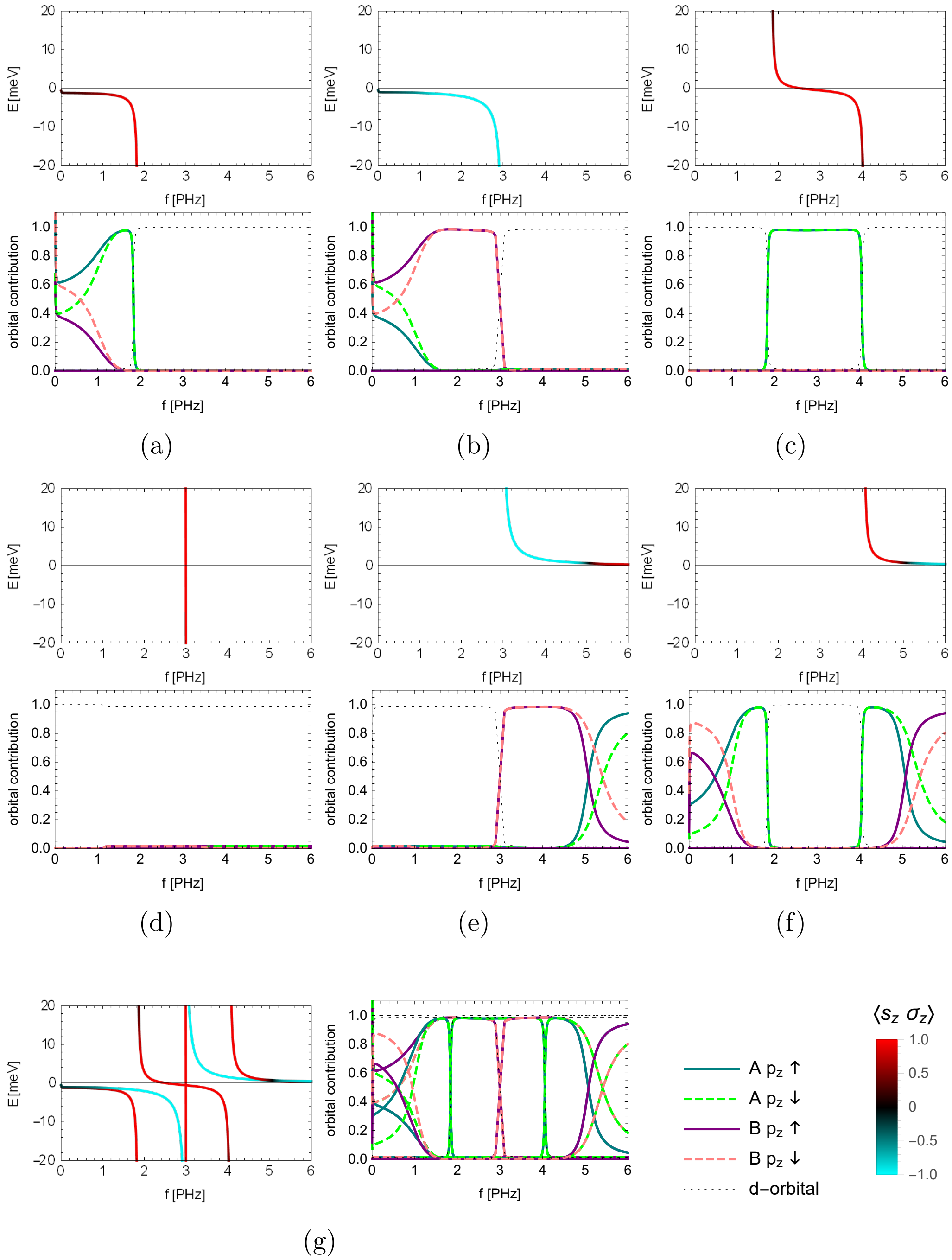

(a) (b) (c)

(d) (e) (f)

(g)

Figure 4.11: Orbital compositions of the Floquet quasi-energies at the K-point under the effect of a circularly polarised electric field with $E_0 = 0.8\,\mathrm{V/nm}$; (a-f) depict pairs of Floquet quasi-energies (upper pictures) and their orbital compositions (lower pictures). Only the energies of spin-up states are depicted as their nearly degenerate spin-down counterparts look similar, but with opposite shading according to $\langle s_z \sigma_z \rangle$. The compositions are shown for both the spin-up and the spin-down states and can be distinguished via solid/dashed lines. (g) shows the composites of (a-f).

Meanwhile, the spin-up valence and conduction band states are also weakly coupled to one another:

- 2 to 3

With this in mind, one can conclude the eigenstates involved in Fig. 4.11:

(a) This energy lies below (b) and belongs to the Floquet valence band. For frequencies below $f = 1.84\,\mathrm{PHz}$, it belongs to a linear combination of the states 2 and 3 of Tab. 4.1, i.e. valence and conduction band of the unperturbed system. The coupling between the states 2 and 3 also couples (a) to (b).
At $f = 1.84\,\mathrm{PHz}$, the states 2 and 6 are at resonance. Below this frequency, the subfigure (c) corresponds to a (-1)-photon replica of the state 6. The avoided crossing between (a) and (c) leads to an energetic shift of (a). As a result, the band gap between (a) and (b) increases as f approaches $1.84\,\mathrm{PHz}$, and the coupling between the states 2 and 3 decreases. This can be seen from the increased sublattice localisation in the orbital composition.
After $f = 1.84\,\mathrm{PHz}$, (c) takes over the 0-photon p-band character of (a), and (a) instead obtains (-1)-photon d-band character. (a) then no longer denotes the Floquet valence band. Instead, (b) becomes the new valence band and (c) the conduction band.

(b) As the frequency increases, the mixing with (a) decreases, and the contribution of state 3 towards the Floquet state of (b) increases, together with the localisation on sublattice B. At $f = 2.99\,\mathrm{PHz}$, (b) exhibits an avoided crossing with (e), corresponding to state 7. Again, the original 0-photon p-band character changes to (-1)-photon d-band character in the process.

(c) After the avoided crossing with (a) at $f = 1.84\,\mathrm{PHz}$, the Floquet state corresponds to state 2 and has 0-photon p-band character. After a second avoided crossing with (f) at $f = 4.05\,\mathrm{PHz}$, this contribution changes to the (-1)-photon replica of state 11 and therefore d-band character.

(d) The Floquet state corresponds to the (-1)-photon replica of state 10. There is no onsite coupling between the states 10 and 2, the latter of which corresponds to (c). State 10 involves the same atomic orbitals as state 2. Since the light field only directly couples atomic orbitals on the same atom if they have different angular momentum quantum numbers l, the only coupling between (c) and (d) stems from matrix elements that couple neighbouring atoms. As a result, the coupling is too weak to be noticeable in the figure.

(e) After the avoided crossing with (b) at $f = 2.99\,\mathrm{PHz}$, (e) corresponds to the 0-photon state 3 and therefore has p-band character. Near $f = 5.1\,\mathrm{PHz}$, it exhibits a second avoided crossing with (f) that exchanges the composition of both respective Floquet states.

(f) This Floquet energy exhibits one avoided crossing with (c) at $f = 4.05\,\mathrm{PHz}$ and one with (e) near $f = 5.1\,\mathrm{PHz}$. The corresponding state of (f) changes first from 11 to 2 and then from 2 to 3. The latter change is only possible because (e) and (f) are energetically close to one another.
In addition to this, the orbital composition shows that there is at least one more avoided crossing at $f = 1.84\,\mathrm{PHz}$. Before this avoided crossing, (f) belongs to the (+1)-photon replica of state 2. The processes that eventually change it to state 11, however, are not depicted in the figure, and will not be detailed, as they have no notable effect on the physics of the 0-photon valence and conduction band.

Every single avoided crossing in Fig. 4.11 induces a band inversion between valence and conduction band. In unperturbed graphene as defined in this thesis, the spin-up valence band is localised on sublattice A and the spin-up conduction band on B. As can be seen from the colours of the Floquet energies in Fig. 4.11g, this relation changes at $f = 1.84\,\mathrm{PHz}$, $f = 2.99\,\mathrm{PHz}$, $f = 4.05\,\mathrm{PHz}$ and near $f = 5.1\,\mathrm{PHz}$. At frequencies below $f = 0.1\,\mathrm{PHz}$, additional effects occur that are not captured by the figure. These effects correspond to a separate phenomenon that will be discussed in section 4.3.2.

The lower parts of Figs. 4.11 (a), (b), (e) and (f) show that the spin-down states behave differently than the spin-up states. To understand this, consider again the discussions in section 3.3.2 and at the end of section 3.3.1:

- The states 1 and 2 correspond to the unperturbed valence band with spin-down and spin-up, respectively.
- The states 3 and 4 correspond to the unperturbed conduction band with spin-up and spin-down, respectively.
- The onsite interaction leads to the coupling 1-9, 2-6, 3-7 and 4-5. Each coupling decreases the energy of the corresponding valence and conduction band state.

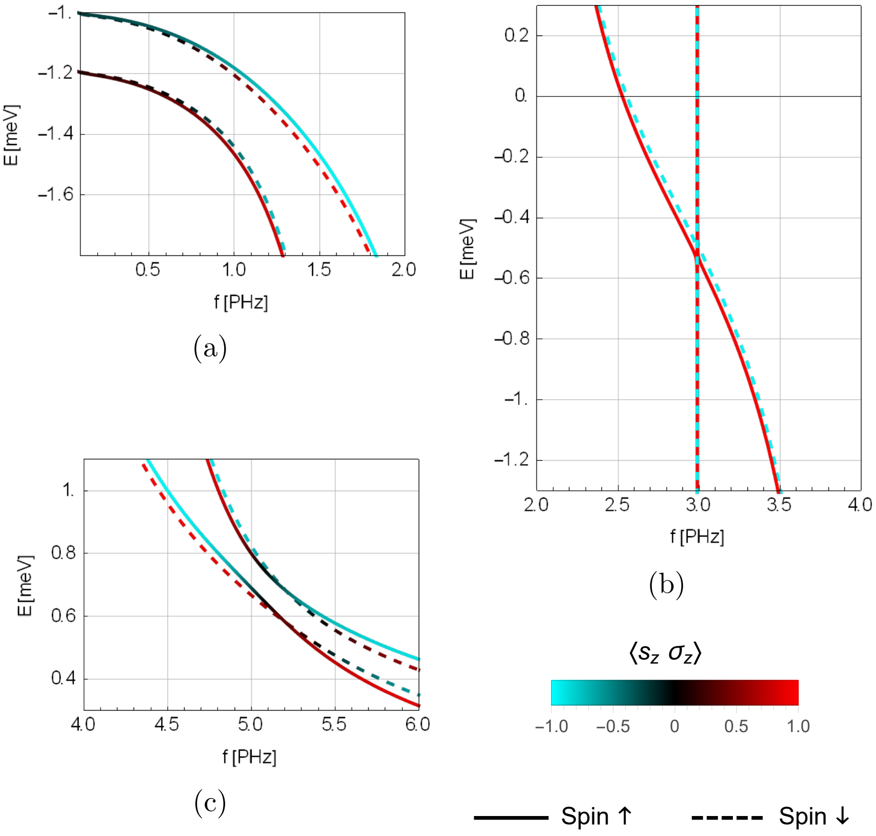

Figure 4.14: Lift of spin degeneracy; The Floquet energies depicted in Fig. 4.11 are no longer spin-degenerate, since the different spins are coupled at different frequencies. At frequencies below $f = 0.1\,\text{PHz}$, higher order effects occur. These effects will not be discussed in this section and will instead be the focus of section 4.3.2.

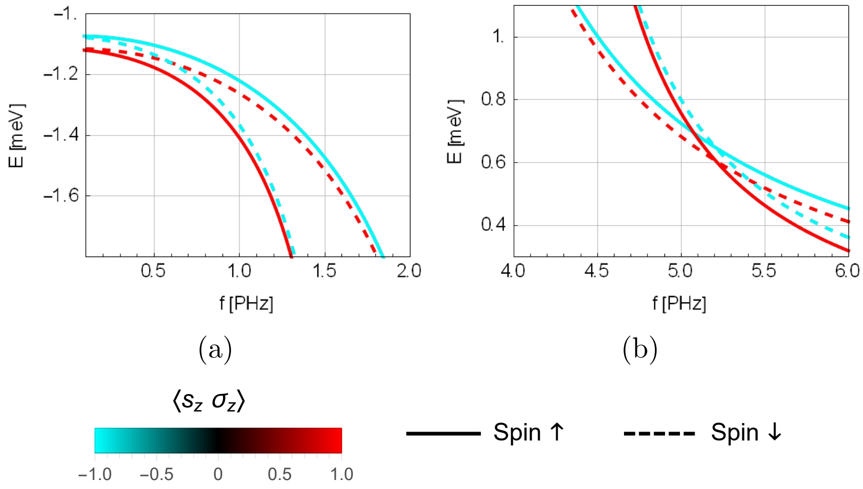

(a) (b)

Figure 4.15: Lift of spin degeneracy without sublattice potential; When the effective sublattice potential M is artificially set to zero, the avoided crossings in Fig. 4.14 become actual crossings.

- The couplings 2-6 and 4-5 occur before the couplings 1-9 and 3-7. As a result, the spin-up valence band and the spin-down conduction band are the first to have their energy decreased.

As a result of these processes, the spin-down valence band would cross the spin-down conduction band if it were not for the effective sublattice potential discussed in section 3.3.2. Because of the latter, the Floquet energies exhibit an avoided crossing as depicted in Fig. 4.14a.

Fig. 4.14c also shows that a similar avoided crossing occurs near $f = 5.1\,\mathrm{PHz}$. One can see from Fig. 4.15 how the Floquet energies would cross if one were to artificially disable the sublattice potential. Notably, Fig. 4.15b involves a crossing of not only the spin-down, but also the spin-up states. The processes leading to this are the same as described above for Fig. 4.14a and Fig. 4.15a, but with different states involved. In this thesis, they will not be discussed in further detail.

The different behaviour of the Floquet energies leads to a lift of the spin degeneracy that can be seen in both Figs. 4.14 and 4.15. Fig. 4.14b shows that this lift of degeneracy is also present away from the frequencies that lead to the processes described above. The energetic difference between the spins is approximately of the magnitude of the band gap of unperturbed graphene, i.e. $\Delta E_{\mathrm{spin}} \approx 42\,\mu\mathrm{eV}$. Since the magnitude of the band gap in

Fig. 4.14 is given by the onsite coupling and the effective mass term, the original SOI gap is only a small perturbation that then lifts the spin degeneracy.

A reversion of the polarisation direction of the light changes the selection rules from section 3.3.1. Instead of a "+", it is then a "−' in Tab. 3.2 that denotes a coupling. As a result, all spin-dependent effects described here are inverted. Spin-down states then behave like the here-described spin-up states and vice versa. Since linearly polarised light is a linear combination of both polarisation directions, it does not give rise to any spin-dependent effects, as will be discussed in the following.

4.2.2 Linear Polarisation

As a linear combination of two opposite circular polarisations, linearly polarised light couples a (-1)-photon state ψ_i and a 0-photon state ψ_j independently of their respective sign in Tab. 3.2. Thus, both a "+" and a "−" denote a coupling. Conclusively, linearly polarised light leads to an increased number of basis states that are involved in every process. Also, the spin-dependent effects of either circular polarisation direction are cancelled by the opposite one. As a result, all Floquet energies of graphene that is irradiated with linearly polarised light are spin-degenerate.

As discussed in section 4.1.2, linearly polarised light does not break time-reversal symmetry. However, it does break the rotational symmetry of the honeycomb lattice. This becomes more apparent when going from a spherical orbital basis to a cubic one: As detailed in section 2.2.3, an electric field in x-direction couples the $\mathrm{p_z}$- and $\mathrm{d_{xz}}$-orbital, whereas a field in y-direction couples the $\mathrm{p_z}$- and the $\mathrm{d_{yz}}$-orbital. For circularly polarised light, the contribution is shifted equally from the $\mathrm{p_z}$- to both the $\mathrm{d_{xz}}$- and the $\mathrm{d_{yz}}$-orbital. For light that is linearly polarised in y-direction, however, the $\mathrm{d_{yz}}$-orbital contribution dominates. Since a $\mathrm{d_{yz}}$-orbital consists a linear combination of spherical harmonics, this bias towards $\mathrm{d_{yz}}$-orbitals manifests in the greater number of basis states involved in every coupling than compared to circular polarisation. As a result, the correlation between real and sublattice spin, $\langle s_z \sigma_z \rangle$ is lifted.

Fig. 4.16 shows the Floquet energies for linearly polarised light as a function of the frequency, together with the corresponding orbital compositions, similarly to Fig. 4.11 before. In the following, only the major differences between Figs. 4.11 and 4.16 will be discussed.

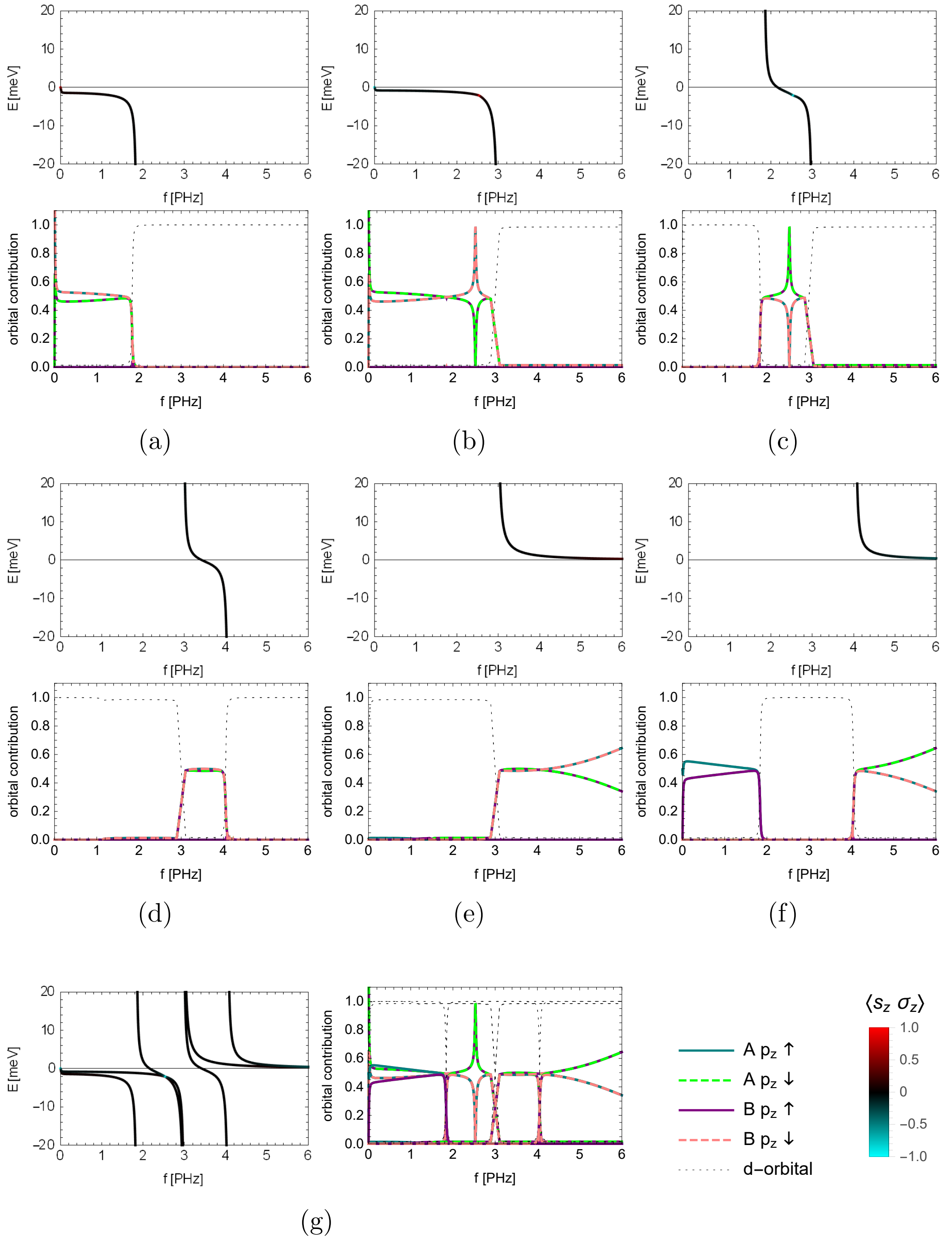

(a) (b) (c)

(d) (e) (f)

(g)

Figure 4.16: Orbital compositions of the Floquet quasi-energies at the K-point under the effect of a linearly polarised electric field with $E_0 = 0.8\,\mathrm{V/nm}$; (a-f) depict pairs of Floquet quasi-energies (upper pictures) and their orbital compositions (lower pictures). Only the energies of spin-up states are depicted as their degenerate spin-down counterparts look similar, but with opposite shading according to $\langle s_z \sigma_z \rangle$. The compositions are shown for both the spin-up and the spin-down states and can be distinguished via solid/dashed lines. (g) shows the composites of (a-f).

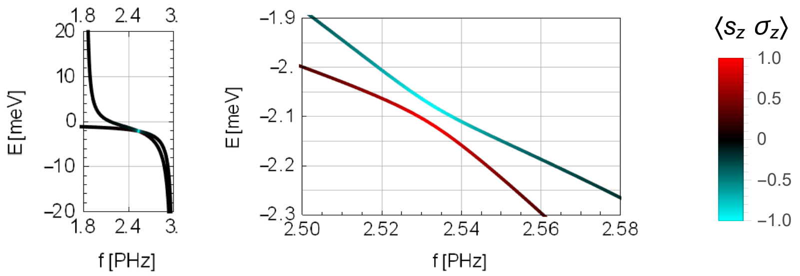

(a) (b)

Figure 4.17: Avoided crossing due to SOI; Two Floquet energies approach one another with increasing frequency. SOI leads to an avoided crossing and to an increased correlation $\langle s_z \sigma_z \rangle$ between real and sublattice spin. (a) and (b) show the same energies, but on different scales.

The first noteworthy difference between the figures is the aforementioned lift of the correlation $\langle s_z \sigma_z \rangle$ in Fig. 4.16. The Floquet energies are depicted mostly in black, indicating $\langle s_z \sigma_z \rangle = 0$. Accordingly, the orbital contributions of both sublattices are nearly identical. Only close to $f = 2.5\,\mathrm{PHz}$, there are spikes in the lower parts of (b) and (c), indicating a strong correlation. This is a result of SOI that leads to an avoided crossing between (b) and (c) which would otherwise cross. Consequently, the correlation $\langle s_z \sigma_z \rangle = \pm 1$ is restored near 2.5 PHz. The avoided crossing is depicted in greater detail in Fig. 4.17.

The second notable change between Figs. 4.11 and 4.16 is that in the latter, there is no straight line crossing without coupling like in 4.11d. The inclusion of both "+" and "−" in Tab. 3.2 leads to fewer restrictions on which states of Tab. 3.1 are coupled to one another. As a result, the argument d from the previous subsection can no longer be made, and the states 2 and 10 are coupled. Similarly, their spin-down counterparts 1 and 9 are coupled as well.

The next subsection will discuss whether the observations of this section are still valid if the light source is not perfectly perpendicular to the sample.

4.2.3 Angular Deflection

As discussed in sections 2.3.1 and 2.5.1, the absence of out-of-plane symmetry can lead to a Rashba effect, possibly rendering graphene topologically trivial. This can be caused by many things like e.g. a substrate the graphene sample is placed on (cf. [112–114]). Another possible cause is an angular deflection of the laser beam irradiating the sample as illustrated in Fig. 4.18.

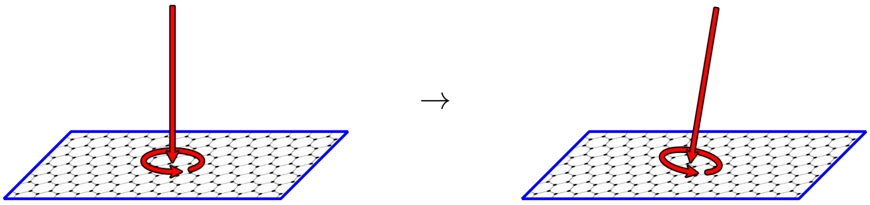

Figure 4.18: As a result of an angular deflection of the incoming laser beam (straight red arrow), the polarisation of the light (circular red arrow) and therefore also the electric field are no longer fully in-plane with the graphene sheet (blue). As a consequence, the system no longer satisfies out-of-plane symmetry.

For an angularly deflected laser beam, the scalar potentials (3.8) and (3.9) derived in section 3.1 are no longer valid. Hence, consider a deflection of an angle α around the x-axis. The electric fields in Eq. (3.2) (pg. 74) then assume the form

$$\vec{E}_{\text{circ}}(\vec{r},t) = E_0 \cdot \begin{pmatrix} \cos(\omega t - \vec{\kappa}\vec{r}) \\ \cos(\alpha)\sin(\omega t - \vec{\kappa}\vec{r}) \\ \sin(\alpha)\sin(\omega t - \vec{\kappa}\vec{r}) \end{pmatrix}, \tag{4.8}$$

$$\vec{E}_{\text{lin}}(\vec{r},t) = \sqrt{2}E_0 \cdot \begin{pmatrix} 0 \\ \cos(\alpha)\sin(\omega t - \vec{\kappa}\vec{r}) \\ \sin(\alpha)\sin(\omega t - \vec{\kappa}\vec{r}) \end{pmatrix} \tag{4.9}$$

with

$$\vec{\kappa} = \frac{1}{\lambda}\begin{pmatrix} 0, \\ -\sin(\alpha) \\ \cos(\alpha) \end{pmatrix}. \tag{4.10}$$

For small[6] α, the dipole approximation of $\vec{\kappa}\vec{r} = 0$ is still valid. It removes the explicit spatial dependence from the electric fields, allowing to again describe

---

[6] For $\alpha = 5°$, one obtains a wave vector $\vec{\kappa} \approx 1/\lambda \cdot (0, -0.087, 0.996)^t \approx 1/\lambda \cdot \vec{e}_z$ whose only component that is not orthogonal to the lattice, is vanishingly small.

the fields exclusively via scalar potentials

$$\Phi_{\mathrm{circ}}(\vec{r},t) = E_0 \cdot (x\cos(\omega t) + (y\cos(\alpha) + z\sin(\alpha))\sin(\omega t))\,, \tag{4.11}$$

$$\Phi_{\mathrm{lin}}(\vec{r},t)) = \sqrt{2}E_0 \cdot (y\cos(\alpha) + z\sin(\alpha))\sin(\omega t). \tag{4.12}$$

Only the effects of circularly polarised light will be depicted in this section. For it, the orbitals to be considered in the computations are 2s, $2\mathrm{p}_{\mathrm{x/y/z}}$, $3\mathrm{d}_{\mathrm{xz/yz}}$ and the effective $4\mathrm{f}_{\mathrm{xyz}}$-orbital (cf. section 2.2.3). The deflection angle will be chosen to be $\alpha = 5°$ which is significantly more than is expected to occur by accident. A frequency screening similar to Figs. 4.11g and 4.16g is depicted in Fig. 4.19. Apart from four new, weakly coupled lines, there is no notable change due to the deflection. The new lines correspond to s- and $\mathrm{p}_{\mathrm{x/y}}$-orbitals with photon expectation values of $\langle\Gamma\rangle = +1$.

Most importantly, the angular deflection does not lead to any Rashba effects. The time-dependent perturbation leaves the Chern numbers computed in section 4.1.2 intact, and graphene irradiated with circularly polarised light is still a Chern insulator. Similarly, the Chern numbers remain unchanged for linearly polarised light. As a consequence, graphene is bound to exhibit topologically protected edge states, as will be demonstrated for both polarisations in section 5.2.2.

As discussed in the context of Eqs. (2.141) and (2.142) (pg. 53), the computation of the the $\mathbb{Z}_2$-topological invariant from the Chern numbers depends on the absence of s_z-nonconserving terms from the model. One could therefore naïvely assume that the the arising Rashba terms in Eq. (2.86) (pg. 27) would destroy the topology of graphene under irradiation with deflected linearly polarised light. The above observation, however, indicates that graphene remains a $\mathbb{Z}_2$-topological insulator, even under an angular deflection. This is attributed to the oscillatory behaviour of the electric field. The z-component of the electric field and therefore the Rashba terms vanish when averaged over an entire time period $t \in [0, 1/\omega)$.

This section has only studied possible Rashba effects as the result of Eq. (2.86) (pg. 27). As computed by Sun at al. [115], higher-order Rashba terms can lead to a significant light-induced Rashba effect. The incorporation of such terms into the model of this thesis is left to future work. Instead, the remainder of this chapter will focus on lower frequencies of the irradiated light.

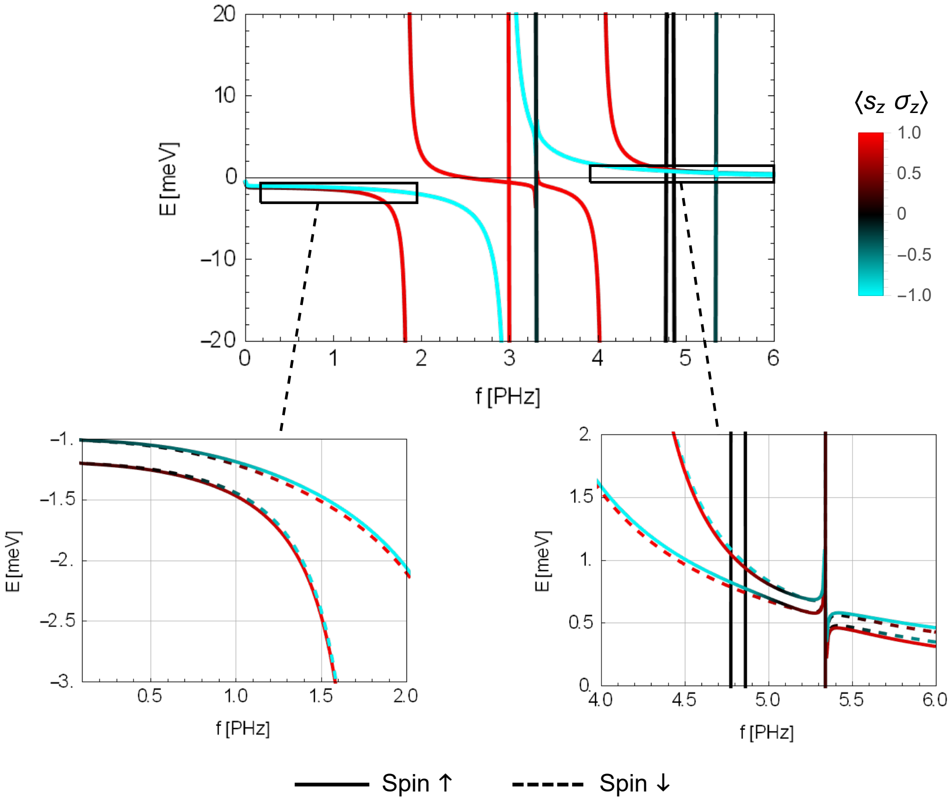

Figure 4.19: Changes to valence and conduction band under irradiation with a not perfectly perpendicular light source; A deflection of the incoming laser beam by $\alpha = 5°$ leads to a qualitatively mostly similar behaviour as for perfectly perpendicular light in Figs. 4.11g and 4.14. The only notable difference are some additional Floquet energies that stem from the additionally included s- and $\mathrm{p}_{x/y}$-orbitals that couple weakly to the other bands. Two intervals have been zoomed-in, to better compare them to Fig. 4.14.

4.3 Lower Frequencies

The frequencies considered thus far have been in the PHz range and therefore correspond to energies of multiple eV. Frequencies around $f = 300\,\mathrm{PHz}$, i.e. a wavelength of $\lambda \approx 100\,\mathrm{nm}$, correspond to an energy of $E_{\mathrm{photon}} \approx 12.4\,\mathrm{eV}$. Since this is above the ionisation energy $E_{\mathrm{Ion}} = 11.26\,\mathrm{eV}$ of elemental carbon [116], this section will instead focus on lower frequencies. First, the visible and ultraviolet spectrum will be considered, then low THz frequencies will be studied. Since the visible spectrum (0.4 - 0.8 PHz) is well below the resonance frequencies, the most important effects on fully periodic graphene will stem from multi-photon processes (cf. [117]). It is therefore necessary to consider a higher Floquet order N than in the previous section where even $N = 1$ was often sufficient for the results to converge.

This section is divided into two parts. Section 4.3.1 will study the visible and ultraviolet spectrum. Then, section 4.3.2 will focus on low THz frequencies.

4.3.1 Visible and Ultraviolet Light

As indicated by perturbation theory, multi-photon processes become weaker with higher order. Thus, the previously considered field strength of $E_0 = 0.8\,\mathrm{V/nm}$ is too weak to properly study the qualitative effects of low frequencies on the graphene sample. For this reason, this section will consider a field strength of $E_0 = 5\,\mathrm{V/nm}$.

As discussed in the context of Fig. 4.5b (pg. 99), the width of the band gap near the resonances scales quadratically with the field strength. The same behaviour has been observed for all phenomena of this section, i.e. band gaps and energetic shifts at $E_0 = 1\,\mathrm{V/nm}$ are of approximately 0.04 times the magnitude of those at $E_0 = 5\,\mathrm{V/nm}$. Even though $E_0 = 5\,\mathrm{V/nm}$ lies almost an order of magnitude above the field strengths in realistic experimental situations (cf. [109]), it will therefore be assumed that the results for lower field strengths are qualitatively comparable to those in this section.

Fig. 4.20 depicts the range of frequencies belonging to the wavelengths between $\lambda = 750\,\mathrm{nm}$ (deep, visible red) and 100 nm (upper end of UV). A Floquet order of $N = 4$, i.e. an emission and absorption of up to four photons is taken into account. As can be seen from the shading, the sublattice-real spin correlation remains intact for circular polarisation, but disappears for linear polarisation, similarly to Fig. 4.16. Only closer inspection of the energies at $f = 2.5\,\mathrm{PHz}$ would again reveal a shading, similar to Fig. 4.17.

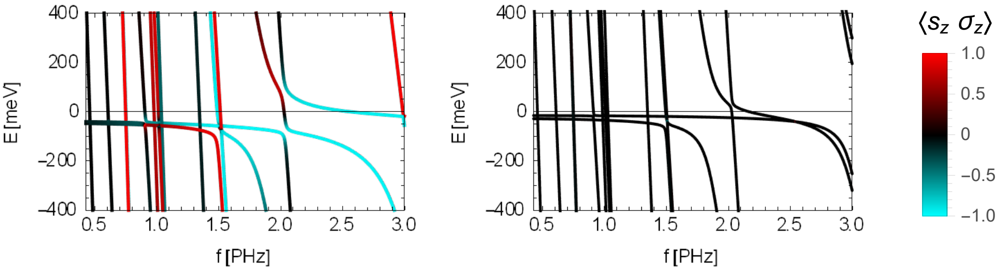

(a) Circular polarisation (b) Linear polarisation

Figure 4.20: Floquet energies at the K-point under irradiation with circularly (a) and linearly (b) polarised light in the visible and ultraviolet spectrum at $E_0 = 5\,\mathrm{V/nm}$ according to Eq. (4.1). While for circular polarisation the correlation between sublattice and real spin is notable for almost all frequencies, for linear polarisation it can only barely be observed if at all.

In the previous sections, the effects of the light field on the quasi-energies have been most notable near the resonances at approximately $f_1 = 1.8\,\mathrm{PHz}$, $f_2 = 3\,\mathrm{PHz}$ and $f_3 = 4\,\mathrm{PHz}$. Fig. 4.20 shows new notable effects when $f = f_i/2$ for $i \in \{1, 2, 3\}$, i.e. $f = 0.9\,\mathrm{PHz}$, $f = 1.5\,\mathrm{PHz}$ or $f = 2\,\mathrm{PHz}$. Similar to how the phenomena of the previous section have been related to single-photon processes, the avoided crossings in Fig. 4.20 can be related to two-photon processes, as they involve the coupling between lines of photon expectation values $\langle\Gamma\rangle = 0$ and $\langle\Gamma\rangle = -2$. As discussed in the context of Eqs. (4.5) and (4.6) (pg. 104), such a coupling occurs in fourth order of perturbation theory. Consequently, it is suppressed by the square of the energy difference to the energetically closest (-1)-photon state.

Recall that the magnitude of the gaps between the Floquet energies scales quadratically with the field strength and is therefore enhanced almost 40-fold compared to those generated in the previous section at field strength $E_0 = 0.8\,\mathrm{V/nm}$. At similar field strengths, the magnitude of the gaps in Fig. 4.20 would therefore be in the sub-meV regime, which would make it difficult to distinguish the effects of the electric field from the intrinsic, SOI-induced band gap. Analogously, to see couplings between p- and d-bands for frequencies lower than $f = 0.9\,\mathrm{PHz}$, an even higher field strength would be necessary. Thus, Fig. 4.20 shows no visible interactions between p- and d-bands for $0.5\,\mathrm{PHz} \leq f \leq 0.9\,\mathrm{PHz}$. However, as will be shown in the next subsection, new effects can be observed for $f < 0.1\,\mathrm{PHz}$, as the frequency approaches the resonances between two p-bands.

4.3.2 THz Frequencies: Floquet Energies at the K-point

At frequencies below $f = 0.1\,\mathrm{PHz} = 100\,\mathrm{THz}$, the coupling between different p-bands dominates compared to the coupling between p- and d-bands. As a result, the effects that will be observed in this subsection will be vastly different from those in the previous sections. d-orbitals will nonetheless play an important role because of the polarisation dependence of their coupling to the p-orbitals.

For the graphene model of this thesis, a new, oscillatory behaviour arises at low THz frequencies. Fig. 4.21a shows the frequency-dependent Floquet energies of valence and conduction band and their replica bands under irradiation with circularly polarised light with frequencies up to $f = 100\,\mathrm{THz}$. No frequencies below $f = 7\,\mathrm{THz}$ are depicted, as they would need a higher Floquet order to converge.
Fig. 4.21b zooms in on the 0-photon valence and conduction band. As will be explained later in this subsection, the notion “0-photon band” is not entirely correct for these bands, as their photon expectation value $\langle\Gamma\rangle$ is zero only for some frequency intervals. However, they will still be referred to as 0-photon bands, since they satisfy $\langle\Gamma\rangle \approx 0$ for frequencies $f > 50\,\mathrm{THz}$.
The 0-photon valence and conduction band exhibit oscillations that, in turn, lead to a band gap that oscillates with the frequency as depicted in Fig. 4.21c. Whenever the gap becomes small, the bands become localised on one respective sublattice, as can be seen from the orbital composition of the conduction band in Fig. 4.21d for spin-up and 4.21e for spin-down.

The sublattice localisation in Fig. 4.21d and 4.21e differs slightly for both spins. Like in section 4.2.1, this is a consequence of of the angular momentum of the light. By the same means, spin degeneracy is lifted as well. This becomes particularly notable whenever valence and conduction band approach one another, as depicted in Fig. 4.22. Moreover, at $f = 20.25\,\mathrm{THz}$, the spin-down bands seem to cross. To understand this behaviour, it is necessary to first understand the cause of the oscillatory behaviour.

The oscillations in Fig. 4.22 are caused by the direct coupling of valence and conduction band to one another. Even though there is only a minor contribution from the d-orbitals to either of them, the coupling between p- and d-orbitals will be shown to be one of the two factors that give rise to the oscillations. In the following, a toy model that only describes valence and conduction band will be employed.

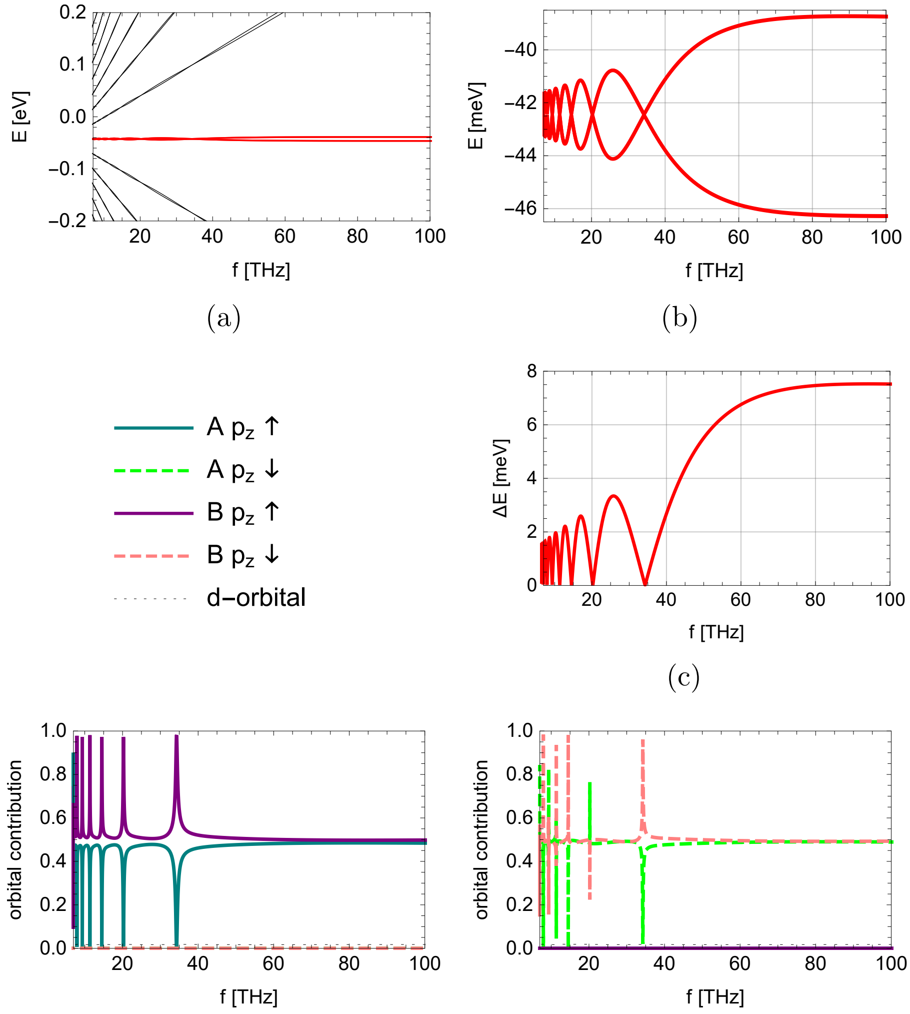

(a) (b)

(c)

(d) (e)

Figure 4.21: Frequency-dependent Floquet energies of graphene at the K-point under irradiation with circularly polarised light of THz frequencies, with a field strength of $E_0 = 5\,\mathrm{V/nm}$ and a Floquet order of $N = 16$; The plethora of black lines in (a) shows several replicas of valence and conduction band. The 0-photon valence and conduction band (red) are depicted separately in (b). (c) shows the gap between them. (d) and (e) depict the orbital composition of the conduction band for spin-up and -down, respectively. From the spikes, a notable sublattice-real spin correlation can be concluded to only occur when the gap in (c) becomes small. No frequencies below $f = 7\,\mathrm{THz}$ are depicted, since a higher Floquet order would be necessary for the states to converge.

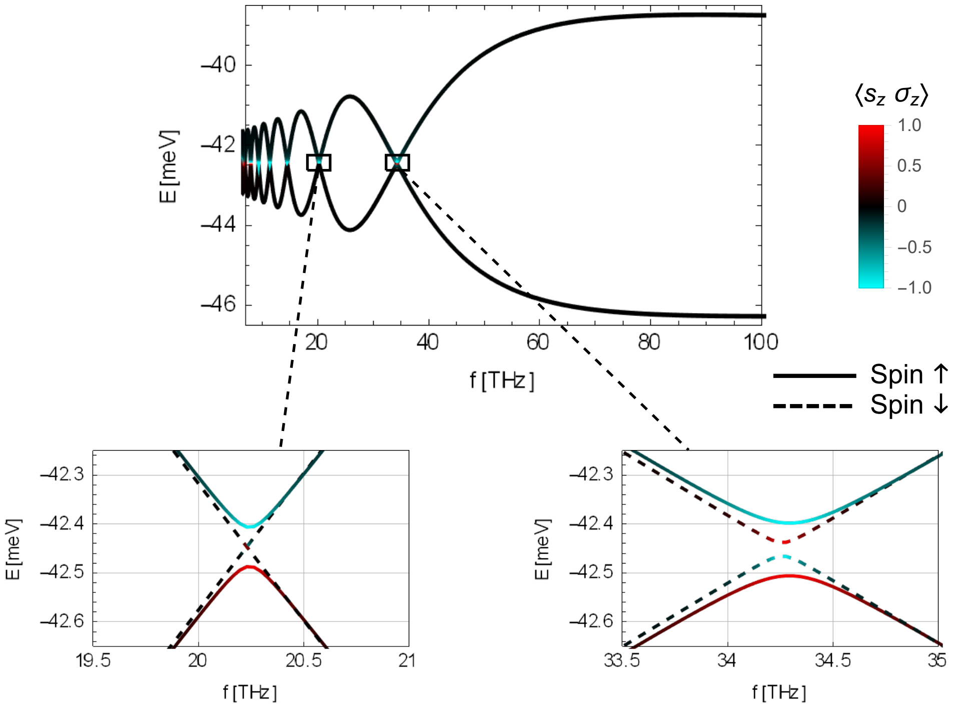

Figure 4.22: Zoom of the frequency-dependent Floquet energies of Fig. 4.21b; Whenever the energies come close, their polarisation $\langle s_z \sigma_z \rangle$ between real and sublattice spin increases, indicating that SOI couples the energies to one another. Spin degeneracy is lifted because of how circularly polarised light couples to the eigenstates of graphene.

Based on the discussions of section 3.3, a model that describes only valence and conduction band coupled by circularly polarised light can be written as

$$H_\sigma(t) := 2M \cdot \sigma_z \sin(\omega t) + C \cdot (\sigma_x \cos(\omega t) + \sigma_y \sin(\omega t)) \tag{4.13}$$

with a sublattice potential M and a coupling term C, both of which are real-valued. The coupling term equals c_1 as it was defined in Eq. (3.37) (pg. 85). It describes the onsite coupling of the electric field. The sublattice potential[7] M equals half the value d_1 defined in Eq. (3.53) (pg. 90), where the factor 1/2 serves to compensate for the preceding 2 in front of the $M \cdot \sigma_z$ in Eq. (4.13). The parameters are thus

$$M \approx \tilde{E}_0 \cdot 34.5\,\text{meV} \qquad \text{and} \qquad C \approx \tilde{E}_0 \cdot 3\,\mu\text{eV}, \tag{4.14}$$

---

[7] Note that the letter M has been used in section 3.3.2 as well, but with a slightly different meaning. It has been repurposed here, since it is the standard symbol for a sublattice potential in most literature.

where $\tilde{E}_0$ denotes the number value of the electric field strength E_0 in V/nm. Note that $H_\sigma(t)$ does not depend on $\vec{k}$, since it shall only serve as a toy model at the K-point.[8] Moreover, it has no time-independent terms, in particular no time-independent sublattice potential. As a result, it has no static band gap. However, a band gap does arise in the Floquet band structure, as can be seen in Fig. 4.23.

The Floquet Hamiltonian for Eq. (4.13) consists of the Fourier components

$$H_1 = \begin{pmatrix} \mathrm{i}M & C \\ 0 & -\mathrm{i}M \end{pmatrix} \qquad \text{and} \qquad H_{-1} = H_1^\dagger. \tag{4.15}$$

All other Fourier components are zero. The overall Floquet Hamiltonian is then of the shape

$$H_{\mathrm{F}\sigma} = \left(\begin{array}{c|c|c|c|c} \ddots & \vdots & \vdots & \vdots & \iddots \\ \hline \cdots & \begin{matrix} -\hbar\omega & 0 \\ 0 & -\hbar\omega \end{matrix} & \begin{matrix} \mathrm{i}M & C \\ 0 & -\mathrm{i}M \end{matrix} & 0 & \cdots \\ \hline \cdots & \begin{matrix} -\mathrm{i}M & 0 \\ C & \mathrm{i}M \end{matrix} & \begin{matrix} 0 & 0 \\ 0 & 0 \end{matrix} & \begin{matrix} \mathrm{i}M & C \\ 0 & -\mathrm{i}M \end{matrix} & \cdots \\ \hline \cdots & 0 & \begin{matrix} -\mathrm{i}M & 0 \\ C & \mathrm{i}M \end{matrix} & \begin{matrix} \hbar\omega & 0 \\ 0 & \hbar\omega \end{matrix} & \cdots \\ \hline \iddots & \vdots & \vdots & \vdots & \ddots \end{array}\right), \tag{4.16}$$

where straight lines have been added to distinguish the Fourier components. For $M = C = 0$, the matrix (4.16) only has diagonal entries in the form of $n\hbar\omega$ with $n \in \mathbb{Z}$. Accordingly, the first graph in Fig. 4.23 only depicts unperturbed straight lines. For $M \neq 0$, the different Floquet replica bands are coupled to one another. With Floquet order $N = 1$, the Floquet Hamiltonian is a 6×6-matrix and only consists of the entries that are written explicitly in Eq. (4.16). Its eigenvalues then are

$$\epsilon \in \{-\sqrt{2M^2 + (\hbar\omega)^2},\ 0,\ +\sqrt{2M^2 + (\hbar\omega)^2}\}. \tag{4.17}$$

In the static limit $\omega \to 0$, they become $-M$, 0 and $+M$. For $C = 0$, the eigenvalues in the static limit have been computed in appendix C. They are

$$\epsilon_m = -2M \cos\left(\frac{m\pi}{2N+2}\right) \qquad \text{with } m \in \{1, 2, ..., 2N+1\}, \tag{4.18}$$

where $N \in \mathbb{N}$ is the Floquet order.

---

[8] The model can be adapted to describe the band structure in a vicinity around the K-point by adding a term $k_x\sigma_x + k_y\sigma_y$, to arrive at a $\vec{k}$-dependent model as used e.g. by Broers and Mathey [41, 42].

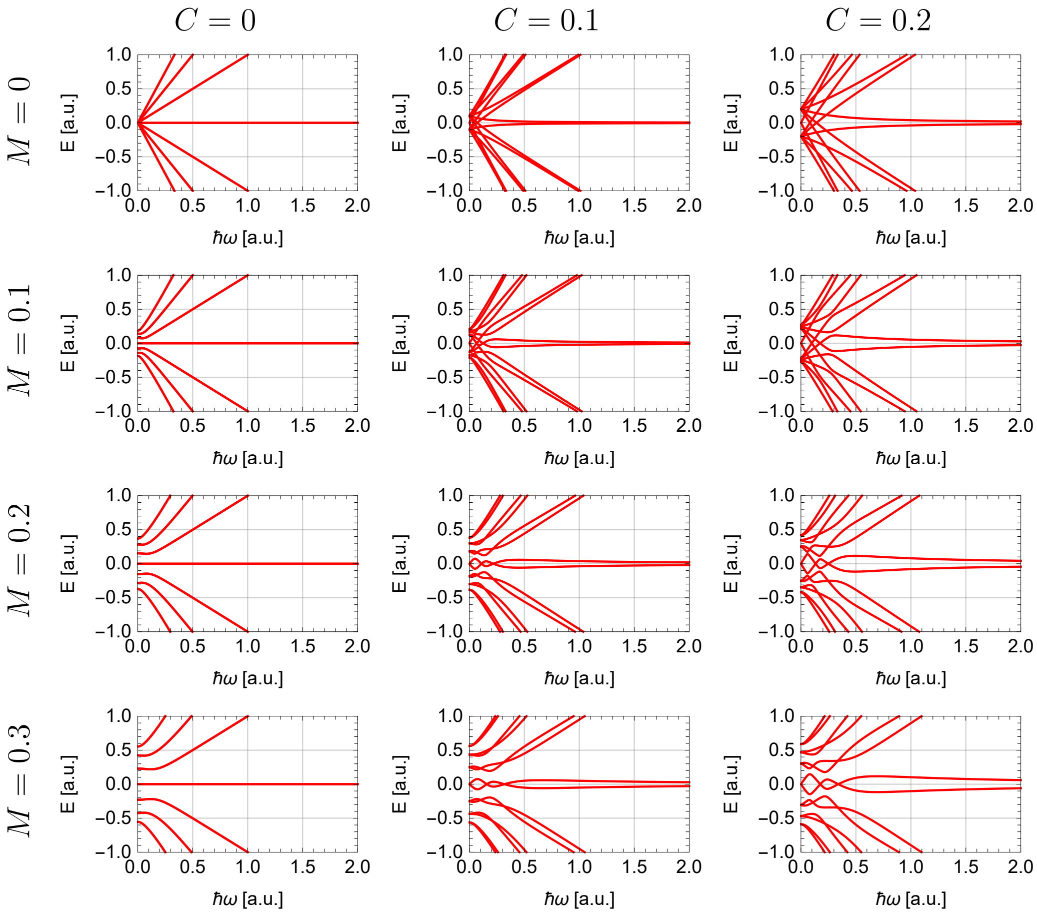

Figure 4.23: Toy model Floquet energies for Floquet order $N = 3$; Depending on the parameters M and C, the toy model (4.13) exhibits different interactions between the replica bands. For increasing M, the energy difference of the energies in the limit $\hbar\omega \to 0$ increases. For increasing C, the degeneracy between the bands is lifted, and avoided crossings become more prominent. In the limit $\omega \to 0$, the Floquet order is insufficient for the energy values to converge towards the correct solutions of the time-dependent system. Their depiction only serves the better understanding of the processes involved.

The eigenvalues can be seen for $N = 3$ in the $C = 0$ column in Fig. 4.23. With increasing $\hbar\omega$, the energies spread further apart, similarly to those for $N = 1$ given in Eq. (4.17). Since $M \neq 0$ denotes a sublattice potential via a matrix σ_z, every eigenstate is perfectly localised on either sublattice A or B. The Floquet energies on both sublattices are identical, giving rise to a two-fold degeneracy of the eigenvalues in Eqs. (4.17) and (4.18).

Before discussing the effects of a non-trivial coupling term C, the opportunity will be used to compare the Floquet spectrum (4.18) to the explicitly time-dependent solutions of the Schrödinger equation for the Hamiltonian (4.13) with $C = 0$. The Schrödinger equation

$$\mathrm{i}\hbar\frac{\partial}{\partial t}\vec{\psi}(t) = H_{\sigma,C\to 0}(t)\vec{\psi}(t) \quad \text{with} \quad H_{\sigma,C\to 0}(t) = 2M \cdot \sigma_z \sin(\omega t) \tag{4.19}$$

has two solutions

$$\vec{\psi}_1(t) = c_1 \cdot \begin{pmatrix} 1 \\ 0 \end{pmatrix} e^{+\frac{2\mathrm{i}M\cos(\omega t)}{\hbar\omega}} \qquad \text{and} \qquad \vec{\psi}_2(t) = c_2 \cdot \begin{pmatrix} 0 \\ 1 \end{pmatrix} \cdot e^{-\frac{2\mathrm{i}M\cos(\omega t)}{\hbar\omega}} \tag{4.20}$$

with complex coefficients $c_{1/2}$. The vector $\vec{\psi}_1(t)$ satisfies

$$\vec{\psi}_1(t) = \underbrace{e^{+\frac{2\mathrm{i}M(\cos(\omega t)-1)}{\hbar\omega}}}_{=:e^{-\frac{\mathrm{i}}{\hbar}\epsilon(t)t}} \cdot \vec{\psi}_1(0), \tag{4.21}$$

where $\epsilon(t)$ is the eigenvalue of the time-evolution operator as it was specified in Eq. (2.187) (pg. 67). Based on Eq. (4.21), $\epsilon(t)$ is defined as

$$\epsilon(t) = -\frac{2M(\cos(\omega t) - 1)}{\omega t}. \tag{4.22}$$

At the time of a full period $t = \tau = 2\pi/\omega$ and in the limit $\omega \to 0$, this reshapes to

$$\epsilon(\tau) = 0 = \epsilon_{N+1}, \tag{4.23}$$

i.e. it corresponds only to the ϵ_m with $m = N+1$ in Eq. (4.18). Based on the discussions of section 2.6.5, one would now assume that the other ϵ_m could be obtained via

$$\epsilon_m = \epsilon_{N+1} + l\hbar\omega \tag{4.24}$$

for some $l \in \mathbb{Z}$. While this would be true for Floquet quasi-energies with $\omega \neq 0$, the energies ϵ_m in Eq. (4.18) were computed for $\omega = 0$. The relation (4.24) therefore is not applicable.

This observation illustrates a problem with the order of limit operations that have been performed. Recall that in the derivation of Eq. (4.18), the Fourier decomposition (4.15) has been performed before the limit operation $\omega \to 0$ was taken. However, the latter operation denotes the transition to the time-independent system. If one were to first take the limit, then the Hamiltonian would reshape to

$$\lim_{\omega\to 0} H_{\sigma,C\to 0}(t) = \lim_{\omega\to 0}(2M \cdot \sigma_z \sin(\omega t)) = 0 \cdot \mathbb{1}_2. \tag{4.25}$$

Consequently, the Floquet Hamiltonian in Eq. (4.16) would only consist of zeroes as well. Its eigenvalues $\epsilon_m = 0$ for all m would therefore be in agreement with Eq. (4.23). This demonstrates that the Floquet matrix does not converge in the limit $\omega \to 0$. However, it does converge for any $\omega \neq 0$. For $\omega = 0$, the eigenvalues $\epsilon_m \neq 0$ in Eq. (4.18) are the instantaneous eigenvalues of $H_{\sigma,C\to 0}(t_0)$ at a fixed time t_0.

Even though the Floquet matrix in Eq. (4.16) does not adequately represent the time-independent limit, it is still a correct analytical continuation of the Floquet matrices[9] for the system with $\omega \neq 0$. It will therefore be used for predictions despite its shortcomings.

For $M = 0$ and $C \neq 0$, the Floquet Hamiltonian $H_{\mathrm{F}\sigma}$ couples states that correspond to n photons and sublattice A to eigenstates with either $n-1$ or $n+1$ photons on sublattice B. Importantly, not all states are coupled to one another. E.g. $H_{\mathrm{F}\sigma,M\to 0}$ couples the state $|A,0\rangle$ only to the state $|B,-1\rangle$, where $|A/B,n\rangle$ denotes a state on sublattice A/B with photon number n. Similarly, the state $|B,0\rangle$ is coupled only to the state $|A,+1\rangle$. This can be deduced from Tab. 3.2 like it has been done in the previous sections. Since the eigenvalues of the matrix $H_{\mathrm{F}\sigma,M\to 0}$ are coupled only in pairs of two, and since all matrix entries are identical with value C, the eigenvalues are

$$\epsilon_{n,\pm}(\omega) = n\hbar\omega + \underbrace{\frac{\hbar\omega}{2} \pm \sqrt{C^2 + \frac{(\hbar\omega)^2}{4}}}_{=:p_\pm(\omega)}, \tag{4.26}$$

where n assumes integer values with $-N \leq n < N$ for the Floquet order N. Note that in the static limit,

$$\lim_{\omega\to 0} \epsilon_{n,\pm} = \pm C. \tag{4.27}$$

---

[9] The Floquet matrices for $\omega \neq 0$ have not been computed analytically. However, Fig. 4.23 shows that their eigenvalues converge to Eq. (4.18) in the limit $\omega \to 0$.

The respectively N-fold degenerate $\epsilon_{n,+}$ and $\epsilon_{n,-}$ correspond to eigenstates

$$\psi_{n,\pm}(\omega) = \frac{1}{\sqrt{p_\pm^2(\omega) + C^2}} \left(-p_\pm(\omega) \cdot |A, n\rangle + C \cdot |B, n+1\rangle \right). \tag{4.28}$$

In the static limit, they reshape to

$$\lim_{\omega \to 0} \frac{1}{\sqrt{2}} \left(\pm |A, n\rangle + |B, n+1\rangle \right), \tag{4.29}$$

i.e. the states have equal contributions of both sublattices. Due to the finite dimension of the matrix $H_{\mathrm{F}\sigma}$, the two states $|A, -N\rangle$ and $|B, N\rangle$ are not coupled to any other states. They therefore have the quasi-energies

$$\epsilon_{N,\pm}(\omega) = \pm N\hbar\omega \tag{4.30}$$

with their corresponding states

$$\psi_{N,+}(\omega) = |B, N\rangle \qquad \text{and} \qquad \psi_{N,-}(\omega) = |A, -N\rangle. \tag{4.31}$$

They arise as a result of the truncation of the Floquet system and can be interpreted as edge states to it, similarly to the definition of edge states for spatial lattices, but for a temporal lattice instead. The truncation is artificial and does not occur in an actual physical system. Hence, the states $\psi_{N,\pm}(\omega)$ are artefacts and will not be studied in further detail. Since they correspond to $(\pm N)$-photon states, their effect on the 0-photon band structure is negligible for sufficiently high Floquet orders N. For a more detailed study the Floquet band structure of the two-level system, see e.g. [118–120].

The behaviour of the Floquet energies $\epsilon_{n,\pm}$ can be seen in the $M = 0$ row in Fig. 4.23. At $\hbar\omega = 0$, they only assume the three values $-C$, 0 and $+C$. Beyond those points, the energies behave nearly linearly with multiples of $\hbar\omega$.

Neither $M \neq 0$ nor $C \neq 0$ alone suffices to give rise to an oscillatory behaviour like in Fig. 4.22. As Fig. 4.23 shows, the behaviour only arises due to the combined effect of both $M \neq 0$ and $C \neq 0$. For $M \neq 0$, the Floquet energies are split into $2N + 1$ pairs that are degenerate with respect to sublattice spin. The parameter $C \neq 0$ then lifts this degeneracy by coupling states that belong to different sublattices and photon numbers to one another. Moreover, this coupling leads to avoided crossings between the energies. The multitude of these avoided crossings is what ultimately gives rise to the oscillatory behaviour. As can be seen in Fig. 4.23 for $C = 0.1$, the energy distances between the Floquet quasi-energies increase with M.

For a field strength of $E_0 = 5\,\mathrm{V/nm}$ like in Figs. 4.21 and 4.22, the parameters assume the values $M = 172.5\,\mathrm{meV}$ and $C = 14.9\,\mu\mathrm{eV}$. Thus, M is significantly larger than C. As discussed above, larger values of M increase the differences between the Floquet energies. The relation $M \gg C$ therefore explains the relative distance of the Floquet energies in Fig. 4.21a from one another.

The only property of Fig. 4.22 left to explain is that the spin-down energies seem to cross at $f = 20.25\,\mathrm{THz}$. To understand this, consider Fig. 4.24. In the figure, the oscillating Floquet energies of the toy model have been shaded based on their photon expectation values $\langle \Gamma \rangle$. The bands assume a shade of orange or azure whenever they cross. This implies that the states no longer exclusively consist of components that correspond to the same photon numbers. Since SOI acts only between components that belong to the same photon number, it is therefore strongly suppressed. As a consequence, the matrix element becomes so small that the spin-down bands seem to cross in Fig. 4.22. However, due to higher-order couplings, the SOI matrix element is never exactly zero. Hence, the energies are bound to exhibit an avoided crossing after all, albeit one that is smaller than the double point precision of the numerical computations. The spin-up bands are energetically further apart, as has been explained with the effects of circularly polarised light in section 4.2. As a consequence, the spin-down bands in Fig. 4.22 appear to be crossing while the spin-up bands show a clear gap.

Since the processes in this subsection involve direct couplings between p-bands, it is necessary to also consider couplings away from the K-point. This will be done in the next subsection.

4.3.3 THz Frequencies: Band Structure Around the K-point

At low frequencies, the replica bands of the graphene band structure are energetically close to one another. As a result, they intersect in the vicinity of the K-point, as can be seen for $f = 35\,\mathrm{THz}$ in Fig. 4.25. The main contribution to the band structure in Fig. 4.25 is the oscillating sublattice potential of Eq. (4.13). Since a $\vec{k}$-dependence drastically increases the complexity of the model (4.13), the analytical computations of this subsection will be restricted to a spinless model with only $\mathrm{p_z}$-orbitals. Nonetheless, the figures will correspond to the original spinful model that includes $\mathrm{p_z}$- and $\mathrm{d_{xz/yz}}$-orbitals.

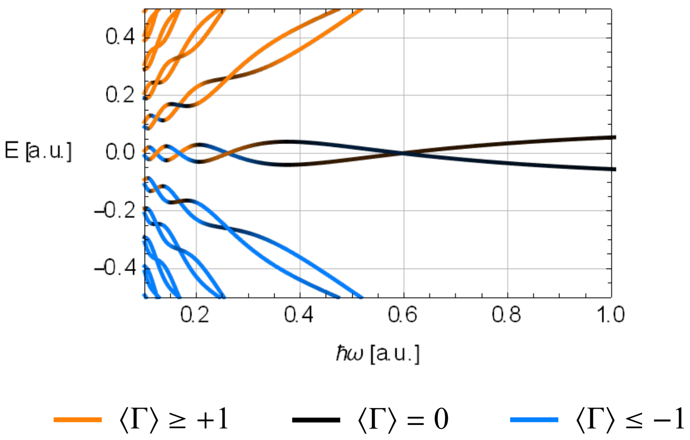

Figure 4.24: Floquet bands of the toy model (4.13) as a function of $\hbar\omega$. The other parameters are $M = 0.5$ and $C = 1/10$ with a Floquet order of $N = 16$. The bands around $E = 0$ exhibit qualitatively the same oscillatory behaviour as in the spinful graphene model in Fig. 4.21a. No results below $\hbar\omega < 0.1$ are depicted, since a higher Floquet order would be necessary for them to converge. For values below $\hbar\omega = 0.4$, the photon expectation values $\langle\Gamma\rangle$ of the bands around $E = 0$ vary as a function of the frequency.

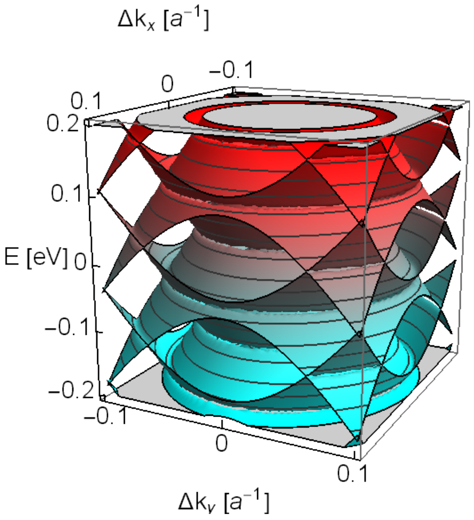

Figure 4.25: Band structure of Graphene around the K-point under irradiation with circularly polarised light of frequency $f = 35\,\mathrm{THz}$ and field strength $E_0 = 5\,\mathrm{V/nm}$; The Floquet replica bands cut one another. The colour only indicates the energy value. Since there are notable numerical artefacts whenever two bands cross, Fig. 4.26b gives a better impression on the actual crossing and anti-crossing behaviour.

In the model restricted to $\mathrm{p_z}$-orbitals, the term C of Eq. (4.13) becomes zero, since the electric field does not couple orbitals of the same n and l quantum numbers. Consequently, the only time-dependent term left in Eq. (4.13) is the oscillating sublattice potential. A similar model describing an oscillating sublattice potential has been studied in detail in the bachelor thesis of Martens [60], supervised by the author. A reproduction of his calculations regarding an oscillating sublattice potential is given in appendix D. In the following, the results of [60] that are relevant for the problem at hand will be summarised and adapted to the graphene system of this thesis.

Spinless graphene that consists only of $\mathrm{p_z}$-orbitals can be expressed similarly to the Haldane model in Eq. (2.87) (pg. 30) as

$$H_0(\vec{k}) = \begin{pmatrix} 0 & h(\vec{k}) \\ h^\dagger(\vec{k}) & 0 \end{pmatrix} \tag{4.32}$$

with functions $h(\vec{k})$ that satisfy the symmetry of the honeycomb lattice and become zero only at the K-points. An oscillating sublattice potential[10] of the form

$$H'(t) = \begin{pmatrix} V\cos(\omega t) & 0 \\ 0 & V\sin(\omega t) \end{pmatrix} \tag{4.33}$$

with perturbation strength V then leads to a Floquet band structure similar to that in Fig. 4.25. It is shown in appendix D that, for a Floquet order of $N = 1$, the toy model defined by Eqs. (4.32) and (4.33) leads to three main observations:

1. Valence and conduction band touch at the K-point ($h(\vec{k}) = 0$). In Fig. 4.25, the K-point is at $\Delta\vec{k} = 0$. It cannot be seen in the figure, since other bands are in front of it. Instead, see Fig. 4.26 for a depiction that only depends on Δk_x.

2. Valence and conduction band exhibit avoided crossings with their Floquet replicas when $|h(\vec{k})| = \hbar\omega/2$. In Figs. 4.25 and 4.26, this occurs at approximately $|\Delta\vec{k}| = 0.025\,\mathrm{a}^{-1}$.

3. Valence and conduction band touch when $|h(\vec{k})| = \hbar\omega$. In Figs. 4.25 and 4.26, this occurs at approximately $|\Delta\vec{k}| = 0.05\,\mathrm{a}^{-1}$.

---

[10] The sublattice potential $H'(t)$ Martens has used differs from that in Eq. (4.13) via a phase between the respective time-dependencies of the sublattice components. This reproduction will keep this phase, to faithfully reproduce the results of [60]. Both toy models lead to a similar qualitative behaviour.

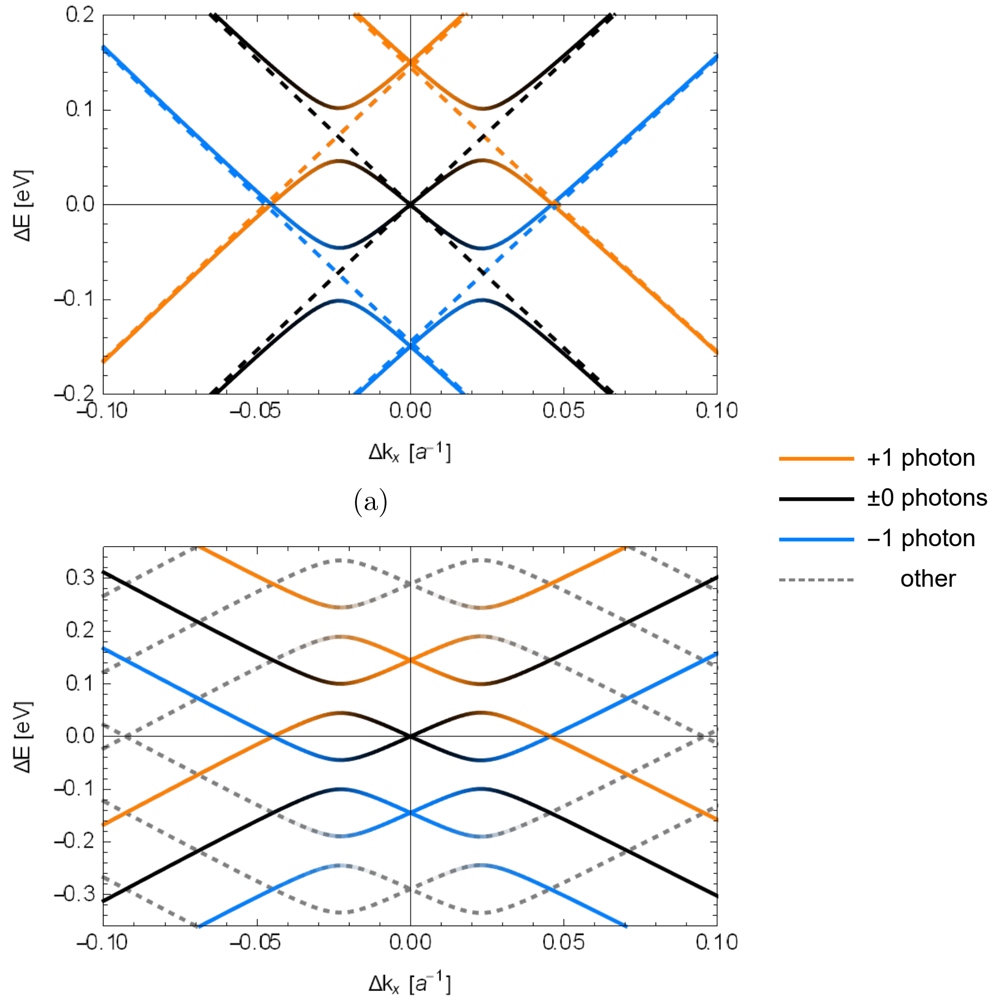

(a)

(b)

Figure 4.26: Cut of the Floquet energies $E = \Delta E - 181.02\,\text{meV}$ of graphene around the K-point under irradiation with circularly polarised light of frequency $f = 35\,\text{THz}$ and field strength $E_0 = 0.8\,\text{V/nm}$; The colours are according to the photonic expectation values. (a) At a Floquet order $N = 1$, the (±1)-photon replica bands exhibit avoided crossings with the 0-photon valence and conduction band. The dashed black lines show the the behaviour of the Floquet replica bands in the field-free limit $E_0 = 0$. (b) At $N > 1$, the Floquet replica bands exhibit avoided crossings not only with the 0-photon bands, but also with one another. The dashed grey lines denote $\pm n$-photon states with $n > 1$

Observations 1 and 3 do not hold true in the actual spinful system with d-orbitals, since SOI and onsite coupling lead to avoided crossings. However, these avoided crossings are significantly smaller than the one described in observation 2, as can be seen in Fig. 4.26 that depicts the spinful system with d-orbitals.

Fig. 4.26a depicts the band structure as a function of only Δk_x for a Floquet order of $N = 1$. The dashed lines in the figure represent the Floquet energies in the field-free limit $E_0 \to 0$. The colours illustrate the photon expectation values $\langle \Gamma \rangle$ of the respective bands. From this shading, one can see how the avoided crossings of observation 2 above involve an exchange of photons. At $|\Delta \vec{k}| = 0.05\,\mathrm{a}^{-1}$, the valence and conduction band touch as described in observation 3. Due to the onsite coupling that is not included in the toy model, those crossings are actually avoided crossings as well. However, the matrix element coupling them is small, since they are a (+1)- and a (−1)-photon state. As explained in the context of Eqs. (4.5) and (4.6) (pg. 104), such bands are coupled only in fourth- and higher-order perturbation theory.

These processes repeat in higher Floquet order, as is depicted in Fig. 4.26b. The result is a multitude of replica bands with dents near $|\Delta \vec{k}| = 0.025\,\mathrm{a}^{-1}$. This behaviour is radially symmetric and gives rise to Fig. 4.25.

Broers and Mathey [41, 42] have studied a similar similar system, albeit with a different model. They observe notable avoided crossings, not only near $|\Delta \vec{k}| = 0.025\,\mathrm{a}^{-1}$, but also whenever other replica bands cross. Moreover, they observe a significant opening of a band gap at the K-point, even at smaller field strengths than used in this thesis. Fig. 4.26 does not show any enhancement of that magnitude. This is attributed to a different choice of parameters that constitute the respective graphene systems. Furthermore, as shown in the previous subsection, the band gap oscillates due to the coupling between p- and d-orbitals.

After this chapter has studied the effects of different frequencies and polarisations on the band structure of fully periodic graphene, the next chapter will study the the edge states of graphene ribbons that are finite in one spatial direction. As a consequence of the altered topological properties of graphene, different kinds of quantum Hall effects will arise.

Chapter 5

Graphene Ribbons

As discussed in sections 4.1.2 and 4.2.3, the topological quantum numbers of graphene depend on the light it is being irradiated with. Circularly polarised light breaks time-reversal symmetry, replacing the $\mathbb{Z}_2$-topological invariant of unperturbed graphene with a $\mathbb{Z}$-topological invariant. Hence, graphene is expected to become a Chern insulator. Linearly polarised light, on the other hand, is time-reversal symmetric and therefore does not affect the $\mathbb{Z}_2$-topological quantum number. As a result, graphene is expected to remain a spin-Hall insulator.
The topological quantum numbers are bulk properties, and graphene is a band insulator. As discussed in section 2.4.4, the non-trivial topology leads to conducting edge states. These edge states and their topologically protected conducting properties will be studied in the following.

This chapter is separated into three parts. In section 5.1, the general concepts and definitions will be discussed. By introducing a unit cell that is periodic in only one spatial direction, the band structure of graphene ribbons will be studied, with and without a light field. Section 5.2 will then discuss the topological properties, in particular the edge states and the type of quantum Hall effect that is to be expected in graphene. After those discussions on topological properties, section 5.3 will discuss finite size effects that have been found to play an important role in the band structure of topologically non-trivial graphene.

5.1 Concepts and Definitions

In section 2.4.4, the emergence of edge states has been discussed for graphene that is periodic in only one spatial direction. A corresponding unit cell is

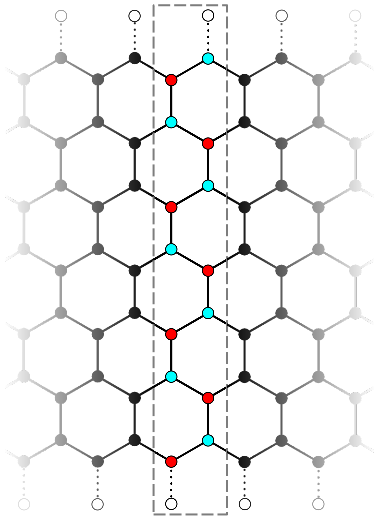

Figure 5.1: Graphene ribbon; By applying periodic boundary conditions in only one direction, the reciprocal space becomes one-dimensional. This unit cell (grey, dashed) contains 14 carbon atoms (red and cyan) and two passivating hydrogen atoms (white). The last carbon atoms before the passivation are considered the edges and belong to sublattice A (red) and sublattice B (cyan), respectively.

again illustrated in Fig. 5.1. At the lower and upper edge of Fig. 5.1, the white atoms represent hydrogen atoms that passivate the otherwise open bonds of the connected carbon atoms. The parameters associated with them in the model of this thesis are given in appendix A. The notion “edge” still relates to the uppermost cyan and the lowermost red carbon atom of Fig. 5.1.

Fig. 5.2a depicts the band structure of an unperturbed graphene ribbon, compared to the band structure under the irradiation with circularly polarised light in Fig. 5.2b. An n-photon state in Fig. 5.2 denotes a state with photon expectation value $n := \langle \Gamma \rangle$ according to definition (2.165) (pg. 62). Like in section 4.1 before, the frequency $f = 3.85\,\mathrm{PHz}$ serves as reference, with a field strength $E_0 = 0.8\,\mathrm{V/nm}$. These parameters have been found to be well-suited for example computations. For the computation of Fig. 5.2, a unit cell with 18 carbon atoms has been considered.[1] The electric field has been included identically to Eqs. (4.11) and (4.12), i.e.

$$\Phi_{\mathrm{circ}}(\vec{r}, t) = E_0 \cdot \left(x \cos(\omega t) + \left(y \cos(\alpha) + z \sin(\alpha) \right) \sin(\omega t) \right), \tag{5.1}$$

$$\Phi_{\mathrm{lin}}(\vec{r}, t)) = \sqrt{2} E_0 \cdot \left(y \cos(\alpha) + z \sin(\alpha) \right) \sin(\omega t) \tag{5.2}$$

with a vanishing angular deflection $\alpha = 0$, unless it is stated otherwise. Fig. 5.2b shows how some of the originally higher-positioned d-bands (grey) have their energies shifted downwards via Floquet formalism and thus reach

---

[1] The figures in this chapter only depict unit cells with 14 carbon atoms. Larger cells are constructed by attaching more carbon atoms in the y-direction.

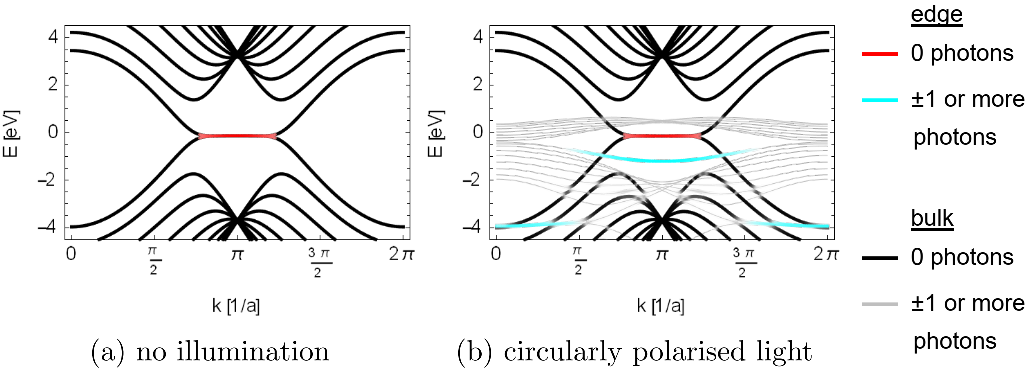

(a) no illumination (b) circularly polarised light

Figure 5.2: Effects on the band structure of a graphene ribbon irradiated by circularly polarised light; With a frequency $f = 3.85\,\mathrm{PHz}$ and a field strength $E_0 = 0.8\,\mathrm{V/nm}$, the energies of several d-bands get shifted close to those of the gap-crossing edge states. States that reside at the edge have been highlighted in red and cyan, depending on their photon expectation value. Some of the grey photonic bands couple to the black electronic bands. The cyan bands are replicas of d-band edge states.

the proximity of the gap-crossing edge states (red). Even though the d-bands do not directly affect the edges, they do couple to the bulk bands, as can be seen in particular around $E = -2\,\mathrm{eV}$ where the 0-photon bulk bands (black) appear to be interrupted. This is due to avoided crossings with the (-1)-photon d-bands similar to those discussed in the context of Fig. 3.3 (pg. 89). At those avoided crossings, the d-bands exchange a photon with the 0-photon p-bands. Fig. 5.2b also depicts cyan bands. These are (-1)-photon replicas of non-topological edge states that form between the d-bands of unperturbed graphene. As was discussed in section 4.1.2, such replica bands are expected to not contribute to the conductive properties of graphene.

Fig. 5.3 depicts a larger interval of Floquet energies for the same setup as Fig. 5.2b. Notably, Fig. 5.3 includes additional 0-photon edge states (red). They correspond to the same d-bands as the aforementioned (-1)-photon replicas and are by the same means not expected to contribute to the conducting properties of graphene. The most significant observation from Fig. 5.3 is that there are no edge states that connect the separate Floquet Brillouin zones. The first Floquet Brillouin zone defined in section 2.6.5 as the interval $(-hf/2, +hf/2] = (-7.96\,\mathrm{eV}, +7.96\,\mathrm{eV}]$. All edge states inFig. 5.3 can be related to edge states that exist in unperturbed graphene as well. Hence, none of them arise from the coupling of different Floquet Brillouin zones.

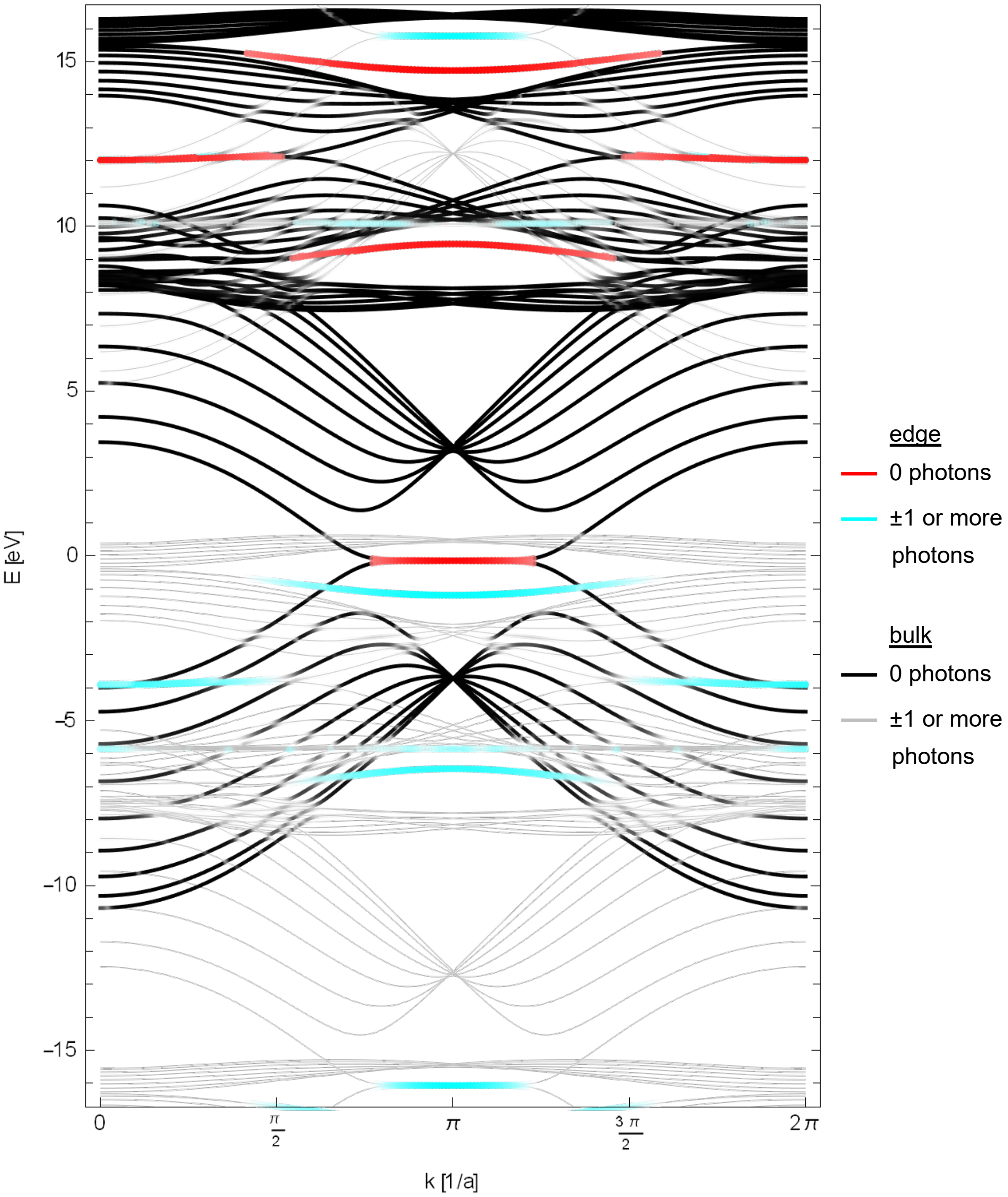

Figure 5.3: Floquet band structure of a graphene ribbon under irradiation with light of frequency $f = 3.85\,\mathrm{PHz}$ and field strength $E_0 = 0.8\,\mathrm{V/nm}$; All Floquet bands can be projected into the first Floquet Brillouin zone defined by the interval $(-hf/2, +hf/2] = (-7.96\,\mathrm{eV}, +7.96\,\mathrm{eV}]$. An interval of twice the length is depicted, to illustrate the periodicity of the Floquet bands. (± 1)-photon replicas of the red bands at $E \approx 0\,\mathrm{eV}$ can be seen in cyan at $E \approx \pm 16\,\mathrm{eV}$. Bands are shaded depending on their photon expectation values and on whether they are localised at the edges or in the bulk.

As discussed in sections 2.6.5 and 4.1.2, the absence of edge states connecting the Floquet Brillouin zones allows to treat the Floquet band structure the same way one would treat a time-independent band structure, i.e. by study of the Chern numbers of the 0-photon band structure. The Chern numbers have been computed in the previous chapter. In the following, it will be discussed how these results affect the band band structure depicted in Figs. 5.2b and 5.3. As explained in section 4.1.2, graphene is expected to be a spin-Hall or a Chern insulator, depending on the polarisation of the light field.

5.2 General Observations

Near the Fermi energy $E_\mathrm{F} = 0.181\,\mathrm{eV}$ of unperturbed graphene, Figs. 5.2b and 5.3 show the existence of edge states in graphene irradiated with circularly polarised light. This section will study these edge states for both circularly and linearly polarised light. Section 5.2.1 will study how the polarisations lead to different types of quantum Hall effects. Section 5.2.2 will then verify these results for an angular deflection of the light field, similar to section 4.2.3.

5.2.1 Quantum Hall Effects

Figs. 5.2b and 5.3, on the depicted scale, look identical for circularly and for linearly polarised light. A closer inspection, however, shows a notably different behaviour of the 0-photon edge states (red). Fig. 5.4 depicts the edge states on a smaller scale around $k = \pi/a$.

Most notably in Fig. 5.4, circularly polarised light lifts the spin degeneracy of the graphene band structure. This phenomenon has already been observed in section 4.2.1 where it was a consequence of the correlation between angular momentum and spin of the eigenstates of the unperturbed graphene Hamiltonian at the K-point. The magnitude of the spin splitting in Fig. 5.4 is smaller than of the spin splittings in section 4.2.1, since $\Delta k = 0$ does not describe the K-point in the Brillouin zone. Instead it describes the projection of an M-point, as can be seen in Figs. 2.17 (pg. 40) and 2.2 (pg. 6). At the M-points, the correlation between spin and angular momentum of the atomic orbitals is significantly weaker than at the K-points.

A second difference between the band structure of graphene irradiated with circularly polarised light in Fig. 5.4 and that of unperturbed graphene is that in Fig. 5.4 the dispersion of the edge states does not depend on the

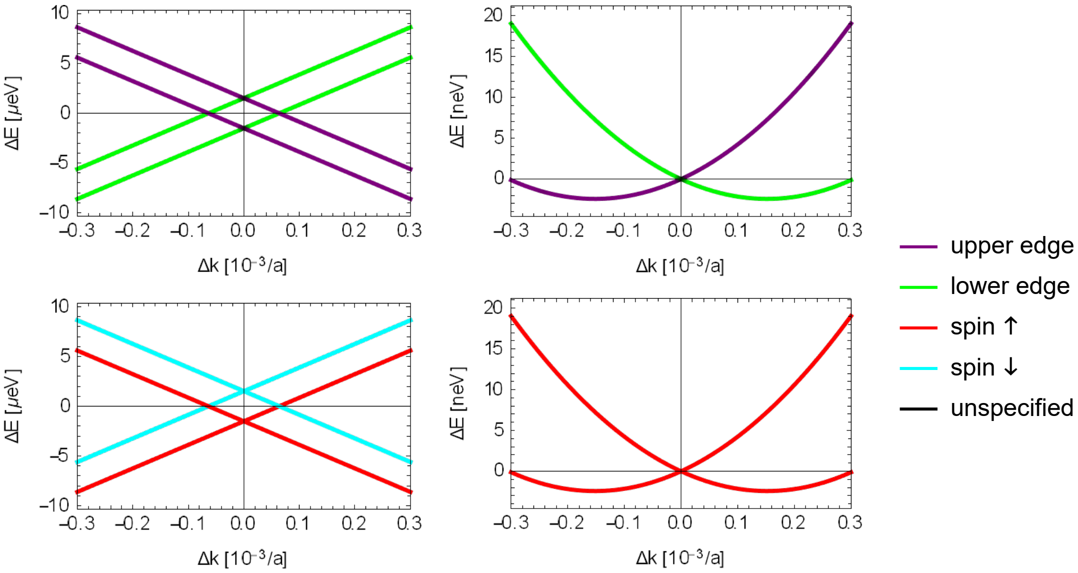

Circular polarisation,
$E = \Delta E - 0.145\,\mathrm{eV}$

Linear polarisation,
$E = \Delta E - 0.158\,\mathrm{eV}$

Figure 5.4: 0-photon edge states around $k = \pi/a$; For linear polarisation (right), the spin-degenerate energies cross similarly to unperturbed graphene. For circular polarisation (left), spin degeneracy is lifted by a competing spin-Hall and photovoltaic Hall effect as illustrated in Fig. 5.5. For linear polarisation, only spin-up bands are depicted. Spin-down states have the same dispersion, but are localised on the respectively opposite edges.

spin. Instead, it only depends on the edge, indicating a quantum anomalous Hall effect as depicted in Fig. 5.5b. More precisely, this is a photovoltaic Hall effect as discussed in section 4.1.2. This is in agreement with the predictions of Oka at al. [47] and the observations of McIver at al. [48].

The photovoltaic Hall effect also gives rise to a different explanation for the lift of spin degeneracy: Fig. 5.5 depicts both the spin-Hall effect and the photovoltaic Hall effect. For spin-up states (red), both Hall effects have the same, anticlockwise propagation direction. The spin-down currents, however, have opposing directions. Since circularly polarised light turns graphene into a Chern insulator, the intrinsic spin-Hall effect therefore supports the spin-up current, but opposes the spin-down one. As a result, the spin-down bands in Fig. 5.4 lie energetically above the spin-up ones for circular polarisation. Oka at al. only considered spinless graphene and therefore did not predict this phenomenon. It is plausible that the spin splitting was not observed by McIver at al., since its magnitude is of only a few µeV.

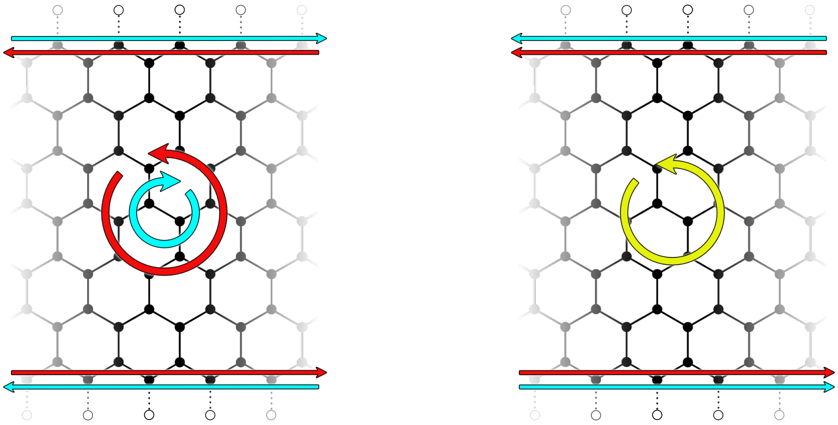

(a) Spin-Hall effect (b) Anomalous/photovoltaic Hall effect

Figure 5.5: Spin-Hall effect and anomalous Hall effect agree for one spin (here: spin-up, illustrated in red) and oppose one another for the other spin (here: spin-down, illustrated in cyan). The angular momentum of circularly polarised light (yellow) induces a photovoltaic Hall effect that competes with the intrinsic spin-Hall effect of graphene.

As opposed to circularly polarised light, linearly polarised light leaves the spin degeneracy intact, as can be seen in the right part of Fig. 5.4. Due to perturbations, the dispersion differs from that of unperturbed graphene as it was depicted in Fig. 2.23 (pg. 49). Nonetheless, Fig. 5.6 shows that the edge states (green and purple) still connect valence and conduction band in the bulk (black), indicating a quantum (spin-)Hall effect.

Recall that in section 3.1.1 the decision was made to exclude $\vec{k}$-non-diagonal terms. The latter arise from the incompatibility of a spatially homogeneous electric field with the periodic boundary conditions of the fully periodic honeycomb lattice. Since the unit cell depicted in Fig. 5.1, is finite in y-direction, it does not give rise to any such $\vec{k}$-non-diagonal terms. The agreement of the spin-Hall effect in Fig. 5.4 with the predictions of section 4.1.2 therefore legitimises the exclusion of the $\vec{k}$-non-diagonal terms in fully periodic graphene.

In section 4.2.3, the topological quantum numbers were shown to not change under an angular deflection of the light source. In the following, the observations of this subsection will be probed against a similar deflection.

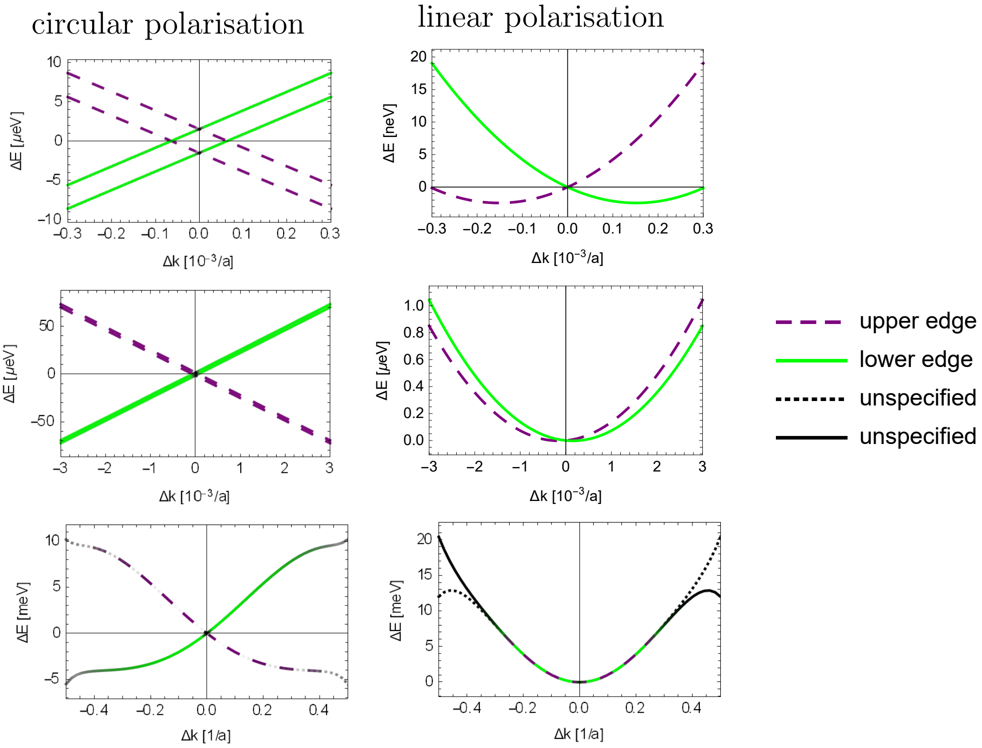

Circular polarisation,
$E = \Delta E - 0.145\,\mathrm{eV}$

Linear polarisation,
$E = \Delta E - 0.158\,\mathrm{eV}$

Figure 5.6: Floquet band structure of a graphene ribbon around $k = \pi/2a$, under irradiation with light of $E_0 = 0.8\,\mathrm{V/nm}$ and $f = 100\,\mathrm{THz}$; A zoom relates the bands in Fig. 5.4 and the red bands at the centre of Fig. 5.3. Bands are solid or dashed, to make it easier to distinguish them from one another. For linear polarisation, only spin-up states bands are depicted.

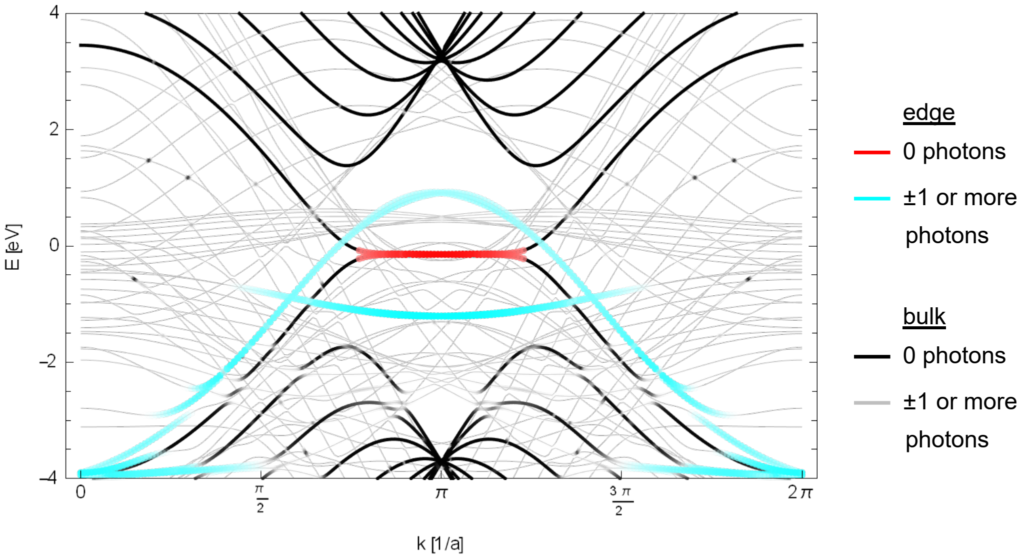

Figure 5.7: Floquet band structure of a graphene ribbon under irradiation with circularly polarised light of frequency $f = 3.85\,\text{PHz}$, field strength $E_0 = 0.8\,\text{V/nm}$ and with a deflection angle $\alpha = 5°$; At the depicted scale, both linear and circular polarisation look identical. Edge and bulk states as well as photon count are distinguished by colours. Edge states of zero photons are close to the Fermi energy.

5.2.2 Angular Deflection

As discussed in section 4.2.3, a deflection can give rise to an out-of-plane component of the electric field and therefore induce a Rashba effect that, in turn, can render graphene topologically trivial. To account for this possibility, Eqs. (5.1) and (5.2) consider a deflection angle α. Fig. 5.7 shows the resulting band structure for $\alpha = 5°$. On the depicted scale, the figure looks identical for both linearly and circularly polarised light.

In Fig. 5.7, a significantly increased number of bands can be observed compared to Fig. 5.2b. This is due to (+1)-photon replicas of s- and $\text{p}_{\text{x/y}}$-orbitals. In section 4.2.3, these additional bands were not as prominent, since only the K-point was studied. Most notably, when comparing Fig. 5.7 to Fig. 5.2, there are new (+1)-photon edge states (cyan) forming an arc around the original 0-photon edge states (red). The additional states are replicas of non-topological edge states that form between the sp^2-hybridised lower bands of unperturbed graphene. Similarly to the (−1)-photon replica d-bands in Fig. 5.2, they are expected to not affect the conducting properties of graphene.

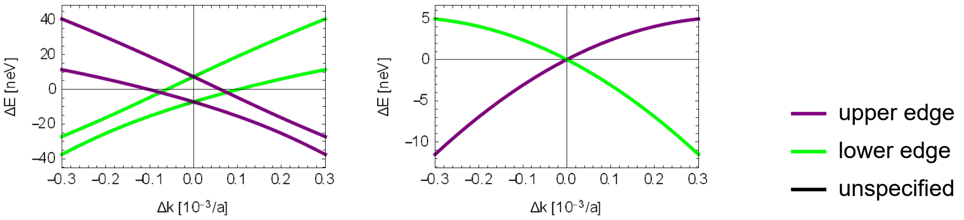

Circular polarisation,
$E = \Delta E - 0.1375\,\mathrm{eV}$

Linear polarisation,
$E = \Delta E - 0.138\,\mathrm{eV}$

Figure 5.8: Floquet band structure of a graphene ribbon around $k = \pi/a$, under irradiation with circularly and linearly polarised light of $E_0 = 0.8\,\mathrm{V/nm}$ and $f = 3.85\,\mathrm{PHz}$, with a deflection angle $\alpha = 5°$; The crossing behaviour of the bands is similar to Fig. 5.4. The dispersion is different due to couplings to s- and other p-bands.

Closer inspection of the 0-photon edge states in Fig. 5.7 again reveals a differentiation between spin-Hall effect and a quantum anomalous Hall effect, depending on the polarisation of the light field. This can be seen in Fig. 5.8 and confirms the observations of section 4.2.3 where it was predicted that graphene would remain a topological insulator even under an angular deflection of the light source. There are two notable differences between Figs. 5.4 and 5.8:

1. The spin splitting due to circularly polarised light is smaller with angular deflection than without it.

2. For linearly polarised light, the deflection leads to a change of the dispersion of the band structure. Unlike in Fig. 5.4, there are no dents at approximately $\Delta k = \pm 0.2 \cdot 10^{-3} a^{-1}$ in Fig. 5.8.

Both observations are attributed to the small energy scales of only a few µeV or neV that cause even small perturbations to have a notable effect. The perturbation in this case is the coupling to the replicas of the sp^2-hybridised lower bands. Moreover, it is possible that the z-component of the electric field does impose a Rashba effect after all, albeit one that is too weak compared to the intrinsic SOI and therefore does not affect the topology (cf. Eq. (2.151) on page 55). The further study of this phenomenon is left to future work.

For circular polarisation, there is one more possible perturbing factor that will only be introduced here, but not be analysed further. The electric fields for both polarisations (under dipole approximation) are of the following form:

$$\vec{E}_{\text{circ}}(\vec{r},\vec{t}) = \begin{pmatrix} \cos(\omega t) \\ \cos(\alpha)\sin(\omega t) \\ \sin(\alpha)\sin(\omega t) \end{pmatrix}, \quad \vec{E}_{\text{lin}}(\vec{r},\vec{t}) = \begin{pmatrix} 0 \\ \cos(\alpha)\sin(\omega t) \\ \sin(\alpha)\sin(\omega t) \end{pmatrix}. \tag{5.3}$$

Via the decomposition

$$\vec{E}_{\text{circ}}(\vec{r},\vec{t}) = \underbrace{\begin{pmatrix} \sin(\alpha)\cos(\omega t) \\ 0 \\ \sin(\alpha)\sin(\omega t) \end{pmatrix}}_{=:\vec{E}_L} + \begin{pmatrix} (1-\sin(\alpha))\cos(\omega t) \\ \cos(\alpha)\sin(\omega t) \\ 0 \end{pmatrix}, \tag{5.4}$$

the circularly polarised electric field obtains an effective angular momentum in y-direction due to the component $\vec{E}_L$. In section 3.3.1, it was the angular momentum in z-direction that gave rise to the Kronecker deltas in Eq. (3.41) (pg. 87). Accordingly, the term $\vec{E}_L$ is expected to give rise to new types of couplings. This assumption is reinforced by the observations of section 2.4.5 regarding the in-plane alignment of the sublattice spin in the Brillouin zone. Even though no notable couplings of this type have been observed in this work, they may become relevant at greater deflections, as the term $\sin(\alpha)$ increases.

So far, this chapter has only explicitly discussed the frequency $f = 3.85\,\text{PHz}$. While this thesis does not make any assumptions on what happens at resonance frequencies, the results for all non-resonance frequencies have been found to be in agreement with those for $f = 3.85\,\text{PHz}$. Thus, the predictions of chapter 4 regarding the edge states of graphene have been confirmed. This, however, is true only for sufficiently wide graphene ribbons. As will be shown in the following, finite-size effects can lift the topological protection of the edge states and split them apart.

5.3 Finite-size Effects

If the finite width of a graphene ribbon is below a certain threshold, it is possible that the edge states of the sample are coupled via the bulk. As a result, the crossing of the edge states is no longer topologically protected, and the edge states split (cf. [121]). As will be demonstrated in this section, such a splitting can be observed for some frequencies if the graphene unit cell depicted in Fig. 5.1 has 72 or fewer carbon atoms.

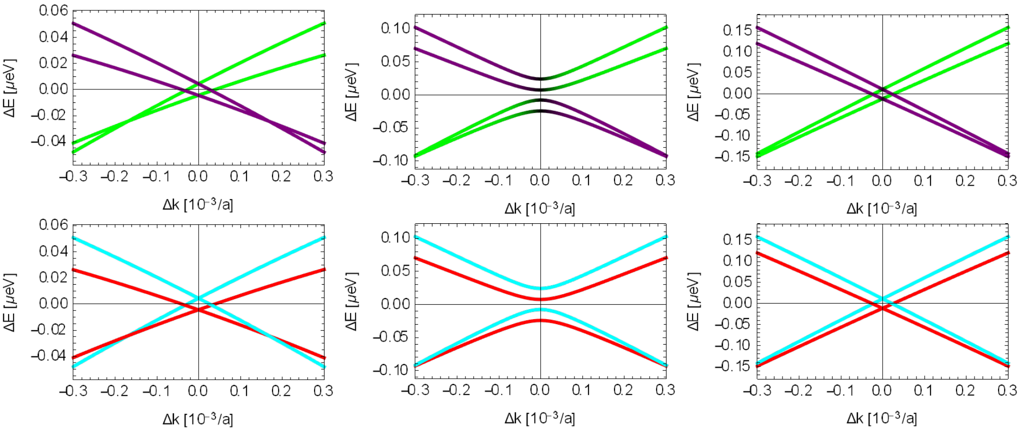

$f = 100\,\mathrm{THz}$,
$E = \Delta E - 0.14\,\mathrm{eV}$

$f = 200\,\mathrm{THz}$,
$E = \Delta E - 0.14\,\mathrm{eV}$

$f = 300\,\mathrm{THz}$,
$E = \Delta E - 0.14\,\mathrm{eV}$

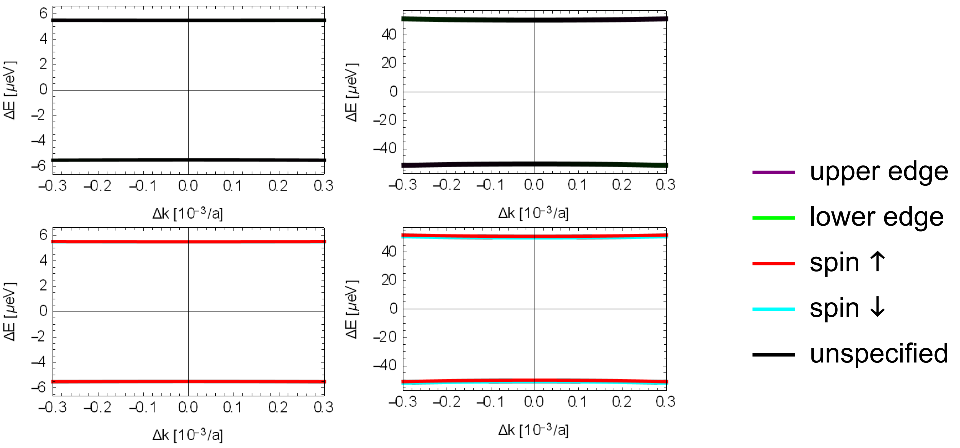

$f = 400\,\mathrm{THz}$,
$E = \Delta E - 0.14\,\mathrm{eV}$

$f = 800\,\mathrm{THz}$,
$E = \Delta E - 0.142\,\mathrm{eV}$

Figure 5.9: Floquet band structure of a graphene ribbon around $k = \pi/2a$, under irradiation with circularly polarised light of field strength $E_0 = 0.8\,\mathrm{V/nm}$ and varying frequency f; The edge states from Fig. 5.14 behave differently, depending on the frequency of the irradiated light. At $f = 800\,\mathrm{THz}$, a resonant coupling enhances a splitting due to finite-size effects. A similar splitting can be seen at the higher resonances $f = 400\,\mathrm{THz}$ and $200\,\mathrm{THz}$.

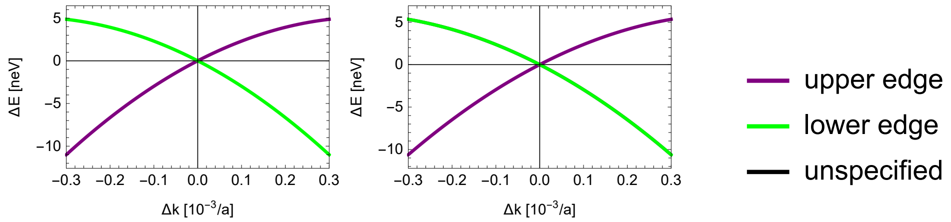

$f = 100\,\mathrm{THz}$,
$E = \Delta E - 0.145\,\mathrm{eV}$

$f = 200\,\mathrm{THz}$,
$E = \Delta E - 0.145\,\mathrm{eV}$

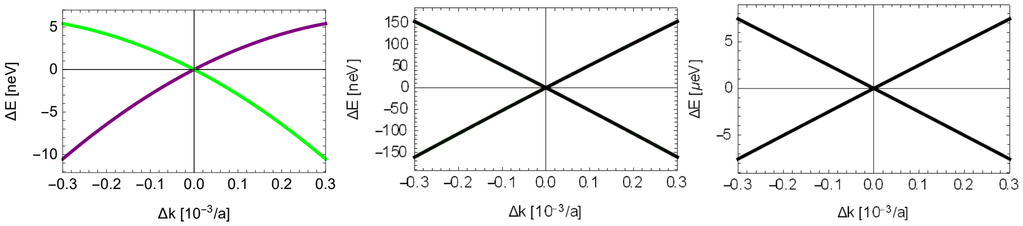

$f = 300\,\mathrm{THz}$,
$E = \Delta E - 0.145\,\mathrm{eV}$

$f = 400\,\mathrm{THz}$,
$E = \Delta E - 0.145\,\mathrm{eV}$

$f = 800\,\mathrm{THz}$,
$E = \Delta E - 0.148\,\mathrm{eV}$

Figure 5.10: Floquet band structure of graphene around $k = \pi/2a$, under irradiation with linearly polarised light with $E_0 = 0.8\,\mathrm{V/nm}$ and varying f; At $f = 800\,\mathrm{THz}$ and $400\,\mathrm{THz}$, resonant couplings enhance finite-size effects.

Actual graphene nanoribbons have a width of 1 to 100 nm (cf. [122]). With a lattice constant of $a = 2.46\,\text{Å}$, this corresponds to approximately 4 to 368 atoms[2] in the y-direction of a unit cell like that in Fig. 5.1. Even though graphene samples with less than 72 atoms are on the smaller size of this already small scale, they are subject of current research (cf. [123, 124]). The finite-size effects and the consequential splitting of the otherwise topologically protected edge states may thus be relevant for experimental setups and will therefore be discussed in further detail in the following.

The edge states of graphene with 18 atoms in y-direction, that is irradiated with circularly and linearly polarised light can be seen in Figs. 5.9 and 5.10, respectively. The negative energetic shift at $f = 800\,\mathrm{THz}$ in both figures is the same as in Fig. 4.3 (pg. 98). Fig. 5.9 also shows a notable splitting of the edge states under irradiation with circularly polarised light of $f = 800\,\mathrm{THz}$. The splitting is of the same order of magnitude as the spin splitting in section 4.2. A similar, albeit smaller splitting can be seen at the integer fractions

---

[2] A width of 100 nm actually corresponds to 367 atoms. However, for an odd number, one edge of Fig. 5.1 would not have a zigzag shape and would instead be a so-called *bearded edge* with carbon atoms that are bonded to only a single other carbon atom, respectively.

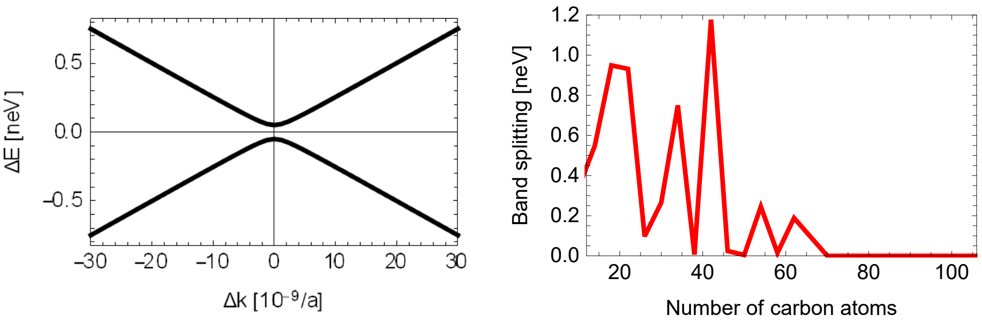

(a) (b)

Figure 5.11: Splitting between the edge states of a graphene ribbon under irradiation of linearly polarised light of frequency $f = 800\,\mathrm{THz}$ with field strength $E_0 = 0.8\,\mathrm{V/nm}$; (a) Under consideration of 18 carbon atoms per unit cell, a splitting occurs between the edge states around $k = \pi/2a$, where $E = \Delta E - 0.145\,\mathrm{eV}$ is the Floquet energy. (b) The magnitude of the splitting varies as a function of the number of carbon atoms per unit cell. For 72 or more atoms, the splitting falls below double point precision. Only unit cells with sublattice A on the lower and sublattice B on the upper edge (cf. Fig. Fig. 5.1) have been taken into account.

$f = 400\,\mathrm{THz}$ and $200\,\mathrm{THz}$. Under irradiation with linearly polarised light, the spins are degenerate. Hence, the splitting of the edge states is significantly smaller. The splitting for $f = 800\,\mathrm{THz}$ in Fig. 5.10 is enhanced in Fig. 5.11a.

Fig. 5.11b shows how the width of the band gap depicted in Fig. 5.11a varies with the number of carbon atoms per unit cell. For 72 or more atoms, the width falls below the computational double point precision. With higher accuracy, it would be expected to decrease exponentially (cf. [121]). For circularly polarised light, the threshold of 72 atoms is the same, but it is not depicted explicitly, here.

The relevance of the frequencies $f = 800\,\mathrm{THz}$, $400\,\mathrm{THz}$ and $200\,\mathrm{THz}$ stems from one specific resonant coupling and its higher resonances. Fig. 5.12 shows the bands of a graphene ribbon at $\Delta k = 0$, i.e. $k = \pi/2$ as a function of the frequency of the irradiated light, with Floquet order of $N = 1$. At $f \approx 829\,\mathrm{THz}$, both an orange and an azure line cross the black line near $E = 0\,\mathrm{eV}$. This implies a threefold crossing of a (+1)- and a (−1)-photon bulk band with the (black) 0-photon edge state. This crossing is in fact the same crossing as was already depicted in Fig. 4.9 (pg. 104).

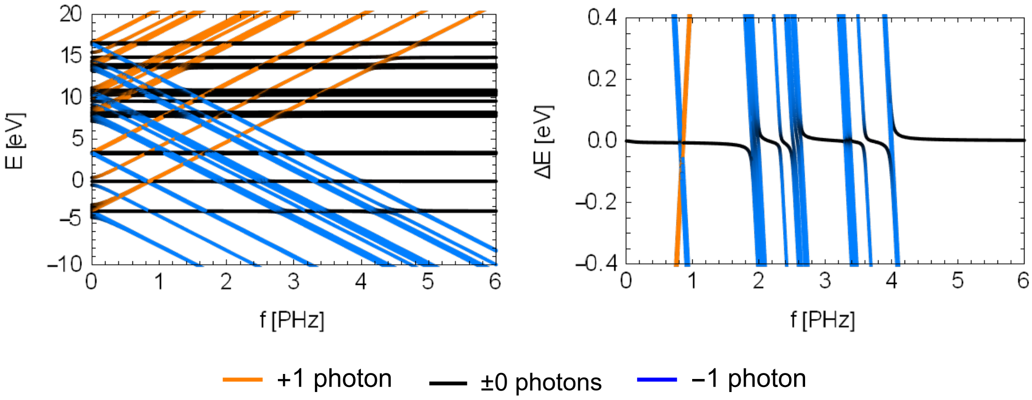

Figure 5.12: Floquet energies of a graphene ribbon at $k = \pi/2a$, under irradiation with circularly polarised light; On the left, energies with an expectation value of (minus) one photon are depicted in orange (azure). On the right, the energies around $\Delta E = E - 135\,\mathrm{meV}$ have been zoomed in on. At approximately 829 THz, both an orange and an azure line cross the black line nearly simultaneously. The field strength is $E_0 = 0.8\,\mathrm{V/nm}$, and there are 18 carbon atoms per unit cell. No $(\pm n)$-photon states with $n > 1$ are depicted.

In the context of Fig. 4.9, it was discussed how a coupling of a (+1)- and a (−1)-photon band is suppressed by the square of the energy difference to the energetically closest 0-photon band (cf. Eqs. (4.5) and (4.6) on page 104). Since the point $\Delta k = 0$ in Figs. 5.9, 5.10 and 5.11a is the projection of the M-point onto a lower dimension,[3] one could naïvely assume that, as in Fig. 4.9, the energy difference to the closest 0-photon band would be more than 2 eV. However, the existence of the edge states reduces this energy difference drastically. As can be seen in Fig. 5.12, the edge states serve as a catalyst between the (+1)- and a (−1)-photon bands that cross at $f \approx 829\,\mathrm{THz}$. It is therefore the lifted topological protection due to the finite width of the graphene ribbon together with the simultaneous coupling to a (+1)- and a (−1)-photon states that gives rise to the significant splitting of the edge states in Figs. 5.9 and 5.10.

On a larger scale, the bands depicted in Figs. 5.9 and 5.10 look like Fig. 5.13. Since the frequencies considered here are in the THz regime, it is necessary to consider high Floquet orders N. However, since the great number of replica bands in Fig. 5.13 makes the figure difficult to interpret, the Floquet band

---

[3] The projection of the band structure onto a lower-dimensional Brillouin zone is illustrated in Fig. 2.17 (pg. 40).

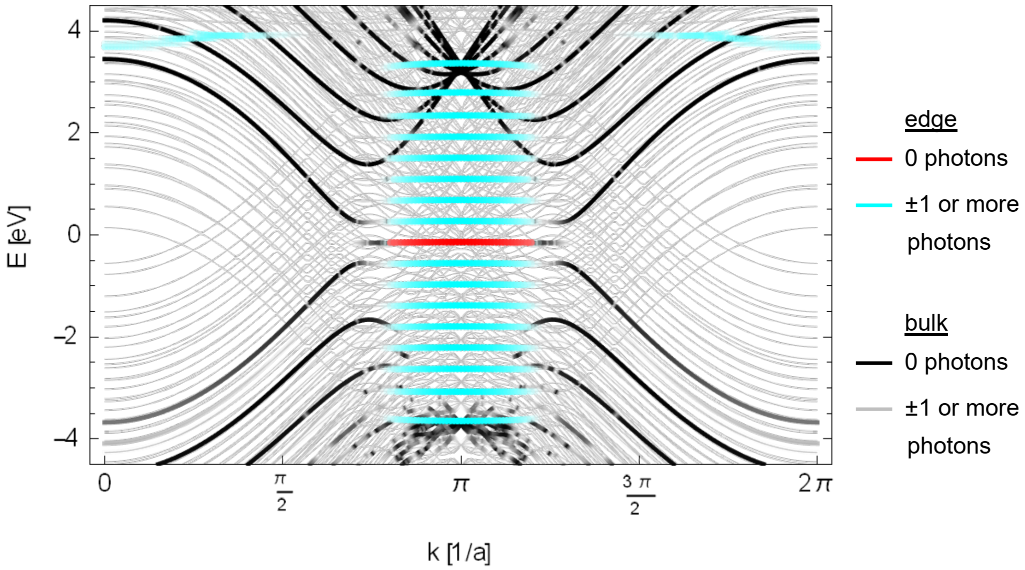

Figure 5.13: Floquet band structure of a graphene ribbon under irradiation with circularly polarised light of frequency $f = 100\,\text{THz}$, field strength $E_0 = 0.8\,\text{V/nm}$ and with a Floquet order of $N = 8$; The Floquet energies of the $2N = 16$ grey and cyan Floquet replicas around the black and red 0-photon bands at the centre differ by multiples of $hf = \hbar\omega$. Around the 0-photon edge states (red), the black lines appear to be interrupted, since they merge into grey ones.

structures for multiple frequencies are depicted in Fig. 5.14 as well, but with only a Floquet order of $N = 1$.

Fig. 5.14 shows how with increasing frequency the Floquet replica bands move closer to the centre until they cross the 0-photon edge states at a frequency of $f = 800\,\text{THz}$. The frequencies of $f = 400\,\text{THz}$ and $200\,\text{THz}$ show no such crossing, since it would be a second- or fourth-order resonance, respectively. The couplings therefore require Floquet orders of $N = 2$ and $N = 4$. As deduced from Fig. 5.12, the actual resonance does not lie at $f = 800\,\text{THz}$, but at $829\,\text{THz}$ instead. This explains why there is no notable splitting for $f = 300\,\text{THz}$ and for $100\,\text{THz}$. The integer multiple of $300\,\text{THz}$ that is closest to resonance is $900\,\text{THz}$ and is therefore not close enough to $829\,\text{THz}$ for the third-order resonance to have a similar effect. Similarly, $100\,\text{THz}$ would need an eighth-order resonance.

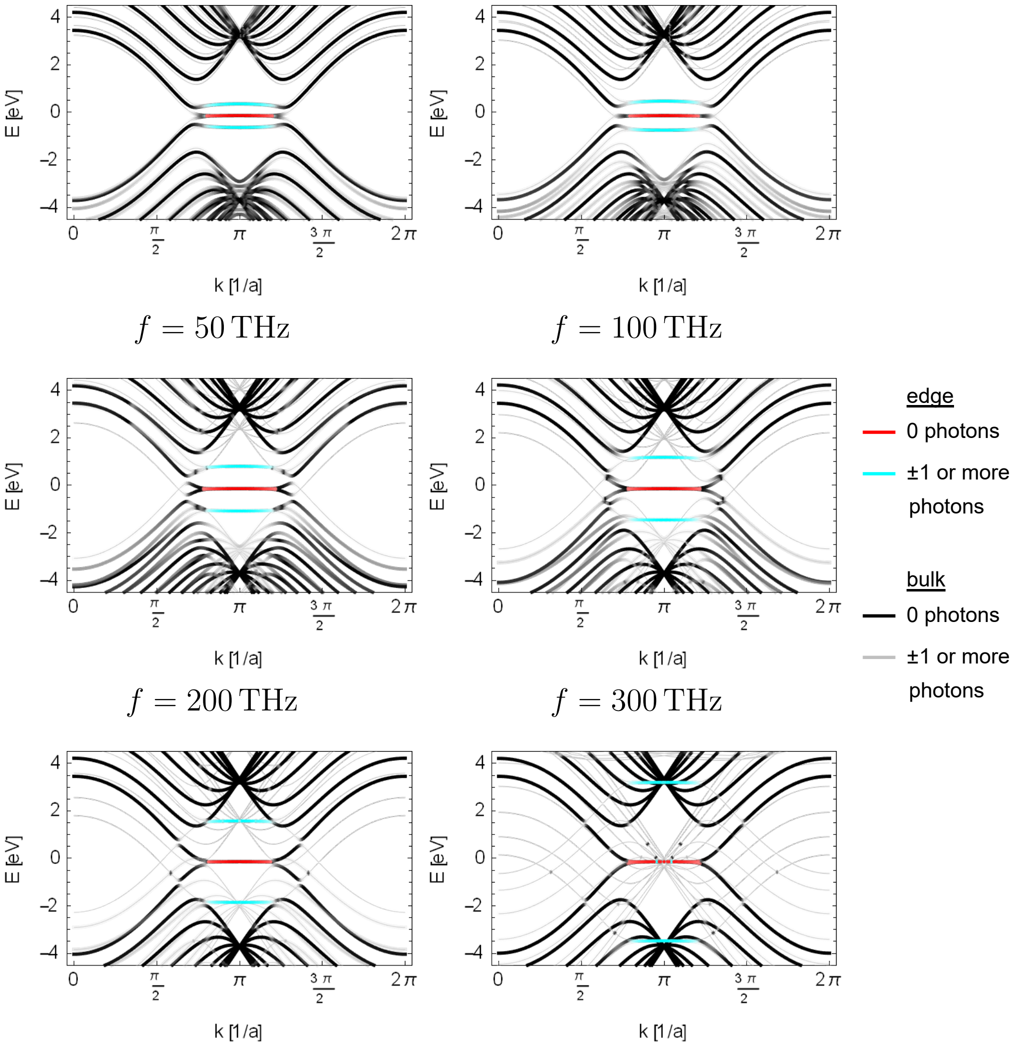

$f = 50\,\mathrm{THz}$ $f = 100\,\mathrm{THz}$

$f = 200\,\mathrm{THz}$ $f = 300\,\mathrm{THz}$

$f = 400\,\mathrm{THz}$ $f = 800\,\mathrm{THz}$

Figure 5.14: Floquet band structure of a graphene ribbon under irradiation with circularly polarised light of field strength $E_0 = 0.8\,\mathrm{V/nm}$ and varying frequency f, with a Floquet order of $N = 1$; As the frequency increases, the Floquet replica bands move across the energy axis. Consequently, replicas and original bands cross, and (±1)-photon bands exhibit avoided crossings with the 0-photon bands near the centre.

Chapter 6

Conclusion and Outlook

In this thesis, Floquet formalism was used to study the effects of light fields on the band structure of a spinful LCAO model of graphene. After preceding analytical observations in chapter 3, chapter 4 focussed on a fully periodic lattice, whereas chapter 5 instead considered a graphene ribbon that is finite in one spatial direction.

Over the course of these chapters, the Floquet band structure of graphene as well as its topology have been found to be strongly dependent on the frequency and, even more so, the polarisation of the light field. Consequently, graphene that is irradiated with linearly polarised light or no light at all is a spin-Hall insulator, whereas circularly polarised light turns it into a Chern insulator. While the latter result on its own is in agreement with [47, 48], a new property has also been observed: The change from a spin-Hall to a Chern insulator lifts spin degeneracy.

In section 5.2.1, the lift of spin degeneracy was attributed to the effects of the angular momentum of the irradiated light. The latter is only partially compatible with the opposing spin-flow directions of the spin-Hall insulator. Due to the spin-Hall effect, the edge currents flow clockwise around the material for one spin and anti-clockwise for the other spin. Since the photovoltaic Hall effect induced by the light leads to the same flow direction for both spins, one current is supported while the other is suppressed. Consequently, the spin degeneracy of the edge states in a graphene ribbon is lifted.

The same lift of degeneracy was also observed in fully periodic graphene. In section 3.3.1, the coupling between eigenstates of unperturbed graphene due to circularly polarised light was determined to be spin-dependent. The resulting lift of spin degeneracy in section 4.2.1 was then found to lead to the aforementioned lift of spin degeneracy for the topologically protected edge states in section 5.2.1.

The observations regarding the topology have also been tested against deflections of the incoming light beam by an angle of 5°. Despite the resulting field component in z-direction, the deflection has been found to not lead to any notable Rashba effects, as was shown in sections 4.2.3 and 5.2.2. This is attributed to the time-dependent oscillation of the electric field that, averaged over a time-period, does not break the out-of-plane symmetry of the system, as opposed to a static electric field.

Further effects on the band structure have been found, including, but not limited to an enhancement of the intrinsic, SOI-induced band gap between the Dirac cones of fully periodic graphene. As shown in section 4.1.1, irradiation with certain PHz frequencies leads to a widening of the band gap by two orders of magnitude. For THz frequencies, the widening is far less prominent, but a different phenomenon occurs: In section 4.3.2, the width of the band gap has been found to oscillate with the frequency of the irradiated light. Based on the results of section 3.3, a toy model was created, to understand and describe this phenomenon. With the help of that model, the oscillations were then shown to be the result of an interplay of a time-dependent onsite coupling term and sublattice potential that lead to two types of interactions between the Floquet replica bands.

In section 4.3.3, one fixed THz frequency was chosen to study the band structure around the K-point. Several avoided crossings between Floquet replica bands were observed. These avoided crossings were found to be similar to those described by a toy model studied in [60], a bachelor thesis that was supervised by the author.

For graphene ribbons that are finite in one spatial direction, THz frequencies were used in section 5.3 to illustrate how higher-order resonant couplings enhance a finite-size effect. In ribbons with a width of 72 or fewer carbon atoms, the otherwise crossing edge states were found to split. This was attributed to the finite width of the ribbon that leads to a lift of the topological protection of the crossing edge states. The magnitude of the consequent splitting was shown to increase drastically at resonance frequencies.

The significant enhancement of the band gap in section 4.1.1 only occurs at frequencies in the PHz regime. Also, the spin splitting in sections 4.2 and 5.2 is only of a magnitude of a few µeV. Both effects are therefore difficult to study experimentally. Otherwise, in particular the band gap widening, would have been valuable for the general study of topological insulators, as the intrinsic graphene band gap is small and bears the danger of being surpassed by thermal excitations of the electrons. The phenomena of section 4.3 and 5.3, on the other hand, are results of frequencies in the THz regime. The oscillations of valence and conduction band as a function of the frequency in section 4.3 occur between 10 and 50 THz and are therefore experimentally verifiable. The finite-size effects of section 5.3 have been found to be significantly enhanced for a multitude of frequencies in the range from 200 to 800 THz and should be taken into account when designing an experiment that studies spin-Hall and quantum (anomalous) Hall effects in graphene.

A possible continuation of this thesis lies in the study of the transition between these Hall effects. The topology of the Floquet band structure has only been studied for circularly and linearly polarised light. A study of elliptically polarised light is expected to give valuable insight on the transition from graphene as a spin-Hall insulator to a no longer spin-degenerate Chern insulator. Moreover, such studies could reveal new topological properties. As discussed in section 2.6.5, Floquet band structures can give rise to topologically protected edge states that cross the boundary of the first Floquet Brillouin zone. While no such edge states have been observed in this thesis, it is possible that elliptically polarised light could have new effects on the topology that do give rise to such states.

It is also possible and appropriate to extend the research of this thesis by expanding the model used in it to account for effects that have been neglected so far. In section 3.1.1, the coupling of different reciprocal vectors $\vec{k}$ via the electric perturbation has been determined to be small in comparison to the coupling between identical $\vec{k}$ and was therefore neglected. A continuation of this thesis should incorporate the terms that couple different $\vec{k}$.
Furthermore, only electric fields have been considered in this thesis. The magnetic component of the light fields has been neglected, as it is significantly weaker than its electric counterpart. Magnetic fields can give rise to interesting spin dynamics. In particular the interplay with the lifted degeneracy of the edge states in chapter 5 should be probed.
In this thesis, no notable Rashba effects have been observed. However, as explained in section 4.2.3, it is possible that higher-order Rashba terms could give rise to such effects. Also, an understanding of greater angular deflections than 5° is expected to be beneficial towards the design of new experiments. The absence of Rashba effects for these deflections should therefore be verified as well.
Ultimately, the thesis has only considered single-electron band structures. A continuation of this thesis should put its results into the broader context of multi-electron systems. In particular, occupation dynamics are important to consider. These should also be studied in the context of thermodynamics as well.

The computations in this thesis have all been performed either in Mathematica or by hand. The Mathematica code has been written in such a way that it is easily accessible for other people to work with it and to reproduce the results of this thesis. The accessibility has been demonstrated by Martens who also performed the computations for his bachelor thesis within the same framework [60]. The code is highly modular and allows to easily change from graphene to other materials with the same lattice symmetry, e.g. silicene. The extension to the latter or possibly similar materials like molybdenum disulphide (MoS_2) is expected to lead to similar results as for graphene. Other than via a change in material, it is also possible to expand the model via the consideration of different geometries. Graphene nanotubes or fullerenes, as well as graphene sheets with ripples are experimentally available shapes. The Mathematica code of this thesis has been written with these geometries in mind and only needs minor modifications for their full implementation. The code will be published in addition to the physical results of this thesis.

Appendix A

Material Parameters

The spinful multi-orbital tight-binding model of this thesis requires numerous parameters most of which have been determined empirically [27, 125, 126] or from first principles [29]. The complete list of parameters is given in Tab. A.1. A cornerstone of this thesis is the simplified LCAO model of Slater and Koster [33]. Its parameters, if available, stem from Gosálbez-Martínez, Palacios and Fernandez [125]. The missing parameters for the hydrogen passivation (cf. Fig. 5.1 on page 40) stem from Huertas-Hernando, Guinea and Brataas [126]. The intrinsic SOI strength has been chosen in such a way that it satisfies the band gap of 42 µeV measured by Sichau at al. [30].

For the effective $\mathrm{f_{xyz}}$-orbital, the parameters have been estimated as discussed in section 2.2.3. Accordingly, their effective Bohr radius has been chosen to be 5/3 times that of carbon. The respective hopping terms $V_{\mathrm{if}\alpha}$ with $i \in \{\mathrm{s}, \mathrm{p}, \mathrm{d}\}$ and $\alpha \in \{\sigma, \pi, \delta\}$ have then been estimated through numerical computations and comparison to the other hopping terms. No hopping between two f-orbitals is considered.

For the coupling of neighbouring atoms via the electric field, an effective atomic radius needs to be assumed. In this thesis, its value is

$$a^*_{\mathrm{Bohr}} = \frac{a_{\mathrm{distance}}}{2} = \frac{a}{2\sqrt{3}} = 0.71\,\text{Å} \tag{A.1}$$

with the distance a_{distance} between two atoms. This is in good agreement with other estimates (cf. [127–129]).

s- and p-orbitals, and general parameters

ϵ_{s}	ϵ_{p}	ϵ_{d}	ϵ_{f}	λ_{I}	a
$-8.8\,\mathrm{eV}$	$0\,\mathrm{eV}$	$12\,\mathrm{eV}$	$26\,\mathrm{eV}$	$2.87\,\mathrm{meV}$	$2.46\,\mathrm{\AA}$

$V_{\mathrm{ss}\sigma}$	$V_{\mathrm{sp}\sigma}$	$V_{\mathrm{pp}\sigma}$	$V_{\mathrm{pp}\pi}$	a_{Bohr}	$a_{\mathrm{Bohr}^*,\mathrm{f}}$
$-7.76\,\mathrm{eV}$	$8.16\,\mathrm{eV}$	$7.48\,\mathrm{eV}$	$3.59\,\mathrm{eV}$	$0.71\,\mathrm{\AA}$	$1.183\,\mathrm{\AA}$

d-orbitals

$V_{\mathrm{sd}\sigma}$	$V_{\mathrm{pd}\sigma}$	$V_{\mathrm{pd}\pi}$
$0\,\mathrm{eV}$	$-4.308\,\mathrm{eV}$	$-0.7\,\mathrm{eV}$

$V_{\mathrm{dd}\sigma}$	$V_{\mathrm{dd}\pi}$	$V_{\mathrm{dd}\delta}$
$-3.949\,\mathrm{eV}$	$0.359\,\mathrm{eV}$	$-2.693\,\mathrm{eV}$

f-orbitals

$V_{\mathrm{sf}\sigma}$	$V_{\mathrm{pf}\sigma}$	$V_{\mathrm{pf}\pi}$
$0\,\mathrm{eV}$	$0\,\mathrm{eV}$	$-1.44\,\mathrm{eV}$

$V_{\mathrm{df}\sigma}$	$V_{\mathrm{df}\pi}$	$V_{\mathrm{df}\delta}$
$0\,\mathrm{eV}$	$-4.24\,\mathrm{eV}$	$-4.15\,\mathrm{eV}$

Hydrogen passivation

$\epsilon_{\mathrm{s,H}}$	$V_{\mathrm{sp}\sigma,\mathrm{H}}$	$V_{\mathrm{ss}\sigma,\mathrm{H}}$
$-2.7\,\mathrm{eV}$	$-4.5\,\mathrm{eV}$	$-4.2\,\mathrm{eV}$

Table A.1: Numerical parameters of graphene used throughout this thesis. ϵ_i is the on-site energy of an orbital i. $V_{ij\alpha}$ is the hopping strength between two neighbouring orbitals i and j, where α denotes how they are bonded to one another. λ_I is the intrinsic SOI strength. The terms for the f-orbitals correspond to the effective f-orbital discussed in section 2.2.3. Terms $V_{\mathrm{ff}\alpha}$ associated with the hopping between two f-orbitals have been assumed zero. For hydrogen atoms, only s-orbitals are considered, and only the coupling to p- and other s-orbitals of neighbouring atoms is taken into account.

Appendix B

$\vec{k}$-non-diagonal Matrix Elements

In the final expression of Eq. (3.19) (pg. 78), there are two summands, the former of which will be discussed here. The summand itself is a sum of the form

$$\sum_{\vec{R}} e^{\mathrm{i}(\vec{k}-\vec{k}')\vec{R}} \cdot R_x \cdot \eta_{n_1,n_2,k,k'}. \tag{B.1}$$

The term $\eta_{n_1,n_2,k,k'}$ is an integral over the unit cell,

$$\eta_{n_1,n_2}(k'-k) := \eta_{n_1,n_2,k,k'} = \int_{\text{u.c.}} e^{-\mathrm{i}(\vec{k}'-\vec{k})\vec{r}} \cdot \psi_{n_1\vec{k}}{}^{\dagger}(\vec{r})\psi_{n_2\vec{k}'}(\vec{r})\; d\vec{r} \tag{B.2}$$

with

$$\psi_{n\vec{k}}(\vec{r},t) := \frac{1}{\sqrt{N}} \sum_{\vec{R}} \sum_{s=\pm 1} f^{s}_{n,\vec{R}}(t) e^{\mathrm{i}\vec{k}\vec{R}} w_n(\vec{r} - (\vec{R} + s \cdot \vec{\delta}/2)), \tag{B.3}$$

according to definition 3.15 (pg. 77). In the following, the sums over lattice vectors $\vec{R}$ and sublattice indices $s = \pm 1$ will be replaced with a sum over lattice sites $\vec{\mathcal{R}} \in \{\vec{R} \pm \vec{\delta}/2\}$. The envelope functions are redefined accordingly, as $f_{n,\vec{R}+s\cdot\vec{\delta}/2} := f^{s}_{n,\vec{R}}(t)$.

Eqs. (B.3) and (B.2) then together yield

$$\int_{\text{u.c.}} e^{-\mathrm{i}(\vec{k}'-\vec{k})\vec{r}} \cdot (\psi_{n_1\vec{k}})^{\dagger}(\vec{r})\psi_{n_2\vec{k}'}(\vec{r})\; d\vec{r} \tag{B.4}$$

$$\begin{aligned}
=&\frac{1}{N}\sum_{\vec{\mathcal{R}},\vec{\mathcal{R}}'} f^*_{n_1,\vec{\mathcal{R}}}(t) f_{n_2,\vec{\mathcal{R}}'}(t)\cdot \\
&\qquad\cdot \int_{\text{u.c.}} e^{-\mathrm{i}(\vec{k}'(\vec{r}-\vec{\mathcal{R}}')-\vec{k}(\vec{r}-\vec{\mathcal{R}}))} \cdot w^*_{n_1}(\vec{r}-\vec{\mathcal{R}})w_{n_2}(\vec{r}-\vec{\mathcal{R}}')\; d\vec{r}
\end{aligned} \tag{B.5}$$

$$\begin{aligned}
=&\frac{1}{N}\sum_{\vec{\mathcal{R}},\vec{\mathcal{R}}'} f^*_{n_1,\vec{\mathcal{R}}}(t) f_{n_2,\vec{\mathcal{R}}'}(t)\cdot e^{-\mathrm{i}\vec{k}\Delta\vec{\mathcal{R}}} \\
&\qquad\cdot \int_{\text{u.c.}} e^{-\mathrm{i}(\vec{k}'-\vec{k})(\vec{r}-\vec{\mathcal{R}}')} \cdot w^*_{n_1}(\vec{r}-\vec{\mathcal{R}}'-\Delta\vec{\mathcal{R}})w_{n_2}(\vec{r}-\vec{\mathcal{R}}')\; d\vec{r}
\end{aligned} \tag{B.6}$$

$$\begin{aligned}
=&\frac{1}{N}\sum_{\vec{\mathcal{R}},\vec{\mathcal{R}}'} f^*_{n_1,\vec{\mathcal{R}}}(t) f_{n_2,\vec{\mathcal{R}}'}(t)\cdot e^{-\mathrm{i}\vec{k}\Delta\vec{\mathcal{R}}} \\
&\qquad\cdot \int_{\text{u.c.}} e^{-\mathrm{i}(\vec{k}'-\vec{k})\vec{r}} \cdot w^*_{n_1}(\vec{r}-\Delta\vec{\mathcal{R}})w_{n_2}(\vec{r})\; d\vec{r}.
\end{aligned} \tag{B.7}$$

From (B.4) to (B.5), the definition (B.3) was used. From (B.4) to (B.5), $\Delta\vec{\mathcal{R}} := \vec{\mathcal{R}}' - \vec{\mathcal{R}}$ was inserted, to simplify the exponential function. From (B.6) to (B.7), the substitution $\vec{\mathcal{R}}' \to \vec{\mathcal{R}}' + \Delta\vec{\mathcal{R}}$ was performed.

Based on the LCAO approach (2.44) described on page 15, the Wannier functions w_n are assumed to be sums of atomic orbital wave functions[1] Φ_n, where n labels the atomic orbital. In the following, the integral at the end of Eq. (B.7) will therefore be evaluated for the following atomic orbitals:

$$\begin{aligned}
\Phi_{2\mathrm{p_z}}(r,\theta,\phi) &= \frac{1}{\sqrt{{a^*_{\text{Bohr}}}^5}}\frac{e^{r/(2a^*_{\text{Bohr}})} r\cos(\theta)}{4\sqrt{2\pi}}, \\
\Phi_{3\mathrm{d_{xz}}}(r,\theta,\phi) &= \frac{1}{\sqrt{{a^*_{\text{Bohr}}}^7}}\frac{e^{-r/(3a^*_{\text{Bohr}})-\mathrm{i}\phi}(1+e^{2\mathrm{i}\phi})r^2\cos(\theta)\sin(\theta)}{81\sqrt{2\pi}}, \\
\Phi_{3\mathrm{d_{yz}}}(r,\theta,\phi) &= \frac{1}{\sqrt{{a^*_{\text{Bohr}}}^7}}\frac{\mathrm{i}e^{-r/(3a^*_{\text{Bohr}})-\mathrm{i}\phi}(-1+e^{2\mathrm{i}\phi})r^2\cos(\theta)\sin(\theta)}{81\sqrt{2\pi}}
\end{aligned} \tag{B.8}$$

with the effective Bohr radius a^*_{Bohr}.

---

[1] The symbol Φ instead of ϕ like in section 2.2.3 has been chosen here to clearly distinguish the wave function from the polar angle with the otherwise same symbol.

The strong localisation of the orbital wave functions allows for the replacement of the integral in Eq. (B.7) with an integral over the entire real space without changing the result significantly.
A second approximation[2] that will be made in the following is that for orbital wave functions the integral vanishes for $\Delta\vec{\mathcal{R}} \neq 0$, i.e. for $\vec{\mathcal{R}} \neq \vec{\mathcal{R}}'$.
Eq. (B.7) then reshapes to

$$\left(\sum_{\vec{\mathcal{R}}} f^*_{n_1,\vec{\mathcal{R}}}(t) f_{n_2,\vec{\mathcal{R}}}(t)\right) \cdot \int_{\mathbb{R}^3} e^{-\mathrm{i}(\vec{k}'-\vec{k})\vec{r}} \cdot \Phi^*_{n_1}(\vec{r})\Phi_{n_2}(\vec{r})\ d\vec{r}. \tag{B.9}$$

Due to the normalisation condition of the envelope functions given in Eq. (2.65) in section (2.2.4), the absolute value of the preceding sum in Eq. (B.9) is bounded from above[3] by 1. In the following, the preceding sum in equation (B.9) will hence be neglected, and only the integral over the atomic orbital wave functions will be considered.
The sum over the y- and the z-components of $\vec{R}$ in Eq. (B.1) results in a Kronecker delta for k_y and k'_y and for k_z and k'_z. Thus, the y and z-dependence in the exponential function of Eq. (B.9) disappears. As a result of this observation and of the preceding assumption, Eq. (B.9) is reduced to

$$\int_{\mathbb{R}^3} e^{-\mathrm{i}(k'_x-k_x)r_x} \cdot \Phi^*_{n_1}(\vec{r})\Phi_{n_2}(\vec{r})\ d\vec{r}. \tag{B.10}$$

To solve this new integral, express x in spherical coordinates and write

$$e^{\mathrm{i}(k_x-k'_x)x} = \sum_{n=0}^{\infty} \frac{((k_x-k'_x)\cdot r\cos(\phi)\sin(\theta))^n}{n!} =:= \sum_{n=0}^{\infty} \frac{\kappa_n}{n!}. \tag{B.11}$$

Thus, instead of solving the entire integral (B.2), the integrals of atomic wave functions times the κ_n of Eq. (B.11) will be solved first and summed over, later. The integrals over the summands are

$$\langle\Phi_{n_1}|\ \kappa_n\ |\Phi_{n_2}\rangle := \tag{B.12}$$
$$\int_{\mathbb{R}^3} ((k_x-k'_x)r\cos(\phi)\sin(\theta))^n \cdot {\Phi_{n_1}}^{\dagger}(r,\theta,\phi)\Phi_{n_2}(r,\theta,\phi)\ r^2\sin(\phi)\ \ dr\ d\theta\ d\phi.$$

---

[2] Not only is the overlap between atomic orbitals on neighbouring atoms small, but also does the factor $e^{-\mathrm{i}(\vec{k}'-\vec{k})\vec{r}}$ lead to an oscillating behaviour that further suppresses the integral.

[3] For a quickly oscillating electric field with a small field strength, the envelope functions $f_{n,\vec{\mathcal{R}}}$ are approximately identical for all lattice vectors $\vec{\mathcal{R}}$ and orbital quantum numbers n_i. In that case, the sum becomes almost exactly 1.

Further, write

$$\Delta k := a_{\mathrm{Lat}} \cdot (k_x' - k_x') \in [0, 2\pi) \tag{B.13}$$

to simplify the handling of Eqs. (B.12) and (B.8). a_{Lat} replaces the lattice constant a to better distinguish it from a^*_{Bohr}. Evaluation of Eq. (B.12) then yields, for $2\mathrm{p_z}$-$2\mathrm{p_z}$

$$\langle \Phi_{2\mathrm{p_z}} | \kappa_n | \Phi_{2\mathrm{p_z}} \rangle = \; ((-1)^n + 1) \cdot (-1)^{n/2+1} \, \frac{(n/2+1)^2 + (n/2+1)}{4} \, \Delta k^n, \tag{B.14}$$

for $3\mathrm{d_{xz}}$-$3\mathrm{d_{xz}}$

$$\langle \Phi_{3\mathrm{d_{xz}}} | \kappa_n | \Phi_{3\mathrm{d_{xz}}} \rangle = \; ((-1)^n + 1) \, \frac{3^{n-1}}{2^{5+n}} \, \frac{6+n}{3+n} \, \Delta k^n \; \Gamma(5+n), \tag{B.15}$$

for $3\mathrm{d_{yz}}$-$3\mathrm{d_{yz}}$

$$\langle \Phi_{3\mathrm{d_{yz}}} | \kappa_n | \Phi_{3\mathrm{d_{yz}}} \rangle = \; ((-1)^n + 1) \, \frac{3^{n-1}}{4\sqrt{\pi}} \, \Delta k^n \; \Gamma(4 + n/2) \; \Gamma((1+n)/2) \tag{B.16}$$

and for $2\mathrm{p_z}$-$3\mathrm{d_{xz}}$

$$\langle \Phi_{2\mathrm{p_z}} | \kappa_n | \Phi_{3\mathrm{d_{xz}}} \rangle = \langle \Phi_{3\mathrm{d_{xz}}} | \kappa_n | \Phi_{2\mathrm{p_z}} \rangle = \; \mathrm{i}\pi \frac{2^{4+n} \cdot 3^{2+n}}{5^{6+n}} (\mathrm{i}\Delta k)^n \frac{\Gamma(6+n)}{\Gamma(3+n/2)\Gamma(-n/2)}, \tag{B.17}$$

where $\Gamma(z)$ is the gamma function.
The remaining two matrix elements for $2\mathrm{p_z}$-$3\mathrm{d_{yz}}$ and $3\mathrm{d_{xz}}$-$3\mathrm{d_{yz}}$ are zero. After executing the sum (B.11), one can write the 3×3 matrix

$$\left(\eta_{n_1,n_2}(\Delta k)\right)_{n_1,n_2 \in \{2\mathrm{p_z}, 3\mathrm{d_{xz}}, 3\mathrm{d_{yz}}\}} \tag{B.18}$$

$$= \begin{pmatrix} \frac{1}{\left(\Delta k^2+1\right)^3} & \frac{829440\mathrm{i}\Delta k}{\left(36\Delta k^2+25\right)^4} & 0 \\ \frac{829440\mathrm{i}\Delta k}{\left(36\Delta k^2+25\right)^4} & -\frac{256\left(63\Delta k^2-4\right)}{\left(9\Delta k^2+4\right)^5} & 0 \\ 0 & 0 & \frac{256}{\left(9\Delta k^2+4\right)^4} \end{pmatrix} \tag{B.19}$$

$$= \begin{pmatrix} \frac{1}{\left(\Delta k^2+1\right)^3} & \frac{b \cdot \mathrm{i}\Delta k}{\left(\left(\frac{6}{5}\Delta k\right)^2+1\right)^4} & 0 \\ \frac{b \cdot \mathrm{i}\Delta k}{\left(\left(\frac{6}{5}\Delta k\right)^2+1\right)^4} & \frac{1-7\left(\frac{3}{2}\Delta k\right)^2}{\left(\left(\frac{3}{2}\Delta k\right)^2+1\right)^5} & 0 \\ 0 & 0 & \frac{1}{\left(\left(\frac{3}{2}\Delta k\right)^2+1\right)^4} \end{pmatrix} \tag{B.20}$$

with $\Delta\vec{k}$ as defined in Eq. (B.13) and $b = 2^{11} \cdot 3^4 / 5^7$.
In Fig. 3.2, the matrix elements $\eta_{n_1,n_2}(\Delta k)$ have been plotted as functions of

$(k'_x - k_x) \cdot a_{\mathrm{Lat}}$. The horizontal axis ranges from 0 to 2π, such that it covers the distance of an entire Brillouin zone.

As a final remark, note that one can see from Fig. 3.2 that $\eta(\Delta k)$ is not Hermitian by itself. However, this is not an issue, since it only needs to satisfy $\eta(\Delta k)^\dagger = \eta(-\Delta k)$, which it does.

Appendix C

Diagonalisation of Tridiagonal Matrices

In section 4.3.2, a Floquet Hamiltonian $H_{\mathrm{F}\sigma}$ (Eq. (4.16), pg. 124) has been defined as

$$H_{\mathrm{F}\sigma} = \left(\begin{array}{c|cc|cc|cc|c}
\ddots & \multicolumn{2}{c|}{\vdots} & \multicolumn{2}{c|}{\vdots} & \multicolumn{2}{c|}{\vdots} & \iddots \\
\hline
\cdots & -\hbar\omega & 0 & \mathrm{i}M & C & \multicolumn{2}{c|}{} & \cdots \\
 & 0 & -\hbar\omega & 0 & -\mathrm{i}M & \multicolumn{2}{c|}{\smash{\raisebox{1.5ex}{0}}} & \\
\hline
\cdots & -\mathrm{i}M & 0 & 0 & 0 & \mathrm{i}M & C & \cdots \\
 & C & \mathrm{i}M & 0 & 0 & 0 & -\mathrm{i}M & \\
\hline
\cdots & \multicolumn{2}{c|}{} & -\mathrm{i}M & 0 & \hbar\omega & 0 & \cdots \\
 & \multicolumn{2}{c|}{\smash{\raisebox{1.5ex}{0}}} & C & \mathrm{i}M & 0 & \hbar\omega & \\
\hline
\iddots & \multicolumn{2}{c|}{\vdots} & \multicolumn{2}{c|}{\vdots} & \multicolumn{2}{c|}{\vdots} & \ddots
\end{array}\right), \quad \text{(C.1)}$$

where straight lines have been added to distinguish its Fourier components. M denotes a sublattice potential and C the strength of an onsite coupling of basis states in the original system.

In the following, the matrix (C.1) will be diagonalised in the static limit $\omega \to 0$ and for $C = 0$. First note that for $C = 0$ the matrix can be separated into a sum of two commuting matrices

$$H^{1}_{\mathrm{F}\sigma} := \left(\begin{array}{c|c|c|c|c} \ddots & \vdots & \vdots & \vdots & \iddots \\ \hline \cdots & \begin{matrix} -\hbar\omega & 0 \\ 0 & 0 \end{matrix} & \begin{matrix} \mathrm{i}M & 0 \\ 0 & 0 \end{matrix} & 0 & \cdots \\ \hline \cdots & \begin{matrix} -\mathrm{i}M & 0 \\ 0 & 0 \end{matrix} & \begin{matrix} 0 & 0 \\ 0 & 0 \end{matrix} & \begin{matrix} \mathrm{i}M & 0 \\ 0 & 0 \end{matrix} & \cdots \\ \hline \cdots & 0 & \begin{matrix} -\mathrm{i}M & 0 \\ 0 & 0 \end{matrix} & \begin{matrix} \hbar\omega & 0 \\ 0 & 0 \end{matrix} & \cdots \\ \hline \iddots & \vdots & \vdots & \vdots & \ddots \end{array}\right) \tag{C.2}$$

and

$$H^{-1}_{\mathrm{F}\sigma} := \left(\begin{array}{c|c|c|c|c} \ddots & \vdots & \vdots & \vdots & \iddots \\ \hline \cdots & \begin{matrix} 0 & 0 \\ 0 & -\hbar\omega \end{matrix} & \begin{matrix} 0 & 0 \\ 0 & -\mathrm{i}M \end{matrix} & 0 & \cdots \\ \hline \cdots & \begin{matrix} 0 & 0 \\ 0 & \mathrm{i}M \end{matrix} & \begin{matrix} 0 & 0 \\ 0 & 0 \end{matrix} & \begin{matrix} 0 & 0 \\ 0 & -\mathrm{i}M \end{matrix} & \cdots \\ \hline \cdots & 0 & \begin{matrix} 0 & 0 \\ 0 & \mathrm{i}M \end{matrix} & \begin{matrix} 0 & 0 \\ 0 & \hbar\omega \end{matrix} & \cdots \\ \hline \iddots & \vdots & \vdots & \vdots & \ddots \end{array}\right). \tag{C.3}$$

Both matrices have the same respectively non-degenerate eigenvalues. These eigenvalues are also the same as those of $H_{\mathrm{F}\sigma}$, with the exception that for $H_{\mathrm{F}\sigma}$ they are degenerate. It thus suffices to find the spectrum of $H^{1}_{\mathrm{F}\sigma}$. Furthermore, since every second row and every second column in $H^{1}_{\mathrm{F}\sigma}$ is zero, its eigenvalues are the same as those of

$$H_{\mathrm{tridiag}} := \begin{pmatrix} \ddots & \ddots & & & & & \\ \ddots & -2\hbar\omega & \mathrm{i}M & & & & \\ & -\mathrm{i}M & -1\hbar\omega & \mathrm{i}M & & & \\ & & -\mathrm{i}M & 0 & \mathrm{i}M & & \\ & & & -\mathrm{i}M & \hbar\omega & \mathrm{i}M & \\ & & & & -\mathrm{i}M & 2\hbar\omega & \ddots \\ & & & & & \ddots & \ddots \end{pmatrix}, \tag{C.4}$$

where all entries that have not been written explicitly are zero. To compute the eigenvalues of H_{tridiag}, consider the characteristic polynomial

$$P(\lambda) = \det(H_{\mathrm{tridiag}} - \lambda\mathbb{1}). \tag{C.5}$$

H_{tridiag} is a tridiagonal matrix, as is $(H_{\text{tridiag}} - \lambda\mathbb{1})$ as well. For an n-dimensional tridiagonal matrix

$$T_n := \begin{pmatrix} a_1 & b_1 & & & \\ c_1 & a_2 & b_2 & & \\ & c_2 & \ddots & \ddots & \\ & & \ddots & \ddots & b_{n-1} \\ & & & c_{n-1} & a_n \end{pmatrix}, \tag{C.6}$$

the determinant satisfies the recurrence relation

$$\det(T_n) = a_n \det(T_{n-1}) - c_{n-1} b_{n-1} \det(T_{n-2}). \tag{C.7}$$

In the limit $\omega \to 0$, it is possible to adapt this relation to $(H_{\text{tridiag}} - \lambda\mathbb{1})$ by inserting $a_i = -\lambda$ and $b_i = c_i^\dagger = \mathrm{i}M$ for all $i \in \mathbb{N}\backslash\{0\}$. The recurrence relation for the characteristic polynomial $P(\lambda)$ as defined in Eq. (C.5) then becomes

$$P_n(\lambda) = -\lambda P_{n-1}(\lambda) - M^2 P_{n-2}(\lambda). \tag{C.8}$$

For a Floquet order of N, the characteristic polynomial of H_{tridiag} is given by P_{2N}, with the first two polynomials defined as

$$P_0(\lambda) = -\lambda \qquad \text{and} \qquad P_1(\lambda) = (\lambda - M)(\lambda + M). \tag{C.9}$$

The recursion relation (C.8) can be used to show via induction that the eigenvalues are

$$\lambda_m = -2M \cos\left(\frac{m\pi}{n+1}\right) \qquad \text{with } m \in \{1, 2, ..., n\}, \tag{C.10}$$

similarly to what Kulkarni, Schmidt and Tsui derived in their book [130] for more general matrices. For Floquet matrices with Floquet order N, the λ_m are the Floquet quasi-energies

$$\epsilon_m = -2M \cos\left(\frac{m\pi}{2N+2}\right) \qquad \text{with } m \in \{1, 2, ..., 2N+1\}. \tag{C.11}$$

For $N = 1$, the eigenvalues are identical to those given in Eq. (4.17) on page 124 in the limit $\hbar\omega \to 0$. For higher N, the eigenvalues in Eq. (C.10) assume algebraic values within the interval $[-2M, 2M]$. Notably, the eigenvalues become dense in this interval as n increases. This indicates the transition from a finite to an infinite system. The Floquet energies can then be interpreted as continuous and reciprocal to the time, similarly to how the $\vec{k}$ that are reciprocal to the spatial coordinates. A more detailed discussion on this connection for a similar system as in this appendix can be found in the article by Blekher, Jauslin and Lebowitz [118].

Appendix D

Oscillating Sublattice Potential

The computations in the following are based on those performed by Martens in his bachelor thesis [60]. Consider p-band graphene similar to Eq. (2.87) on page 30, i.e.

$$H_0(\vec{k}) = \begin{pmatrix} 0 & h(\vec{k}) \\ h^\dagger(\vec{k}) & 0 \end{pmatrix} \tag{D.1}$$

with functions $h(\vec{k})$ that do not need to be specified further for the computations in the following.
A sublattice potential is then introduced via

$$H'(t) = \begin{pmatrix} V\cos(\omega t) & 0 \\ 0 & V\sin(\omega t) \end{pmatrix}, \tag{D.2}$$

where V is the strength of the sublattice potential in units of eV.
The Fourier decomposition of the overall Hamiltonian $H(\vec{k}, t) := H_0(\vec{k}) + H'(t)$ according to Eq. (2.157) (pg. 60) results in the Floquet matrices

$$H_{\pm 1} = \begin{pmatrix} \frac{1}{2} & 0 \\ 0 & \mp\frac{1}{2\mathrm{i}} \end{pmatrix} \tag{D.3}$$

with H_0 defined in Eq. (D.1) and $H_{\pm i} = 0$ for $i > 1$.
The eigenvectors of the matrix (D.1) are given in Eq. (2.95) (pg. 33). They can be rewritten as

$$\vec{v}_{\mathrm{V/C}}(\vec{k}) := \frac{1}{\sqrt{2}} \begin{pmatrix} \mp\frac{h(\vec{k})}{|h(\vec{k})|} \\ 1 \end{pmatrix} \tag{D.4}$$

with eigenvalues

$$E_{V/C}(\vec{k}) = \mp|h(\vec{k})|. \tag{D.5}$$

Via a basis transformation with the matrix $S(\vec{k}) := (\vec{v}_V(\vec{k}), \vec{v}_C(\vec{k}))$, the matrices $H_0(\vec{k})$ and $H_{\pm 1}(t)$ reshape to

$$G_0(\vec{k}) := S^\dagger H_0(\vec{k}) S = \begin{pmatrix} -|h(\vec{k})| & 0 \\ 0 & +|h(\vec{k})| \end{pmatrix} \tag{D.6}$$

and

$$G_{\pm 1} := \frac{1}{V} S^\dagger H_{\pm 1} S = \frac{1}{4} \begin{pmatrix} 1 \pm \mathrm{i} & -1 \pm \mathrm{i} \\ -1 \pm \mathrm{i} & 1 \pm \mathrm{i} \end{pmatrix}. \tag{D.7}$$

From the matrices (D.6) and (D.7), it is possible to define a Floquet Hamiltonian $H_\mathrm{F}(\vec{k}) := H_\mathrm{F}^0(\vec{k}) + V \cdot H_\mathrm{F}^S$, where

$$H_\mathrm{F}^0(\vec{k}) := \begin{pmatrix} G_0(\vec{k}) - \hbar\omega & 0 & 0 \\ 0 & G_0(\vec{k}) & 0 \\ 0 & 0 & G_0(\vec{k}) + \hbar\omega \end{pmatrix}, \; H_\mathrm{F}^S := \begin{pmatrix} 0 & G_{+1} & 0 \\ G_{-1} & 0 & G_{+1} \\ 0 & G_{-1} & 0 \end{pmatrix}. \tag{D.8}$$

The matrix $H_\mathrm{F}^0(\vec{k})$ is diagonal. Its six eigenvalues are

$$\epsilon^0_{V/C}(\vec{k}) := \mp|h(\vec{k})| \qquad \text{and} \qquad \epsilon^0_{V/C,\pm}(\vec{k}) := \epsilon^0_{V/C}(\vec{k}) \pm \hbar\omega. \tag{D.9}$$

The corresponding eigenvectors are of the form $\vec{e}_i$ with $i \in \{1,2,3,4,5,6\}$. Since $\vec{e}_i^{\,t} H_\mathrm{F}^S \vec{e}_i = 0$ for all i, the first-order perturbation terms for H_F^S vanish. In second order, however, the energies $\epsilon^0_{V/C}(\vec{k})$ are modified by terms

$$\epsilon^2_V(\vec{k}) = -\epsilon^2_C(\vec{k}) = -\frac{V^2}{4} \cdot \frac{|h(\vec{k})|}{|2h(\vec{k})|^2 - \hbar^2\omega^2}. \tag{D.10}$$

These correction terms are depicted as a function of $h(\vec{k})$ in Fig. D.1a. The figure uses arbitrary units, as the strength of the sublattice potential has been set to $V = 1$. Since the functions (D.10) are divergent for $|h(\vec{k})| = \hbar\omega/2$, the perturbative approach above is insufficient to cover the perturbative corrections for all values of $h(\vec{k})$. For that reason, consider only the eigenvectors

$$\vec{v}^{\,0}_{C,-}(\vec{k}) := \vec{e}_2 \qquad \text{and} \qquad \vec{v}_V^{\,0}(\vec{k}) := \vec{e}_3 \tag{D.11}$$

with their respective unperturbed eigenenergies

$$\epsilon^0_{C,-}(\vec{k}) = |h(\vec{k})| - \hbar\omega \qquad \text{and} \qquad \epsilon^0_V(\vec{k}) = -|h(\vec{k})|. \tag{D.12}$$

These eigenvectors and eigenenergies correspond to the conduction band with one emitted photon ($\vec{v}^{\,0}_{C,-}(\vec{k})$ and $\epsilon^0_{C,-}(\vec{k})$) and the unperturbed valence band

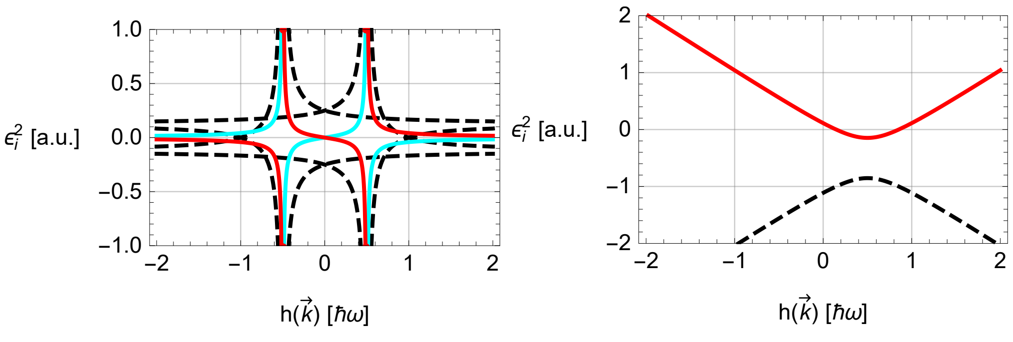

(a) (b)

Figure D.1: Second order perturbation theory corrections to the energies of 0-photon valence (cyan) and conduction band (red) and their (±1)-photon Floquet replica bands (black, dashed); (a) The corrections to the energies of the 0-photon valence and conduction band cross at $h(\vec{k}) = 0$ and diverge at $|h(\vec{k})| = \hbar\omega/2$. (b) Quasi-degenerate perturbation theory shows that the 0-photon valence band and the (-1)-photon conduction band actually exhibit an avoided crossing at $|h(\vec{k})| = \hbar\omega/2$. The figure is inspired by the bachelor thesis of Martens [60].

($\vec{v}_V{}^0(\vec{k})$ and $\epsilon_V^0(\vec{k})$), respectively. The coupling between these is what gives rise to one of the divergences in Eq. (D.10). The part of the Floquet Hamiltonian H_F describing these two states and their interaction can be written as

$$(H_\mathrm{F}(\vec{k}))_{(2,3)} := \begin{pmatrix} \epsilon^0_{C,-}(\vec{k}) + (H^S_\mathrm{F})_{(2,2)} & (H^S_\mathrm{F})_{(2,3)} \\ (H^S_\mathrm{F})_{(3,2)} & \epsilon^0_V(\vec{k}) + (H^S_\mathrm{F})_{(3,3)} \end{pmatrix} = \begin{pmatrix} |h(\vec{k})| - \hbar\omega & -1+\mathrm{i} \\ -1-\mathrm{i} & -|h(\vec{k})| \end{pmatrix}, \tag{D.13}$$

where the subscripts (i,j) denote the i'th row and the j'th column of the respective matrix. The eigenvalues of the matrix in Eq. (D.13) are

$$\epsilon^2_\pm = -\frac{\hbar}{2} \pm \frac{1}{2\sqrt{2}}\sqrt{V^2 + 2(\hbar\omega - 2|h(\vec{k})|)}, \tag{D.14}$$

where the index "+" denotes the correction to the 0-photon valence band and "−" to the (-1)-photon conduction band.

The energies (D.14) are depicted in Fig. D.1b. As can be seen from the figure, they actually exhibit an avoided crossing for $h(\vec{k}) = \hbar\omega/2$. Analogously, the other divergences of Eq. (D.10) turn into avoided crossings as well.

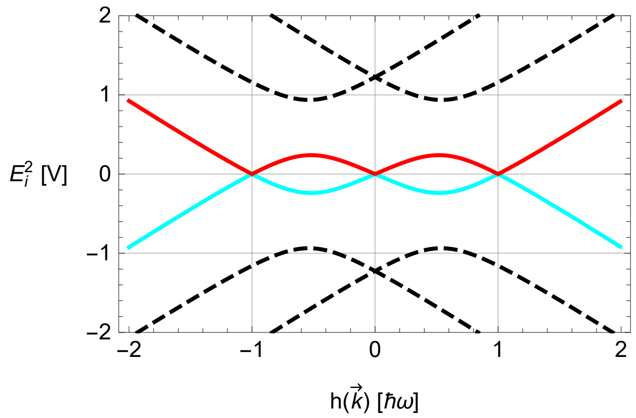

Figure D.2: Floquet quasi-energies of spinless graphene with a time-dependent sublattice potential of $V\cos(\omega t)$ on sublattice A and $V\sin(\omega t)$ on sublattice B, with Floquet order $N = 1$; Valence (cyan) and conduction band (red) touch at $h(\vec{k}) = 0$ and $|h(\vec{k})| = \hbar\omega$. Between those values, the bands exhibit avoided crossing with Floquet replica bands (black, dashed) at $|h(\vec{k})| = \hbar\omega/2$. Close the $K^{(\prime)}$-point, $|h(\vec{k})|$ scales linearly with the distance $|\vec{k} - \vec{K}^{(\prime)}|$.

The actual, non-perturbative eigenvalues of the Floquet Hamiltonian H_F are depicted in Fig. D.2. They touch at $h(\vec{k}) = 0$, exhibit avoided crossings at $|h(\vec{k})| = \hbar\omega/2$ and again touch at $|h(\vec{k})| = \hbar\omega$.

Bibliography

[1] W. H. Bragg, "The Reflection of X-Rays by Crystals", *Nature*, vol. 91, no. 2280, pp. 477–477, Jun. 1913, ISSN: 1476-4687. DOI: `10.1038/091477b0`.

[2] F. Bloch, "Über die Quantenmechanik der Elektronen in Kristallgittern", *Zeitschrift für Physik*, vol. 52, no. 7, pp. 555–600, Jul. 1929, ISSN: 0044-3328. DOI: `10.1007/BF01339455`.

[3] G. Czycholl, *Theoretische Festkörperphysik Band 1 - Grundlagen: Phononen und Elektronen in Kristallen.* ISBN 978-3-662-47140-1, ISBN 978-3-662-47141-8 (eBook), DOI 10.1007/978-3-662-47141-8: Springer Spektrum, 2016.

[4] G. Czycholl, *Theoretische Festkörperphysik Band 2 - Anwendungen: Nichtgleichgewicht, Verhalten in äußeren Feldern, kollektive Phänomene.* ISBN 978-3-662-53700-8, ISBN 978-3-662-53701-5 (eBook), DOI 10.1007/978-3-662-53701-5: Springer Spektrum, 2017.

[5] N. W. Ashcroft and N. D. Mermin, *Solid State Physics.* Holt-Saunders, 1976.

[6] H. P. Boehm, A. Clauss, G. O. Fischer and U. Hofmann, "Das adsorptionsverhalten sehr dünner kohlenstoff-folien", *Zeitschrift für anorganische und allgemeine Chemie*, vol. 316, no. 3-4, pp. 119–127, 1962. DOI: `https://doi.org/10.1002/zaac.19623160303`.

[7] K. Seibert *et al.*, "Femtosecond carrier dynamics in graphite", *Phys. Rev. B*, vol. 42, pp. 2842–2851, 5 Aug. 1990. DOI: `10.1103/PhysRevB.42.2842`.

[8] K. S. Novoselov *et al.*, "Two-dimensional gas of massless Dirac fermions in graphene", *Nature*, vol. 438, no. 7065, pp. 197–200, Nov. 2005, ISSN: 1476-4687. DOI: `10.1038/nature04233`.

[9] Y. Zhang, Y.-W. Tan, H. L. Stormer and P. Kim, "Experimental observation of the quantum Hall effect and Berry's phase in graphene", *Nature*, vol. 438, no. 7065, pp. 201–204, Nov. 2005, ISSN: 1476-4687. DOI: `10.1038/nature04235`.

[10] M. I. Katsnelson, K. S. Novoselov and A. K. Geim, "Chiral tunnelling and the Klein paradox in graphene", *Nature Physics*, vol. 2, no. 9, pp. 620–625, Sep. 2006, ISSN: 1745-2481. DOI: `10.1038/nphys384`.

[11] C. L. Kane and E. J. Mele, "Quantum Spin Hall Effect in Graphene", *Phys. Rev. Lett.*, vol. 95, p. 226 801, 22 Nov. 2005. DOI: `10.1103/PhysRevLett.95.226801`.

[12] J. K. Asbóth, L. Oroszlány and A. Pályi, "A Short Course on Topological Insulators", *Lecture Notes in Physics*, 2016, ISSN: 1616-6361. DOI: `10.1007/978-3-319-25607-8`.

[13] M. V. Berry, "Quantal Phase Factors Accompanying Adiabatic Changes", *Proceedings of the Royal Society of London. Series A, Mathematical and Physical Sciences*, vol. 392, no. 1802, pp. 45–57, 1984, ISSN: 00804630.

[14] D. Tong, *Lectures on the Quantum Hall Effect*, 2016. DOI: `10.48550/ARXIV.1606.06687`.

[15] F. D. M. Haldane, "Model for a Quantum Hall Effect without Landau Levels: Condensed-Matter Realization of the "Parity Anomaly"", *Phys. Rev. Lett.*, vol. 61, pp. 2015–2018, 18 Oct. 1988. DOI: `10.1103/PhysRevLett.61.2015`.

[16] F. D. M. Haldane, "Berry Curvature on the Fermi Surface: Anomalous Hall Effect as a Topological Fermi-Liquid Property", *Phys. Rev. Lett.*, vol. 93, p. 206 602, 20 Nov. 2004. DOI: `10.1103/PhysRevLett.93.206602`.

[17] C. L. Kane and E. J. Mele, "Z_2 Topological Order and the Quantum Spin Hall Effect", *Physical Review Letters*, vol. 95, no. 14, Sep. 2005, ISSN: 1079-7114. DOI: `10.1103/physrevlett.95.146802`.

[18] L. Fu and C. L. Kane, "Topological insulators with inversion symmetry", *Phys. Rev. B*, vol. 76, p. 045 302, 4 Jul. 2007. DOI: `10.1103/PhysRevB.76.045302`.

[19] M. Dyakonov and V. Perel, "Possibility of Orienting Electron Spins with Current", *Soviet Journal of Experimental and Theoretical Physics Letters*, vol. 13, p. 467, May 1971.

[20] M. Dyakonov and V. Perel, “Current-induced spin orientation of electrons in semiconductors”, *Physics Letters A*, vol. 35, no. 6, pp. 459–460, 1971, ISSN: 0375-9601. DOI: `https://doi.org/10.1016/0375-9601(71)90196-4`.

[21] A. Altland and M. R. Zirnbauer, “Nonstandard symmetry classes in mesoscopic normal-superconducting hybrid structures”, *Physical Review B*, vol. 55, no. 2, pp. 1142–1161, Jan. 1997. DOI: `10.1103/physrevb.55.1142`.

[22] A. Kitaev, V. Lebedev and M. Feigel’man, “Periodic table for topological insulators and superconductors”, in *AIP Conference Proceedings*, AIP, 2009. DOI: `10.1063/1.3149495`.

[23] C.-K. Chiu, J. C. Teo, A. P. Schnyder and S. Ryu, “Classification of topological quantum matter with symmetries”, *Reviews of Modern Physics*, vol. 88, no. 3, Aug. 2016. DOI: `10.1103/revmodphys.88.035005`.

[24] J. C. Y. Teo and C. L. Kane, “Topological defects and gapless modes in insulators and superconductors”, *Phys. Rev. B*, vol. 82, p. 115 120, 11 Sep. 2010. DOI: `10.1103/PhysRevB.82.115120`.

[25] R. Roy and F. Harper, “Periodic table for Floquet topological insulators”, *Phys. Rev. B*, vol. 96, p. 155 118, 15 Oct. 2017. DOI: `10.1103/PhysRevB.96.155118`.

[26] M. Luo, “Topological edge states of a graphene zigzag nanoribbon with spontaneous edge magnetism”, *Phys. Rev. B*, vol. 102, p. 075 421, 7 Aug. 2020. DOI: `10.1103/PhysRevB.102.075421`.

[27] H. Min, J. E. Hill, N. A. Sinitsyn, B. R. Sahu, L. Kleinman and A. H. MacDonald, “Intrinsic and Rashba spin-orbit interactions in graphene sheets”, *Phys. Rev. B*, vol. 74, p. 165 310, 16 Oct. 2006. DOI: `10.1103/PhysRevB.74.165310`.

[28] Y. Yao, F. Ye, X.-L. Qi, S.-C. Zhang and Z. Fang, “Spin-orbit gap of graphene: First-principles calculations”, *Phys. Rev. B*, vol. 75, p. 041 401, 4 Jan. 2007. DOI: `10.1103/PhysRevB.75.041401`.

[29] S. Konschuh, M. Gmitra and J. Fabian, “Tight-binding theory of the spin-orbit coupling in graphene”, *Phys. Rev. B*, vol. 82, p. 245 412, 24 Dec. 2010. DOI: `10.1103/PhysRevB.82.245412`.

[30] J. Sichau *et al.*, “Resonance Microwave Measurements of an Intrinsic Spin-Orbit Coupling Gap in Graphene: A Possible Indication of a Topological State”, *Phys. Rev. Lett.*, vol. 122, p. 046 403, 4 Feb. 2019. DOI: `10.1103/PhysRevLett.122.046403`.

[31] J. Sichau, *Electron Spin Resonance Studies on Spin-Orbit Interactions in Graphene - PhD thesis.* `https://ediss.sub.uni-hamburg.de/bitstream/ediss/6041/1/Dissertation.pdf`: Universität Hamburg, 2019.

[32] S. Konschuh, *Spin-Orbit Coupling Effects From Graphene To Graphite - PhD thesis.* `https://epub.uni-regensburg.de/22863/`: Universität Regensburg, 2011.

[33] J. C. Slater and G. F. Koster, "Simplified LCAO Method for the Periodic Potential Problem", *Phys. Rev.*, vol. 94, no. 1498, Jun. 1954. DOI: `\url{https://doi.org/10.1103/PhysRev.94.1498}`.

[34] M. Inglot and V. Dugaev, "Absorption of Twisted and Linearly Polarized Light in Graphene with Rashba Spin-Orbit Interaction", *Acta Physica Polonica A*, vol. 132, pp. 193–195, Jul. 2017. DOI: `10.12693/APhysPolA.132.193`.

[35] Y.-X. Wang and F. Li, "Edge states and phase diagram for graphene under polarized light", *Physica B: Condensed Matter*, vol. 492, pp. 1–6, 2016, ISSN: 0921-4526. DOI: `https://doi.org/10.1016/j.physb.2016.03.029`.

[36] M. S. Mrudul and G. Dixit, "Controlling valley-polarisation in graphene via tailored light pulses", *Journal of Physics B: Atomic, Molecular and Optical Physics*, vol. 54, no. 22, p. 224 001, Nov. 2021. DOI: `10.1088/1361-6455/ac41ae`.

[37] P. H. W. Domcke and D. Tannor, "Driven Quantum Systems", *Special Issue: Chemical Physics*, vol. 217, no. 2–3, pp. 117–416, 1905.

[38] G. Floquet, "Sur les équations différentielles linéaires à coefficients périodiques", fr, *Annales scientifiques de l'École Normale Supérieure*, vol. 2e série, 12, pp. 47–88, 1883. DOI: `10.24033/asens.220`.

[39] W. Magnus and S. Winkler, *Floquet's Theorem, §1.2 in Hill's Equation.* ISBN 0486637387 (print version, paperback) 9780486150291 (electronic version) 9780486495651 (print version): NY : Dover, 1979, pp. 3–8.

[40] T. Oka and S. Kitamura, "Floquet Engineering of Quantum Materials", *Annual Review of Condensed Matter Physics*, vol. 10, no. 1, pp. 387–408, 2019. DOI: `10.1146/annurev-conmatphys-031218-013423`.

[41] L. Broers and L. Mathey, "Observing light-induced Floquet band gaps in the longitudinal conductivity of graphene", *Communications Physics*, vol. 4, Nov. 2021. DOI: `10.1038/s42005-021-00746-6`.

[42] L. Broers and L. Mathey, “Detecting light-induced Floquet band gaps of graphene via trARPES”, *Physical Review Research*, vol. 4, no. 1, Jan. 2022. DOI: `10.1103/physrevresearch.4.013057`.

[43] M. A. Sentef *et al.*, “Theory of Floquet band formation and local pseudospin textures in pump-probe photoemission of graphene”, *Nature Communications*, vol. 6, no. 1, p. 7047, May 2015, ISSN: 2041-1723. DOI: `10.1038/ncomms8047`.

[44] M. Schüler and M. A. Sentef, “Theory of subcycle time-resolved photoemission: Application to terahertz photodressing in graphene”, *Journal of Electron Spectroscopy and Related Phenomena*, vol. 253, p. 147 121, Dec. 2021. DOI: `10.1016/j.elspec.2021.147121`.

[45] X. L. Weijie Wang and H. Xie, “Floquet bands and photon-induced topological edge states of graphene nanoribbons”, *Chinese Physics B*, vol. 30, no. 6, 66701, p. 66 701, 2021. DOI: `10.1088/1674-1056/abddaa`.

[46] Y. Chen, Y. Wang, M. Claassen, B. Moritz and T. P. Devereaux, “Observing photo-induced chiral edge states of graphene nanoribbons in pump-probe spectroscopies”, *npj Quantum Materials*, vol. 5, no. 1, p. 84, Nov. 2020, ISSN: 2397-4648. DOI: `10.1038/s41535-020-00283-5`.

[47] T. Oka and H. Aoki, “Photovoltaic Hall effect in graphene”, *Phys. Rev. B*, vol. 79, p. 081 406, 8 Feb. 2009. DOI: `10.1103/PhysRevB.79.081406`.

[48] J. W. McIver *et al.*, “Light-induced anomalous Hall effect in graphene”, *Nature Physics*, vol. 16, no. 1, pp. 38–41, Nov. 2019. DOI: `10.1038/s41567-019-0698-y`.

[49] R. Nandee, M. A. Chowdhury, A. Shahid, N. Hossain and M. Rana, “Band gap formation of 2D materialin graphene: Future prospect and challenges”, *Results in Engineering*, vol. 15, p. 100 474, 2022, ISSN: 2590-1230. DOI: `https://doi.org/10.1016/j.rineng.2022.100474`.

[50] B. Guo, Q. Liu, E. Chen, H. Zhu, L. Fang and J. R. Gong, “Controllable N-Doping of Graphene”, *Nano Letters*, vol. 10, no. 12, pp. 4975–4980, 2010, PMID: 20968305. DOI: `10.1021/nl103079j`.

[51] A. Lherbier, X. Blase, Y.-M. Niquet, F. ç. Triozon and S. Roche, “Charge Transport in Chemically Doped 2D Graphene”, *Phys. Rev. Lett.*, vol. 101, p. 036 808, 3 Jul. 2008. DOI: `10.1103/PhysRevLett.101.036808`.

[52] D. Usachov *et al.*, “Nitrogen-Doped Graphene: Efficient Growth, Structure, and Electronic Properties”, *Nano Letters*, vol. 11, no. 12, pp. 5401–5407, 2011, PMID: 22077830. DOI: `10.1021/nl2031037`.

[53] X. Wang *et al.*, “N-Doping of Graphene Through Electrothermal Reactions with Ammonia”, *Science*, vol. 324, no. 5928, pp. 768–771, 2009. DOI: `10.1126/science.1170335`.

[54] S.-M. Choi, S.-H. Jhi and Y.-W. Son, “Controlling Energy Gap of Bilayer Graphene by Strain”, *Nano Letters*, vol. 10, no. 9, pp. 3486–3489, 2010, PMID: 20677793. DOI: `10.1021/nl101617x`.

[55] T. Zhang and H. Gao, “Toughening graphene with topological defects: a perspective”, *Journal of Applied Mechanics*, vol. 82, no. 5, p. 051 001, 2015.

[56] J. P. Hague, “Tunable graphene band gaps from superstrate-mediated interactions”, *Phys. Rev. B*, vol. 84, p. 155 438, 15 Oct. 2011. DOI: `10.1103/PhysRevB.84.155438`.

[57] J. P. Hague, “Polarons in highly doped atomically thin graphitic materials”, *Phys. Rev. B*, vol. 86, p. 064 302, 6 Aug. 2012. DOI: `10.1103/PhysRevB.86.064302`.

[58] Y. A. Bychkov and É. I. Rashba, “Properties of a 2D electron gas with lifted spectral degeneracy”, *ZhETF Pisma Redaktsiiu*, vol. 39, p. 66, Jan. 1984.

[59] U. R. Singh *et al.*, “Sublattice symmetry breaking and ultralow energy excitations in graphene-on-*h*BN heterostructures”, *Phys. Rev. B*, vol. 102, p. 245 134, 24 Dec. 2020. DOI: `10.1103/PhysRevB.102.245134`.

[60] K. H. Martens, *Zeitlich getriebene Bandstruktur in Graphen - bachelor thesis*. Universität Hamburg, 2021.

[61] B. A. Foreman, “Consequences of local gauge symmetry in empirical tight-binding theory”, *Phys. Rev. B*, vol. 66, p. 165 212, 16 Oct. 2002. DOI: `10.1103/PhysRevB.66.165212`.

[62] T. B. Boykin and P. Vogl, “Dielectric response of molecules in empirical tight-binding theory”, *Phys. Rev. B*, vol. 65, p. 035 202, 3 Dec. 2001. DOI: `10.1103/PhysRevB.65.035202`.

[63] T. B. Boykin, R. C. Bowen and G. Klimeck, “Electromagnetic coupling and gauge invariance in the empirical tight-binding method”, *Phys. Rev. B*, vol. 63, p. 245 314, 24 Jun. 2001. DOI: `10.1103/PhysRevB.63.245314`.

[64] T. G. Pedersen, K. Pedersen and T. Brun Kriestensen, “Optical matrix elements in tight-binding calculations”, *Phys. Rev. B*, vol. 63, p. 201 101, 20 May 2001. DOI: `10.1103/PhysRevB.63.201101`.

[65] J.-M. Jancu, R. Scholz, F. Beltram and F. Bassani, “Empirical spds* tight-binding calculation for cubic semiconductors: General method and material parameters”, *Phys. Rev. B*, vol. 57, pp. 6493–6507, 11 Mar. 1998. DOI: `10.1103/PhysRevB.57.6493`.

[66] K. Lendi, “Extension of the Slater-Koster tables for tight-binding calculations to f electrons”, *Phys. Rev. B*, vol. 9, pp. 2433–2440, 6 Mar. 1974. DOI: `10.1103/PhysRevB.9.2433`.

[67] A. V. Verkhovtsev, R. G. Polozkov, V. K. Ivanov, A. V. Korol and A. V. Solov’yov, “Hybridization-related correction to the jellium model for fullerenes”, *Journal of Physics B: Atomic, Molecular and Optical Physics*, vol. 45, no. 21, p. 215 101, Sep. 2012. DOI: `10.1088/0953-4075/45/21/215101`.

[68] C. Yannouleas and U. Landman, “Stabilized-jellium description of neutral and multiply charged fullerenes $C_{60}^{x\pm}$”, *Chemical Physics Letters*, vol. 217, no. 3, pp. 175–185, 1994, ISSN: 0009-2614. DOI: `https://doi.org/10.1016/0009-2614(93)E1404-5`.

[69] M. E. Madjet, H. S. Chakraborty, J. M. Rost and S. T. Manson, “Photoionization of C60: a model study”, *Journal of Physics B: Atomic, Molecular and Optical Physics*, vol. 41, no. 10, p. 105 101, May 2008. DOI: `10.1088/0953-4075/41/10/105101`.

[70] J. Schmalian, “Lecture Notes: Condensed Matter Theory I (TKM1)”, 2011, URL: `https://www.tkm.kit.edu/downloads/TKM%5FI%5F2011%5Flecture%5Fnotes.pdf`, Accessed: 2022-11-22.

[71] C. F. Hart and D. Emin, “Time evolution of a Bloch electron in a constant electric field”, *Phys. Rev. B*, vol. 37, pp. 6100–6104, 11 Apr. 1988. DOI: `10.1103/PhysRevB.37.6100`.

[72] D. Emin and C. F. Hart, “Existence of Wannier-Stark localization”, *Phys. Rev. B*, vol. 36, pp. 7353–7359, 14 Nov. 1987. DOI: `10.1103/PhysRevB.36.7353`.

[73] L. Kleinman, “Comment on “Existence of Wannier-Stark localization””, *Phys. Rev. B*, vol. 41, pp. 3857–3858, 6 Feb. 1990. DOI: `10.1103/PhysRevB.41.3857`.

[74] L. L. Foldy and S. A. Wouthuysen, “On the Dirac Theory of Spin 1/2 Particles and Its Non-Relativistic Limit”, *Phys. Rev.*, vol. 78, pp. 29–36, 1 Apr. 1950. DOI: `10.1103/PhysRev.78.29`.

[75] H. Murayama, *221B Lecture Notes Relativistic Quantum Mechanics.* `http://hitoshi.berkeley.edu/` [Online; no longer available]: Berkeley University of California, [Online; accessed 18-January-2022].

[76] R. Quade, *Spin and sublattice spin in an extended tight binding model of graphene - bachelor thesis.* `https://www2.physnet.uni-hamburg.de/services/bibliothek/Examensarbeiten/bachelor/___Bachelorarbeiten/Quade___Robin___2017.pdf` [Online; accessed 20-January-2022]: University of Hamburg, [Online; accessed 20-January-2022].

[77] L. Banszerus *et al.*, “Observation of the Spin-Orbit Gap in Bilayer Graphene by One-Dimensional Ballistic Transport”, *Phys. Rev. Lett.*, vol. 124, p. 177 701, 17 May 2020. DOI: `10.1103/PhysRevLett.124.177701`.

[78] Sumit (`https://physics.stackexchange.com/users/26843/sumit`), *Derivation of Rashba spin-orbit coupling in tight-binding model*, Physics Stack Exchange, URL: `https://physics.stackexchange.com/q/246757` (version: 2020-06-04).

[79] D. J. Thouless, M. Kohmoto, M. P. Nightingale and M. den Nijs, “Quantized Hall Conductance in a Two-Dimensional Periodic Potential”, *Phys. Rev. Lett.*, vol. 49, pp. 405–408, 6 Aug. 1982. DOI: `10.1103/PhysRevLett.49.405`.

[80] A. Akhmerov *et al.*, *Online course on topology in condensed matter.* `https://topocondmat.org/` [Online; accessed February 2022]: TU Delft, [Online; accessed February 2022].

[81] D. Xiao, M.-C. Chang and Q. Niu, “Berry phase effects on electronic properties”, *Reviews of Modern Physics*, vol. 82, no. 3, pp. 1959–2007, Jul. 2010, ISSN: 1539-0756. DOI: `10.1103/revmodphys.82.1959`.

[82] D. R. Hofstadter, “Energy levels and wave functions of Bloch electrons in rational and irrational magnetic fields”, *Phys. Rev. B*, vol. 14, pp. 2239–2249, 6 Sep. 1976. DOI: `10.1103/PhysRevB.14.2239`.

[83] R. Peierls, “Zur Theorie des Diamagnetismus von Leitungselektronen”, *Zeitschrift für Physik*, vol. 80, pp. 763–791, 1933.

[84] A. H. Castro Neto, F. Guinea, N. M. R. Peres, K. S. Novoselov and A. K. Geim, “The electronic properties of graphene”, *Reviews of Modern Physics*, vol. 81, no. 1, pp. 109–162, Jan. 2009, ISSN: 1539-0756. DOI: `10.1103/revmodphys.81.109`.

[85] U. Mizutani, *Introduction to the Electron Theory of Metals.* Cambridge University Press, 2001. DOI: `10.1017/CBO9780511612626`.

[86] W. A. Gó mez-Arias and G. G. Naumis, "Analytical calculation of electron group velocity surfaces in uniform strained graphene", *International Journal of Modern Physics B*, vol. 30, no. 03, p. 1 550 263, Jan. 2016. DOI: `10.1142/s021797921550263x`.

[87] N. Hao, P. Zhang, Z. Wang, W. Zhang and Y. Wang, "Topological edge states and quantum Hall effect in the Haldane model", *Physical Review B*, vol. 78, no. 7, Aug. 2008. DOI: `10.1103/physrevb.78.075438`.

[88] J. de Lisle *et al.*, "Detection of Chern numbers and entanglement in topological two-species systems through subsystem winding numbers", *New Journal of Physics*, vol. 16, no. 8, p. 083 022, Aug. 2014. DOI: `10.1088/1367-2630/16/8/083022`.

[89] E. Alba, J. K. Pachos and J. J. García-Ripoll, "Winding number order in the Haldane model with interactions", *New Journal of Physics*, vol. 18, no. 3, p. 033 022, Mar. 2016. DOI: `10.1088/1367-2630/18/3/033022`.

[90] T. Schmirander, *Spin-Orbit Coupling Effects and Magnetism of the Topological Edge States of Graphene - PhD thesis.* `https://ediss.sub.uni-hamburg.de/handle/ediss/9221`: Universität Hamburg, 2021.

[91] M. O. Goerbig and G. Montambaux, *Dirac Fermions in condensed matter and beyond*, 2014. DOI: `10.48550/ARXIV.1410.4098`.

[92] C. Kane, "Chapter 1 - Topological Band Theory and the Z2 Invariant", in *Topological Insulators*, ser. Contemporary Concepts of Condensed Matter Science, M. Franz and L. Molenkamp, Eds., vol. 6, Elsevier, 2013, pp. 3–34. DOI: `https://doi.org/10.1016/B978-0-444-63314-9.00001-9`.

[93] H. Elvang and Y.-t. Huang, *Scattering Amplitudes*, 2013. DOI: `10.48550/ARXIV.1308.1697`.

[94] Wikipedia, *Chirality (physics).* `https://en.wikipedia.org/wiki/Chirality_(physics)` [Online; accessed 11-March-2022]: Wikimedia Foundation, Inc., [Online; accessed 11-March-2022].

[95] E. S. Meckes, *The Random Matrix Theory of the Classical Compact Groups* (Cambridge Tracts in Mathematics). Cambridge University Press, 2019. DOI: `10.1017/9781108303453`.

[96] Y. Hatsugai, “Chern number and edge states in the integer quantum hall effect”, *Phys. Rev. Lett.*, vol. 71, pp. 3697–3700, 22 Nov. 1993. DOI: `10.1103/PhysRevLett.71.3697`.

[97] Y. Yao *et al.*, “First principles calculation of anomalous hall conductivity in ferromagnetic bcc fe”, *Physical Review Letters*, vol. 92, no. 3, Jan. 2004. DOI: `10.1103/physrevlett.92.037204`.

[98] R. S. K. Mong and V. Shivamoggi, “Edge states and the bulk-boundary correspondence in dirac hamiltonians”, *Phys. Rev. B*, vol. 83, p. 125 109, 12 Mar. 2011. DOI: `10.1103/PhysRevB.83.125109`.

[99] F. Schindler *et al.*, “Higher-order topological insulators”, *Science Advances*, vol. 4, no. 6, eaat0346, 2018. DOI: `10.1126/sciadv.aat0346`.

[100] J. H. Shirley, “Solution of the Schrödinger Equation with a Hamiltonian Periodic in Time”, *Phys. Rev.*, vol. 138, B979–B987, 4B May 1965. DOI: `10.1103/PhysRev.138.B979`.

[101] M. S. Rudner, N. H. Lindner, E. Berg and M. Levin, “Anomalous edge states and the bulk-edge correspondence for periodically driven two-dimensional systems”, *Phys. Rev. X*, vol. 3, p. 031 005, 3 Jul. 2013. DOI: `10.1103/PhysRevX.3.031005`.

[102] N. H. Lindner, G. Refael and V. Galitski, “Floquet topological insulator in semiconductor quantum wells”, *Nature Physics*, vol. 7, no. 6, pp. 490–495, Jun. 2011, ISSN: 1745-2481. DOI: `10.1038/nphys1926`.

[103] T. Kitagawa, E. Berg, M. Rudner and E. Demler, “Topological characterization of periodically driven quantum systems”, *Phys. Rev. B*, vol. 82, p. 235 114, 23 Dec. 2010. DOI: `10.1103/PhysRevB.82.235114`.

[104] A. D. Bandrauk, F. Fillion-Gourdeau and E. Lorin, “Atoms and molecules in intense laser fields: gauge invariance of theory and models”, *Journal of Physics B: Atomic, Molecular and Optical Physics*, vol. 46, no. 15, p. 153 001, Jul. 2013, ISSN: 1361-6455. DOI: `10.1088/0953-4075/46/15/153001`.

[105] G. H. Wannier, “Dynamics of Band Electrons in Electric and Magnetic Fields”, *Rev. Mod. Phys.*, vol. 34, pp. 645–655, 4 Oct. 1962. DOI: `10.1103/RevModPhys.34.645`.

[106] J. M. Luttinger, “The Effect of a Magnetic Field on Electrons in a Periodic Potential”, *Phys. Rev.*, vol. 84, pp. 814–817, 4 Nov. 1951. DOI: `10.1103/PhysRev.84.814`.

[107] W. Kohn, "Theory of Bloch Electrons in a Magnetic Field: The Effective Hamiltonian", *Phys. Rev.*, vol. 115, pp. 1460–1478, 6 Sep. 1959. DOI: `10.1103/PhysRev.115.1460`.

[108] M. Schüler, J. A. Marks, Y. Murakami, C. Jia and T. P. Devereaux, "Gauge invariance of light-matter interactions in first-principle tight-binding models", *Physical Review B*, vol. 103, no. 15, Apr. 2021. DOI: `10.1103/physrevb.103.155409`.

[109] M. Schüler *et al.*, "How Circular Dichroism in Time- and Angle-Resolved Photoemission Can Be Used to Spectroscopically Detect Transient Topological States in Graphene", *Phys. Rev. X*, vol. 10, p. 041 013, 4 Oct. 2020. DOI: `10.1103/PhysRevX.10.041013`.

[110] M. V. Durnev, "Photovoltaic Hall effect in the two-dimensional electron gas: Kinetic theory", *Phys. Rev. B*, vol. 104, p. 085 306, 8 Aug. 2021. DOI: `10.1103/PhysRevB.104.085306`.

[111] M. Nakamura, "De haas-shubnikov oscillation of the impurity band in n-type germanium", *Journal of the Physical Society of Japan*, vol. 22, no. 3, pp. 830–832, 1967. DOI: `10.1143/JPSJ.22.830`.

[112] A. Bayani, M. Ashwin Kishore and K. Larsson, "The influence by substrate morphology on the Rashba band splitting in graphene", *Results in Physics*, vol. 17, p. 103 065, 2020, ISSN: 2211-3797. DOI: `https://doi.org/10.1016/j.rinp.2020.103065`.

[113] A. Ló pez and R. A. Molina, "Photoprotected spin Hall effect on graphene with substrate induced Rashba spin-orbit coupling", *Journal of Physics: Condensed Matter*, vol. 32, no. 20, p. 205 701, Feb. 2020. DOI: `10.1088/1361-648x/ab6cc0`.

[114] Y. S. Dedkov, M. Fonin, U. Rüdiger and C. Laubschat, "Rashba Effect in the Graphene/Ni(111) System", *Physical Review Letters*, vol. 100, no. 10, Mar. 2008. DOI: `10.1103/physrevlett.100.107602`.

[115] L. Sun, X. Ma, J. Liu and M. Zhao, "Laser-driven anisotropic and nonlinear rashba spin splitting in gaas monolayer", *Phys. Rev. B*, vol. 104, p. 085 140, 8 Aug. 2021. DOI: `10.1103/PhysRevB.104.085140`.

[116] K. O. Alexander Kramida and Y. Ralchenko, "Periodic Table: Atomic Properties of the Elements", National Institute of Standards and Technology, Gaithersburg, MD, Tech. Rep. NIST SP 966, version 14, 2019, [Online; accessed 08-January-2023].

[117] M. Rodriguez-Vega, M. Lentz and B. Seradjeh, "Floquet perturbation theory: Formalism and application to low-frequency limit", *New Journal of Physics*, vol. 20, Sep. 2018. DOI: `10.1088/1367-2630/aade37`.

[118] P. M. Blekher, H. R. Jauslin and J. L. Lebowitz, "Floquet spectrum for two-level systems in quasiperiodic time-dependent fields", *Journal of Statistical Physics*, vol. 68, no. 1, pp. 271–310, Jul. 1992, ISSN: 1572-9613. DOI: `10.1007/BF01048846`.

[119] H.-J. Schmidt, "The floquet theory of the two-level system revisited", *Zeitschrift für Naturforschung A*, vol. 73, no. 8, pp. 705–731, Jun. 2018. DOI: `10.1515/zna-2018-0211`.

[120] H.-J. Schmidt, J. Schnack and M. Holthaus, *Floquet theory of the analytical solution of a periodically driven two-level system*, 2018. DOI: `10.48550/ARXIV.1809.00558`.

[121] B. Zhou, H.-Z. Lu, R.-L. Chu, S.-Q. Shen and Q. Niu, "Finite Size Effects on Helical Edge States in a Quantum Spin-Hall System", *Phys. Rev. Lett.*, vol. 101, p. 246 807, 24 Dec. 2008. DOI: `10.1103/PhysRevLett.101.246807`.

[122] X.-Y. Wang, A. Narita and K. Müllen, "Precision synthesis versus bulk-scale fabrication of graphenes", *Nature Reviews Chemistry*, vol. 2, no. 1, p. 0100, Dec. 2017, ISSN: 2397-3358. DOI: `10.1038/s41570-017-0100`.

[123] D. J. Rizzo *et al.*, "Topological band engineering of graphene nanoribbons", *Nature*, vol. 560, no. 7717, pp. 204–208, Aug. 2018, ISSN: 1476-4687. DOI: `10.1038/s41586-018-0376-8`.

[124] D. J. Trainer *et al.*, "Artificial Graphene Nanoribbons: A Test Bed for Topology and Low-Dimensional Dirac Physics", *ACS Nano*, vol. 16, no. 10, pp. 16 085–16 090, 2022, PMID: 35969666. DOI: `10.1021/acsnano.2c04361`.

[125] D. Gosálbez-Martínez, J. J. Palacios and J. Fernández-Rossier, "Spin-orbit interaction in curved graphene ribbons", *Physical Review B*, vol. 83, no. 11, Mar. 2011, ISSN: 1550-235X. DOI: `10.1103/physrevb.83.115436`.

[126] D. Huertas-Hernando, F. Guinea and A. Brataas, "Spin-orbit coupling in curved graphene, fullerenes, nanotubes, and nanotube caps", *Phys. Rev. B*, vol. 74, p. 155 426, 15 Oct. 2006. DOI: `10.1103/PhysRevB.74.155426`.

[127] B. Cordero *et al.*, "Covalent radii revisited", *Dalton Trans.*, pp. 2832–2838, 21 2008. DOI: `10.1039/B801115J`.

[128] R. T. Sanderson, "Electronegativity and bond energy", *Journal of the American Chemical Society*, vol. 105, no. 8, pp. 2259–2261, 1983. DOI: `10.1021/ja00346a026`.

[129] J. C. Slater, "Atomic radii in crystals", *The Journal of Chemical Physics*, vol. 41, no. 10, pp. 3199–3204, 1964. DOI: `10.1063/1.1725697`.

[130] D. Kulkarni, D. Schmidt and S.-K. Tsui, "Eigenvalues of tridiagonal pseudo-toeplitz matrices", *Linear Algebra and its Applications*, vol. 297, no. 1, pp. 63–80, 1999, ISSN: 0024-3795. DOI: `https://doi.org/10.1016/S0024-3795(99)00114-7`.

Acknowledgements

There are many people I want to thank for supporting me during my work on this thesis. In general, I am grateful towards all of my supervisors, colleagues, friends, family members and people who helped me in the past years. In the following, I want to express my gratitude to those who had the greatest impact on this thesis.

First, I want to thank my two supervisors Prof. Dr. Daniela Pfannkuche and Dr. Marta Prada. Daniela Pfannkuche has been there for me all the time and supported me throughout the entirety of this project. Meanwhie, she never showed signs of exhaustion when I bombarded her with questions. During the past years, she has taught me a lot, and she has always been there for me whenever I needed help. I absolutely cannot emphasise enough how grateful I am to her, and I will miss the time working under her supervision. Marta Prada has not only been my supervisor, but she is also one of the two people behind the original draft that gave rise to my PhD thesis. Hence, I would not even be able to write this paragraph if it was not for her. She has guided me through many steps of this thesis and helped me a lot. Her expertise has been invaluable for me, and I am truly grateful to her.

The other person behind the draft is Dr. Alexander Chudnovskiy. I want to thank him for helping me initiate this project and also for offering his help whenever I needed it.

Prof. Dr. Tim Wehling has my gratitude for agreeing to grade my thesis. Without hesitation, he was able to answer to my rather sudden request, thereby taking a burden from me.

Further, I want to thank Prof. Dr. Michael Potthoff and Dr. Thore Posske for helping me understand topology in condensed matter systems. They were able to guide me when I encountered phenomena I did not understand on my own. They thereby not only assisted me with my thesis, but even helped me deepen my understanding of physics in general.

My gratitude also goes towards Binne Sörine Krüger who supervised the scholarship through which I was employed the first three years of my thesis. A scholarship comes with some difficulties compared to regular employment, but she did an outstanding job at helping me whenever things got difficult.

I want to thank my whole family. In particular, my parents Marlies and Bernd Bartelmann and my brother Magnus Bartelmann always had my back, and they allowed me to fully focus on my thesis without having to worry about anything else. I am fully aware of how I should not take this for granted, and thus I am all the more grateful towards them.

I consider myself incredibly lucky to have many amazing friends. Each and every one of them would be deserving of an entire paragraph here. In the following, I want to highlight those who specifically helped me with this thesis. In particular, Dr. Thorben Schmirander provided a lot of help: He was the one who taught me the basics of graphene and showed me several phenomena related to it. I have asked him for advice so many times that I lost track, and I feel deeply indebted to his help. He even helped me by proofreading large portions of this thesis despite having a full-time job at the time.
Robin Quade also read large parts of my thesis and gave me invaluable advice. Moreover, I am impressed by the speed and accuracy with which he did so. He has my deep gratitude for not only providing massive help, but for also being able to do so on a very spontaneous note.
Further proofreading has been performed by Jan Plettenberg who has been a friend to me since I started my bachelor's degree. I cannot mention him without also mentioning Dr. Lennart Döppenschmitt. Both of them are great friends who helped and encouraged me throughout all my studies. I therefore want to thank them for accompanying me through everything that happened during the past decade.
I also want to thank Anastasia Veialko for countless inspiring discussions on the aesthetics of my figures. I have always strived for this work to be pleasing to look at. She helped me achieve that by providing artistic advice. Moreover, she helped me learn something about art while studying physics.

In addition to support for the thesis, I also received aid in the preparation of the disputation. In particular, I therefore want to thank Dr. Karel Výborný, who allowed me to present and discuss my results in Prague.

As a final note, I want to thank my dog Nero. I have been working on this thesis during the times of a pandemic, and I cannot imagine how I would have endured these times without him.

Eidesstattliche Versicherung / Declaration on oath

Hiermit versichere ich an Eides statt, die vorliegende Dissertationsschrift selbst verfasst und keine anderen als die angegebenen Hilfsmittel und Quellen benutzt zu haben.

Hamburg, den ______________ Unterschrift: ____________________________